NOTE TO USERS

Page(s) not included in the original manuscript are unavailable from the author or university. The manuscript was microfilmed as received

xvi - xviii

This reproduction is the best copy available.

UMI°

EFFECT OF MICROALLOYING ON MICROSTRUCTURE AND HOT WORKING BEHAVIOR FOR AZ31 BASED MAGNESIUM ALLOY

By Lihong Shang

A Thesis Submitted to the Faculty of Graduate Studies and Research in Partial Fulfillment of the Requirements for the Degree of Doctor of Philosophy

Department of Mining and Materials Engineering McGill University Montreal, Quebec, Canada

April 2008



Library and Archives Canada

Published Heritage Branch

395 Wellington Street
Ottawa ON K1A 0N4
Canada

Bibliothèque et Archives Canada

Direction du Patrimoine de l'édition

395, rue Wellington Ottawa ON K1A 0N4 Canada

> Your file Votre référence ISBN: 978-0-494-66660-9 Our file Notre référence ISBN: 978-0-494-66660-9

NOTICE:

The author has granted a non-exclusive license allowing Library and Archives Canada to reproduce, publish, archive, preserve, conserve, communicate to the public by telecommunication or on the Internet, loan, distribute and sell theses worldwide, for commercial or non-commercial purposes, in microform, paper, electronic and/or any other formats.

The author retains copyright ownership and moral rights in this thesis. Neither the thesis nor substantial extracts from it may be printed or otherwise reproduced without the author's permission.

AVIS:

L'auteur a accordé une licence non exclusive permettant à la Bibliothèque et Archives Canada de reproduire, publier, archiver, sauvegarder, conserver, transmettre au public par télécommunication ou par l'Internet, prêter, distribuer et vendre des thèses partout dans le monde, à des fins commerciales ou autres, sur support microforme, papier, électronique et/ou autres formats.

L'auteur conserve la propriété du droit d'auteur et des droits moraux qui protège cette thèse. Ni la thèse ni des extraits substantiels de celle-ci ne doivent être imprimés ou autrement reproduits sans son autorisation.

In compliance with the Canadian Privacy Act some supporting forms may have been removed from this thesis.

While these forms may be included in the document page count, their removal does not represent any loss of content from the thesis.

Conformément à la loi canadienne sur la protection de la vie privée, quelques formulaires secondaires ont été enlevés de cette thèse.

Bien que ces formulaires aient inclus dans la pagination, il n'y aura aucun contenu manquant.



Abstract

The formability of Mg alloy sheet in the as-hot rolled condition depends on the microstructure developed during hot rolling. In general, the formability of Mg alloys is improved by finer grain sizes. 'Microalloying' levels of calcium (Ca), strontium (Sr), and cerium (Ce) have been found to refine the as-cast structure, but there is no information as to whether this effect will be reflected in the as-hot worked structure and formability. Thus, in this work, the effects of microalloying levels of calcium (Ca), strontium (Sr), and cerium (Ce) on the microstructures (from as-cast to as-hot rolled) and subsequent hot deformation behavior of AZ31, nominally 3% Al, 1% Zn, and 0.3%Mn, were systematically investigated.

To include the effect of solidification rate these alloys were cast in different moulds (preheated steel mould, Cu-mould, and water cooled Cu-mould). One-hit compression testing at temperatures between 250 °C \sim 400 °C, strain rates of 0.001, 0.01, 0.1 s⁻¹, and strains from 0.2 up to 1.0, was performed to investigate the basic hot compression behavior, while two-hit compression testing was conducted to determine the static softening behavior. Hot rolling of the microalloyed AZ31 alloys was then carried out to study the effects of microalloying on as-hot rolled structure under two sets of rolling schedules. To investigate the formability of these microalloyed sheets, tensile tests were completed over a temperature range between ambient and 450 °C, at strain rates between 0.1 and 0.0003 s⁻¹.

Results show that Ca and Sr act to refine the as cast grain size and the second phases, consistently promoting fine and uniform as-hot rolled grain structure. With regard to grain refinement, calcium has the strongest effect, whereas Ce is most effective for second phase refinement. In addition, microalloying retards grain growth during hot tensile testing. Multiple alloying presents a combined and complementary effect.

A refined and uniform grain structure combined with well dispersed and thermally stable second phases significantly improves the hot formability of AZ31 sheets by promoting dynamic recrystallization (DRX) in the matrix, resisting grain coarsening, and retarding the development of cavitation and necking. Under the superplastic condition of 450 °C and 0.0003 s⁻¹, the elongation was improved by 17% with Ca only, 26% with Ca and Ce, 51% with Ca and Sr, and 59% with Ca, Sr and Ce.

Résumé

La formabilité de l'alliage de magnésium AZ31 (soit 3 % Al, 1 % Zn et 0,2 % Mn) dépend de la microstructure générée par le laminage à chaud. En réduisant la taille des grains, il est possible d'améliorer la formabilité. L'ajout de faibles quantités de microalliages de calcium (Ca), de strontium (Sr) et de cérium (Ce) permet d'affiner la structure de coulée, mais rien n'indique que l'effet sera similaire sur la structure déformée à chaud ainsi que sur la formabilité. Le présent travail porte donc sur les effets des microalliages de Ca, Sr et Ce sur les microstructures et le comportement d'AZ31 suivant la déformation à chaud.

Pour tenir compte de l'effet du taux de solidification, les alliages ont été coulés dans différents moules (moule d'acier préchauffé, moule de cuivre et moule de cuivre refroidi à l'eau). Les tests de compression ont été réalisés à des températures variant entre 250 °C et 400 °C à des vitesses de déformation de 0.001, 0.01 et 0.1 s⁻¹, et pour des déformations allant de 0.2 à 1.0. L'effet de la restauration statique a ensuite été étudié au moyen de tests de compression double (two-hit compression testing). Ensuite, des lingots de composition AZ31 microallié ont été laminés à chaud selon deux programmes de laminage pour étudier les effets du microalliage sur la microstructure. Les feuilles microalliées ont ensuite été soumises à des essais de traction à des températures variant entre la température ambiante et 450 °C, à des vitesse de déformation allant de 0.1 à 0.0003 s⁻¹.

Les résultats montrent que l'ajout de Ca et Sr a pour effet de favoriser une microstructure fine et uniforme. Ca produit l'effet le plus notable sur la grosseur des grains, tandis que Ce se révèle le plus efficace pour l'affinage des précipités. De plus, le microalliage retarde la croissance des grains pendant les essais de traction à chaud. La présence de multiples éléments d'alliage produit un effet combiné et complémentaire.

Une microstructure fine jumelée à des précipités uniformément répartis et thermiquement stables améliore significativement la formabilité à chaud d'AZ31 en favorisant la recristallisation dynamique dans la matrice, en résistant à la croissance du grain et en retardant la cavitation et le necking. Sous la condition superplastique de 450 °C et 0.0003 s⁻¹, l'élongation a été améliorée de 17 % avec seulement Ca, de 26 % avec Ca et Ce, de 51 % avec Ca et Sr, et de 59 % avec Ca, Sr et Ce.

Acknowledgements

First of all, I would like to thank my graduate supervisor, Professor Stephen Yue, for generating such an interesting and practical Ph.D. project for me, and for his excellent guidance and constant support throughout the project. His scientific insight, invaluable suggestions, and confidence in my abilities have been extremely encouraging to me as a great source of inspiration, which are greatly appreciated.

Special thanks are attributed to research scientists who were engaged in this collaborative project: Dr. Elhachmi Essadiqi, Dr. Amjad Javaid, and Dr. Claude Galvani at Materials Technology Laboratory-CANMET; Dr. Ravi Verma, Dr. Jon Carter, Dr. Carl Fuerst and Dr. Paul Krajewski at General Motors, who provided great assistance and constructive suggestions on my research work, and arranging related casting, rolling and tensile tests. I am tremendously grateful for their input and support.

Many thanks go to the professors in the department for their precious advice on my project: Prof. Mihriban O. Pekguleryuz in alloy design and casting, Prof. Jerzy A. Szpunar for crystallography and texture analysis, Prof. John Jonas for deformation flow behavior, Prof. Raynald Gauvin for SEM analysis, and Prof. In-Ho Jung for phase thermodynamic prediction. Special thanks to our technicians, Mr. Edwin Fernandez and Mr. Pierre Vermette in specimen preparation for various tests of this project.

I wish to thank all my colleagues at McGill who made my stay here filled with friendship, learning, and fun. Many thanks to the Mg-research group: Emilie Hsu, Faramarz Zarandi, Hualong Li, Rocco Varano, Luke W. F. Mackenzie, Geoff Seale, Geremi Vespa, Jennifer Cocle, and Mohsen Shahi; and the deformation research group: Jesica Calvo Muñoz, Phuong Vo, Ehab Samuel, Etienne Martin, Jinbo Qu, Youjiang He, Salim Brahimi, Ahmad Rezaeian, Arya Fatehi, Ahmad Chamanfar, and Abdelbaset Elwazri. Special thanks go to Lan Jiang, Xin Zhang, Xinran Wang, Li Zhang, and Yaneth

Aguilar-Diaz for the interesting and enjoyable times. All of you have made my time of study here at McGill memorable.

I am very grateful to the Natural Sciences and Engineering Research Council of Canada and to General Motors of Canada, for funding this project.

Finally, I would like to extend my sincere appreciation to all the people in my family, in particular, my husband Li and our son Yang, for their unconditional love, continuous support and infinite encouragement.

TABLE OF CONTENTS

	Page
Abstra	cti
	éiii
Acknow	vledgementsv
	of Contentsvii
List of	Figures xii
List of	Tablesxix
	CHAPTER 1
Introdu	uction1
Refere	nces
	CHAPTER 2
Literat	ure Review6
2.1	Alloying Effect on Properties of Mg6
2.1.1	General Principles of Alloying
2.1.2	Alloying Effect on Strengthening
2.1.2.1	Solid Solution Strengthening
2.1.2.2	Precipitation Strengthening
2.1.2.3	Grain Boundary Strengthening
2.1.3	Main Alloying Elements in Mg Alloys
2.1.4	Existing Commercial Wrought Mg-alloys and Further Improvement
2.2	Deformation Characteristics of Mg
2.2.1	Slip Systems
2.2.2	Twinning
2.2.3	Anisotropy21
2.3	Dynamic Recrystallization (DRX) of Mg23
2.3.1	Different Mechanisms
2.3.1.1	Bulging mechanism (conventional DRX or discontinuous DRX)

2.3.1.2	Subgrain mechanism (continuous DRX)	24
2.3.1.3	Twinning DRX mechanism (TDRX)	25
2.3.1.4	Dislocation Mechanism	26
2.3.2	Factors influencing DRX	26
2.3.2.1	Deformation Conditions	26
2.3.2.2	Initial Grain Size	27
2.3.2.3	Initial Texture	27
2.3.2.4	Alloying Elements	28
2.4	Mg-sheet Producing	28
2.4.1	Conversional Processing.	28
2.4.2	Innovative Strip Casting and Subsequent Rot Rolling Processing	29
2.5	Summary	32
Refere	nces	33
	CHAPTER 3	
Resear	rch Objectives	40
	CHAPTER 4	
Experi	imental Procedure	41
4.1	As-cast Sample Preparation	41
4.1.1	Alloy Design	41
4.1.2	Raw Materials	43
4.1.3	Casting Moulds	4 4
4.1.4	Casting Moulus.	
7.1.7	Casting Conditions	
4.2		4 4
	Casting Conditions	44
4.2	Casting Conditions Compression Testing	4445
4.2 4.2.1	Casting Conditions Compression Testing Specimens	
4.2 4.2.1 4.2.2	Casting Conditions Compression Testing Specimens Facilities	
4.2 4.2.1 4.2.2 4.2.3	Casting Conditions Compression Testing Specimens Facilities Test Schedules and Conditions	
4.2 4.2.1 4.2.2 4.2.3 4.3	Casting Conditions Compression Testing Specimens Facilities Test Schedules and Conditions Rolling Experiments	

4.4.1	Ambient Temperature Tensile Testing	51
4.4.1.1	Specimens	51
4.4.1.2	Facilities and Test Conditions	52
4.4.2	Elevated Temperature Tensile Testing	52
4.4.2.1	Specimens	52
4.4.2.2	Facilities	53
4.4.2.3	Test Conditions	53
4.5	Characterization	53
4.5.1	Chemical Composition Analysis	. 53
4.5.2	Microstructure Analysis	. 54
4.5.2.1	Sample Selection	. 54
4.5.2.2	Sample Preparation	. 54
4.5.2.3	Optical Metallography	. 55
4.5.2.4	SEM with EDS Analysis	. 55
4.5.2.5	Electron Probe Microanalysis (EPMA)	. 55
4.5.2.6	Electron Backscattered Diffraction Analysis (EBSD)	. 56
4.5.3	Measurement of Lattice Parameters (a, c, c/a)	. 56
4.5.4	Texture Measurement for Sheet Materials	. 56
Refere	nces	. 57
	CHAPTER 5	
Alloy I	Design and Casting	
5.1	Results	
5.1.1	Chemical Composition Analysis and Alloying Efficiency	
5.1.2	Microstructural Analysis	
	Grain Structure	
5.1.2.2	Formation of Second Phases by Alloying	
5.1.3	Measurement of Lattice Parameters	
5.2	Discussion	
5.2.1	Effect of Cooling Rate on Microstructure	
	Grain Size	
	Intermetallic Phases	
5.2.2	Effect of Ca. Sr. and Ce on Microstructure	. 72

5.2.2.1	Effect of Ca and Sr on Grain Size	72
	Effect of Ca, Sr and Ce on the Formation of Second Phases	
5.2.3	Effect of c/a Ratio (lattice parameter) on Deformation	
5.3	Summery	
Refere	nces	76
	CHAPTER 6	
Compr	ression Testing	78
6.1	Results	78
6.1.1	One Hit Compression Testing	78
6.1.1.1	Flow Behavior of AZ31	78
6.1.1.2	Dynamic Recrystallization (DRX) in AZ31	79
6.1.1.3	Alloying Effect on Hot Compressive Behaviors of AZ31	86
6.1.2	Two Hit Compression Testing	91
6.1.2.1	Flow Behavior and Interpass Softening	91
6.1.2.2	Microstructure Evolution	92
6.2	Discussion	94
6.2.1	Influence of Deformation Conditions on the Flow Behavior	94
6.2.2	Dynamic Recrystallization (DRX) Mechanisms	97
6.2.2.1	Discontinuous DRX and Continuous DRX	97
6.2.2.2	Particle Stimulated Nucleation (PSN)	99
6.2.2.3	Twinning Induced DRX (TDRX)	100
6.2.3	Effect of Alloying on DRX	101
6.2.4	Alloying Effect on Interpass Softening	103
6.3	Summery	103
Refere	ences	105
	CHAPTER 7	
Rolling	g	
7.1	Results	
7.1.1	Reheating Experiment	108
7.1.2	Condition of the As-rolled sheets	110
7.1.3	As-Hot Rolled Microstructure	111

7.1.4	As-Annealed Microstructure	. 118
7.1.5	Texture Measurement for As-Rolled Sheets	. 119
7.2	Discussion	. 126
7.2.1	Hot Deformation Mechanisms under Rolling Conditions	. 126
7.2.2	Effect of Microalloying on Microstructure during Hot Rolling and Annealing	. 130
7.2.3	Effect of Microalloying on the Texture of AZ31 Based Sheets	. 131
7.3	Summery	. 132
Refere	nces	. 134
	CVI A PATED O	
	CHAPTER 8	105
	Testing	
8.1	Results	
8.1.1	Ambient Temperature Tensile Testing	
8.1.2	Elevated Temperature Tensile Testing	
	Flow Behaviour under Various Conditions	
	Fracture Behaviour	
8.1.2.3	Interrupted Testing under Superplastic Deformation Conditions	. 146
8.2	Discussion	. 150
8.2.1	Effect of Microalloying on Ambient Temperature Properties	. 150
8.2.2	High-temperature Deformation Mechanisms	. 152
8.2.3	Effect of Microalloying on Superplasticity	. 154
8.2.3.1	Second Phases and Grain Structure	. 154
8.2.3.2	Microstructure Evolution and Occurrence of DRX	. 159
8.3	Summery	. 163
Refere	nces	165
Conclu	CHAPTER 9	. 166
~ JHUIU		
	CHAPTER 10	
Contri	butions to Original Knowledge	. 171

LIST OF FIGURES

Figure	Page
Fig.2.1	Atomic diameters of the elements and the favorable size factor with respect to magnesium [6]
Fig.2.2	Mechanical properties of developed (Mg-Al7.1Zn0.60Mn0.30) alloy compared with AZ80 alloy [40]
Fig.2.3	Mechanical properties of Mg-Li-Al alloys and AM20 standard alloy [44]
Fig.2.4	Mechanical properties of Mg-Li-Zn alloys and ZM21 standard alloy [44]
Fig.2.5	Mg-sheet has advantage over steel sheet and Al-sheet for body panel: E is the elastic modulus, ρ is the density, and Rp0.2 is yield strength [49]
Fig.2.6	Dependence of ductility on grain size [50]
Fig.2.7	Principal slip systems and twinning: (a) the $(0001) < 11\overline{2}0 >$ basal slip system, (b) the $\{10\overline{1}0\} < 11\overline{2}0 >$ prismatic slip system, (c) the $\{1\overline{2}12\} < \overline{1}\overline{1}23 >$ second order pyramidal slip system, d) $\{1\overline{1}01\} < 11\overline{2}0 >$ and $\{1\overline{1}02\} < 11\overline{2}0 >$ first order pyramidal slip systems, e) the $\{10\overline{1}0\} < 10\overline{1}\overline{2} >$ twinning, f) the $\{10\overline{1}2\} < \overline{1}011 >$ twinning [53-59].
Fig.2.8	Uniaxial compression test under different temperatures [60]
Fig.2.9	An example of double twinning of $\{10\overline{1}1\}$ - $\{10\overline{1}2\}$ for the Mg-0.2Ce% cold rolled to 10% reduction: a) $\{10\overline{1}1\}$ twin boundaries $(56^{\circ} < 11\overline{2}0 > \pm 5^{\circ})$, b) $\{10\overline{1}2\}$ twin boundaries $(86^{\circ} < 11\overline{2}0 > \pm 5^{\circ})$, c) bounders expected from $\{10\overline{1}1\}$ - $\{10\overline{1}2\}$ double twinning $(38^{\circ} < 11\overline{2}0 > \pm 5^{\circ})$, and d) interpretation of twins B and C [64]
Fig.2.10	Stress-strain curves for AZ31B: a) Tension and Compression for the material as extruded, b) Tension for the sheet as annealed, c) Compression for sheet as annealed [67]
Fig.2.11	Microstructural mechanism map for pure magnesium (I - the area of transformation of initial twins into recrystallised grains) [72]
Fig.2.12	Schematic diagram showing the CDRX- "subgrain" by progressive lattice rotation and dynamic recovery at grain boundaries [77]
Fig.2.13	AZ31 sheet produced by conventional process at laboratory [92]

Fig.2.14	Development and application of Mg-strip casting technology [94]
Fig.2.15	As-cast microstructure of AZ31 and ZEK100 after DC and twin belt strip casting $^{[94]}$. 31
Fig.2.16	Strain values of Mg sheets rolled from different cast feedstock of AZ31 sheets (surface milled before rolling to 6 mm thickness and the same rolling schedule for all specimens (non-optimized)) [104]
Fig.4.1	The flowchart of experimental procedure
Fig.4.2	Configuration of casting moulds and corresponding samples: a) steel mould, b) copper mould, c) copper mould with water cooling
Fig.4.3	Specimens or compression experiment: a) from plate casting, b) from disk shape casting
Fig.4.4	Compression test set up: a) MTS testing machine, b) sample in radiant furnace 47
Fig.4.5	Compression test schedules: a) one hit test, b) two hit test
Fig.4.6	Rolling facilities to make Mg-sheets
Fig.4.7	Configuration of tensile specimens tested at ambient temperature, TD: transverse direction, RD: rolling direction
Fig.4.8	Configuration of tensile specimens tested at elevated temperature per ASTM E2448-06
Fig.4.9	Elevated temperature testing machine: a) set-up, b) furnace
Fig.4.10	Surfaces examined in microstructure analysis: a) as cast, b) compressed, c) as-rolled, and d) tensile tested
Fig.5.1	An Optical metallographes of grain size for AZ31 alloy cast under different cooling conditions: a) direct chilling, b) steel mould, c) copper mound
Fig.5.2	EBSD maps of grain size in surface region of samples cast in copper mould: a) AZ31, b) AZ31+0.19%Sr, and c) AZ31+0.19%Ca
Fig.5.3	Optical metallographes of grain size in samples of AZ31 and AZ31 with Ca cast under different cooling conditions: a) AZ31 in steel mould, b) AZ31+0.17%Ca in steel mould
Fig.5.4	The Optical metallographs of second phases in samples cast in copper mould: a) AZ31, b) AZ31+0.23%Ca, c) AZ31+0.19%Sr, d) AZ31+0.20%Ce, e) AZ31+0.22%Ca+0.20%Ce, f) AZ31+0.17%Sr+0.16%Ce, and g) AZ31+0.17%Ca+0.18%Sr+0.18%Ce

Fig.5.5	Optical metallographs of samples cast in copper mould: a) AZ31+0.22%Ca+0.20%Ce, and b) AZ31+0.17%Ca+0.18%Sr+0.18%Ce
Fig.5.6	SEM of second phases in AZ31+0.22%Ca+0.20%Ce alloy cast in copper mould 63
Fig.5.7	Typical phases in AZ31+Ca+Sr+Ce alloy heat treated at 450 °C for 10 hours 64
Fig.5.8	WDS maps for phases of Al-Ca and Al-Sr
Fig.5.9	WDS maps for phases of Al-Ca-Sr in AZ31+Ca+Sr+Ce alloy heat treated at 450 °C for 10 hours Al-Ca and Al-Sr
Fig.5.10	WDS maps and EDS spectrums for phases of Al-Ce-Mn and Al-Ce in AZ31+Ca+Sr+Ce alloy heat treated at 450 °C for 10 hours
Fig.5.11	Phase diagram predicted with FactSage TM for AZ31 alloy at equilibrium condition 67
Fig.5.12	Phase diagram predicted with FactSage TM for AZ31 with 0.2%Ca at equilibrium condition
Fig.5.13	Phase diagram predicted with FactSage TM for AZ31 with 0.2%Ce at equilibrium condition
Fig.5.14	Phase diagram predicted with FactSage TM for AZ31 with 0.2%Ca+0.2%Sr+0.2%Ce at equilibrium condition
Fig.5.15	X-ray diffraction spectrums for alloys of AZ 31 and AZ31 with Ce, cast in Cu-mould 71
Fig.6.1	Compression flow curves for AZ31 base alloy tested at temperatures of 250 °C \sim 400 °C: a) strain rate of 0.1/s, and b) strain rate of 0.01/s
Fig.6.2	Compression flow curves for AZ31 base alloy tested at temperatures of 300 °C, strain rates of 0.1/s, 0.01/s, and 0.001/s
Fig.6.3	As-cast microstructure of the AZ31 alloy: (a) optical image, (b) EBSD map of as-cast grains, (c) SEM image of second phase
Fig.6.4	Compression flow curves for AZ31 base alloy tested at 350 °C, strain rate of 0.01/s, and strains of 0.2 up to 1.0
Fig.6.5	Fraction of DRX using EBSD maps for samples compressed at 350 °C, strain rate of $0.01s^{-1}$: a) $\varepsilon = 0.2$; b) $\varepsilon = 0.4$; c) $\varepsilon = 0.6$; and d) $\varepsilon = 1.0$. Inverse pole figure map represents the grain orientations, and grains in red have (0001) poles perpendicular to the compression direction
Fig.6.6	SEM microstructures show particle stimulated nucleation (PSN) grains associated with particles in the samples deformed at 350°C, a strain rate of 0.01s ⁻¹ , and to strains: a) 0.2, b) 0.6, and c) 0.8

Fig.6.7	EBSD maps for samples compressed at 350 °C, strain rate of $0.01s^{-1}$, and $\varepsilon = 0.2$;, a) orientation map: new DRX-grains near these particles (black zone without index), b) the map of kernel average misorientation shows that the higher density (yellow and green colors) near particles, c)second phase particles.
Fig.6.8	EBSD maps of twin identification for samples compressed at strain rate $0.01s^{-1}$, and strains: a) $\varepsilon = 0.2$, b) $\varepsilon = 0.4$, c) $\varepsilon = 0.6$, and d) $\varepsilon = 1.0$
Fig.6.9	Alloying effect on compression flow curves tested at 350°C: a) strain rate of 0.1s ⁻¹ , b) strain rate of 0.01 s ⁻¹
Fig.6.10	Microstructure for samples at 350 °C, strain rate: 0.01s ⁻¹ , and strain: 0.2, a) AZ31, b) AZ31+0.19%Ca
Fig.6.11	Microstructure evolution during hot compression at 350 °C, strain rate of 0.01s ⁻¹ , and strains from 0.2 to 1.0: a ₁), b ₁), c ¹) and d ₁) corresponding to the alloy of AZ31; a ₂), b ₂), c ₂) and d ₂) corresponding to the alloy of AZ31with 0.19%Ca
Fig.6.12	Microstructure for C-series samples at 350 °C, strain rate: 0.01s ⁻¹ , and strain: 1.0, a)AZ31, b) AZ31+0.19%Ca, c) AZ31+0.19%Sr, and d)AZ31+0.16%Ce
Fig.6.13	Two hits compression flow curves for alloys of AZ31 and AZ31 with Ca+Sr+Ce tested at 400 °C, strain rate of $0.1s^{-1}$, interpass heating at 400 °C for 3 minutes, the true strain of first hit: ϵ_1 = 0.22, the true strain of second hit: ϵ_2 =0.03
Fig.6.14	Microstructure evolution of two hit compression specimens for two alloys (a: preheating for 10 mins at start of the first hit, b: after the first hit to ε =0.22, and c: after the first hit for 3 mins just before the second hit): a_1), b_1), and c_1) corresponding to the alloy of AZ31; a_2), b_2), and c_2) corresponding to the alloy of AZ31with 0.19%Ca + 0.20%Sr + 0.20%
Fig.6.15	Strain hardening rate – strain curves for AZ31 samples compressed at a strain rate of 0.1 s ⁻¹ , temperatures of 250 °C, 300 °C, 350 °C, and 400 °C
	Microstructures of compression samples deformed to a true strain of 0.6 and $\dot{\epsilon}$ = 0.1 s ⁻¹ at different temperatures: a) 250 °C; b) 300 °C; c) 350 °C; and d) 400 °C
Fig.6.17	Microstructures of compression samples deformed at 300 °C to a true strain of 0.6: a) $\dot{\epsilon}$ = 0.1 s ⁻¹ , b) $\dot{\epsilon}$ = 0.01 s ⁻¹ , and c) $\dot{\epsilon}$ = 0.001 s ⁻¹
Fig.6.18	EBSD maps of grains and kernel average misorientation (1 \sim 5 deg) for sample compressed at 350 °C, strain rate 0.01 s ⁻¹ : a) strain 0.2 and b) strain 1.0
Fig.6.19	WDS Twinning induced dynamic recrystallization in the alloy of AZ31 with 0.22% Ca + 0.22% Sr + 0.21% Ce, compressed at 400 °C, strain rate 0.1 s-1, and a strain 0.22 101
Fig.7.1	Reheating time effect on the grain structure and second phases: a and b) as-cast; c and d) reheating at 450 °C for 15 min; e and f): reheating at 450 °C for 1 hour

LIST OF TABLES

Table	Page
Table 2.1	Typical mechanical properties of unalloyed magnesium at 20 °C [1]
Table 2.2	Characteristics of Mg could be affected by alloying [2]
Table 2.3	Solid solubility limits for binary magnesium alloys [6]
Table 2.4	Alloying effects on magnesium properties [2, 10, 15-18, 20, 32-48]
Table 2.5	Nominal compositions and typical room-temperature tensile properties of wrought magnesium alloys [2]
Table 2.6	Independent slip systems in HCP metals [53]
Table 4.1	Raw materials series one (wt.%)
Table 4.2	Raw materials series two (wt.%)
Table 4.3	Chemical composition of Mischmetal (wt.%)
Table 4.4	Compositions of AZ31-based sheets rolled at CANMET
Table 4.5	Rolling conditions and typical rolling schedule
Table 4.6	Standards for phase analysis with EPMA
Table 5.1	Chemical composition for alloys cast with raw materials series I (wt. %) 59
Table 5.2	Chemical composition for alloys cast with raw materials series II (wt. %)
Table 5.3	Alloy efficiency in two series raw materials (%)
Table 5.4	Second phase analysis with EPMA and FactSage TM prediction
Table 5.5	Results of full scanning and full peaks fit with GSAS and GM software using different machines at GM and McGill
Table 5.6	Growth restriction factor (GRF) values for Ca and Sr in Mg binary alloys
Table 6.1	Representation of twin systems in EBSD maps
Table 6.2	The fraction of softening due to interpass heating for two hit compression testing 92

Table 6.3	Critical strains to initiate DRX for compression specimens tested at strain rate of 0.1s ⁻¹ and temperature of 350 °C
Table 8.1	Mechanical properties at room temperature for AZ31-base sheets rolled at 300°C and 20% reduction per pass, annealed at 400 °C for 10 minutes
Table 8.2	Mechanical properties at room temperature for AZ31-base sheets rolled at 400°C and 30% reduction per pass, annealed at 400 °C for 10 minutes
Table 8.3	Strain rate sensitivity component (m) and stress exponent (n) under various testing conditions
Table 8.4	Statistic results of area fraction (%) of second phases in tensile samples

Chapter 1

Introduction

To reduce the weight of cars, and thereby increase fuel economy, improve performance, and reduce emissions, growing attention has been given to magnesium (Mg) because it has the lowest density of common structural metals, but with reasonable strength and stiffness. Weight savings around 50% and 25% can be achieved using Mg instead of steel and aluminum, respectively, while maintaining the design at equal stiffness and strength [1]. Automobile manufacturers have reduced vehicle weight by the use of magnesium die castings, which account for about 30% of the total reported consumption of Mg alloys [2, 3]. However, only 1% of the total yearly Mg production is used for wrought products today, with even smaller number for flat rolled materials [4, 5]. This low level of usage is a result of three main factors: the comparatively limited coldworkability due to the lack of slip systems in hexagonal close-packed (HCP) crystal structure, the high production cost resulting from time consuming rolling operation, and the lack of research both in sheet alloy development and innovation of manufacturing processes [6-8].

To date, among the few Mg wrought alloys in use, there are only two alloys, AZ31 and ZM21, (nominal compositions of Mg-3%Al-1%Zn-0.2%Mn and Mg-2%Zn-0.5%Mn), with marginally acceptable formability, used for commercial sheet and plate making, in which AZ31 remains the more popular of the two alloys because of its better

proprieties both in strength and ductility than those of ZM21 ^[9]. Moreover, the costly production makes many target applications in automobile weight savings difficult to realize, including the body, the interior, and the chassis.

It has long been recognized that refining the microstructure is beneficial to the improvement of ductility ^[10]. Therefore, alloying additions and optimization of sheet processing to obtain a refined as-rolled microstructure could be a way to improve the formability of AZ31 alloy.

With respect to the effect of alloying additions, there is some evidence that refining the initial as-cast microstructure helps to refine the as-hot worked microstructure in extruded material ^[11]. It has been found that calcium (Ca) and strontium (Sr) can refine the as-cast microstructure in high aluminum content Mg-alloys (AZ91 and AZ80) ^[12-14]. In addition, Ca is effective for the prevention of ignition and oxidation of Mg alloys during melting ^[15-17], and the rollability of magnesium sheet would be improved due to the decrease of oxidation ^[8].

Since components made from Mg sheet are usually formed at elevated temperatures, another way to improve hot formability might be by microalloying with rare earth elements to generate thermal stable precipitates, so that a fine grain size in sheets would be maintained during hot forming. Cerium (Ce) has been successfully used to increase the creep resistance at elevated temperature in casting Mg-alloys, such as in Mg-4%Y-3%Ce-0.7%Zr (WE54) alloy [18, 19]. Moreover, Ce showed its effect on the reduction of c/a ratio in Mg HCP crystal structure in a Mg-Ce binary system [20], which may be beneficial to the improvement of formability. However, researches concerning these effects on the most commonly used wrought AZ31 alloy at a 'microalloying' level (<0.5%) are rarely seen [21, 22].

Recently, twin roll strip casting and subsequent hot rolling processes have been attempted to produce magnesium sheet to reduce the manufacturing cost since they have been successfully applied in the production of stainless steel and non-heat treatable aluminum sheets. Many encouraging reports in lab trials have been noticed in this

innovative process ^[23-27]; this is likely to be the large scale processing future of Mg sheet. Hence, it is important to investigate the effect of solidification rates on microstructure and hot working behavior.

Therefore, in this work, the effect of microalloying additions of Ca, Sr and Ce on microstructure and hot deformation behavior of AZ31 based wrought magnesium alloy, in conjunction with solidification rates, was systematically investigated. A brief literature review of alloying effect on the properties of Mg, deformation characteristics and dynamic recrystallization of Mg, and Mg-sheet processing is presented in Chapter 2. Research objectives are stated in Chapter 3. Experimental details are described in Chapter 4, including alloy design and casting, hot compression testing, sheet rolling, tensile testing, and microstructure characterization. The results are presented and discussed in the following four chapters: alloy design and casting (Chapter 5), compression testing (Chapter 6), rolling experiment (Chapter 7), and tensile testing (Chapter 8). Finally, overall conclusions and contributions to original knowledge of this research are given in Chapter 9 and Chapter 10, respectively.

References:

- 1. S. Das, "Magnesium for Automotive Applications: Primary Production Cost Assessment", JOM, 55 (11), (2003), p 22-26
- 2. S. Schumann and F. Friedrich, "Strategies to Overcome Technological Barriers to Increase the Use of Magnesium in Cars", 58th Annual World Magnesium Conference, Int. Magnesium Association, May 20-22, 2001, Brussels, Belgium.
- 3. S. Schumann and F. Friedrich, "The Use of Magnesium in Cars-Today and in Future", Proc. Int. Conference on Magnesium Alloys and Their Applications, Edited by B.L. Mordike and K.U. Kainer, (Wolfsburg 1998), p 3-13
- 4. W. Sebastian, K. Droder, and S. Schumann, "Magnesium Alloys and Their Applications", Edited by K.U. Kainer, DGM Wiley-VCH, (2000), p 602
- 5. R.L. Edgar, "Global Overview on Demand and Applications for Magnesium Alloys", Proc. Int. Congress on Magnesium Alloys and Their Applications, München, Edited by K.U. Kainer, Wiley-VCH-Verlag GmbH, Weinheim, (2000), p 3-8
- 6. P.G. Patridge, "The Crystallography and Deformation Modes of Hexagonal Close-Packed Metals", Review. Metallurgical Reviews, 118, (1967), p 169-194

- L. Barnes, "Rolled Magnesium Products: what goes around, comes around", Proc. 49th Annual World Magnesium Conference, Int. Magnesium Association, May 12-15, Chicago, U.S.A., (1992), p 29-43
- 8. H. E. Friedrich and B.L. Mordik, "Magnesium technology: metallurgy, design data, applications", Sringer Verlag Berlin Heiegerg, (2006), p 74, p 269-289, p 80
- 9. J.R. Davis, & Associates (eds), "Alloying Understanding the Basic", ASM International, Materials Park, OH44073-0002, (2001) www.asminternational.org, p 436
- 10. J.A.Chapman and D.V. Wilson, "The Room-temperature Ductility of Fine Grained magnesium", J. Inst. Met., 91, (1962), p39-40
- 11. M.R. Bartnett, D. Atwell, C. Davies, and R. Schmidt, "Grain Refinement of Magnesium Alloy ZM20 Prior to and During Extrusion", Proceedings of the 2nd International Light Metals Technology Conference, 8-10 June, 2005, St. Wolfgang, Austria, Edited by Helmut Kaufmann, p 161-166
- 12. Q. Wang, W. Chen, X. Zeng, Y. Lu, W. Ding, Y. Zhu, and X. Xu, "Effect of Ca Addition on the Microstructure and Mechanical Properties of AZ91 Magnesium Alloy", Journal of Materials Science, 36, (2001), p 3035-3040
- 13. M. Fujita, N. Sakate; S. Hirahara, and Y. Yamanoto, "Development of Magnesium Forged Road Wheel", JSAE Review, 16, (1995), p 283-301
- 14. J.E. Gruzleski and A. Aliravci, "Low Porosity, Fine-Grain Sized Strontium Treated Magnesium alloy Castings", US Patent US005143564A, Sept. 1992
- M. Sakamoto and S. Akiyama, "Suppression of Ignition and Burning of Molten Mg Alloys by Ca Bearing Stable Oxide Film", Journal of Materials Science Letters, 16, (1997), p 1048-1050
- 16. S. Akiyama, "Flame-Resistant Magnesium Alloys by Calcium", J. Jpn. Foundry Eng. Soc., 68(1), (1994), p 38
- 17. B.S. You, W.W. Park, and I.S. Chung, "The Effect of Calcium Additions on the Oxidation Behavior in Magnesium Alloys", Scripta Mater., 42, (2000), p1089-1094
- 18. M.M. Avedesian and H. Baker (eds.), "ASM Specialty Handbook: Magnesium and Magnesium Alloys", ASM International, Materials Park, Oh. U.S.A., (1999), p 15
- 19. B.L. Mordike, "Creep-resistant Magnesium Alloys", Materials Science and Engineering A, 324, (2002), p 103-112
- 20. G.V. Raynor, "The Physical Metallurgy of Magnesium and Its Alloys", (Pergamon Press, London, New York, Paris, Los Angeles, (1959), p 83
- 21. Y. Liu, W.P. Chen, W.W. Zhang, W. Zhang, and Y.Y. Li, "Study on the Bending-Bulging formability" of AZ31 Mg alloy sheet by microalloying of RE and Ca", Rare Metal Materials and Engineering, 35 (6), (2006), p 925-928
- 22. B. Tang, X.S. Wang, S.S. Li, D.B. Zeng, and R. Wu, "Effects of Ca Combined with Sr additions on Microstructure and Mechanical Properties of AZ91D Magnesium Alloy", Materials Science and Technology, 21(N0.5), (2005), p 574-578
- 23. R.V. Allen, D.R. East, T.J. Johnson, W.E. Borbidge, and D. Liang, "Magnesium Alloy Sheet Produced by Twin Roll Casting", TMS, Magnesium Technology, (2001), p 75-79

- 24. S.S. Park, J.G. Lee, H.C. Lee, and N.J. Kim, "Development of Wrought Mg Alloys via Strip Casting", TMS, Magnesium Technology, (2004), p 107-112
- 25. M. Numano, N. Mori, Y. Nakai, and N. Kawabe, "Properties of AZ31 and AZ91 Sheets Made by Twin Roll Casting", Materials Science Forum, 539-543, (2007), p 1650-1655
- 26. G.T. Bae, S.S. Park, D.H. Kang, Y.S. Oh, and N.J. Kim, "Twin-Roll casting of Mg Alloys", Proceedings of the Light Metals Technology Conference, Sept. 24-26, 2007, Saint-Sauveur, Quebec, Canada, (2007), p 183-188
- 27. R. Kawalla, M. Oswald, M. Ullmann, C. Schmidt, H. P. Vogt, and N. D. Cuong, "Development of a Strip-Rolling Technology for Mg Alloys Based on the Twin-Roll-Casting Process", in Proceedings of Magnesium Technology 2008, ed. M.O. Pekguleruz et al., TMS, New Orleans, (2008), p 177-182.

Chapter 2

Literature Review

To investigate the feasibility of using alloying approach and alternative sheet processing to improve the formability of magnesium and decrease the manufacturing cost of Mg-sheets, it is necessary to have a better understanding of the effect of alloying on mechanical properties, fundamental deformation characteristics, and sheet producing processes associated with magnesium. It is the purpose of the present review to summarize the previous work in this area.

2.1 Alloying Effect on Properties of Mg

Pure magnesium is seldom used in structural applications due to limitations of mechanical properties and poor corrosion and oxidation behavior. Table 2.1 shows the typical mechanical properties of unalloyed magnesium at room temperature ^[1]. It is noted that the yield strength and ductility are very low for both as-cast and wrought Mg. In addition, the elongation data of wrought Mg displays a wide range, which suggests inconsistent properties. All these are unacceptable for structural functions, although strength can be reinforced by strain hardening or by decreasing the grain size (thermal mechanical processes or casting at high solidification rate). Therefore, alloying is required to improve the properties for structural applications.

Table 2.1 Typical mechanical properties of unalloyed magnesium at 20 ${}^{\circ}C^{[1]}$

Form and	Tensile strength	0.2% tensile yield strength	0.2% compressive yield strength	Elongation in 50 mm	Hardness	
section	(MPa)	(MPa)	(MPa)	(2 in.), %	HRE	HB(a)
Sand cast, 13 mm (1/2in.) diam	90	21	21	2 - 6	16	30
Extrusion, 13 mm (1/2in.) diam	165 - 205	69 -105	34 - 55	5 - 8	26	35
Hard rolled sheet	180 - 220	115 -140	105 - 115	2 - 10	48 - 54	45 - 47
Annealed sheet	160 - 195	90 -105	69 - 83	3 - 15	37 - 39	40 - 41

⁽a) 500 kg load, 10 mm diam ball

2.1.1 General Principles of Alloying

Based on the general alloying principles of metals, the characteristics of Mg that could be affected by alloying are shown in Table 2.2 ^[2]. Some chemical elements are needed to make it perform better and/or fabricate favorably. Considering the main requirements of wrought Mg-alloys, the effects of alloying on strengthening mechanisms, castability, and formability are a focus of the alloy design.

Table 2.2 Characteristics of Mg could be affected by alloying [2]

Mechanical properties	Processing properties		
Room-temperature strength	Castability		
Creep resistance	Formability		
Fatigue resistance	Joining ability		
Service properties	Physical properties		
Corrosion / Oxidation resistance	Elastic modulus		

2.1.2 Alloying Effect on Strengthening

It is well known that the plastic deformation of a metal occurs by glide of dislocations in the metal under most conditions ^[3]. When the resolved shear stress (the stress acting on the slip plane in the slip direction) achieves a critical value, plastic deformation initiates, corresponding to the yield stress (σ_y). Since alloyed polycrystals of Mg contain various defects, such as dislocations, vacancies, foreign atoms, precipitates, etc., these defects may restrict the dislocation movement. Therefore, alloying is a very efficient approach to improve the strength of Mg by increasing resistance to dislocation motion in such a manner of forming solid solution or/and precipitates as well as refining grain size.

2.1.2.1 Solid Solution Strengthening

According to Hume-Rothery's rules ^[4, 5], four main factors enhance the formation of substantial solid solution: (1) the difference of atom size is within ±15% range, (2) similar crystal structure, (3) similar electronegativity, and (4) use of alloying elements with higher valency than the host. The shaded band in Figure 2.1 shows that Mg with an atomic diameter of 0.320 nm has a favorable size factor for solid solubility with a various range of solute elements ^[6]. Possible elements to form solid solution with Mg are cadmium, lithium, aluminum, zinc, indium, thallium, scandium, silver, yttrium, lead, etc. Table 2.3 lists the solid solubility limits for binary Mg-alloys ^[6].

Solid solution strengthening is due to the fact that solute atoms change the lattice parameters of Mg (both a and c) and modify the binding forces. The yield stress of dilute Mg based alloys is described by Equation 2.1^[7] or Equation 2.2 ^[8].

$$\sigma_{ys} = \sigma_{y0} + Z_L G(\delta^2 + \beta^2 \eta^2)^{3/2} c^{2/3}$$
 (Equation 2.1)

$$\sigma_{YS} = \sigma_{Y0} + Z_F G(|\delta| + \beta |\eta|)^{3/2} c^{1/2}$$
 (Equation 2.2)

Where σ_{Y0} is yield stress of pure Mg, Z_F and Z_L are constant, G is the shear modulus, δ is the misfit size parameter ($\delta = (da/dc)/a$), β is between 1/20 and 1/16, η is modulus misfit parameter ($\eta = (dG/dc)/G$), and c is the atomic solution concentration in

both equations. The value of η can be estimated using Equation 2.3, where G1 is the shear modulus of the alloying metal ^[7].

$$\eta = 2(G1-G)/(G1+G)$$
 (Equation 2.3)

The solution hardening rates of Mg-Li, Mg-Al, and Mg-Zn were compared, and the experimental results showed that Zn has a relatively higher solution hardening rate, Al is in an intermediate level, and Li has a relatively low value ^[9].

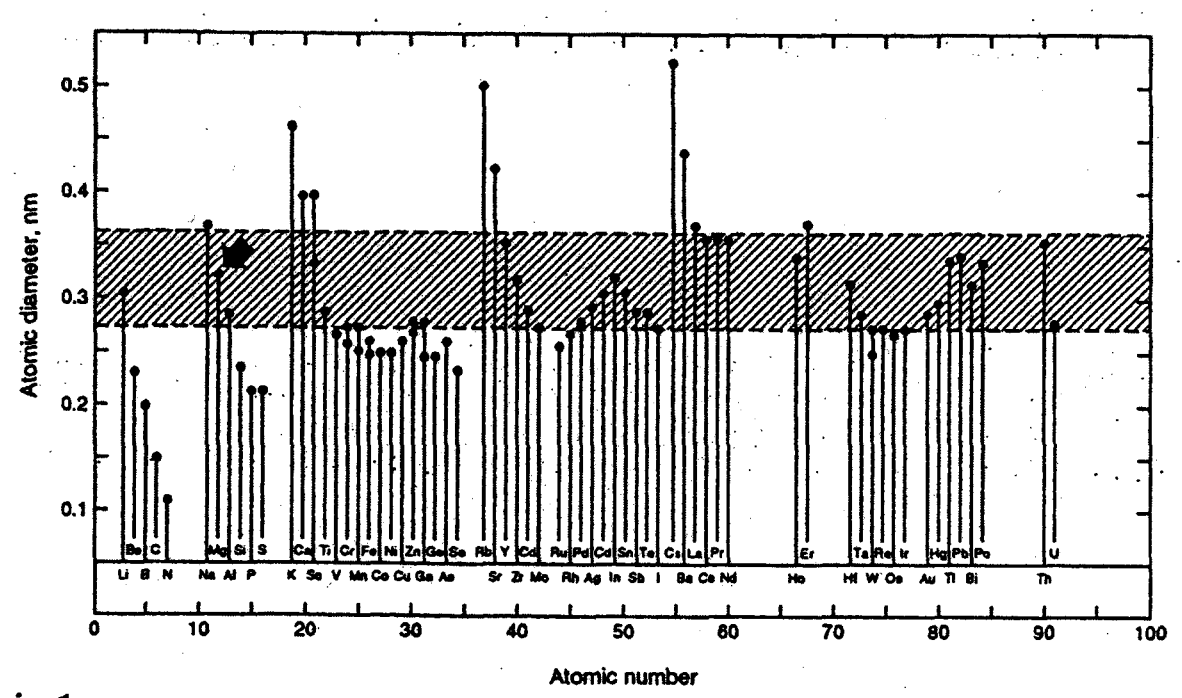


Figure 2.1 Atomic diameters of the elements and the favorable size factor with respect to magnesium [6]

Table 2.3 Solid solubility limits for binary magnesium alloys $^{[6]}$

Element	Atomic percent	Weight percent	System
Lithium	17.0	5.5	Eutectic
Aluminum	11.6	12.7	Eutectic
Silver	3.8	15.0	Eutectic
Yttrium	3.35	12.4	Eutectic
Zinc	2.4	6.2	Eutectic
Neodymium	~0.1	~0.6	Eutectic
Zirconium	1.0	3.8	Peritectic
Manganese	1.0	2.2	Peritectic
Thorium	0.52	4.75	Eutectic
Cerium	0.1	0.5	Eutectic
Cadmium	100	100	Complete solid solution
Indium	19.4	53.2	Peritectic
Thallium	15.4	60.5	Eutectic
Scandium	~15	~24.5	Peritectic
Lead	7.75	41.9	Eutectic
Thulium	6.6	31.8	Eutectic
Scandium	~15	~24.5	Eutectic
Lead	7.75	41.9	Eutectic
Thulium	6.3	31.8	Eutectic
Terbium	4.6	24.0	Eutectic
Tin	3.35	14.5	Eutectic
Gallium	3.1	8.4	Eutectic
Ytterbium	1.2	8.0	Eutectic
Bismuth	1.1	8.9	Eutectic
Calcium	0.82	1.35	Eutectic
Samarium	~1.0	~6.4	Eutectic
Gold	0.1	0.8	Eutectic
Titanium	0.1	0.2	Peritectic

2.1.2.2 Precipitation Strengthening

Most binary Mg alloys show eutectic or peritectic systems as shown in Table 2.3 ^[6]. Since solid solubility generally decreases with decreasing temperature and second phases usually precipitate. Such a feature can be used to achieve a strong response to age hardening. Probable aging precipitation strengthening was seen in some alloy systems ^[10, 11]: Mg-Al, Mg-Zn, Mg-RE (Nd), Mg-Y-Nd, Mg-Th, and Mg-Ag-RE (Nd), etc. Also, Precipitates with high melting point formed during solidification can be maintained over a wide temperature range (180 ~ 300 °C), which is a key to developing creep resistant Mg-alloys, such as Mg-RE ^[12-15], Mg-Sc ^[12], Mg-Si ^[16], and Mg-Al with other additions (Ca, Sr., Bi, and Sb) ^[16-19].

It is worth noting that manganese (Mn) is a very important precipitate modifier in Mg-Al and Mg-Al-Zn alloys. Mn in Mg increases yield strength and does not affect tensile strength. It can remove iron and other heavy-metal elements by forming relatively harmless intermetallics to improve the saltwater resistance. Thus, commercial alloys usually contain less than 1.5 wt% Mn, and its solid solubility in Mg-Al alloys is reduced to about 0.3 wt% [10, 20].

Precipitate strengthening depends on the features of these particles, such as volume fraction, size, distribution etc., and also on the interaction between precipitates and the Mg matrix (coherent or incoherent). Dislocations may shear particles or bow out between particles; the stress to overcome precipitates can be generally expressed as Equation 2.4 [21, 22].

$$\sigma_{vp} = MF/bL$$
 (Equation 2.4)

Where, M is the Taylor factor, F is the mean obstacle strength, b is the magnitude of the Burgers vector, and L is the average particle spacing along the dislocation line.

2.1.2.3 Grain Boundary Strengthening

To reduce the grain size by alloying is another approach to strengthen Mg-alloys through the Hall-Petch relationship (Equation 2.5) $^{[23-25]}$, where d is the average grain diameter, σ_0 is a constant and Ky is the stress intensity factor for plastic yielding.

$$\sigma_{\gamma d} = \sigma_0 + K_{\gamma} d^{-1/2}$$
 (Equation 2.5)

Studies in Mg and Mg alloys show that σ_0 and Ky are related to the critical resolved shear stress (CRSS) for the basal slip and non-basal slip operation, respectively ^[26-31]. Equations 2.6 and 2.7 give the formulae of σ_0 and Ky, and K_y depends on temperature, texture, composition, and materials preparation.

$$\sigma_0 = M\tau_0$$
 (Equation 2.6)

$$K_{\nu} = CM[M * Gb/(1-\nu)]^{1/2} \tau_{NB}^{-1/2}$$
 (Equation 2.7)

Where M is the Taylor factor (M = $4 \sim 6.5$ is used in Mg and Mg-alloys), τ_0 is the CRSS for basal slip, C is a numerical constant, M* is the Sachs orientation factor for the accommodating system, ν is Poisson's constant, G is the shear modulus, and b is the magnitude of the Burgers vector, τ_{NB} is the CRSS for non-basal slip.

Experimental results provide evidence that certain levels of Al (1 ~ 9 wt.%), Ca (0.1~0.8 wt.%), Si (0.1~0.5 wt.%), and Zr (0.04 ~ 0.32 wt.%) in pure Mg result in a reduction in grain size [32]. Note that the grain size significantly decreases at low alloying levels with these additions, and the degree of grain refinement decreases with further additions. With small amount of these additions, Zr, Ca and Si show a more significant effect on the grain refinement to pure Mg, in which Zr has a strongest effect, and Al produces a moderate gain reduction. In addition, studies of the addition of Sr (0.01~1.0 wt.%) in Mg-Al alloys show the effect of grain refinement [32-34]; this is more significant in low-Al content alloys. Another investigation of the effect of 0.4% Ca on AZ91 exhibits a refined grain structure and increased yield strength but a decrease in elongation to fracture. Combined additions of Ca (0.4 wt.%) and Sr (0.05~0.10 wt.%) can improve the elongation and maintain the higher yield strength of AZ91^[35]. This indicates that refining grain size by microalloying (<0.5wt.%) could be a promising way to decrease grain size

to increase mechanical properties; and using multiple alloying approach would achieve a combined and optimized effects.

2.1.3 Main Alloying Elements in Mg Alloys

Numerous studies have been done to improve the properties of Mg-based alloys. In this literature review, the effects of main alloying elements (Al, Zn, Mn, Li, Si, Ca, Sr, Ce, Y, Zr, Sn) on related properties: mechanical properties, castability and hot deformation behavior are considered. Table 2.4 lists their effects based on two strengthening mechanisms (solid solution and precipitation) and several aspects associated to its formability (ductility, initial grain size, and lattice parameters) [2, 10, 15-18, 20, 32-48]. In addition, some important remarks are given. It is noted that effects of alloying are significant and the interactions between these elements are also noteworthy. A careful alloy design is needed to fit a specific purpose.

2.1.4 Existing Commercial Wrought Mg-alloys and Further Improvement

According to product types, specific Mg-alloys can be classified as casting, wrought or filler metal. Table 2.5 displays the nominal compositions and typical tensile properties of the most common commercial wrought Mg-alloys. As can be seen, only two alloys, AZ31 and ZM21, are used for sheet and plate making among several kinds of Mg wrought alloys (AZ: magnesium-aluminum-zinc-manganese, ZK: magnesium-zinc-zirconium, and ZM: magnesium-zinc-manganese) [2]. AZ31 is generally acceptable with an intermediate strength and ductility, and AZ31 sheet is considered a good substitute for steel sheet and Al-sheet for transportation applications due to competitive specific stiffness and specific strength, as shown in Figure 2.5 [49]. However, the limited ductility of magnesium at room temperature and currently high cost manufacturing process (hot rolling from casting slabs) have hampered the wide production of Mg-sheets. Hence, it is necessary to further improve the formability of AZ31.

Table 2.4 Alloying effects on magnesium properties $^{[2, 10, 15-18, 20, 32-48]}$

	Str	Strength		Grain size	a, c, c/a		
Element	Solid solution	Precipitate former	Ductility	refiner	in binary Mg alloys	Remarks	
Al	٧	1	↑↓	٧	a↓ c↓ c/a↑	a) Al has the most favourable effect on Mg: improves strength, hardness, and castability. 6~7wt% shows the optimum combination of strength and ductility, e.g. Mg-Al7.1Zn0.60Mn0.30 is an optimum alloy applied for forged road wheels as shown in Figure 2.2 [40]; b) porosity (vol%) increases with Al up to 11 wt% [41].	
Zn	√	√			a↓ c↓ c/a same	a) Zn has a very strong age hardening effect in wrought Mg-alloys without Al; b) Zn is usually used with Al to improve the corrosion resistance by removing the harmful elements of Fe and Ni; but >1 wt %Zn increases hot-tearing susceptibility in Mg-alloys with 7~10 wt% Al, adding RE can decrease the weakness in alloys with high Zn (> 0.8 wt%) ^[42]	
Mn	٧	٧				a) Mn removes Fe and heavy-metal elements to improve saltwater resistance; b) studies in AZ 31, AZ41 and AZ61 alloys with 0.25%Mn appear to improve the elevated temperature ductility of these alloys [43]	
Li	√		↑		a↓ c↓ c/a↓	a) >12wt% Li gives 100% BCC structure, good ductility but low strength ^[44] ; b) MgLi crystal with low amounts of additions (Al, Zn, Mn, RE, Sr, Zr, Ca) allows a significant increase in ductility even in the HCP lattice system and a comparable strength as shown in Figures 2.3-2.4 ^[44]	
Y	1	7				Mg-Y alloys has hot strength and creep resistance [15]	
Ce	V	√			c/a↓	Ce increases creep properties [45] and mechanical properties of ZA80 [46]	
Са		1		٧		a) grain-refiner; b) effectively to prevent ignition and oxidation of the Mg-alloys during melting [35-37]; c) 0.5~2.0%Ca increases tensile strength at 150°C ^[47]	
Zr				V		a) strongest grain-refiner, b) usually not be used in Mg-Al or Mg-Mn alloys [48]	
Sr				1		a) grain-refiner and porosity decreaser for Mg-Al-Zn alloys ^[34] ; b) Mg-Al-Sr alloys: precipitation of Al ₄ Sr-α(Mg) eutectic improves the creep resistance [17]	
Si		√		7		a) Si increases fluidity and castability; b) a higher Si content in Mg alloys improves its creep resistance [16]	
Sn	1	1			a↓ c↑ c/a↑	a) Sn increases the ductility of Mg-alloys with small amount of Al; b) it reduces the tendency for the alloy to crack while being hot worked, and better for forging [45]	

Note: √ means alloying elements have effects on related properties;

↑↓ means there is an optimum concentration for the property.

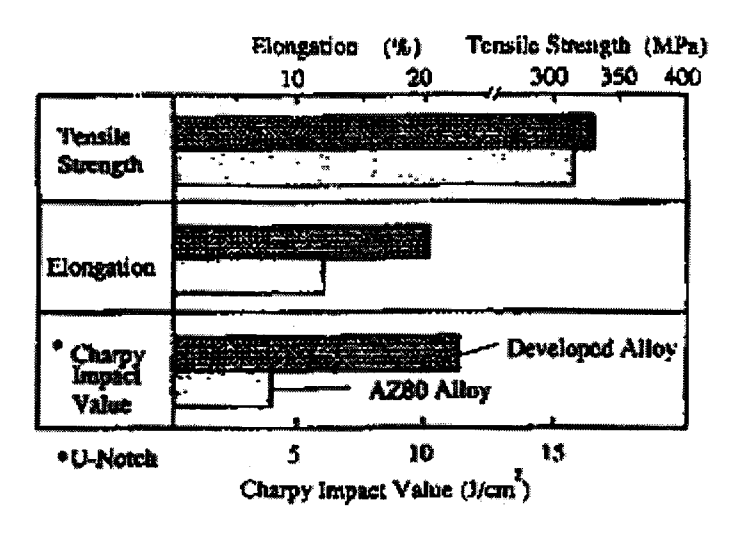


Figure 2.2 Mechanical properties of developed (Mg-Al7.1Zn0.60Mn0.30) alloy compared with AZ80 alloy $^{[40]}$

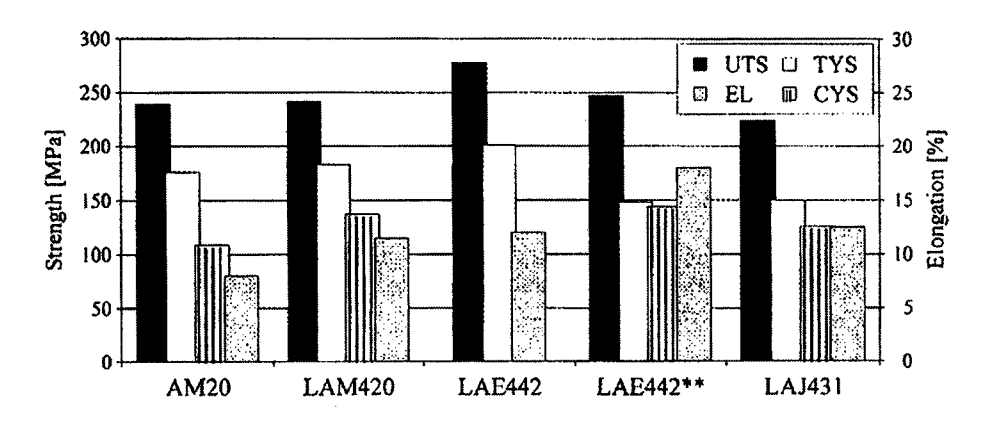


Figure 2.3 Mechanical properties of Mg-Li-Al alloys and AM20 standard alloy [44]

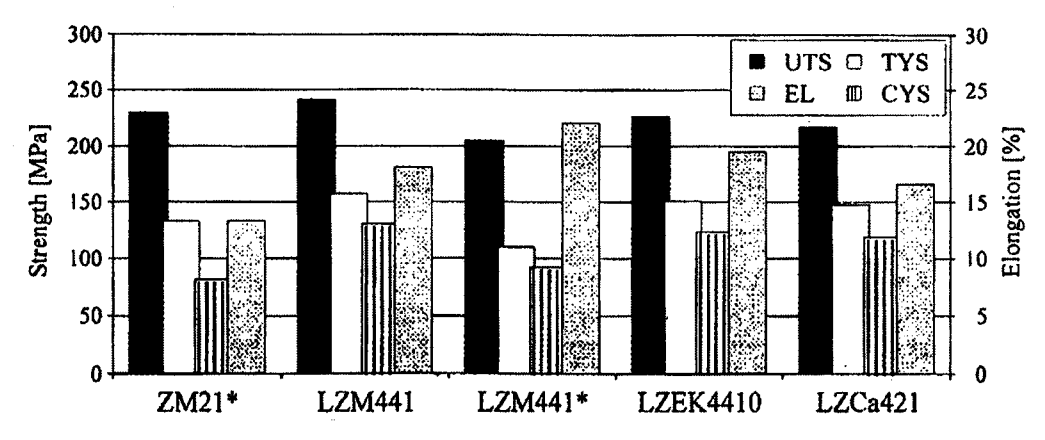


Figure 2.4 Mechanical properties of Mg-Li-Zn alloys and ZM21 standard alloy [44]

Table 2.5 Nominal compositions and typical room-temperature tensile properties of wrought magnesium alloys $^{[2]}$

		Compos	ition (%	(o)	Tensile	Tensile yield	Elongation in	Hardness	
Alloy	Al	Mn	Zn	Zr	strength (MPa)	strength (MPa)	50 mm (%)	(HRC)	
Forgings								-	
AZ31B-F	3.0	0.20	1.0		260	170	15	50	
AZ61A-F	6.6	0.15	1.0		295	180	12	55	
AZ80A-T5	8.5	0.12	0.5		345	250	6	72	
AZ80A-T6	8.5	0.12	0.5	<u> </u>	345	250	11	75	
M1A-F		1.2		_	250	160	7	47	
ZK31-T5			3.0	0.6	290	210	7		
ZK60A-T5			5.5	0.45	305	215	16	65	
ZK61-T5			6.0	0.8	275	160	7		
ZM21-F		0.5		2.0	200	125	9		
Extruded bars and shapes									
AZ10A-F	1.2	0.2	0.4		240	145	10		
AZ31B and C-F(h)	3.0	0.2	1.0		255	200	12	49	
AZ61A-F	6.5	0.15	1.0		305	205	16	60	
AZ80A-T5	8.5	0.12	0.5		380	275	7	80	
M1A-F		1.2			255	180	12	44	
ZC71-T6		0.5	6.5		295	324	3	70-80	
ZK21A-F			2.3	0.45	260	195	4		
ZK31-T5			3.0	0.6	295	210	7		
ZK40A-T5			4.0	0.45	275	255	4		
ZK60A-T5			5.5	0.45	350	285	11	82	
ZM21-F	 	0.5	2.0		235	155	8		
Sheet and plate							,		
AZ31B-H24	3.0	0.20	1.0		290	220	15	73	
ZM21-0		0.5	2.0		240	120	11		
ZM21-H24		0.5	2.0		250	165	6		

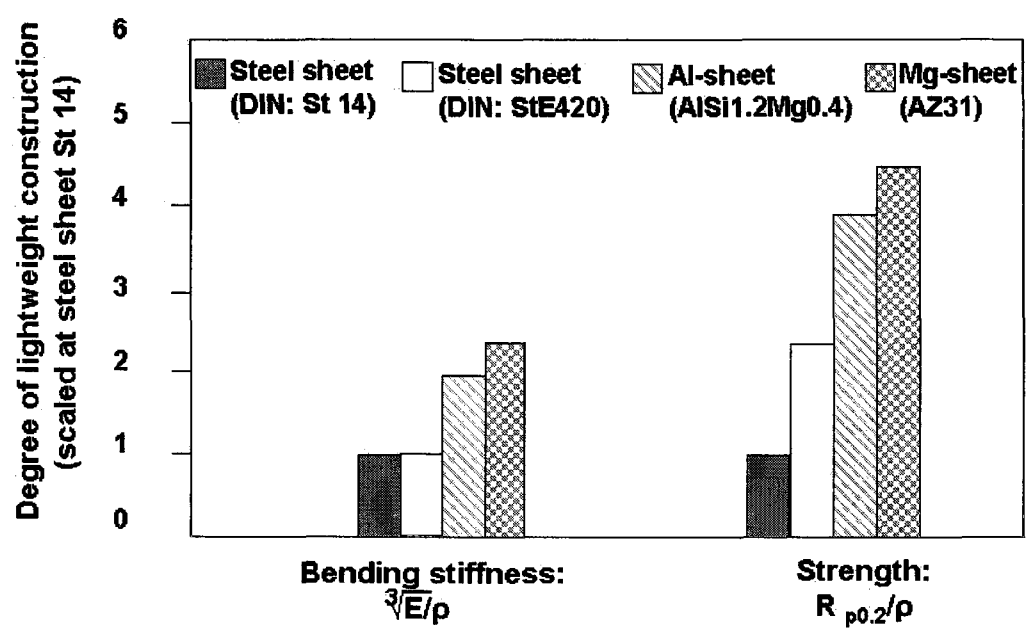


Figure 2.5 Mg-sheet has advantage over steel sheet and Al-sheet for body panel: E is the elastic modulus, ρ is the density, and Rp0.2 is yield strength ^[49]

It has been long recognized that the room temperature ductility of Mg-alloys can be significantly enhanced by decreasing the grain size as shown in Figure 2.6 ^[50]. A study on microalloyed AZ31 with 0.3%Ca and 0.3%Ce to improve the room temperature properties and bending-bulging formability has been conducted ^[51]. The experimental results show a finer microstructure and improved mechanical properties (UTS: 284 MPa and EL: 23.2% under the annealed condition of 300 °C for 4 hours); meanwhile, it exhibits better bending and drawing-bulging formability, which is significantly improved with increasing temperature. Nevertheless, the specific reasons related to this improvement were not revealed. Therefore, a systematic investigation regarding the effects of microalloying on microstructures (from casting, rolling, up to further deformation) and hot working behaviours of AZ31 is required to have a better understanding related mechanisms for further development wrought Mg alloys for sheet producing.

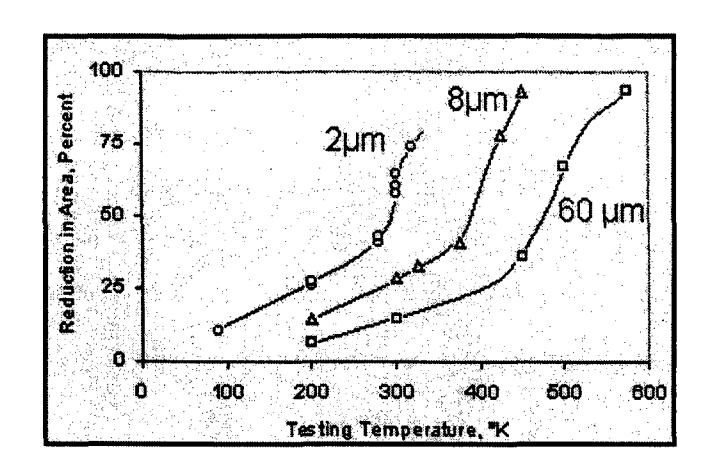


Figure 2.6 Dependence of ductility on grain size [50]

2.2 Deformation Characteristics of Mg

For hexagonal close-packed (HCP) Mg (c/a=1.623), its deformation modes consist of slips and twinning. The main slip and twinning planes and directions in Mg unit cell are demonstrated in Figure 2.7, and the independent slip systems are listed in Table 2.6.

2.2.1 Slip Systems

When a crystal of a metal is deformed, slip takes place by the movement of dislocations" in the metal ^[39]. Based on Von Mises's theory ^[52], more than five independent slip systems are required to perform uniform deformation without failure. The HCP structure of Mg serves as a base to understand the limited formability. According to the studies of the critical resolved shear stresses (CRSSs) of active main slip and twinning systems vs. temperature ^[53-59] summarized in Figure 2.7, it can be seen that only basal plane slip occurs at room temperature (Figure 2.7a). Since there is only one set of basal planes, the plasticity is limited at room temperature. However, at elevated temperatures (> 225 °C for Mg single crystal), prismatic and pyramidal slip systems are activated (Figures 2.7b and 2.7c) due to a dramatic reduction in their critical resolved

shear stresses. The activation of these extra slip systems significantly improves the ductility of magnesium. Consequently, the fabrication of Mg-alloys is mostly associated with elevated temperatures. Figure 2.8 displays the transition to much improved workability at 250 °C ^[60].

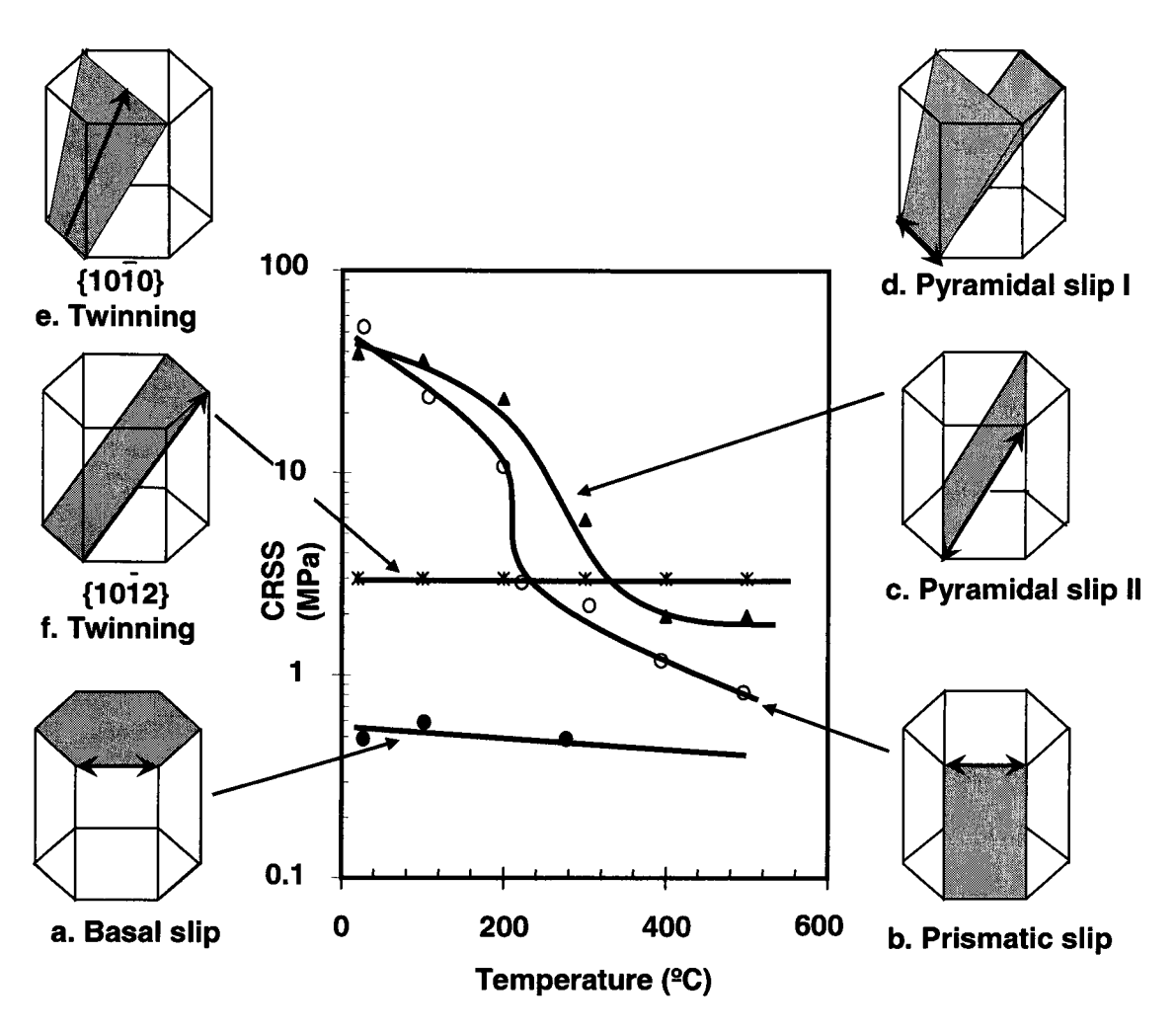


Figure 2.7 Principal slip systems and twinning: (a) the $(0001) < 11\overline{2}0 >$ basal slip system, (b) the $\{10\overline{1}0\} < 11\overline{2}0 >$ prismatic slip system, (c) the $\{1\overline{2}12\} < \overline{1}\overline{1}23 >$ second order pyramidal slip system, d) $\{\overline{1}01\} < 11\overline{2}0 >$ and $\{\overline{1}02\} < 11\overline{2}0 >$ first order pyramidal slip systems, e) the $\{10\overline{1}0\} < 10\overline{1}\overline{2} >$ twinning, f) the $\{10\overline{1}2\} < \overline{1}011 >$ twinning [53-59]

Slip	Burgers			No of slip system		
System	vector type	Slip direction	Slip plane	Total	Independent	
1	a	<1120>	Basal (0001)	3	2	
2	a	<1120>	Prism type I $\{10\overline{1}0\}$	3	2	
3	a	<1120>	1^{st} -order pyramidal type I $\{10\overline{1}1\}$	6	4	
4	c+a	<1123>	2^{nd} -order pyramidal type II $\{11\overline{2}2\}$	6	5	

Table 2.6 Independent slip systems in HCP metals [53]

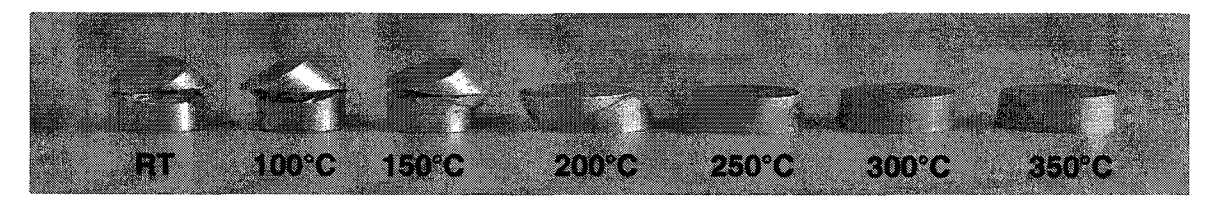


Figure 2.8 Uniaxial compression test under different temperatures [60]

2.2.2 Twinning

In addition to deformation by slip, Mg will deform by twinning if the basal plane is unfavorably oriented $^{[39,61]}$. The twinning process is a co-operative movement of atoms in which individual atoms move only a fraction of the interatomic spacing relative to each other. It was found that twinning is more often activated on the $\{10\overline{1}2\}$ planes in the $<\overline{1}011>$ directions in Mg (Figure2.7d); this is known as extension twinning because there is a consequent length increase along the c-axis. Note that, up to about 200 °C, the CRSS to activate $\{10\overline{1}2\}$ twinning is lower than those required to activate the non-basal slip systems. Therefore, twinning provides another independent deformation mechanism in conjunction with basal slip to aid plastic deformation of Mg at low temperatures. In the

case of deformation at high temperatures, twinning is reduced. This may be a result of the operation of non-basal slip systems as indicated in Figure 2.7.

Contraction twinning $\{10\overline{1}0\} < 10\overline{12} > \text{is seen (Figure 2.7e)}$ when compression is applied along the c-axis ^[61]. In addition, in cases where larger strains are applied to c-axis, twinning taking place within the reoriented primary twins (i.e. double twinning) has been observed, which is $\{10\overline{1}1\}$ twinning followed by $\{10\overline{1}2\}$ twinning and $\{10\overline{1}3\}$ twinning followed by $\{10\overline{1}2\}$ twinning followed by $\{10\overline{1}2\}$ twinning followed by $\{10\overline{1}2\}$ twinning followed twins for Mg-0.2%Ce cold rolled to 10% reduction ^[64]. The operation of second-order twinning could considerably increase the total plastic strain since unfavorable oriented grains for slip and twining are reoriented into a more favorable position after twinning ^[52]. A recent investigation on the effect of $\{10\overline{1}1\}$ - $\{10\overline{1}2\}$ double twins on the static recrystallization during annealing for two Mg alloys reveals that recrystallization induced by double twins is easier than that of primary twins ^[65]. The results suggest that generation of double twins under severe deformation conditions would lead to a softening during deformation. On the other hand, high local stress concentrations may be generated due to double twining, which may induce the formation of microcracks or voids ^[66].

2.2.3 Anisotropy

The limited slip and twinning systems determines the anisotropy of mechanical properties at ambient temperature deformation of Mg. Figure 2.10 compares the stress-strain curves obtained from tensile and compression testing at room temperature for wrought AZ31 products (as extruded and as-annealed sheet) [67]. As can be seen, these curves are not identical, and plastic anisotropy is still observed in annealed sheets. This will lead to a strong effect on the process of metal sheet drawing [68]. An investigation of fracture mechanism and forming limit in deep-drawing of AZ31 sheet shows that an early stage, fracture easily occurs when drawing at room temperature; elevating the

temperature increases the drawing ratio due to the decrease in anisotropy ^[69]. The results of polycrystal plasticity modeling suggest that the activation of <c+a> slip may lead to the decrease in deformation asymmetry ^[70].

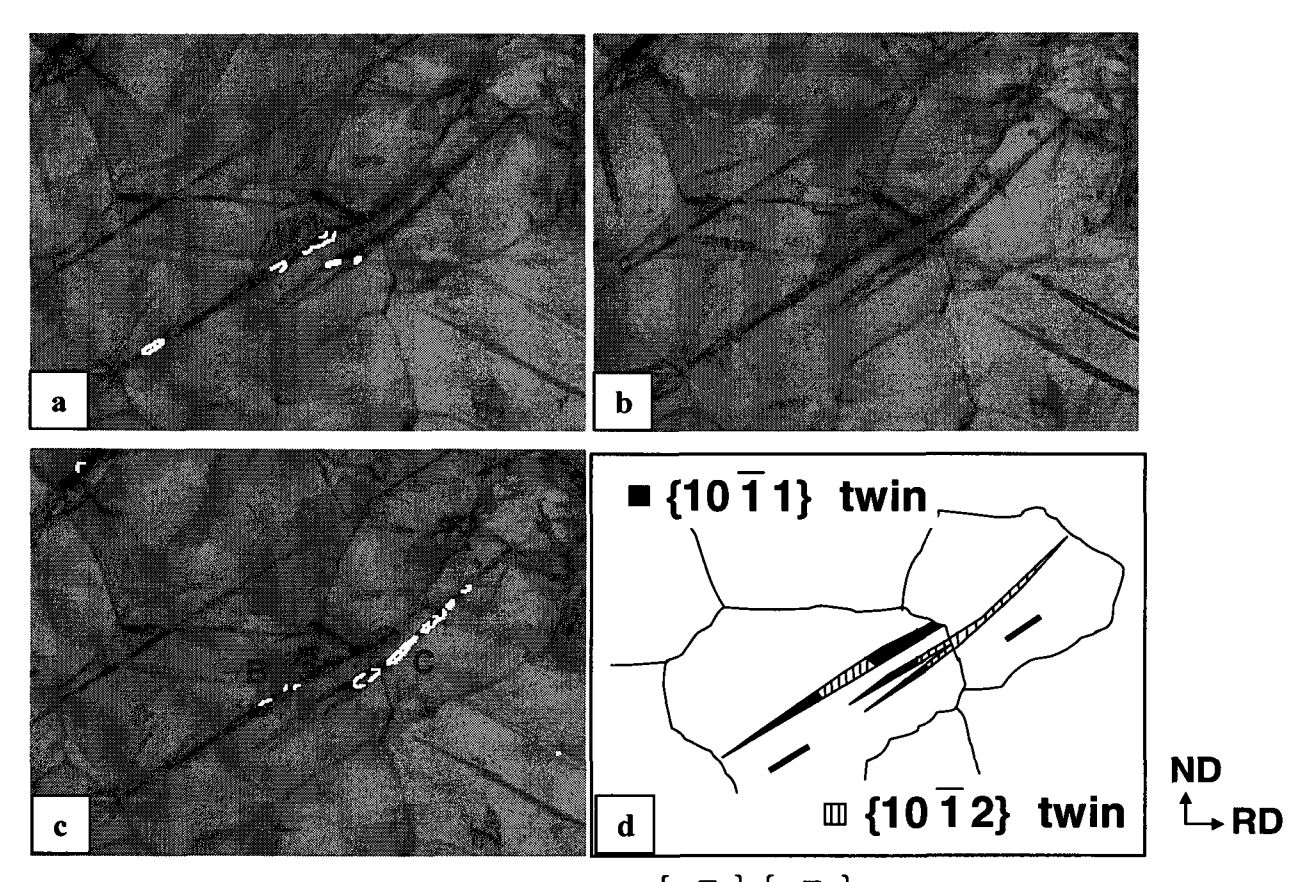


Figure 2.9 An example of double twinning of $\{10\overline{1}1\}$ - $\{10\overline{1}2\}$ for the Mg-0.2Ce% cold rolled to 10% reduction: a) $\{10\overline{1}1\}$ twin boundaries (56° <11 $\overline{2}0$ > ±5°), b) $\{10\overline{1}2\}$ twin boundaries(86° <11 $\overline{2}0$ > ±5°), c) bounders expected from $\{10\overline{1}1\}$ - $\{10\overline{1}2\}$ double twinning (38° <11 $\overline{2}0$ >±5°), and d) interpretation of twins B and C [64]

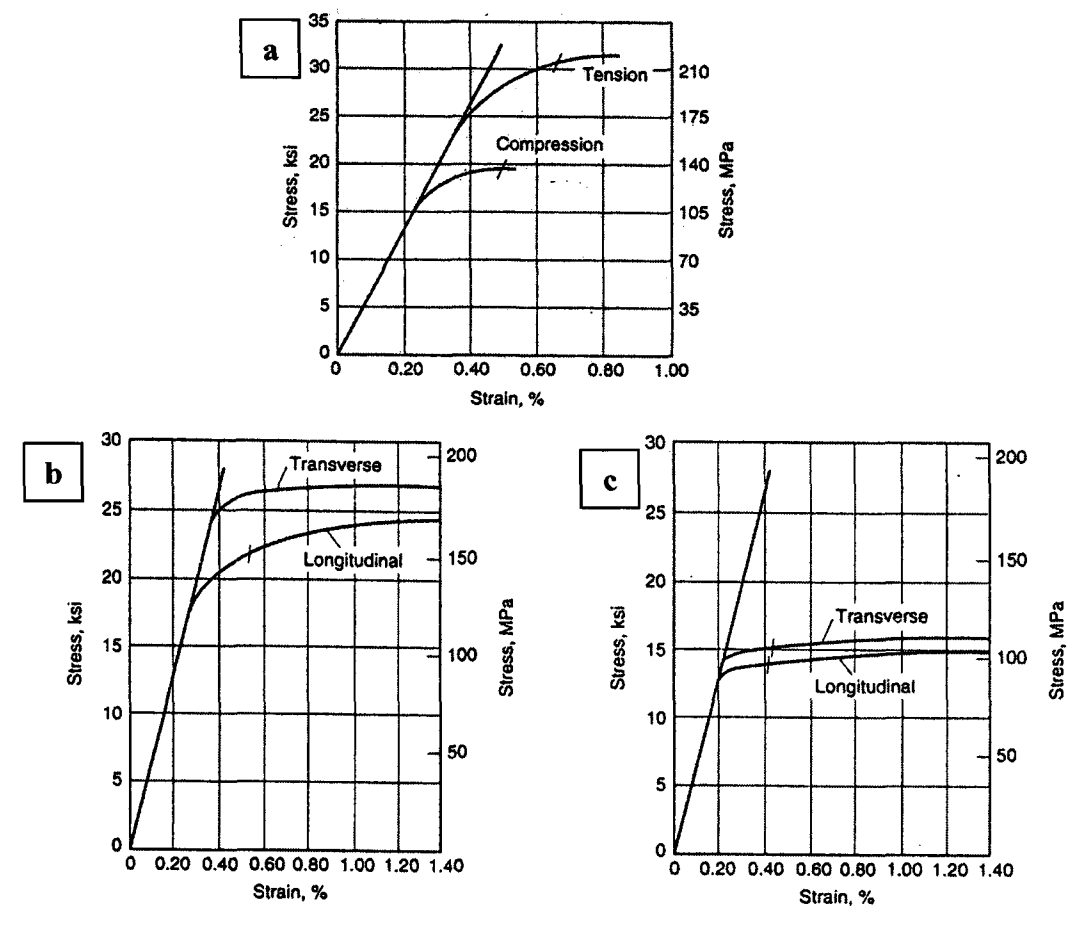


Figure 2.10 Stress-strain curves for AZ31B: a) tension and compression for the material as extruded, b) tension for the sheet as annealed, c) compression for sheet as annealed [67]

2.3 Dynamic Recrystallization (DRX) of Mg

DRX occurs during thermomechanical processes and plays a key role in removing work hardening and refining the initial microstructure, thus improving formability and determining the final properties of wrought Mg-alloys. Numerous studies have been conducted regarding the mechanisms [71-76], and Kaibyshev et al. generated a deformation mechanism map to illustrate the possible DRX-mechanisms under varying conditions of temperature and strain (Figure 2.11) [72]. As can be seen, there are four kinds of mechanisms responsible for DRX of Mg: bulging (discontinuous) DRX, subgrain (continuous) DRX, twinning induced DRX, and dislocation pileup induced DRX.

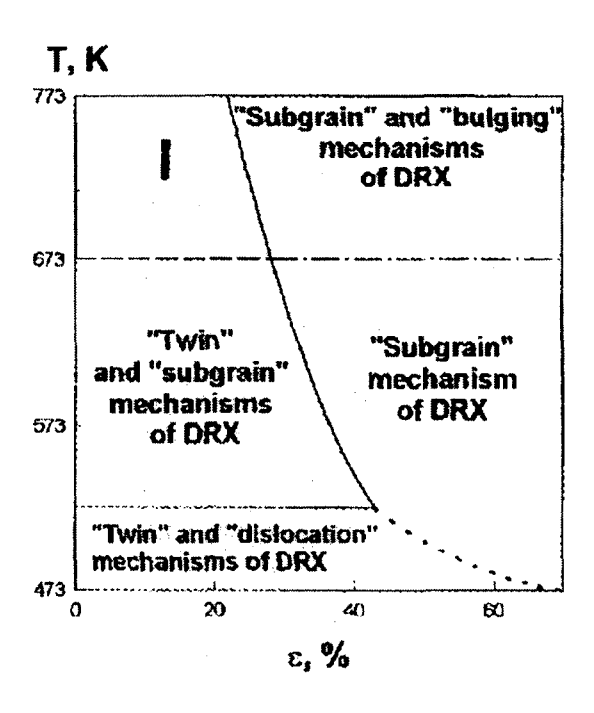


Figure 2.11 Microstructural mechanism map for pure magnesium (I - the area of transformation of initial twins into recrystallised grains)^[72]

2.3.1 Different Mechanisms

2.3.1.1 Bulging (Discontinuous) DRX

Bulging or discontinuous DRX is associated with local migration of initial boundaries, e.g. at preexisting high angle grain boundaries. The heterogeneity of crystallographic slip is responsible for the local migration of high-angle boundaries in Mg and Mg-based alloy during hot deformation ^[76]. The boundary migrates under a driving pressure arising from the dislocation density difference across the boundary. It usually moves into material which has a high dislocation density, and this boundary movement reduces the dislocation density to around zero by recrystallization ^[86].

2.3.1.2 Subgrain (Continuous) DRX

The operation of subgrain or continuous DRX ^[77, 78] is due to the high efficiency of dynamic recovery. New grains are formed progressively within the deformed original grains from the continuous increase of the subgrain boundary misorientations. Therefore, it occurs during hot deformation and does not involve the nucleation and growth of grains using the pre-existing boundaries as bulging DRX does. Figure 2.12 presents the operation of subgrain DRX ^[77]. First, a local shearing near grain boundaries occurs (Figure 2.12a) due to the inhomogeneous plasticity. Dynamic recovery of geometrically necessary dislocations then occurs (Figure 2.12b). Finally, the subgrains or grains form by lattice rotations which are driven by the high locally stored energy (Figure 2.12c).

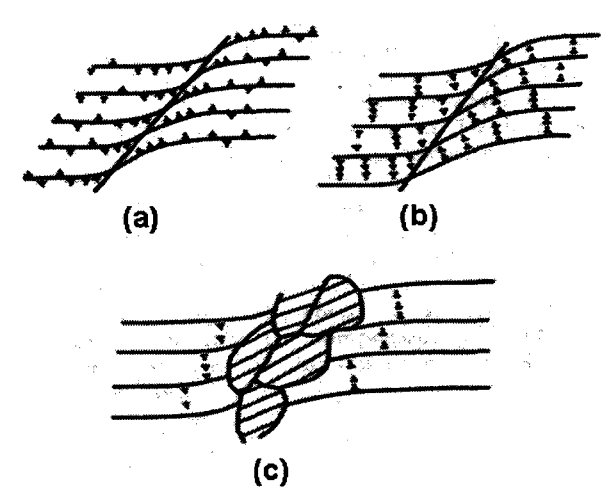


Figure 2.12 Schematic diagram showing the CDRX- "subgrain" by progressive lattice rotation and dynamic recovery at grain boundaries [77]

2.3.1.3 Twinning Induced DRX

There have been many studies of the nucleation of DRX grains at twins ^[72, 74, 79-82]. Three kinds of nucleation of TDRX were observed: i) nucleation by mutual intersection of primary twins; ii) nucleation by subdivision of coarse primary twin lamellae by fine secondary twins; and iii) nucleation by subdivision of primary twin lamellae by transverse low-angle boundaries. With further straining, twin boundaries transform into random boundaries. It was observed that the size of TDRX-grains is similar to the width of the twin, which suggests that the DRX grain size could be controlled by twinning. It is

interesting to note that TDRX still operated at temperatures of $300^{\circ}\text{C} \sim 400^{\circ}\text{C}$ during a torsion test for AZ31 alloy ^[81]. This suggests that TDRX could be used for controlling grain size during thermomechanical processing.

2.3.1.4 Dislocation DRX

Plastic deformation at low temperatures of 150 °C ~ 200 °C yields extensive twinning and dense dislocation pile-ups within initial grains. The "dislocation" recrystallization involves the intersection of slip and twin boundaries leading to the formation of high angle boundaries. A very low DRX volume fraction was observed ^[82].

2.3.2 Factors influencing DRX

2.3.2.1 Deformation Conditions

Mwenbela et al. studied the microstructural development of AZ31 (Mg-2.8Al-0.88Zn-0.01Mn) and AZ31-Mn (Mg-3.2Al-1.1Zn-0.34Mn) ingots by hot torsion testing ^[83]. The microstructural analysis reveals that DRX initiates at about 300 °C, at 0.1s⁻¹ and become more widespread with increasing temperature and decreasing strain rate. The same tendency was observed for the DRX-grain size, i.e. DRX-grains become larger with decreasing Z, which is the Zener-Hollomon parameter ^[84], having the physical meaning of so-called temperature-compensated strain rate as shown in Equation 2. 8.

$$Z = \varepsilon \exp(Q/RT)$$
 (Equation 2.8)

Q: activation energy for deformation, 130 kJ/mol and 138 kJ/mol for the low and high Mn alloys respectively;

T: deformation temperature (K);

 ε : strain rate (s⁻¹);

R: universal gas constant (R=8.314 J/(mol·K)).

The strain effect on DRX of AZ31 alloy (with an initial grain size of 22.5 μ m) was revealed from the observations of microstructural evolution in an interrupting torsion

testing. Tested at 350 °C and strain rate of 0.01s⁻¹, it was noted that the volume fraction of DRX gradually increases, but a completely dynamically recrystallized structure was not achieved even after a strain of 2.0 ^[85].

2.3.2.2 Initial Grain Size

Basically, the material with finer-grains will recrystallize more quickly than those with coarser grains ^[86]. A finer-grained structure increases the density of grain boundaries; therefore, the nucleation sites for DRX increase. On the other hand, the finer grain size also reduces the areas of inhomogeneities such as shear and deformation bands in which the DRX-grains may initiate.

It was also noted that the DRX mechanism of Mg is closely related to initial grain size. Bulging is only effective when the initial grain size is large enough for crystallographic slip to be heterogeneous, and the nucleation is suppressed when the initial grain size is reduced. In Mg-1%Mn-4%Al alloy, the bulging mechanism ceased as the grain size reducing from 85 to 24 µm ^[76].

Twinning is also more difficult when the grain sizes become smaller and, in fact, the yield stress for twinning also obeys a Hall-Petch type relation (Equation 2.5) [87]. Thus, there is a less possibility for TDRX to operate in the fine grain structure.

2.3.2.3 Initial Texture

Limited investigations have been made into the effect of the initial texture on DRX mechanisms in Mg. Kaibyshev pioneered the research by compression testing Mg-6wt% Zn-0.65wt% Zr at 300 °C and a strain rate of 2.8x10⁻³ s⁻¹ [88]. Samples were cut at different angles formed by compression axes and the basal planes (0°, 45°, and 90°). The results revealed that more DRX was observed in samples oriented 0° and 90° to the basal planes, and the DRX is slow in the sample orientated 45° to the basal planes. This indicates that texture plays a role in the kinetics of DRX. However, another investigation by Barnett using the wrought AZ31 [89] shows that the progress of DRX is only weakly

sensitive to the starting texture but it is more dependent on the deformation conditions and initial grain size.

2.3.2.4 Alloying Elements

There is a lack of study pertaining to the effects of individual alloying additions on the DRX of Mg during hot deformation. A few experimental results show that some DRX-grains form near the particles (Mg-Al and/or Al-Mn) in as-cast AZ31 during hot compression test ^[90, 91]. This suggests that DRX by particle simulated nucleation (PSN) may occur in Mg-alloys at certain conditions.

Kaibyshev and Sitdikov compared the dynamically recrystallized grain size of pure Mg and Mg-1%Mn-4%Al ^[71]. It was found that the DRX-grain size for pure-Mg is 3 to 4 times larger than that of Mg alloys with additions of Mn and Al under the same conditions. This indicates that alloying elements in the form of solid solute in Mg or forming second phases in Mg may affect DRX-grain size.

2.4 Mg-sheet Producing

2.4.1 Conversional Processing

In the conventional route to produce Mg-sheet, the process is usually as follows: i) direct chill (DC) casting process to cast slabs (e.g. the size of 0.3m x 1m x 2m); ii) homogenizing the slabs for several hours (e.g. at 450 °C); iii) hot rolling (480 °C ~ 300 °C) in several passes in a reversing hot mill to 5~6 mm; iv) final finish rolling in several passes of 5~20% reduction, with annealing the sheet (typically at 340 °C) before each finishing pass. The finishing part of hot rolling is time consuming, limits productivity, and has a high operating cost ^[92, 93]. Figure 2.13 demonstrates the sheet microstructure and the conventional process in laboratorial trial ^[92].

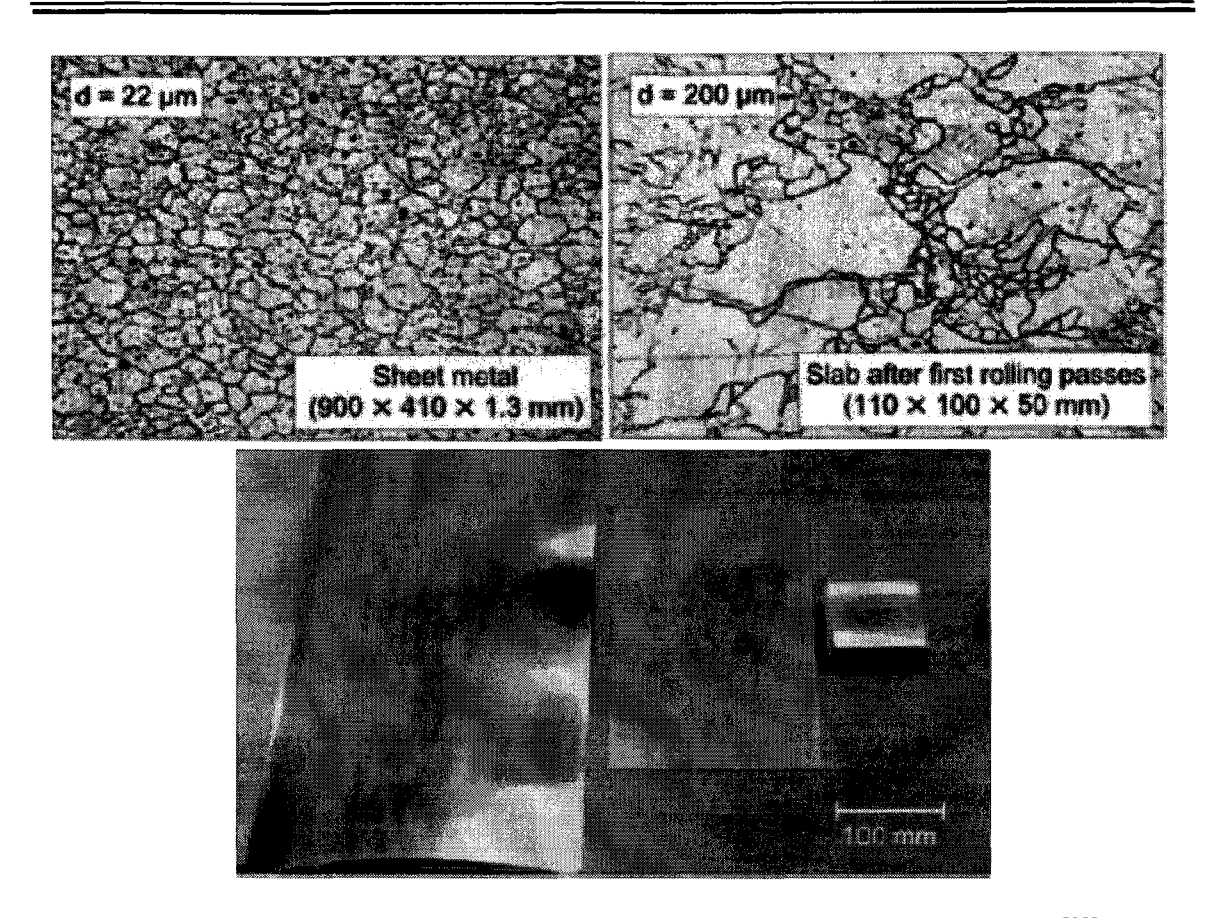


Figure 2.13 AZ31 sheet produced by conventional process at laboratory [92]

2.4.2 Innovative Strip Casting and Subsequent Rot Rolling Processing

To decrease the production cost and improve the properties (especially the formability) of Mg-sheet, different strip casting processes have been developed to reduce the thickness of starting slabs to around 6 mm, greatly decreasing the number of rolling passes. The current development and application of Mg-strip casting technology is summarized in Figure 2.14 by Bach et al. [93-103]. Note that twin roll casting is most common, in which thin strip and high productivity can be achieved. However, only alloys with a small solidification range can be processed safely since the rolling pressure is applied during solidification. Belt casters can be used for casting alloys with large solidification ranges due to the "moving die" design, but are still under development.

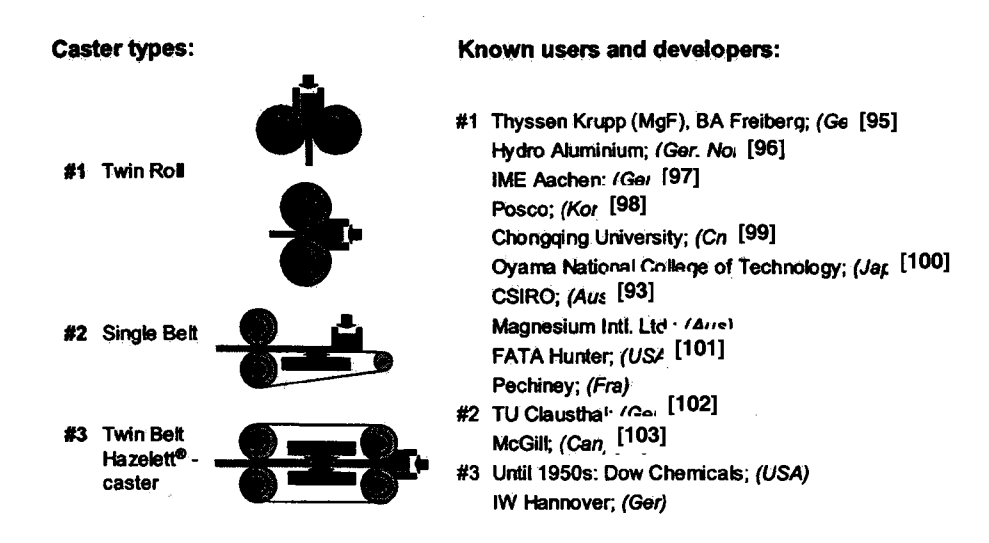


Figure 2.14 Development and application of Mg-strip casting technology [94]

Two alloys of AZ31 and ZEK100 were cast in to 8 mm thickness strips by twin belt Hazelett[®] caster, and their as-cast microstructure was compared with those of cast by DC process (Figure 2.15) ^[94]. As can be seen, the high cooling rate generates a finer average grain size in strip casting sample, and the Zr refined Al-free alloy shows a much strong refining due to adding Zr addition. Figure 2.16 shows the room temperature tensile test results for AZ31 sheet with a thickness of 1 mm after annealing at 300 °C for 30 min ^[104]. Again, sheets produced from strip casting present a better ductility, presumably because of a finer, more uniform grain size.

Many studies in optimization of process parameters and microstructure for twin roll casting process to improve mechanical properties have been conducted in recent years [93, 95-101, 104-106]. These process parameters include superheating temperature, velocity of roller, roll gap, and tribological aspects, etc. The results have shown that there is great potential to apply the innovative process into real industrial production, e.g. in the report of Numano et al. AZ31 has been successfully cast by twin roll caster and rolled into 0.5mm thickness sheets without peeling (i.e. machining) the surface prior to hot rolling, and the sheet produced from twin roll cast strip has better mechanical properties and higher drawability than that of commercial sheet [104].

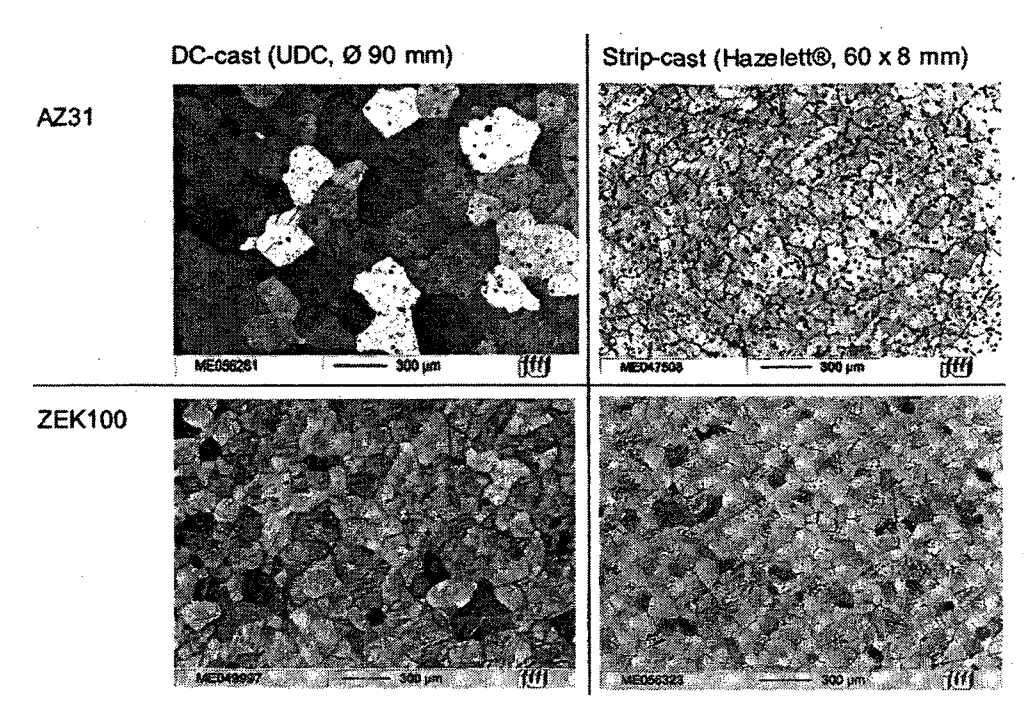


Figure 2.15 As-cast microstructure of AZ31 and ZEK100 after DC and twin belt strip casting $^{[94]}$

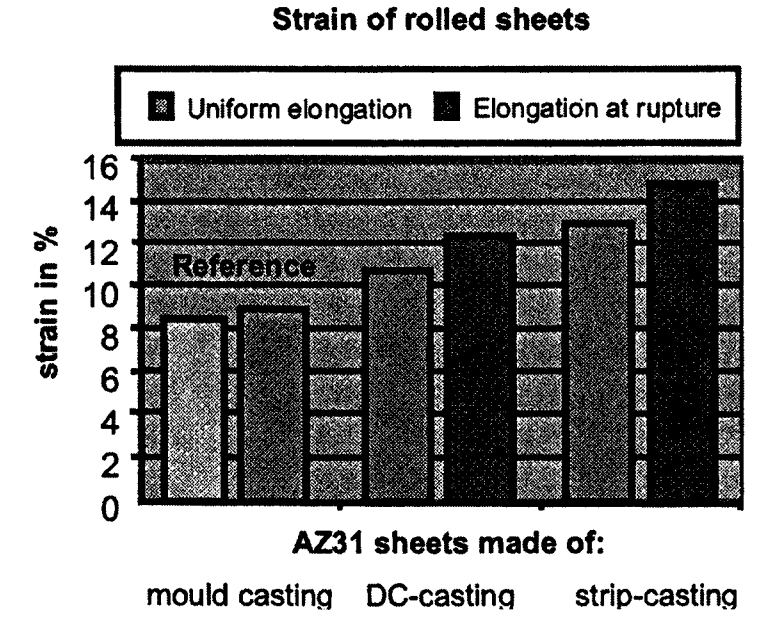


Figure 2.16 Strain values of Mg sheets rolled from different cast feedstock of AZ31 sheets (surface milled before rolling to 6 mm thickness and the same rolling schedule for all specimens (non-optimized))^[104]

2.5 Summary

Based on the literature review above, some general indications regarding alloying effect, deformation and DRX modes, and sheet processing associated with Mg, can be summarized as follows:

- Alloying is an effective way to enhance the strength of Mg by solid solution strengthening (e.g. Li, Al, Mn, Zn, Y, Ce), precipitation strengthening (e.g. Al, Si, Ca, Zn, Y, Mn, Ce), and grain refining (e.g. Zr, Ca, Sr, Al, Si);
- Microalloying Mg with a single element (e.g. Zr, Ca, and Si) shows a more significant refining effect on grain size;
- Room temperature ductility of Mg-alloys can be significantly enhanced by decreasing grain size;
- Multiple microalloyed Mg-alloy could have an improved ductility without adversely affecting strength;
- Deformation at room temperature combine slip and twinning, leading to a poor formability of Mg, due to lack of five independent slip systems for uniform deformation of HCP crystal structure;
- The activation of slip systems and twining depends on the specific deformation conditions under which the CRSSs can be attained. At elevated temperature, all the slip systems are activated due to the dramatic decrease in CRSSs of non-basal slip systems, and twinning is suppressed, so that the formability of Mg is significantly improved;
- The anisotropy of mechanical properties in room temperature deformation of Mg is a result of the limited slip and twinning systems, which can be improved by increasing temperature through the operation of non-basal slip systems, in addition to the basal system;

- The mechanisms of DRX occurring during hot deformation rely on the deformation conditions and are affected by the initial status of materials (e.g. grain size and composition). At high temperature and low strain rate (low Z), bulging DRX and subgrain DRX operate, while at low temperature and high strain rate (high Z), twinning induced DRX occurs. Moreover, small initial grain size suppresses twins and therefore suppresses bulging DRX and twinning induced DRX;
- The DRX volume fraction increases with increasing strain during hot deformation;
- Producing AZ31 by strip casting generated a more refined as-cast microstructure than commercials DC casting process; and the mechanical properties of Mg sheet produced by strip casting were also better than that produced by DC casting process in lab trials;

References:

- 1. M.M. Avedesian and H. Baker (eds.), "ASM Specialty Handbook: Magnesium and Magnesium Alloys", ASM International, Materials Park, Oh. U.S.A., (1999), p 10
- 2. J.R. Davis & Associates (eds), "Alloying Understanding the Basic", (ASM International, Materials Park, OH44073-0002), (2001) www.asminternational.org, p 4, P 436-452
- 3. R.W. Hertzberg, "Deformation and Fracture Mechanics of Engineering Materials", Third Edition, John Wiley & Sons, printed in U.S.A and Canada, (1989), p 81
- 4. W. Hume-Rothery and B.R. Coles, "Atomic Theory for Students of Metallurgy", The Institute of Metals, London, fifth (revised) reprint, (1969), p 342-343
- 5. W. Hume-Rothery, R. W. Smallman and C. W. Haworth, "The Structure of Metals and Alloy"s, The Institute of Metals, London, (1969), p 110-135
- 6. M.M. Avedesian and H. Baker (eds.), "ASM Specialty Handbook: Magnesium and Magnesium Alloys", ASM International, Materials Park, Oh. U.S.A., (1999), p 12-13
- 7. R.L. Fleischer, "Strengthening of Metals", (Ed. D. Peckner), Reinhold, New York, p 29
- 8. R. Labusch, "A Statistical Theory of Solid Solution Hardening", Physica Status Solidi (b), 41, (1970), p 659-669
- 9. P. Lukáč, "Solid Solution Hardening in Mg Single Crystals", Physica Statatus Solidi (a), 131, (1992), p 377-390
- 10. M.M. Avedesian and H. Baker (eds.), "ASM Specialty Handbook: Magnesium and Magnesium Alloys", ASM International, Materials Park, Oh. U.S.A., (1999), p 14-15

- 11. C.S. Roberts, "Magnesium and Its Alloys", John Wiley & Sons, (1960), p 17
- 12. B.L. Mordike, "Creep-resistant Magnesium Alloys", Materials Science and Engineering, A324, (2002), p 103-112
- 13. J.F. King and S. Thistlthwaite, "Magnesium Alloys and Their Applications", DGM-Informationsges, Oberursel, Germany, (1992), p 327-334
- 14. J.F. King, "Advances in Material Technology International", Sterling, (1990), p 12-19
- 15. M. Suzuki, R. Lnoue, M. Sugihara, H. Sato, J. Koike, K. Maruyama, and H. Oikawa, "Effects of Yttrium on Creep Behavior and Deformation Substructures of Magnesium", Materials Science Forum, 350-351, (2000), p 151-156
- 16. A.A. Luo, "Materials Comparison and Potential Applications of Magnesium Automobiles", TMS, Magnesium Technology (2000), p 89-97
- 17. E.B. Baril, P. Labelle, and M.O. Pekgulerguz, "Elevated Temperature Mg-Al-Sr: Creep Resistance, Mechanical Properties, and Microstructure", JOM, November (2003), p 34-39
- 18. K. Ozturk, Y. Zhong, A.A. Luo, and Z.K. Liu, "Creep Resistant Mg-Al-Ca Alloys: computational Thermodynamics and Experimental Investigation", JOM, November (2003), p 40-44
- 19. G., Yuan, Y. Sun, and W. Ding, "Effects of Bismuth and Antimony Additions on the Microstructure and Mechanical Properties of AZ91 Magnesium Alloy", Materials Science and Engineering A, 308, (2001), p 38-44
- 20. H. E. Friedrich and B. L. Mordike, "Magnesium Technology Metallurgy, Design Data, Applications", Springer Verlag, (2006), p 79-82
- 21. V. Gerold, "Dislocations in Solids, Vol.4", (Ed. F.R.N. Nabarro), North-Holland, Amsterdam, (1979), p 219
- 22. B. Reppich, "Materials Science and Technoloty, Vol.6", (Eds. R. Cahn, P. Haasen, and E.J. Kramer), VVH, Weinheim, (1993), p 311
- 23. E.O. Hall, "The Deformation and Ageing of Mild Steel: III Discussion of Results", Proceedings of the Physical Society, (1951), 64B, p 747-753
- 24. N.J. Petch, "The cleavage strength of polycrystals", Journal of the Iron and Steel Institute, London, 174, (1953), p 25-28
- 25. R. Armstrong, I. Codd, R. M. Douthwaite, and N. J. Petch, "The Plastic Deformation of Polycrystalline Aggregates", Philosophical Magazine, 7, Issue 73, January (1962), p 45-58
- 26. F. E. Hauser, P. R. Landon, and J. E. Dom: "Fracture of Magnesium Alloys at Low Temperature", Transactions AIME, J. of Metals, 206, May (1956), p 589-593
- 27. D.V. Wilson, "The Ductility of Polycrystalline Magnesium below 300 K", Journal of Institute of Metals, 98, (1970), p 133-143
- 28. R.G. Sambasiva and Y.V.R.K. Prasad, "Grain boundary strengthening in strongly textured magnesium produced by hot rolling", Metallurgical and Materials Transactions A, 13, (1982), p 2219-2226

- 29. R.G. Sambasiva and Y.V.R.K. Prasad, "Contribution of Texture to the Strengthening and Fracture in Hot-rolled Magnesium-12.7 at. % Cadmium Alloy", Journal of Materials Science, 18, (1983), p 2385-2392
- G. Nussbaum, P. Sainfort, G. Regazzoni, and H. Gjestland, "Strengthening Mechanisms in the Rapidly Solidified AZ91 Magnesium Alloy", Scripta Metallurgica., 23, (1989), p 1079-1084
- 31. H. Jones, "Enhancement of Properties and Performance of Materials by Rapid Solidification Processing", 97-98, (1994), Key Engineering Materials, p 1-12
- 32. Y.C. Lee, A.K. Dahle, and D.H. St. John, "Grain Refinement of Magnesium", TMS, Magnesium Technology 2000, (2000), p 211-218
- 33. C.A. Aliravci, J.E. Gruzleski, and F.C. Dimayuga, "Effect of Strontium on the Shrinkage Microporosity in Magnesium Sand Castings", AFS Transactions, 1992, p 92-115
- 34. J.E. Gruzleski and A. Aliravci, "Low Porosity, Fine-Grain Sized Strontium Treated Magnesium alloy Castings", US Patent US005143564A, Sept. (1992)
- 35. B. Tang, X.S. Wang, S.S. Li, D.B. Zeng, and R. Wu, "Effects of Ca Combined with Sr additions on Microstructure and Mechanical Properties of AZ91D Magnesium Alloy", Materials Science and Technology, 21(N0.5), (2005), p 574-578
- 36. M. Sakamoto, and S. Akiyama, "Suppression of Ignition and Burning of Molten Mg, Alloys by Ca Bearing Stable Oxide Film", Journal of Materials Science Letters, 16, (1997), p 1048-1050
- 37. S. Akiyama, "Flame-Resistant Magnesium Alloys by Calcium", J. Jpn. Foundry Eng. Soc., 68(1), (1994), p 38
- 38. B.S. You, W.W. Park, and I.S. Chung, "The Effect of Calcium Additions on the Oxidation Behaviour in Magnesium Alloys", Scripta mater., 42, (2000), p 1089-1094
- 39. G.V. Raynor, "The Physical Metallurgy of Magnesium and Its Alloys", Pergamon Press (London, New York, Paris, Los Angerles), (1959), p 98-102, p 216-247
- 40. M.Fujita, N. Sakate, S. Hirahara, and Y. Yamanoto, "Development of Magnesium Forged Road Wheel", JSAE Review 16, (1995), p 283-301
- 41. P.L. Schaffer, Y.C. Lee, and A.K. Dahle, "The Effect of Aluminum Content and Grain Refinement on Porosity Formation in Mg-Al Alloys", TMS, Magnesium Technology (2001), p 87-94
- 42. Y. Wang, Q. Wang, C. Ma, W. Ding, and Y. Zhu, "Effects of Zn and RE Additions on the Solidification Behavior of Mg-9Al Magnesium Alloy", Materials Science & Engineering A, (2002), p 1-5
- 43. S. Yue, R. Verma, E. Essadiqi, G.Seale and G. Vespa, "Effect of Chemical Composition and Microstructure on Elevated Temperature Tensile Properties of AZ-Type Mg Alloy sheet", Proceedings of the Third International Conference on Light Metals Technology, September 24-26, (2007), Saint-Sauveur, Quebec, Canada, p 210-214
- 44. F.W. Bach, M. Schaper, and C. Jaschik, "Influence of Lithium on hcp Magnesium Alloys", Materials Science Forum, 419-422, (2003), p 1037-1042

- 45. H. E. Friedrich and B. L. Mordike, "Magnesium Technology Metallurgy, Design Data, Applications", Springer Verlag, (2006), P 80-82
- W. Xiao, S. Jia, J. Wang, Y. Wu, and L. Wang, "Effects of Cerium on the Microstructure and Mechanical Properties of Mg-20Zn-8Al alloy", Materials Science & Engineering A, 474 (Issues 1-2), (2008), p 317-322
- 47. Q. Wang, W. Chen, X. Zeng, Y. Lu, W.Ding, Y. Zhu, and X. Xu, "Effect of Ca Addition on the Microstructure and Mechanical Properties of AZ91 Magnesium Alloy", Journal of Materials Science, 36, (2001), p 3035-3040
- 48. Q. Ma, D.H. StJohn, M.T. Frost, "A New Zirconium-rich Master Alloy for the Grain Refinement of Magnesium Alloys", K.U. Kainer (Ed.), Magnesium, Proceedings of 6th International Conference on Magnesium Alloys and their Applications, Wolfsburg, Germany, Pub. DGM, (2003), p 706–712
- 49. P. Juchmann and S. Wolff, "Magnesium Sheet Components for Ultralight Construction", 59th Annual World Magnesium Conference, International Magnesium Association, Montreal, May 19-21, proceedings, (2002), p 49-54
- 50. J.A. Chapman, and D.V. Wilson, "The Room-temperature Ductility of Fine Grained Magnesium", J. Inst. Met., 91, (1962), p 39-40
- 51. Y. Liu, W.P. Chen, W.W. Zhang, W. Zhang, and Y.Y. Li, "Study on the Bending-Bulging formability' of AZ31 Mg alloy sheet by microalloying of RE and Ca", Rare Metal Materials and Engineering, 35 (6), (2006), p 925-928
- 52. M.H. Yoo, "Slip, Twinning, and Fracture in Hexagonal Closed-Packed Metals", Metallurgical Transactions A, 12, (1981), p 409-418
- 53. P.G. Partridge, "The Crystallography and Deformation Modes of Hexagonal Close-packed Metals", Metallurgical Reviews, 118, (1967), p 169-194
- 54. M.M. Avedesian and H. Baker (eds.), "ASM Specialty Handbook: Magnesium and Magnesium Alloys", ASM International, Materials Park, Oh. U.S.A., (1999), p 7
- 55. P. Ward Flynn, J. Mote, and J.E. Dorn, "On the Thermally Activated Mechanism of Prismatic Slip in Magnesium Single Crystals", TMS-AIME, 221, (1961), p 1149-1154
- 56. T. Obara, H. Yoshinga, and S.Morozum, "{12-22} <-1-123> Slip System in Magnesium", Acta Metallurgica, 21, (1973), p 845-853
- 57. R.E. Reed-Hill and W.D. Robertson, "Pyramidal Slip in Magnesium", Acta Metallurgica, TMS-AIME, 212, (1958), p 256-259
- 58. S.R. Agnew, M.H. Yoo, and C.N. Tome, "Application of Texture Simulation to Understanding Mechanical Behavior of Mg and Solid Solution Alloys Containing Li or Y", Acta Materialia, 49, (2001), p 4277-4289
- 59. M.R. Barnett, "A Taylor Model Based Description of the Proof Stress of Magnesium AZ31 during Hot Working", Metallurgical and Materials Transactions A, 34, (2003), p 1799-1806
- M.R. Barnett, "Hot Working Magnesium AZ31", thermomechanical Processing, Mechanics, Microstructure & Control, ed. E.J. Palmiere, M. Mahfouf and C. Pinna, Sheffield University, Shefield (2003), p 56-62

- 61. R.W.K. Honeycombe, "The Plastic Deformation of Metals", (Edward Arnold Ltd, London), (1984), p 209
- 62. R.E. Reed-Hill, "A Study of the {10-11} and {10-13} Twinning Modes in Magnesium", TMS-AIME, 218, June (1960), p 554-558
- 63. W.H. Hartt and R.E. Reed-Hill, "The Irrational Habit of Second-Order {10-11}-{10-12} Twins in Magnesium", Transactions AIME, 239, October (1967), p 1967-1511
- 64. M.R. Barnett, M.D. Nave, and C.J. Bettles, "Deformation Microstructures and Textures of Some Cold Rolled Mg Alloys", Materials Science and Engineering A, 386, (2004), p 205-211
- 65. L. Jiang, J.J. Jonas and R. Mishra, "Effect of {10-11} Contraction and {10-11}-{10-12} Double Twins on the Subsequent Deformation Behavior of Two Mg Alloys", in Proceedings of Magnesium Technology 2008, ed. M.O. Pekguleruz et al., TMS, New Orleans, (2008), p 257-261
- 66. W.H. Hartt and R.E. Reed-Hill, "Internal Deformation and Fracture at Second-order {10-11}-{10-12} Twins in Magnesium", Transactions, TMS-AIME, 242, (1968), p 1127-1133
- 67. M.M. Avedesian and H. Baker (eds.), "ASM Specialty Handbook: Magnesium and Magnesium Alloys", ASM International, Materials Park, Oh. U.S.A., (1999), p 166
- 68. W. Truszkowski, "The Plastic Anisotropy in Single Crystals and Polycrystalline Metals", Kluwer Academic Publishers, printed in the Netherlands, (2001), p 5-7
- 69. M. Kohzu, Fl Yoshida, H. Somekawa, M. Yoshikawa, S. Tanabe, and K. Higashi, "Fracture mechanism and Forming Limit in Deep-Drawing of Magnesium Alloy AZ31", Materials Transactions, 42 No.7, (2001), p 1273-1276
- 70. S.R. Agnew and O. Duygulu, "A Mechanistic Understanding of the Formability of Magnesium: Examining the Role of Temperature on the Deformation Mechanisms", Materials Science Forum, 419-422, (2003), p 177-188
- 71. R.O. Kaibyshev and O.S. Sitdikov, "Structural Changes during Plastic Deformation of Pure Magnesium", The Physics of Metals and Metallography, 73 (No.6), (1992), p 635-642
- 72. R.O. Kaibyshev and O.S. Sitdikov, "Dynamic Recrystallisation and Mechanisms of Plastic Deformation", The Third International Conference on Recrystallisation and Related Phenomena, (1996), p 203-209
- A. Galiyev, R. Kaibyshev, and G. Gottstein, "Correlation of Plastic Deformation and Dynamic Recrystallisation in Magnesium Alloy ZK60", Acta Materialia, 49, (2001), p 1199-1207
- 74. O. Sitdikov and R. Kaibyshev, "Dynamic Recrystallisation in Pure Magnesium", Materials Transactions, 42 (No.9), (2001), p 1928-1937
- 75. R.O. Kaibyshev, O. S. Sitdikov, and A.M. Galiev, "Mechanisms of Plastic Deformation in Magnesium: I. Deformation Behavior of Coarse-Grained Magnesium", The Physics of Metals and Metallography, 80 (No.3), (1995), p 354-360
- 76. R.O. Kaibyshev and O. S. Sitdikov, "The Relation of Crystallographic Slip and Dynamic Recrystallization to the Local Migration of Grain Boundaries: I. Experimental Results", The Physics of Metals and Metallography, 78 (No.4), (1994), p 420-427

- 77. S.E. Ion, F.J. Humphreys, and S.H. White, "Dynamic Recrystallisation and the Development of Microstructure during the High Temperature Deformation of Magnesium", Acta Metallurgica, 30, (1982), p 1909-1919
- 78. A. Galiyev, R.Kaibyshev, and T. Sakai, "Continuous Dynamic Recrystallisation in Magnesium Alloy", Materials Science Forum, 419-422, (2003), p 509-514
- 79. H.J. McQueen, M. Myshlaev, M. Sauerborn, and A. Mwembela, "Flow Stress Microstructures and Modeling in Hot Extrusion of Magnesium Alloys", TMS, Magnesium Technology, (2000), Nashville, Tennessee, U.S.A, p 355–362
- 80. H.J. McQueen, A. Mwembela, and M.M. Myshlyaev, "Microstructural Evolution and Strength in Hot Working of ZK60 and Other Mg Alloys", Canadian Metallurgical Quarterly, 42 (1), (2003), p 97-112
- 81. M.M. Myshlyaev, H. J. McQueen, A. Mwembela and E. Konopleva, "Twinning, Dynamic Recovery and Recrystallization in Hot Worked Mg-Al-Zn Alloy", Materials Science and Engineering A, 337, (2002), p121-133
- 82. A.M. Galiyev, R.O. Kaibyshev, and G. Gottstein, "Grain Refinement of ZK60 Magnesium Alloy during Low Temperature Deformation", TMS, Magnesium Technology, (2002), Seattle, Washington, U.S.A, p 181-185
- 83. A. Mwembela, E.B. Konopleva and H.J. McQueen, "Microstructural Development in Mg Alloy AZ31 during Hot Working", Scripta Materialia, 37 No.11, (1997), p1789-1795
- 84. P.D. Hodgson, "Microstructure modeling for property prediction and control", Journal of Materials Processing, 60 (1-4), (1996), p 27-33
- 85. A.G. Beer and M.R. Brnett, "The Hot Working Flow Stress and Microstructure in Magnesium AZ31", Magnesium Technology 2002, Edited by H.I. Kaplan, TMS, (2002), p 193-198
- 86. F.J. Humphreys and M. Hatherly, "Recrystallization and Related Annealing Phenomena", second edition, Oxford (2004), p 427-431, p 227-228
- 87. S. Mahajan and D.F. Williams, "Deformation Twinning in Metals and Alloys", International Metallurgical Reviews, 18, (1997), p 43-61
- 88. O.A Kaibyshev, "Relationship between Mechanisms of Deformation and Development of Dynamic Recrystallisation", Recrystallisation'90. 1990: Minerals, Metals & Materials Society
- 89. Barnett, M.R.: "Recrystallisation During and Following Hot Working of Magnesium Alloy AZ31", Materials Science Forum, 419-422, (2003), p 571-577
- L. Jiang, G. Huang, S. Godet, J.J. Jonas and A.A. Luo, "Particle-stimulated Nucleation of Dynamic Recrystallization in AZ31 Alloy at Elevated Temperatures", Materials Science Form, 488-489, (2005), p 261-264
- 91. A.G. Beer and M.R Barnett, "Microstructural Development during Hot Working of Mg-3Al-1Zn", Metallurgical and Materials Transactions A, 38A, August (2007), p 1856-1866
- 92. H. E. Friedrich and B. L. Mordike, "Magnesium Technology Metallurgy, Design Data, Applications", Springer Verlag, (2006), P 272-275

- 93. D. Liang and C.B. Cowley, "The Twin-Roll Strip Casting of Magnesium", CSIRO, JOM, May (2004), p 26-28
- 94. Fr.-W. Bach, M.Rodman, A. Rossberg and M. Hepke, "Magnesium Sheet Production Today and Tomorrow", Magnesium Technology in the Global Age, 45th Annual Confrerence of Metallurgists of CIM, Montreal, Canada, Edited by M.O. Pekguleryuz and L.W. F. Mackenzie, (2006), p 255-268
- 95. B. Engl, "Eine neue herstellungsmethode und Anwendungspotenitiale für Magnesiumlech", ThyssenKrupp Techforum, 12, (2004), p 14-21
- 96. L. Löchte, H.Westengen, and J.Rodseth, "An efficient Route to Magnesium Alloy Sheet: Twin Roll Casting and Hot Rolling", 13 Magnesium Abnehmerseminar, Aalen, (2005)
- 97. B. Friedrich, and R. Sauermann, "Magnesium Thin Strip Casting", EMC2003, Germany, 3, (2003), p1350-1351
- 98. S.S. Park, J.G. Lee, H.C. Lee, and N.J. Kim, "Development of Wrought Mg Alloys Via Strip Casting", Proceedings TMS Annual Meeting, Charlotte-NC, (2004), p107-112
- 99. C. Yang, P. Ding, D. Zhang, and F. Pan, "The Microstructure and P427rocessing in Twin Roll Casting of Magnesium Alloy Strip", Materials Science Forum, 488-489, (2005), p 427-430
- 100.H. Watari, N. Koga, R. Paisarn, and T. Haga, "Formability of Magnesium Alloy Sheets Manufactured by Semi-Solid Roll Strip Casting", Materials Science Forum, 449-452, (2004), p 181-184
- 101.C. Romanowski, A. Troeano, B. Taraglio, and S. Hamer, "Twin Roll Casting Technology for Magnesium Sheet", conference lecture, Magnesium broad horizons, Moscow, Nov. 2005
- 102.L. Wondraczek, "Untersuchungen zur herstellung von Magnesiumbändern im DSC-Verfahren", Dissertation (TU Clausthal), ISBN 3-89720-768-0
- 103.J.S. Kim, M. Isac, and R.I.L. Guthrie, "Metal-Mold Heat Transfer and Solidification of Magnesium Alloys in Belt Casting Process", Magnesium Technology 2004, Proceedings TMs, Charlotte-NC, (2004), p 247-255
- 104.M. Numano, N. Mori, Y. Nakai, and N. Kawabe, "Properties of AZ31 and AZ91 Sheets Made by Twin Roll Casting", Materials Science Forum, 539-543, (2007), p 1650-1655
- 105.G.T. Bae, S.S. Park, D.H. Kang, Y.S. Oh, and N.J. Kim, "Twin-Roll casting of Mg Alloys", Proceedings of the Light Metals Technology Conference, Sept. 24-26, 2007, Saint-Sauveur, Quebec, Canada, (2007), p 183-188
- 106.R. Kawalla, M. Oswald, M. Ullmann, C. Schmidt, H. P. Vogt, and N. D. Cuong, "Development of a Strip-Rolling Technology for Mg Alloys Based on the Twin-Roll-Casting Process", in Proceedings of Magnesium Technology 2008, ed. M.O. Pekguleruz et al., TMS, New Orleans, (2008), p 177-182

Chapter 3

Research Objectives

Based on the literature review, there are few workers are investigating AZ31 for the purpose of sheet products, and there is a noticeable absence of efforts at optimizing the microstructures in sheet processing. In particular, the concept of microalloying seems to have potential, but, very little attention has been paid to the effects of microalloying of AZ31 on the hot deformation behavior.

Thus, the research objectives of the present work are:

- i) To investigate the effects of microalloying (Ca, Sr, and Ce) on the microstructures of AZ31 under various conditions: casting, hot-compression testing, rolling, annealing, and hot-tensile testing;
- ii) To examine the behavior of the above alloys during hot compression to develop concepts for the design of hot rolling processing;
- iii) To study the behavior of these alloys during hot tensile testing to evaluate the hot formability mechanisms;
- iv) To propose microalloy compositions for AZ31 alloys with improved formability for producing Mg-sheets.

Chapter 4

Experimental Procedure

Figure 4.1 shows the flowchart of the entire experimental procedure. The experimental work consists of five main parts; (i) design new alloys by microalloying commercially produced AZ31 alloy with Ca, Sr and Ce, and cast samples under different solidification conditions by using different moulds (steel, copper, and copper with water cooling); (ii) hot compression testing of the as-cast structures to examine hot compression behaviors, which may help to understand processes taking place during hot rolling; (iii) rolling to sheet in the MTL-CANMET laboratory hot mill; and (iv) investigating the hot formability of the sheet by tensile testing. Throughout all of the above four parts, microstructure characterization was performed, and is effectively the fifth part. The details are described as follows.

4.1 As-cast Sample Preparation

4.1.1 Alloy Design

Based on the literature review and the general requirements of wrought Mg-alloys, microalloying additions of Ca, Sr and Ce were added to a commercially obtained base alloy AZ31. Ca and Sr were used as grain refiner for initial as cast materials; and Ce was

added with the expectation of reducing the c/a ratio in Mg lattice. Moreover, all of these additions may produce new thermal stable second phases in based alloy AZ31, which could affect the hot formability of AZ31. To predict the formation of such new phases, FactSageTM software for chemical thermodynamics, developed jointly between **Thermfact/CRCT** (Montreal, Canada) and **GTT-Technologies** (Aachen, Germany), was used to calculate the possible intermetallic phases during solidification. The actual results were determined by phase analysis in as-cast samples with Electron Probe Microanalysis (EPMA).

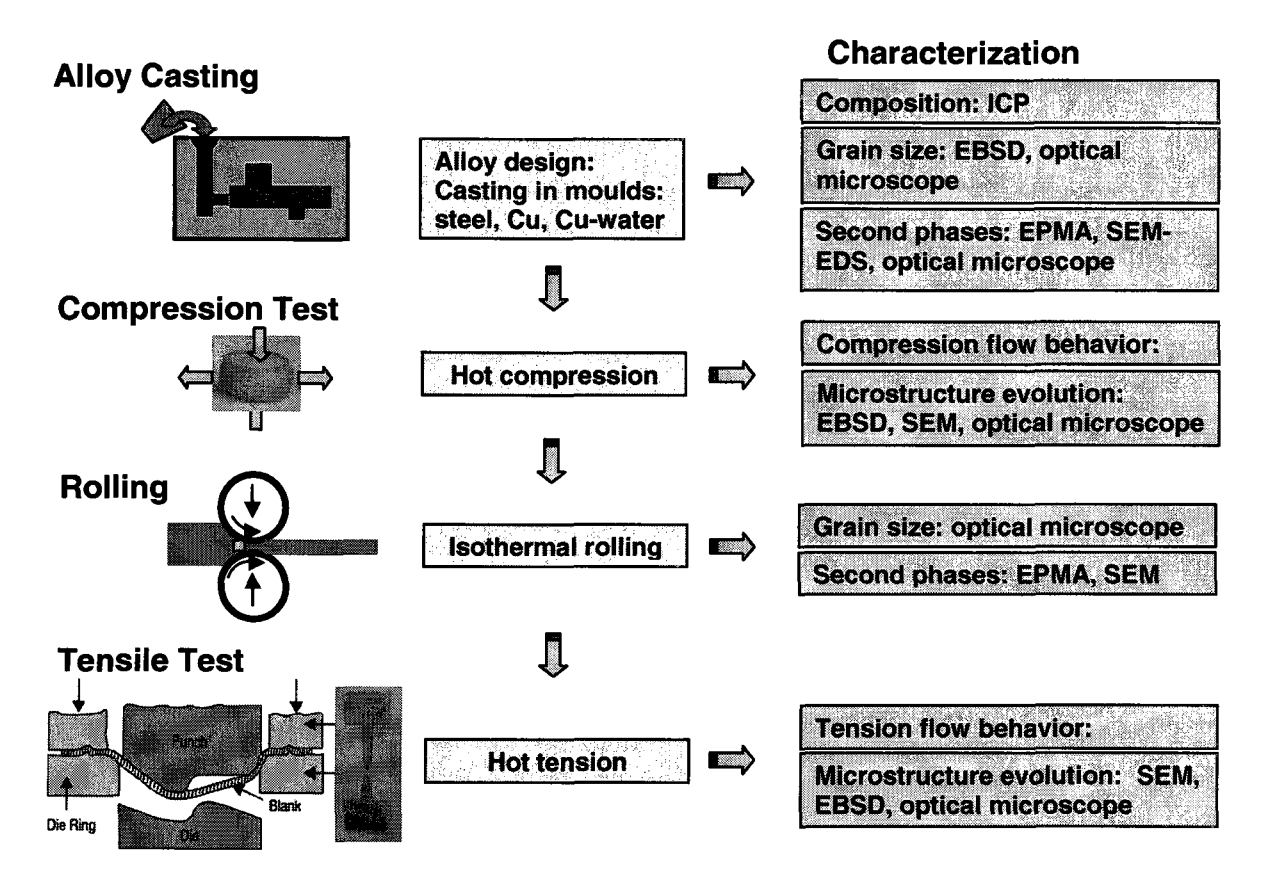


Figure 4.1 The flowchart of experimental procedure

In this work, eight experimental alloys, based on commercial AZ31, were designed with target compositions as follows.

1) AZ31 (reference)

- 2) AZ31 alloy + 0.2%Ca
- 3) AZ31 alloy + 0.2%Sr
- 4) AZ31 alloy + 0.2%Ce
- 5) AZ31 alloy + 0.2%Ce + 0.2%Ca
- 6) AZ31 alloy + 0.2%Sr + 0.2%Ce
- 7) AZ31 alloy + 0.2%Ce + 0.2%Ca + 0.2%Sr
- 8) AZ31 alloy + 0.2%Ca + 0.2%Sr

4.1.2 Raw Materials

In order to test the repeatability of microalloying and the sensitivity to raw materials, two series of raw materials were selected as shown in Tables 4.1 and 4.2. Commercial AZ31 billets with the nominal composition of Mg-3%Al-1%Zn-0.3%Mn, by weight were used. One was purchased from Timminco Inc.; another was purchased from American Iron & Metals Company Inc. There are some differences in the contents of Al and Mn. Alloying additions of Ca and Sr were added using different master alloys of Mg-Ca and Sr-Al. Considering alloying costs, cerium was added as the pure metal and mischmetal (which contains 55% Ce, but is about 50% cheaper)^[1] to compare their alloying efficiency. Table 4.3 shows the composition of the mischmetal.

Table 4.1 Raw materials series one (wt.%)

AZ31: Timminco (supplier's data)									Alloy	Pure Metal
Al	Zn	Mn	Fe	Ni	Cu	Si	Ca	Mg-Ca	Sr-Al	Ce
3.50	0.98	0.47	0.0015	0.0005	0.0013	0.029	0.001	70-30	90-10	100

Table 4.2 Raw materials series two (wt.%)

AZ31: American Iron & Metals Company Inc (supplier's data)								Maste	r Alloy	Mischmetal
Al	Zn	Mn	Fe	Ni	Cu	Si	Ca	Mg-Ca	Sr-Al	Ce
3.00	1.00	0.20	0.0005	0.0005	0.005	0.010	0.004	20-80	90-10	56

Ce La Pd Nd Fe Mg Al Si Mn

0.23

5.2

Table 4.3 Chemical composition of mischmetal (wt. %)

0.21

0.2

0.06

0.05

4.1.3 Casting Moulds

55.9

30.5

6.8

Three kinds of permanent moulds were used in this study to generate different solidification conditions: steel mould preheated at 400 °C, copper mould used at ambient temperature, and copper mould with water cooling. Figure 4.2 shows the different configuration of these moulds and samples that were cast. The small plate samples (102 mm x 127 mm x 25.4 mm) were cast in the preheated steel mould; disk shaped samples (Φ40 mm x 10 mm) were produced in the Cu-mould; and large plates (130 mm x 280 mm x 12.7 mm) were cast in the water cooled mould.

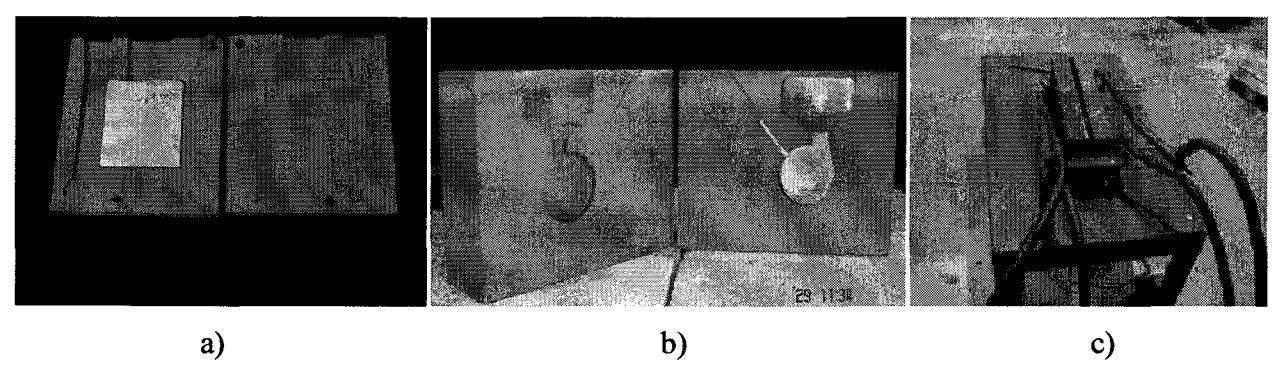


Figure 4.2 Configuration of casting moulds and corresponding samples: a) steel mould; b) copper mould; c) copper mould with water cooling

4.1.4 Casting Conditions

The small plate and disk samples were cast at McGill University, and the large plates were cast at Materials Technology Laboratory - CANMET located in Ottawa, Ontario, Canada. Electric resistance furnaces were used. To minimize oxidation, and

obtain high alloying efficiency and sound casting samples, the following casting procedure was used.

- The electric furnace was preheated to 750 °C;
- Small pieces of AZ31 alloy were placed in a mild steel crucible in the electrical resistance furnace in a controlled atmosphere ($CO_2 + 0.5\%$ SF₆);
- Adding alloying additions in the order of Ca, Sr, and Ce (when using multiple alloy additions);
- Adding alloying additions at 690 °C for 10 mins for a single addition, 15 mins total for two different alloy additions (i.e. 5 mins after one addition and 10 mins after the second), and 20 mins total for three different additions (i.e. 5 mins + 5mins + 10 mins);
- Stirring after adding and then after every 5 mins;
- Degassing at 730 °C with argon for the liquid metal to cast large plates (130 mm x 280 mm x 12.7 mm) in a water cooled copper mold;
- Preheating steel moulds at 400 °C;
- Pouring at 730 °C.

4.2 Compression Testing

The deformation in the hot rolling process is a complex combination of shear and compression strains. In the laboratory, such a combination is difficult to achieve and usually compression and torsion are used separately to indicate hot rolling behaviors. In this work, studies were limited to hot compression tests.

4.2.1 Specimens

Cylindrical compression specimens were machined from cast samples as shown in Figure 4.3. The specimens from plate castings had a dimension of 11.4 mm in height and 7.6 mm in diameter, and the specimens from disk castings were 9.0 mm in height and 6.0 mm in diameter. All specimens had the same ratio of height and diameter (H/D=1.5) to facilitate comparison of flow results.

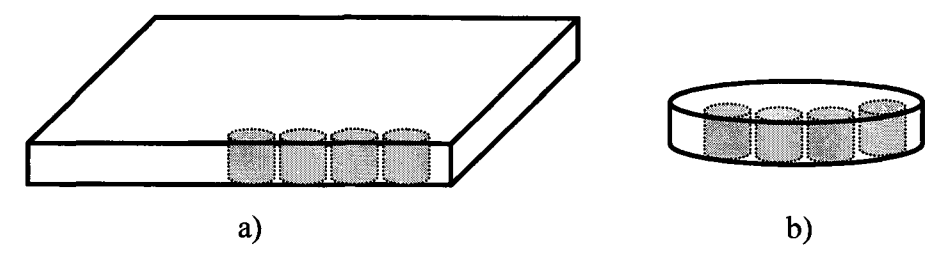


Figure 4.3 Specimens for compression experiment: a) from plate casting, b) from disk shape casting

4.2.2 Facilities

The compression test was performed in the Hot Deformation Laboratory at McGill University on a computer controlled servo-hydraulic materials testing system (MTS) with a 100 kN capacity, equipped with a radiant furnace, as shown in Figure 4.4. During testing, high purity argon was used to minimize oxidization. In addition, mica sheets coated with boron nitride paste were used for lubrication to diminish the coefficient of friction during hot compression testing.

4.2.3 Test Schedules and Conditions

One- and two-hit hot compression tests were performed under isothermal and constant true strain rate conditions. Figure 4.5 presents the testing parameters corresponding to two schedules.

One hit isothermal compression tests were carried out at 250 °C to 400 °C, and at constant true strain rates of $0.1s^{-1}$, $0.01s^{-1}$, and 0.001 s⁻¹ for specimens cast in different moulds to determine the continuous stress-strain curves so that the effects of

microalloying on flow behavior and dynamic recrystallization can be observed. To examine the microstructure evaluation during hot compression and check the repeatability of testing results, interrupted tests were performed to strains of 0.2, 0.4, 0.6, 0.8, up to 1.0 for some selected conditions.

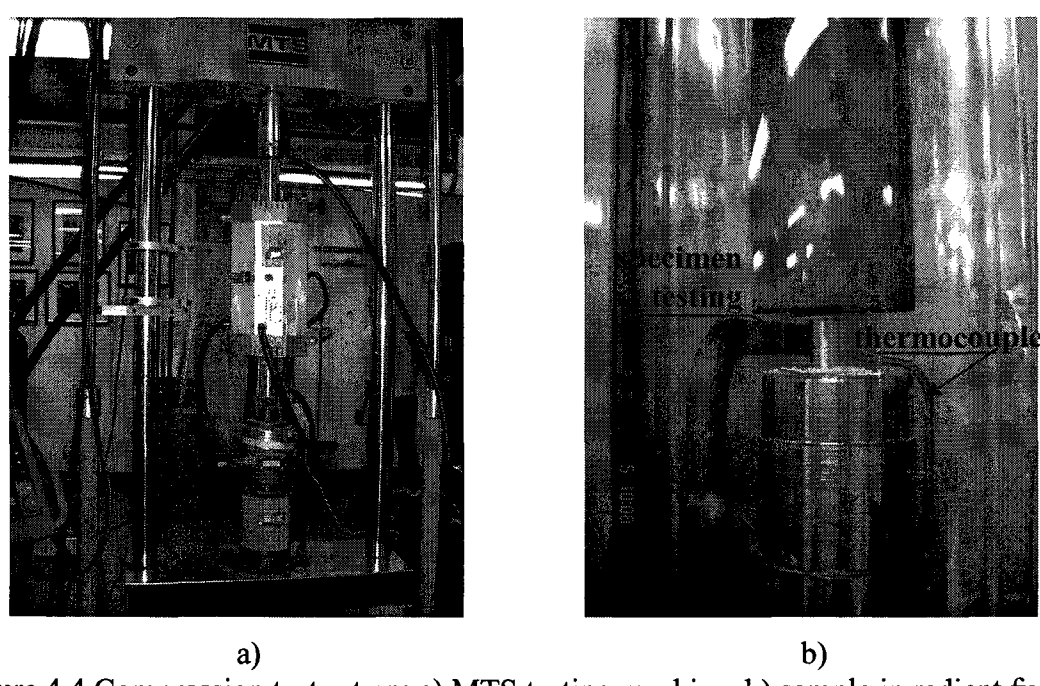


Figure 4.4 Compression test set up: a) MTS testing machine, b) sample in radiant furnace

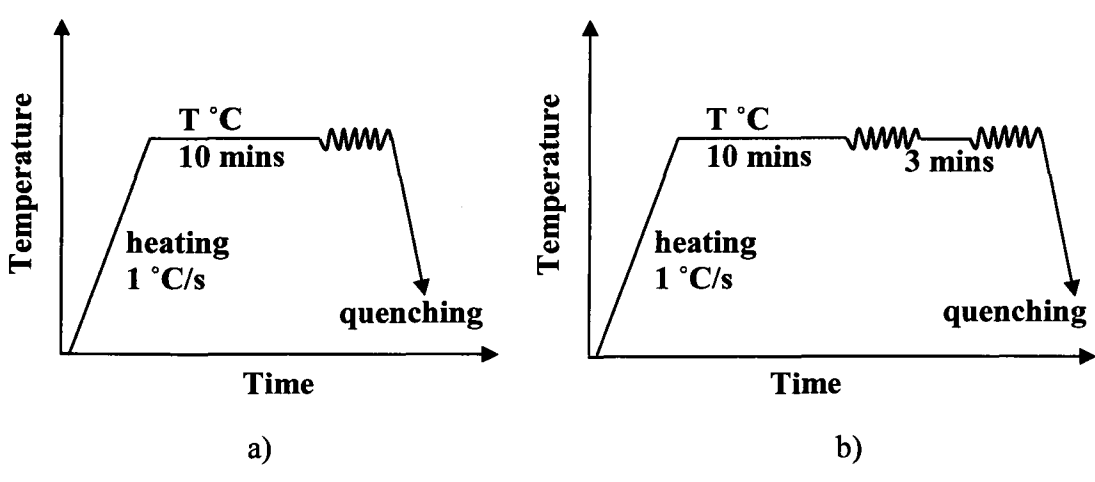


Figure 4.5 Compression test schedules: a) one hit test, b) two hit test

Two-hit isothermal compression tests were conducted to a strain below 1.0: true strains of 0.22 (20% reduction per pass) for the first hit, and a true strain of 0.03 (just after the nominal yield stress at offset strain of 0.02) for second hit. The purpose of the tests was to study whether there is interpass restoration, and to quantify this effect, if any. At a test temperature of 400 °C and a strain rate of 0.1s⁻¹, the interpass time of 3 min was selected based on the conditions used for the isothermal rolling experiments. Interrupted tests (before the first hit compression, immediately after the first compression hit, and immediately before the second compression hit) were performed to identify the microstructure evolution during this test.

The raw data of load and displacement were converted into true stress (in MPa) and true strain by the following equations:

$$\sigma = -\frac{F}{A_0} \cdot \frac{h_i}{h_0}$$
 (Equation 4.1)

$$\varepsilon = -\ln\left(\frac{h_i}{h_0}\right)$$
 (Equation 4.2)

Where F is the load, A_0 is the initial cross-sectional area, h_i is the instantaneous height, and h_0 is the initial height of the sample.

To quantify the critical strain to initiate the dynamic recrystalization (DRX) during the hot compression test, the σ - ϵ data were regressed into a 9th order polynomial smoothed stress-strain curve by Excel. Based on the mathematical principles and following equation ^[2], the inflection point in the $\ln(d\sigma/d\epsilon)$ - ϵ is the same point as the inflection point in the θ - σ curve (where θ is the work hardening rate, $d\sigma/d\epsilon$), corresponding to the onset of dynamic recrystallization. By using Maple 10 software, the inflection point in the $\ln(d\sigma/d\epsilon)$ - ϵ can be calculated.

$$\left(\frac{\partial \theta}{\partial \sigma}\right)_{\varepsilon} = \left(\frac{\partial \ln \theta}{\partial \varepsilon}\right)_{\varepsilon}$$
 (Equation 4.3)

The fractional softening between two hits was determined using the 0.2% offset

method, for which the equation to be used is as follows [3]:

$$X = \frac{\sigma_m - \sigma_{v2}}{\sigma_m - \sigma_{v1}}$$
 (Equation 4.4)

Here σ_{y1} and σ_{m} are the initial 0.2% offset yield stress and the flow stress after first hit, respectively, and σ_{y2} is the offset yield stress of the second hit.

During the compression testing, at least two samples were tested to check the repeatability since casting defects may generate some errors.

4.3 Rolling Experiments

4.2.1 Rolling Facilities

Isothermal rolling experiments were conducted at CANMET to make Mg-sheets for designed alloys. Table 4.4 displays the compositions for the alloys rolled. Figure 4.6 shows the set up of the Stanat pilot-scale reversing mill, preheating and inter-pass heating furnace, and data recording system.

Table 4.4 Compositions of AZ31-based sheets rolled at CANMET

Target composition	%Al	%Zn	%Mn	%Ca	%Ce	%Sr
AZ31	3.00	1.06	0.31	-	-	-
AZ31+0.2%Ca	2.96	1.04	0.27	0.20	<u>-</u>	-
AZ31+0.2%Ce	2.94	1.02	0.26	0.20	-	-
AZ31+0.2%Ca+0.2%Ce	2.99	0.99	0.27	0.21	0.20	-
AZ31+0.2%Ca+0.2%Sr+0.2%Ce	3.00	1.03	0.27	0.21	0.20	0.20
AZ31+0.2%Ca+0.2%Sr	3.00	0.98	0.26	0.21	-	0.21



Figure 4.6 Rolling facilities to make Mg-sheets

4.2.2 Rolling Schedules

Table 4.5 demonstrates two typical rolling schedules corresponding to two rolling conditions. Two typical rolling temperatures of 300 °C and 400 °C were selected based on previous hot compression testing and other studies in as-rolled structures ^[4]. Plates with a thickness of 12.7 mm cast in water cooled Cu-mould were cut and machined into small plates with a dimension of 70 mm x 110 mm x 11 mm. These plates were reheated at 450 °C for 1 hour in a resistance furnace, and then rolled into sheets with a thickness of approximate 1.6 mm using. Interpass reheating for $2 \sim 3.5$ mins was needed to increase the temperature back to desired rolling temperature since there is a considerable temperature drop (50 to 100 °C) in the roll gap.

Table 4.5 Rolling conditions and typical rolling schedules

		Conditio	n 1		Condition 2				
Rolling conditions	Preheating: 450°C, 1 hr	Rolling: 300 °C, 20	per pass	Preheating 450°C,1 hr	Rolling: 400 °C, 30% red. per pass				
Passes	Roll gap (mm)	Total Red. (%)	Red. (%)	Strain rate (s ⁻¹)	Roll gap (mm)	Total Red.(%)	Red. (%)	Strain rate (s ⁻¹)	
1	9.53	15.73	15.73	5.60	8.38	25.84	25.84	7.36	
2	7.62	20.00	20.00	6.95	6.10	46.07	27.27	8.81	
3	6.10	46.07	20.00	7.78	4.06	64.04	33.33	11.58	
4	4.83	57.30	20.83	8.89	2.79	75.28	31.25	13.66	
5	3.68	67.42	23.68	9.54	1.91	83.15	31.82	16.65	
6	2.79	75.28	24.14	12.41	1.27	88.76	33.33	20.71	
7	2.16	80.90	22.73	13.78					
8	1.65	85.39	23.53	15.98					
9	1.27	88.76	23.08	18.07					

4.3 Tensile Testing

In order to investigate the general mechanical properties at room temperature and study their hot deformation behaviors of the sheet microstructures, tensile tests were performed at ambient temperature and elevated temperature at the Technical Center of General Motors located at in Warren, Michigan, USA.

4.4.1 Ambient Temperature Tensile Testing

4.4.1.1 Specimens

The configuration of tensile specimens for ambient temperature test is illustrated in Figure 4.8, which were machined from rolled sheets and annealed at 400 °C for 10 min. The tensile directions were parallel to the rolling direction.

4.4.1.2 Facilities and Test Conditions

The testing was conducted using 5582 screw-driven Instron machine with a constant cross-head pulling speed of 10 mm/min and a 25.4 mm gauge sensor.

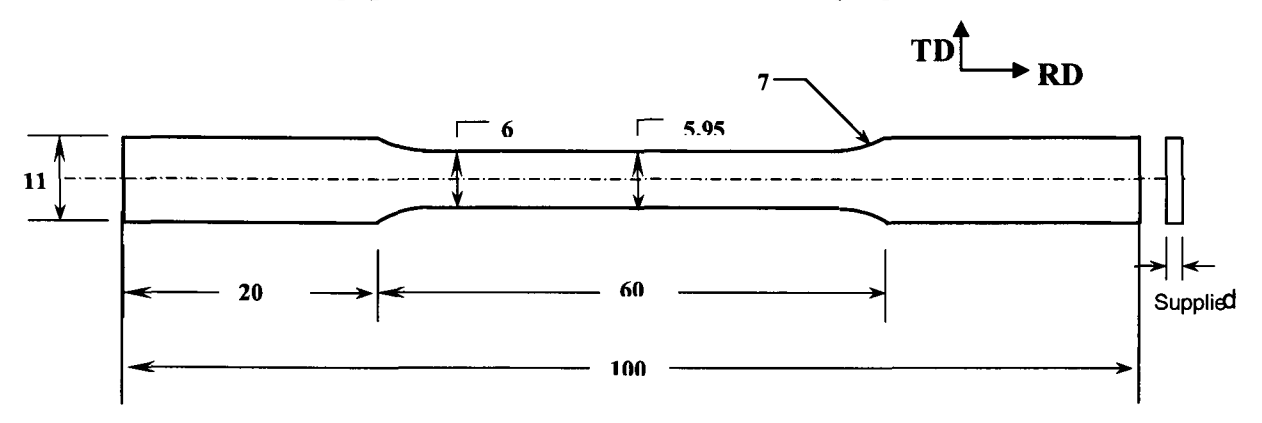


Figure 4.7 Configuration of tensile specimens tested at ambient temperature, TD: transverse direction, RD: rolling direction

4.4.2 Elevated Temperature Tensile Testing

4.4.2.1 Specimens

The specimens for elevated temperature tension testing (Figure 4.8) had a shorter gauge length to accommodate the much larger strains at fracture.

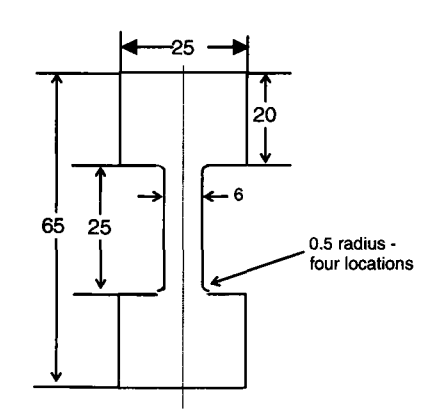


Figure 4.8 Configuration of tensile specimens tested at elevated temperature per ASTM E2448-06 [5]

4.4.2.2 Facilities

Tests were performed using 5568 Instron machine, with an Instron 3119-007 furnace and a Merlin data acquisition system (Figure 4.9). A uniform chamber temperature was maintained by a ventilation fan. Two thermocouples were used for the control of testing temperature, one monitoring the chamber temperature, and the other for the temperature of the lower anvil.

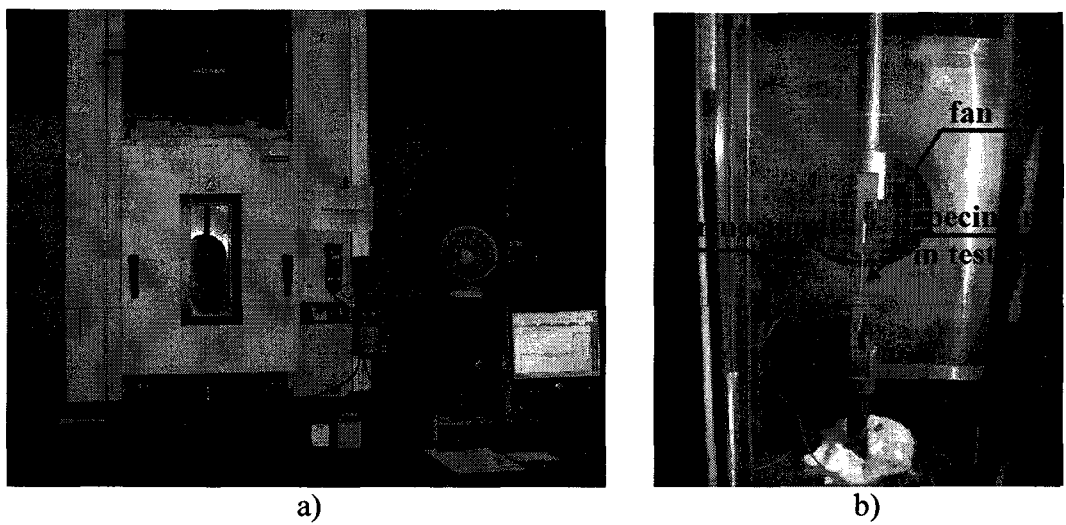


Figure 4.9 Elevated temperature testing machine: a) set-up, b) furnace

4.4.2.3 Test Conditions

The tests were carried out at temperatures of 300 °C, 400 °C, and 450 °C; constant true strain rates of $0.1s^{-1}$, $0.01s^{-1}$, $0.001s^{-1}$, and $0.0003s^{-1}$. Tests were interrupted during testing at 450 °C and strain rate of $0.0003s^{-1}$, to examine the microstructure evolution and neck development. The specimens were heated to the test temperature and held for 10 mins prior to testing, they were pulled to failure or selected strains.

4.5 Characterization

4.5.1 Chemical Composition Analysis

Chemical compositions of the alloys were analyzed by Inductively Coupled Plasma Spectrometry (ICP). These data also were used to quantify the efficiency (i.e. retention) of alloying elements.

4.5.2 Microstructure Analysis

4.5.2.1 Sample Selection

The sections that examined microstructurally are shown in Fig. 4.10. For the ascast samples in the middle region of the surfaces near the mould were examined. For hot compression samples, examination was performed the middle area of the planes parallel to the compression axis, in which the most uniform and severe deformation is found ^[6]. For rolled and tensile samples, the longitudinal surfaces (planes defined by rolling and normal directions) were examined.

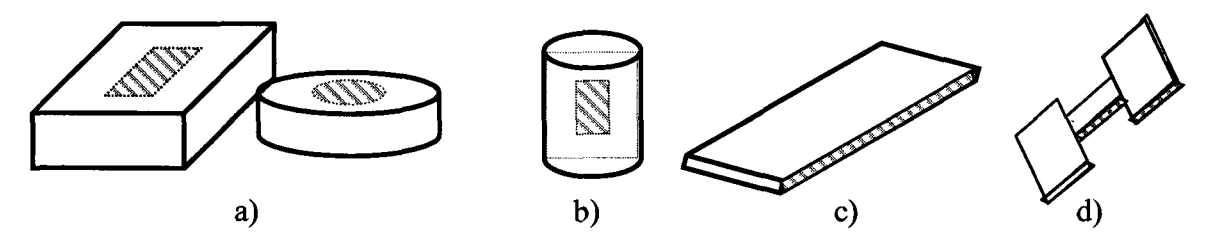


Figure 4.10 Surfaces examined in microstructure analysis: a) as cast, b) compressed, c) as-rolled, and d) tensile tested

4.5.2.2 Sample Preparation

Samples for conventional microstructure examination were sectioned using a diamond blade and cold mounded, and then were mechanically ground with SiC papers (from No. 600, No.800, up to No.1200) and polished with diamond paste (3 μ m to 1 μ m). Chemical polishing with 10% nital solution was used to eliminate fine scratches. To avoid losing the small second phase particles, the chemical polishing time was

minimized. Samples were finally etched for 2-3s with a reagent of 10 ml acetic acid, 4.2g picric acid, 10ml H₂O and 70 ml ethanol.

Samples for analysis with electron backscattered diffraction (EBSD) were not mounted, in preparation for electro-polishing. They were ground with SiC papers and polished with diamond paste (3 µm to 1µm) manually, then electro-polished at -30 °C using a solution containing 60 ml nitric acid and 140 ml pure ethanol. After EBSD, the specimens were etched with same picric-acetic reagent to examine particles using SEM.

4.5.2.3 Optical Metallography

An Epiphot 200 Nikon Optical Microscope with Clemex Image Analyzer was used to examine the microstructures.

4.5.2.4 SEM with EDS Analysis

A Hitachi S-4700 SEM and a Philips XL30 FEG SEM with energy dispersive (EDS) were utilized to characterize second phases in various specimens, including their distribution, morphology, size, and qualitative composition. Fracture surfaces of tensile specimen were also examined with SEM.

4.5.2.5 Electron Probe Microanalysis (EPMA)

To quantitatively analyze the compositions of new phases formed by microalloying in designed alloys, a JEOL JXA-8900L EPMA machine was employed. The standards used in the analysis are listed in Table 4.6. During the testing, at least five particles for each phase were detected to improve the statistics.

Table 4.6 Standards for phase analysis with EPMA

Al	Mg	Mn	Zn	Ca	Ce	Sr
Spinel	MgO	Spessartine	Willemite	Diopside	CeO ₂	SrTiO ₃

The second phase areal fraction (%) was estimated by using the brightness thresholding function in the analysis software of JEOL EPMA MANU. The threshold values were set to cover almost all of the second phase particles in back-scattered electron images. For each sample, ten BSE images were taken at a low magnification of 100. Then the average value was determined.

4.5.2.6 Electron Backscattered Diffraction Analysis (EBSD)

EBSD technique with TSL data collection and analysis software were used to study the deformed structure, such as the nucleation of recrystalized grains and the development of dynamic recrystalization (DRX) during hot deformation. Due to its high resolution in identifying grain boundaries, it was also used for quantitative analysis of grain size and volume fraction (%) of DRX. Since it is found that there is a relationship between the orientation contrast on EBSD and the diffraction contrasts of dislocations in TEM ^[7, 8], local orientation changes known as the Kernel Average Misorientation in EBSD analysis (each point orientation compared to the neighboring points) ^[9] was used to quantify the dislocation densities in deformed structures. During the data treatment, minor cleaning and consistency are required.

4.5.3 Measurement of Lattice Parameters (a, c, c/a)

In order to examine the changes in lattice parameters (a, c, and c/a) associated with Ce addition, X-ray diffraction measurements were performed at General Motors R&D Center, and McGill University. The data were analyzed with GSAS software to fit all the peaks of magnesium diffraction pattern. In addition, the GM data were also analyzed using GM software to perform a cross check.

4.5.4 Texture Measurement for Sheet Materials

Sheets rolled at 300 °C with 20% reduction per pass were selected to measure the crystallographic texture. The specimens were ground to the middle thickness with SiC

paper (from No. 600, No.800, up to No.1200), and chemical polishing for 30 s with 10% nital solution. A Siemens D-500 X-ray diffractometer equipped with a texture goniometer with Mo radiation were used. The (0002), (1-100) and (10-11) pole figures were measured from 90° to 10° sample tilt at 5° per step. The data were analyzed using Textool software to calculate orientation distribution functions and poles figures.

References:

- 1. J. B. Hedrick, "Rare Earths, U.S. Geological Survey Minerals Yearbook 2005", U.S. Department of the interior and U.S. Geological Survey, December (2006), p 60.1-60.14
- 2. E.I. Poliak and J.J. Jonas, "A one-parmenter approach to determining the critical conditions for the initiation of dynamic recrystallization", Acta Materialia, 44 (Issue 1), (1996), p 127-136
- 3. A. Najafizadeh, J.J. Jonas, G. R. Stewart, and E.I. Poliak, "The Strain Dependence of Postdynamic Recrystallization in 304 H Strainless Steel", Metallurgical and Materials Transactions A, 37, June (2006) p1889-1906
- 4. G. Vespa, R. Verna, J. Carter, E. Essadiqi, and S. Yue, "Effect of Hot Rolling Parameters on the Hot Tensile Behavior of AZ31 Magnesium Sheet", in Proceedings of Magnesium Technology 2007, ed. R.S. Beals et al., TMS, Orlando, (2007), p 69-74
- 5. ASTM E2448-06
- 6. G.E. Dieter, H.A. Kuhn, and S.L. Semiatin (eds), "Handbook of Workability and Process Design", ASM International, Materials Park (OH44073-0002), (2003), p 58
- 7. F. Yin, T. Hanamura, T. Inoue, and K. Nagai, "Fiber Texture and Substructural Features in the Caliber-Rolled Low-Carbon Steels", Metallurgical and Materials Transactions A, 35, February (2004), p 665-677
- 8. X. Huang and D.J. Jenson in A.J. Schwartz, M. Kumar, and B.L. Adams, editor., "Electron Backscattering Diffraction in Material Science", Kluwer Acadamic / Plenum Publishers, New York, (2000), p 265-276
- 9. EDAX TSL OIM Analysis manual, 2004

Chapter 5

Alloy Design and Casting

5.1 Results

5.1.1 Chemical Composition Analysis and Alloying Efficiency

To investigate the alloying efficiency and its sensitivity to raw materials, two series of raw materials were used. The results of chemical composition analysis for the designed alloys (AZ31 with target value additions of 0.2% of each of Ca, Sr and Ce) are displayed in Table 5.1 (Series I) and Table 5.2 (Series II). The alloying efficiency in AZ31 under these specific casting conditions is summarized in Table 5.3. By comparison, it can be noted that Ca and Sr are not significantly sensitive to variations in these raw materials, but Ce shows a somewhat higher alloying efficiency for pure Ce than that for mischmetal. However, whether Ce is added pure or in the form of miscmetal, the alloying efficiency drops significantly in the presence of Ca and Sr. The results suggest that selected casting conditions are basically suitable to achieve designed compositions. To increase the alloying efficiency of Ce, slightly higher melting temperature and/or longer holding times are needed, especially when Ca and Sr are present.

Table 5.1 Chemical composition for alloys cast with raw materials series I (wt. %)

Alloy	Al	Zn	Mn	Ca	Sr	Ce
AZ31	3.298	0.906	0.355	-	-	-
AZ31+Ca	3.441	0.886	0.428	0.229	-	-
AZ31+Sr	3.503	0.881	0.400	-	0.187	-
AZ31+Ce	3.381	0.915	0.452	-	-	0.212
AZ31+Ca+Ce	3.412	0.877	0.392	0.215	-	0.203
AZ31+Sr+Ce	3.471	0.877	0.394	-	0.174	0.163
AZ31+Ca+Sr+Ce	3.568	0.886	0.389	0.215	0.200	0.132

Table 5.2 Chemical composition for alloys cast with raw materials series II (wt. %)

Alloy	Al	Zn	Mn	Ca	Sr	Ce
AZ31	2.668	0.773	0.296	0.017	-	-
AZ31+Ca	2.807	0.774	0.316	0.190	-	-
AZ31+Sr	3.038	0.739	0.310	0.006	0.190	-
AZ31+Ce	2.662	0.763	0.321	0.023	-	0.155
AZ31+Ca+Ce	2.824	0.801	0.307	0.177	-	0.096
AZ31+Sr+Ce	3.022	0.815	0.311	0.018	0.213	0.144
AZ31+Ca+Sr+Ce	2.882	0.778	0.299	0.177	0.182	0.165

Table 5.3 Alloy efficiency in two series raw materials (%)

Alloy	Ca		Sr		Ce	
	Series I	Series II	Series I	Series II	Series I	Series II
AZ31+Ca	97	90				
AZ31+Sr			85	80		
AZ31+Ce				-	100	80
AZ31+Ca+Ce	90	85	<u> </u>		100	50
AZ31+Sr+Ce			80	100	80	72
AZ31+Ca+Sr+Ce	90	85	90	85	65	55

5.1.2 Microstructural Analysis

5.1.2.1 Grain Structure

Grain size under different cooling conditions

Figure 5.1 compares the grain sizes of the same AZ31 base alloy cast in different moulds. As revealed by optical microscopy and subsequently quantified by EBSD, with increasing cooling (solidification) rate the grain size reduces considerably.

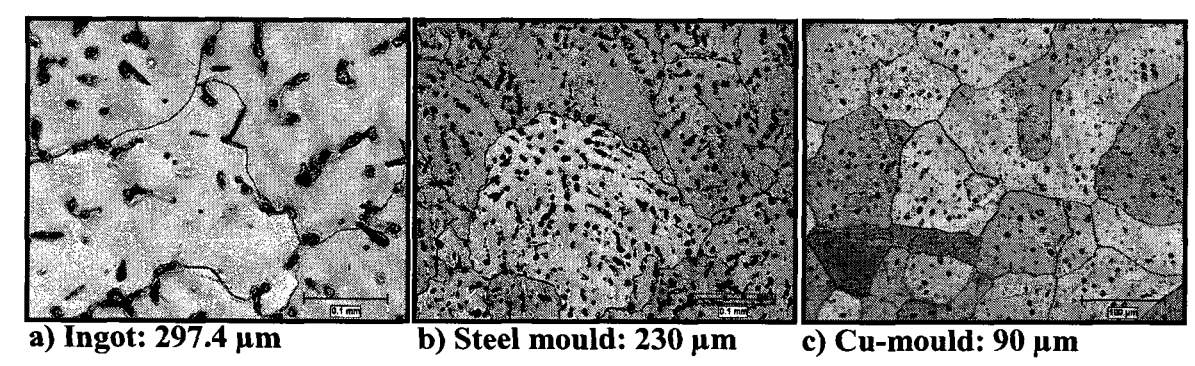


Figure 5.1 Optical metallographes of grain size for AZ31 alloy cast under different cooling conditions: a) direct chilling, b) steel mould, c) copper mound

Grain size with additions of Ca and Sr under same cooling conditions

The refining effect of Ca and Sr on grain size was characterized using samples cast in copper mound with the same content of 0.19% (Figure 5.2). As can be seen, both additions of Ca and Sr can be used as a grain refiner; and Ca has much more significant effect on the grain refinement than that of Sr.

Grain size with additions of Ca in conjunction with different cooling conditions

The combined effect of alloying additions and cooling conditions is observed by comparing samples cast in copper and steel moulds for alloys of AZ31 and AZ31 with Ca, respectively (Figures 5.2 and 5.3). It is noted that even smaller grains were obtained by microalloying with Ca under a higher cooling rate, even though the grain size was already reduced dramatically by the increased cooling rate.

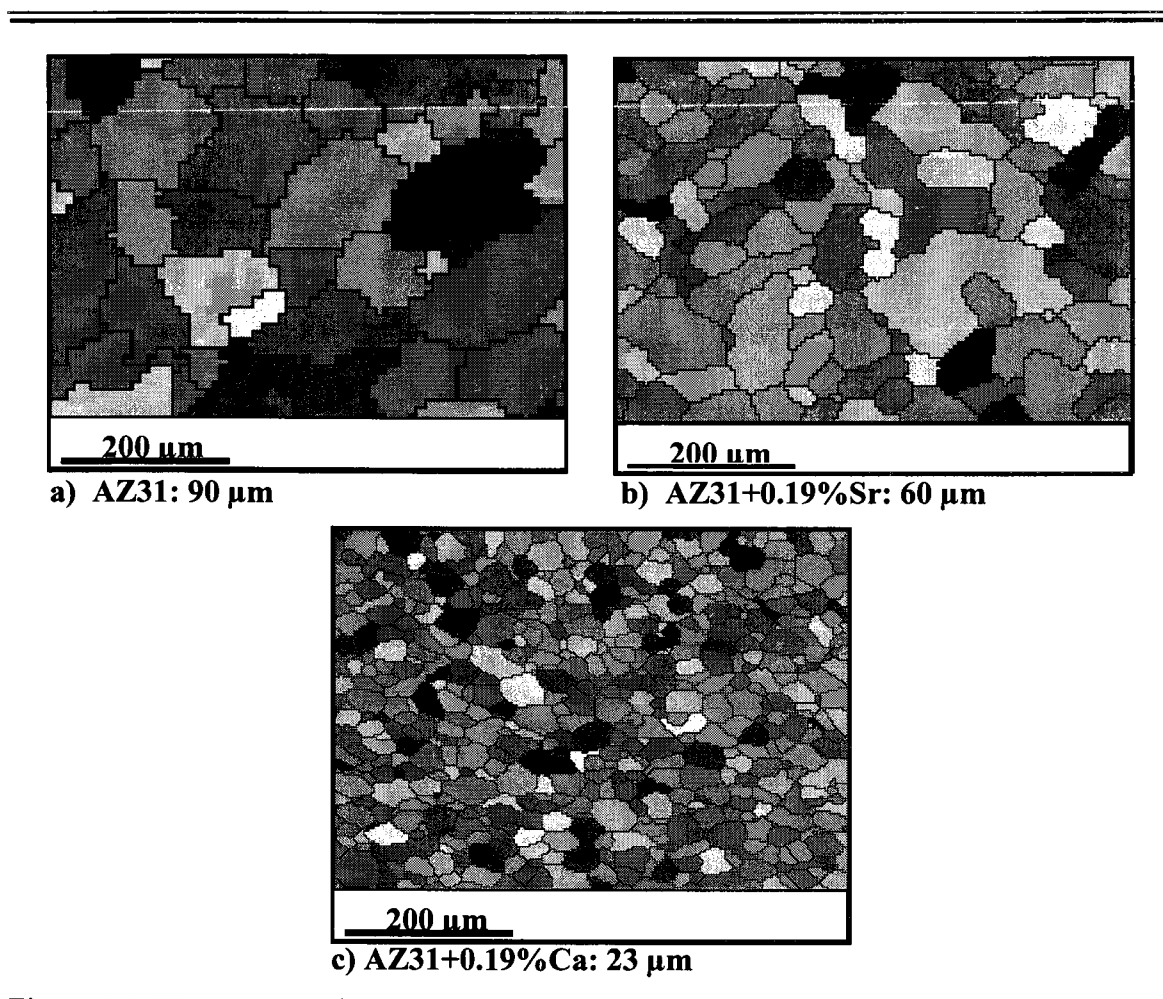


Figure 5.2 EBSD maps of grain size in surface region of samples cast in copper mould: a) AZ31, b) AZ31+0.19%Sr, and c) AZ31+0.19%Ca

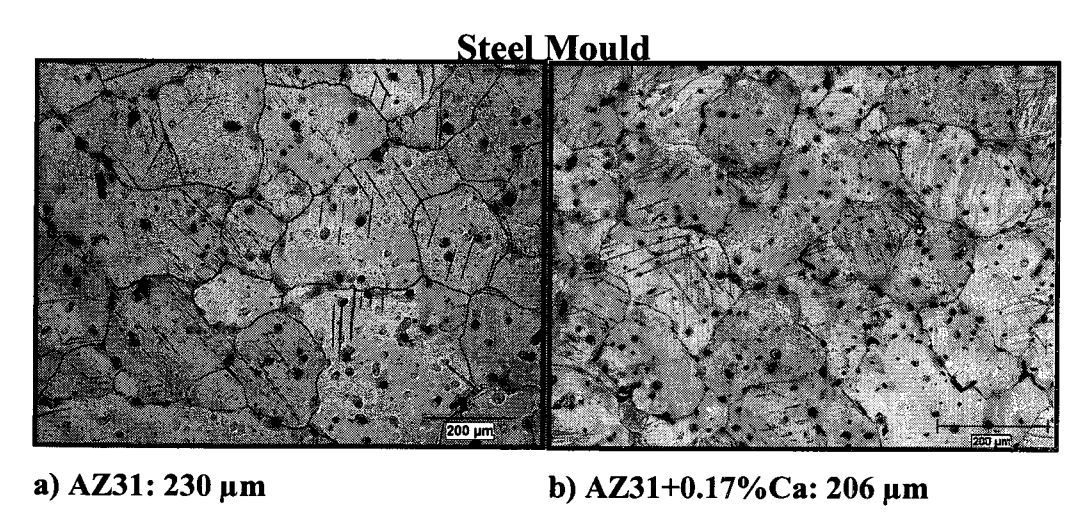


Figure 5.3 Optical metallographes of grain size in samples of AZ31 and AZ31 with Ca cast under different cooling conditions in steel mould: a) AZ31, b) AZ31+0.17%Ca

5.1.2.2 Formation of Second Phases by Alloying

Refinement and distribution of second phases

The second phases in microalloyed AZ31 alloys cast in copper mould are presented in Figure 5.4. Smaller second phases were observed for all alloys with alloying additions compared with the base alloy of AZ31 (Figure 5.4a). The most noticeable refinement of second phases concerning these alloys is due to Ce (Figures 5.4d, e, f, and g), regardless of adding it individual or multiply added with Ca and/or Sr. A refined microstructure consisting of small grain size and dispersive second phases was observed in these multiple alloyed compositions of AZ31 with Ca and Ce, and AZ31 with Ca, Sr and Ce, as shown in Figure 5.5. and Figure 5.6.

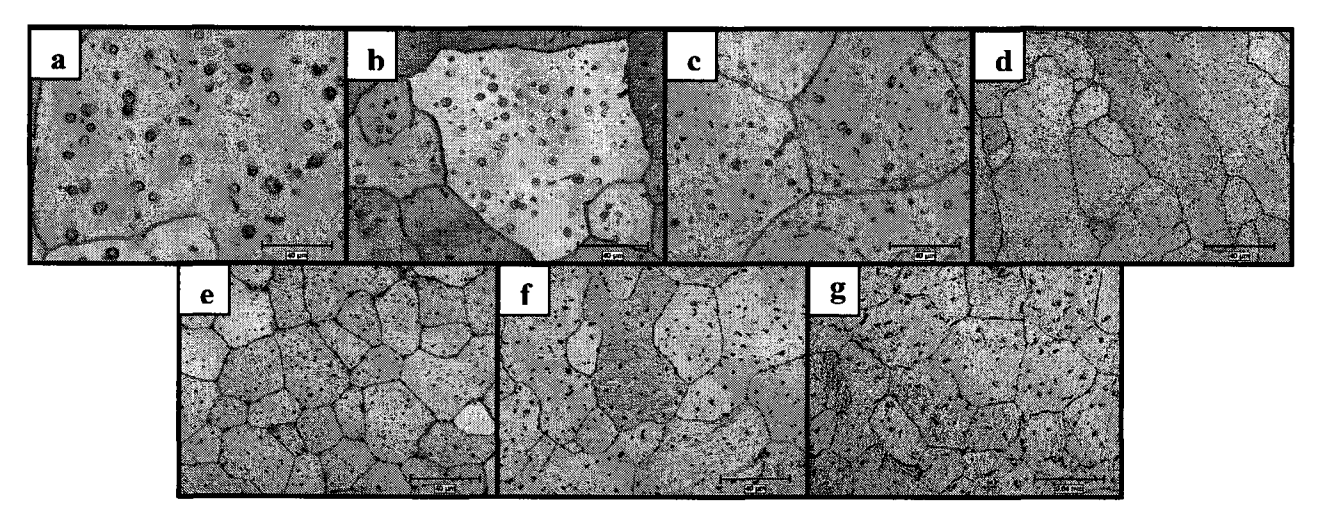


Figure 5.4 Optical metallographs of second phases in samples cast in copper mould: a) AZ31, b) AZ31+0.23%Ca, c) AZ31+0.19%Sr, d) AZ31+0.20%Ce, e) AZ31+0.22%Ca+0.20%Ce, f) AZ31+0.17%Sr+0.16%Ce, and g) AZ31+0.17%Ca+0.18%Sr+0.18%Ce

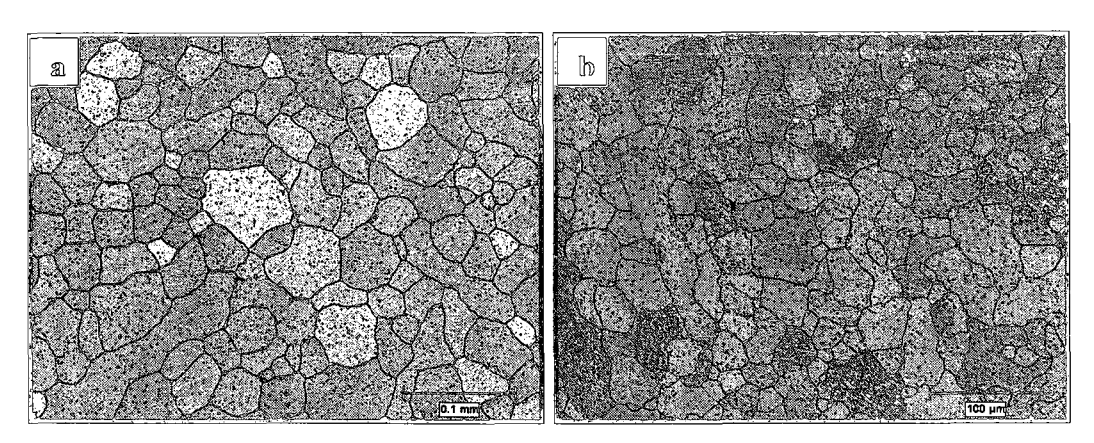


Figure 5.5 Optical metallographs of samples cast in copper mould: a) AZ31+0.22%Ca+0.20%Ce, and b) AZ31+0.17%Ca+0.18%Sr+0.18%Ce

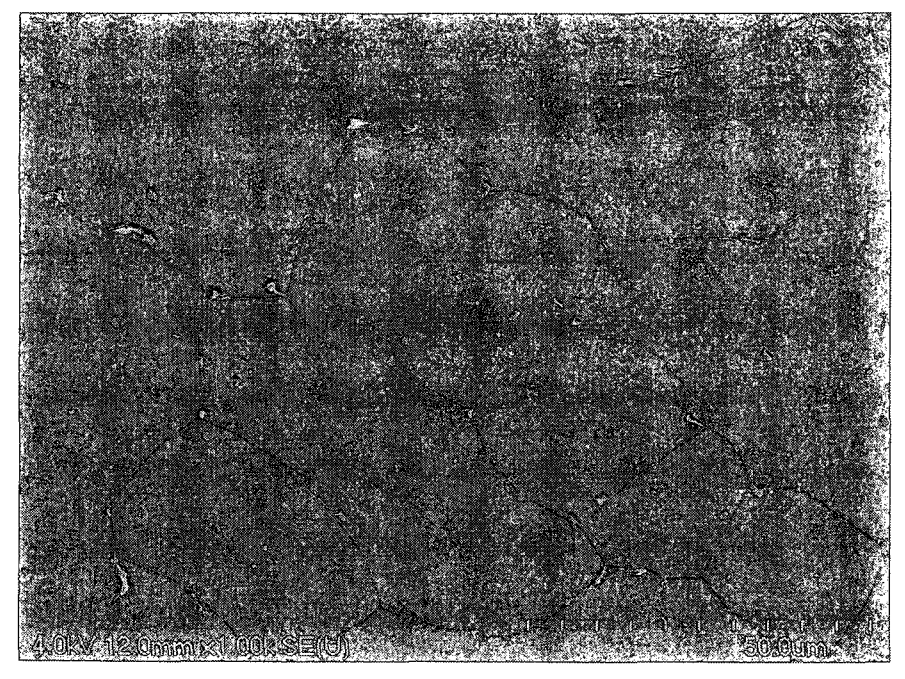


Figure 5.6 SEM of second phases in AZ31+0.22%Ca+0.20%Ce alloy cast in copper mould

Composition analysis of second phases with EPMA and FactSage TM

To reduce the matrix effect on the accuracy of EPMA analysis, the samples cast in steel mould were selected because a larger size (\geq 3 μ m) of second phases can be

obtained. In addition, all the samples were solution-treated at 450 °C for 10 hours to show what particles are present at the beginning of hot rolling.

Based on the brightness or contrast differences in these particles, different phases can be distinguished as illustrated in Figure 5.7. The Ce bearing particles show the brightest because of the much higher atomic number of Ce compared to Ca, Sr etc. Figures 5.8 to 5.10 show the wavelength dispersive spectrometer (WDS) maps and EDS-spectrums for typical phases (Al-Ca, Al-Sr, Al-Ca-Sr, Al-Ce-Mn, and Al-Ce) observed in the multiple alloyed AZ31 with three additions (Ca, Sr, and Ce).

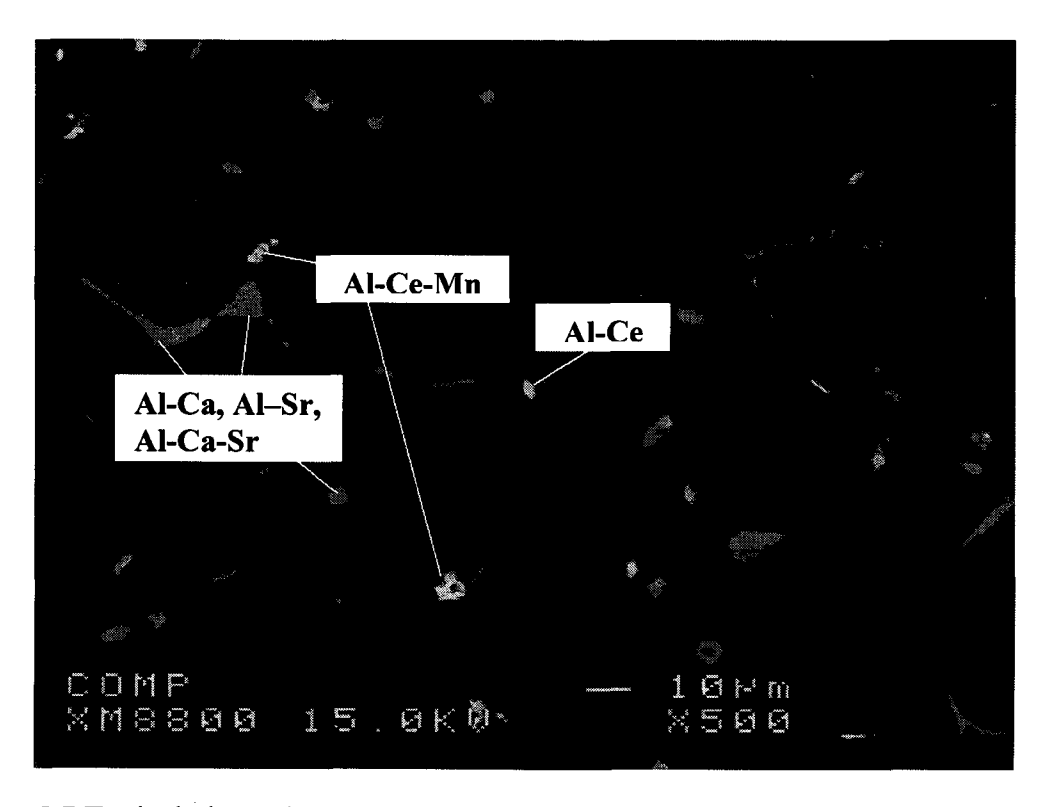


Figure 5.7 Typical phases in AZ31+Ca+Sr+Ce alloy heat treated at 450 °C for 10 hours

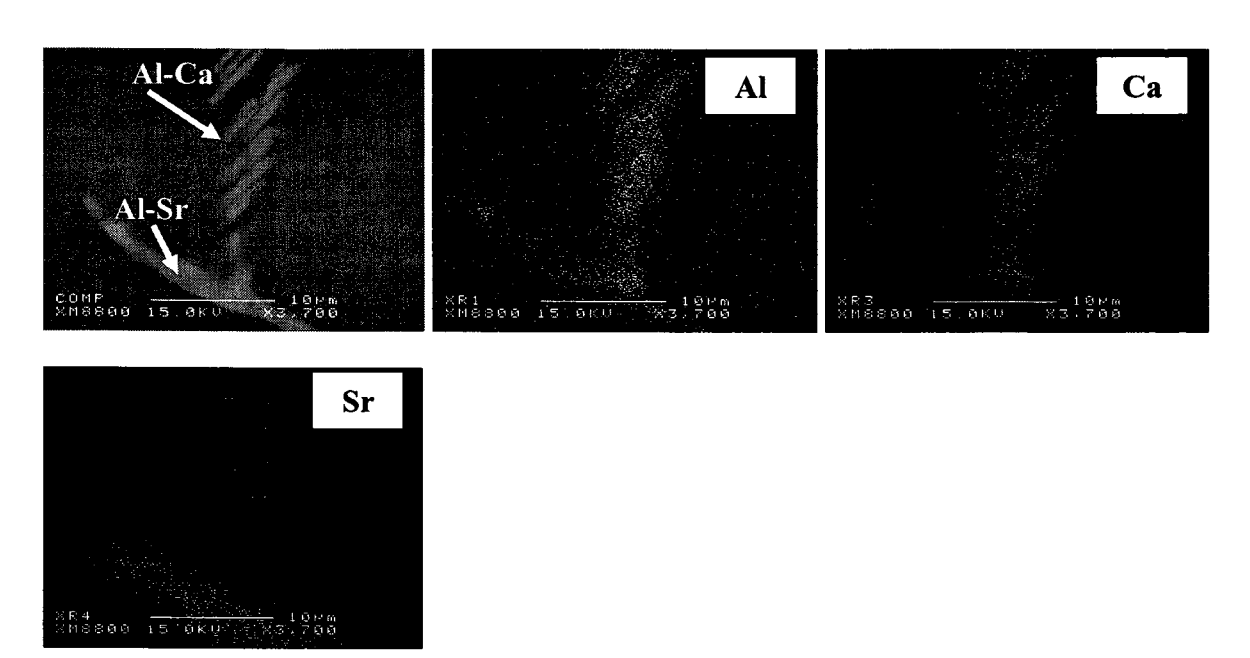


Figure 5.8 WDS maps for phases of Al-Ca and Al-Sr

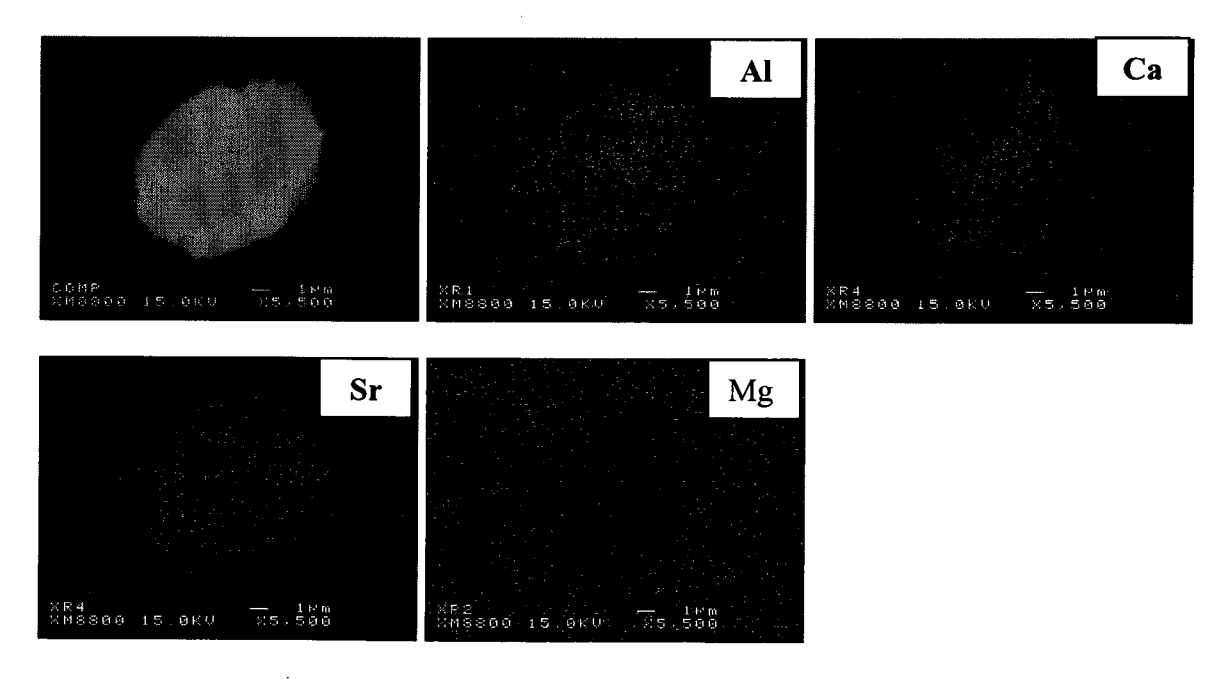


Figure 5.9 WDS maps for phase of Al-Ca-Sr in AZ31+Ca+Sr+Ce alloy heat treated at 450 °C for 10 hours

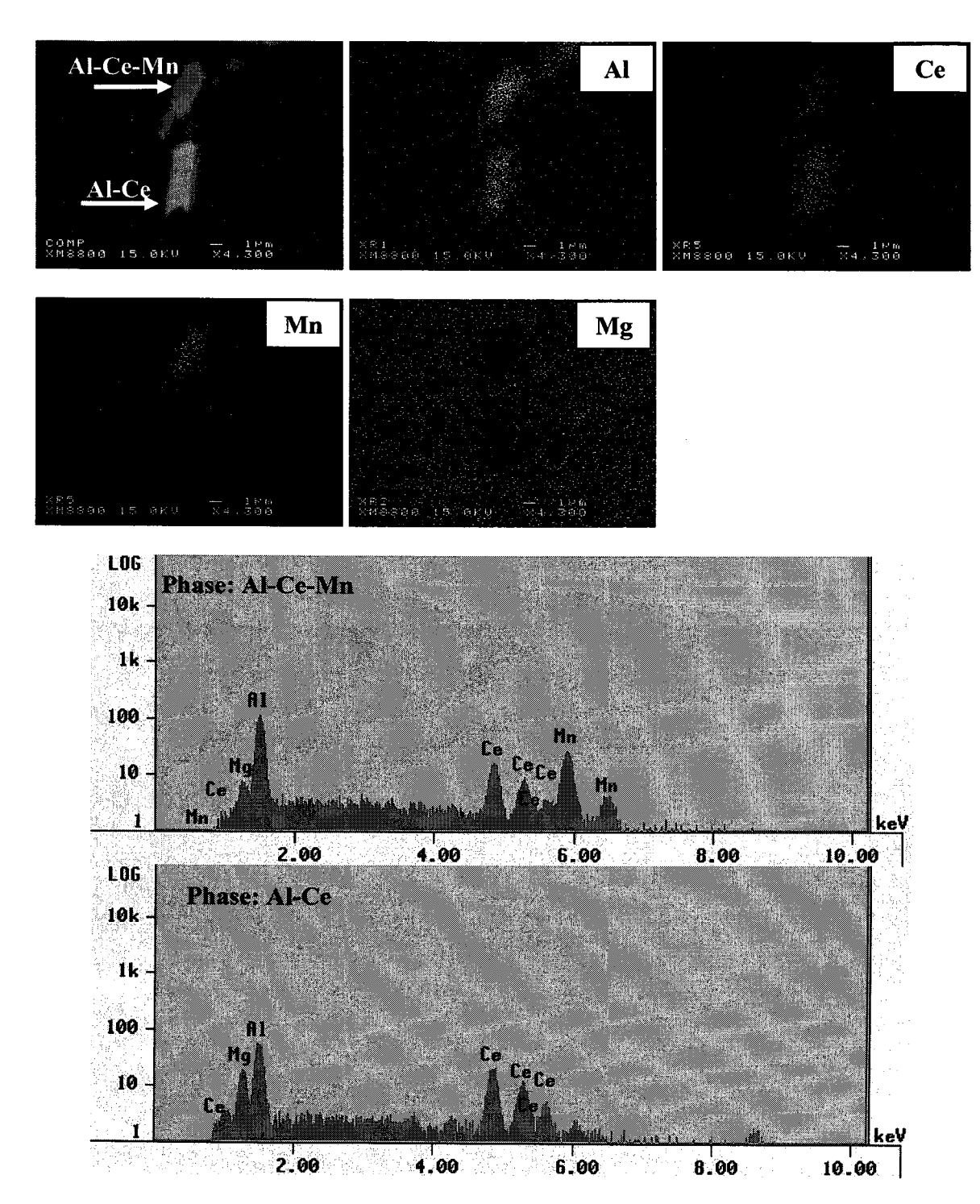


Figure 5.10 WDS maps and EDS spectrums for phases of Al-Ce-Mn and Al-Ce in AZ31+Ca+Sr+Ce alloy heat treated at 450 $^{\circ}\text{C}$ for 10 hours

Figures 5.11 to 5.14 show the equilibrium phase transitions for AZ31 alloy, AZ31+Ca, AZ31+Ce and AZ31+Ca+Sr+Ce alloys predicted using FactSageTM thermochemical software. In the calculations, the amount of alloying elements are fixed at Al = 3.5, Zn = 0.9, Mn = 0.4, Ca = 0.2, Ce = 0.2 wt%. For AZ31, solidification of alpha-Mg phase is calculated to begin at about 630 °C, and at the same temperature Al₈Mn₅ begins to precipitate. Then, solidification finishes at 540 °C. With decrease of the temperature, the Al_xMn_y phase composition changes. Mg₁₇Al₁₂ beta phase then forms below about 200 °C.

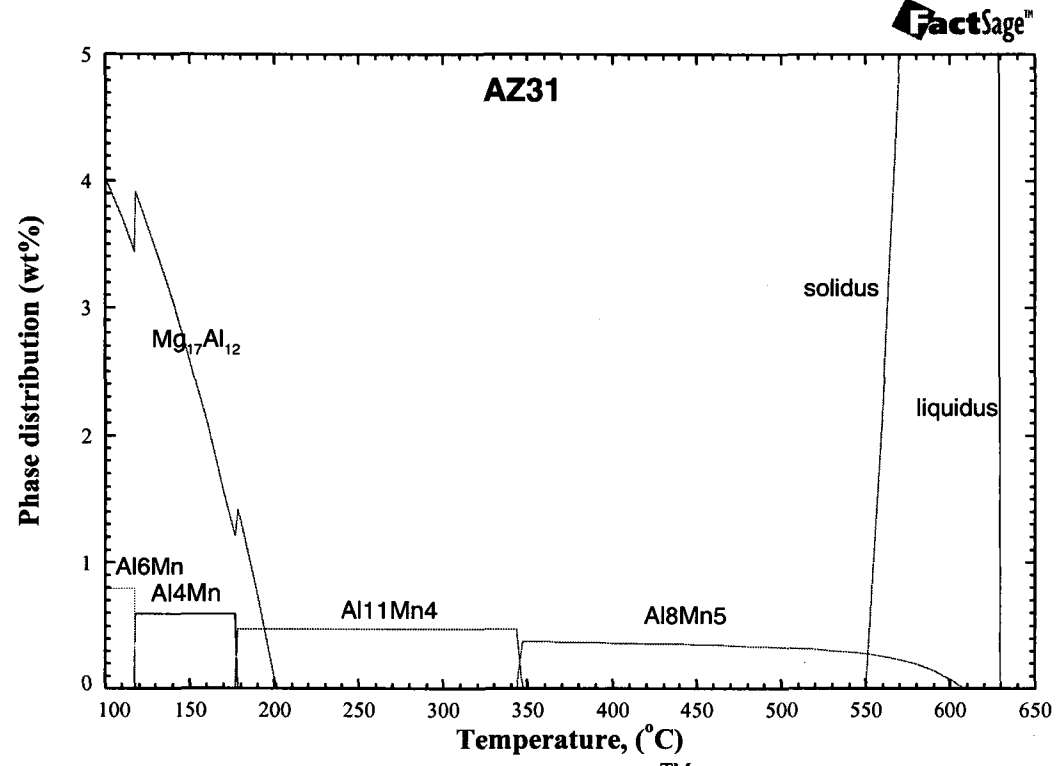


Figure 5.11 Phase diagram predicted with FactSageTM for AZ31 alloy at equilibrium condition

In the case of the AZ31+Ca alloy, Al₂Ca precipitates at 540 °C and is stable down to room temperature. Thermodynamic calculations show that all the Ca is consumed in the formation Al₂Ca. In the case of AZ31+Ce alloy, Al₈CeMn₄ forms at 580 °C and Al₁₁Ce₃ forms at 450 °C. For the alloy AZ31 with multiple additions (Ca, Sr, and Ce), Al₂Ca and Al₂Sr phases form at 530 °C down to room temperature. Also, Al₄Sr precipitates at 450 °C.

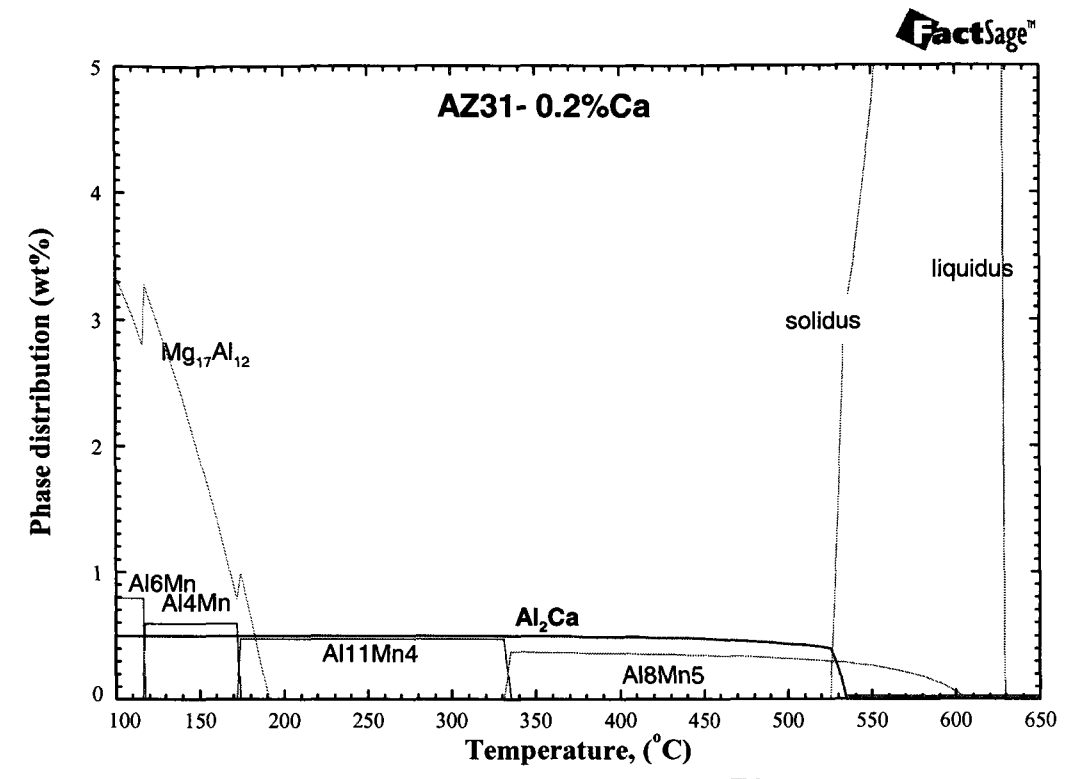


Figure 5.12 Phase diagram predicted with FactSageTM for AZ31 with 0.2%Ca at equilibrium condition

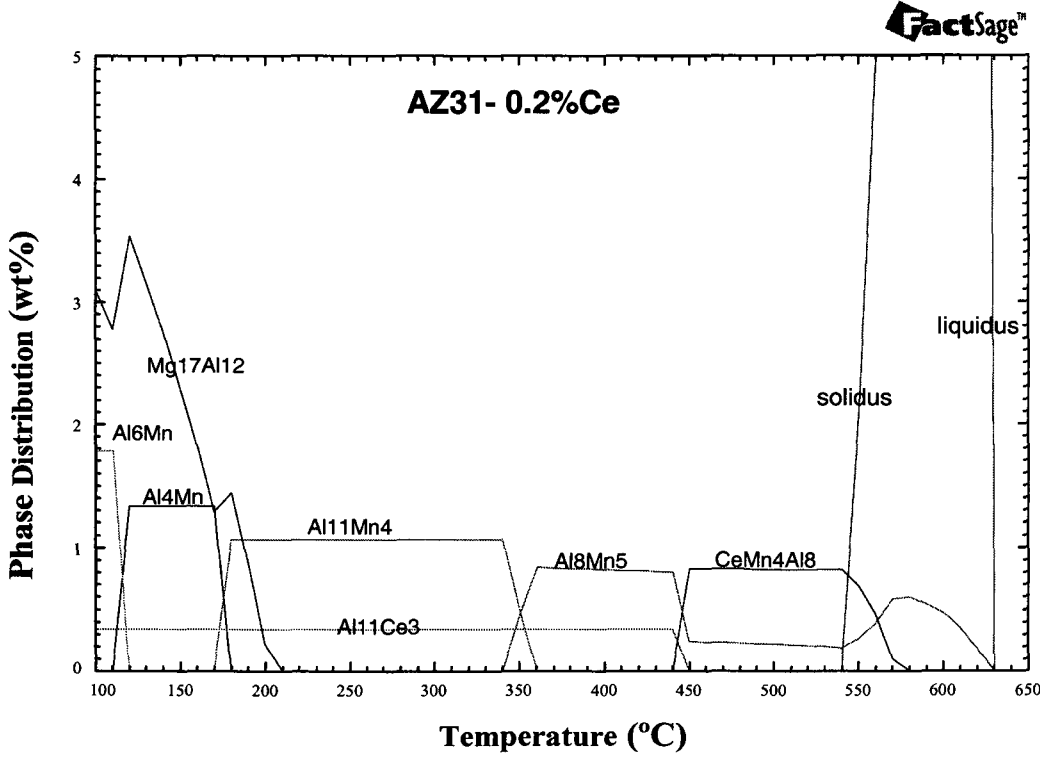


Figure 5.13 Phase diagram predicted with $FactSage^{TM}$ for AZ31 with 0.2%Ce at equilibrium condition

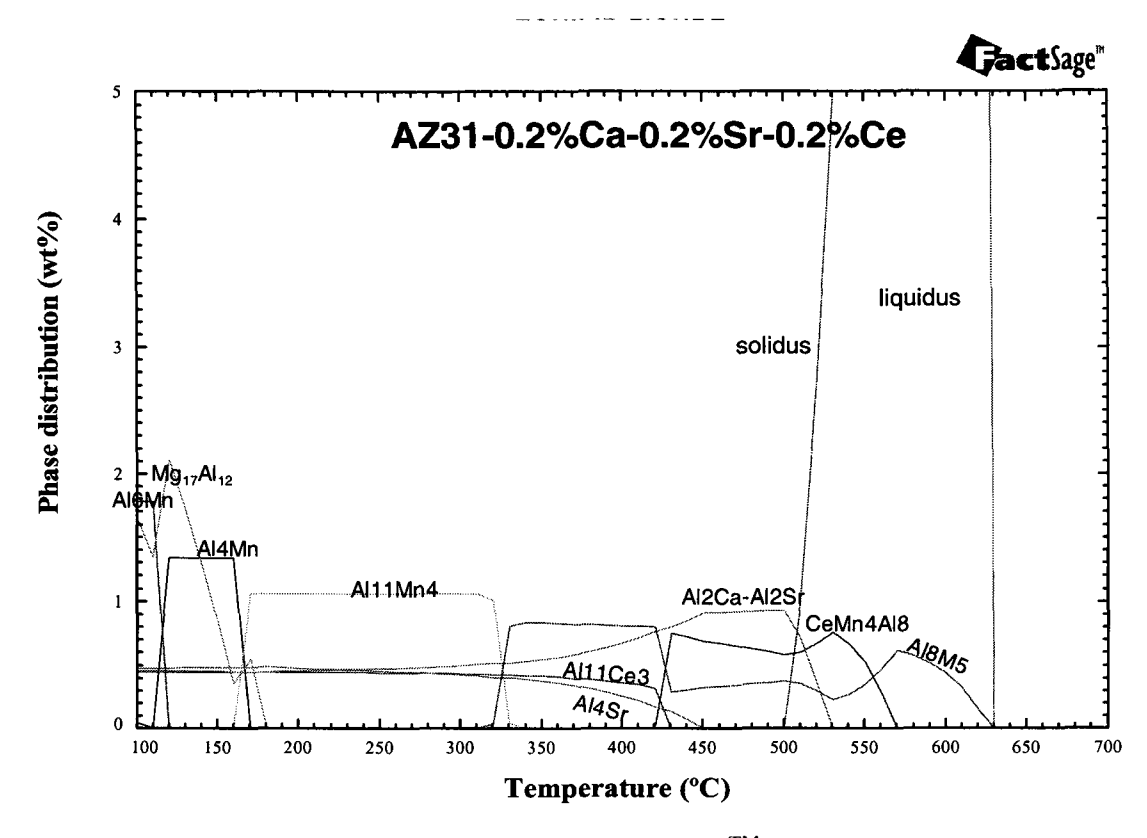


Figure 5.14 Phase diagram predicted with FactSageTM for the alloy of AZ31+ 0.2%Ca+0.2%Sr+0.2%Ce at equilibrium condition

It is also noticed that the amount of $Mg_{17}Al_{12}$ precipitates decreases as microalloying levels increase. In addition, the start temperature of $Mg_{17}Al_{12}$ phase is predicted to be higher for alloy with Ce compared to plain AZ31, whereas Ca and Sr additions lower the $Mg_{17}Al_{12}$ precipitation temperature.

The second phases analyzed by EPMA and predicted by FactSageTM thermodynamic calculations are compared in Table 5.4. All specimens analyzed were solution-treated at 450 °C for 10 hours. Almost all of the predicted phases were found in the specimens. Since phases of Al₁₁Ce₃ and Al₄Sr predicted to be dissolved close to 450 °C, they might not be observed.

Table 5.4 Second phase analysis with EPMA and FactSageTM prediction

Alloys	Phases analyzed by EPMA	Phases above 450 °C predicted by FactSage
AZ31	Al ₈ Mn ₅	Al ₈ Mn ₅
AZ31+Ca	$Al_8Mn_5 \ Al_2Ca$	$ ext{Al}_8 ext{Mn}_5 ext{Al}_2 ext{Ca}$
AZ31+Ce	$Al_{11}Ce_3$ Al_8Mn_5 Al_8CeMn_4	Al ₁₁ Ce ₃ Al ₈ Mn ₅ Al ₈ CeMn ₄
AZ31 +Ca+Ce	Al ₈ Mn ₅ Al ₂ Ca Al ₈ CeMn ₄	Al_8Mn_5 Al_2Ca Al_8CeMn_4 $Al_{11}Ce_3$
AZ31 +Ca+Sr+Ce	Al_8Mn_5 Al_8CeMn_4 $Al_{11}Ce_3$ Al_2Ca Al_2Sr $Al_2(Sr, Ca)$	$egin{array}{c} Al_8Mn_5 \ Al_8CeMn_4 \ Al_{11}Ce_3 \ Al_2Ca-Al_2Sr \ Al_4Sr \end{array}$

5.1.3 Measurement of Lattice Parameters

To investigate the effect of Ce on lattice parameters of Mg, X-ray diffraction was performed. A detectable shift of peaks in spectrum with Ce was observed as shown in Figure 5.15, which could indicate some changes in lattice parameters (a, c, and c/a). Table 5.5 presents the results of lattice parameters by full scanning (20: 10~120°) and calculating with full peak fitting. To cross check, specimens were measured at McGill University and GM Technical Center using different machines; and the raw data were also dealt with different softwares. The results show that there is a slight reduction in the c/a ratio, which may be beneficial to the formability of AZ31 alloy, as will be discussed.

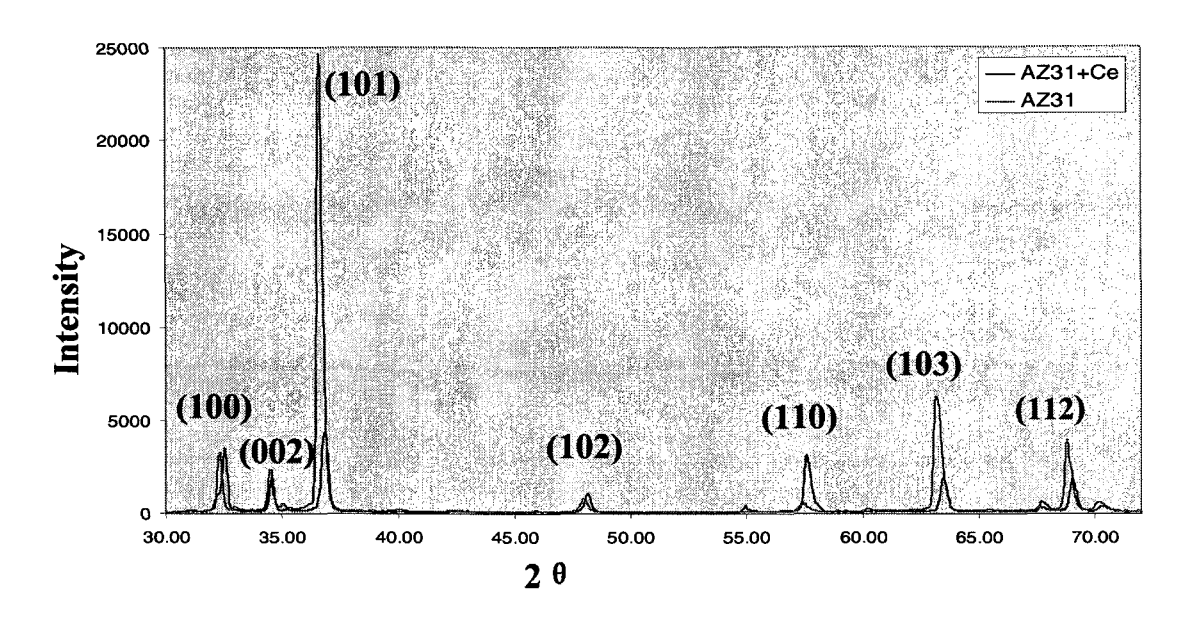


Figure 5.15 X-ray diffraction spectrums for alloys of AZ 31 and AZ31 with Ce, cast in Cu-mould

Table 5.5 Results of full scanning and full peaks fit with GSAS and GM sofeware using different machines at GM and McGill

Composition	c/a value: with GM data with GSAS	c/a value: with GM data with GM software	c/a value: with McGill data with GSAS
AZ31	1.6244	1.6245	1.6245
AZ31+0.16%Ce	1.6242	1.6240	1.6242
AZ31+0.18%Ca+0.10%Ce	1.6241	1.6240	1.6238
AZ31+0.18%Ca+0.18%Sr+0.17%Ce	1.6240	1.6234	1.6239

5.2 Discussion

5.2.1 Effect of Cooling Rate on Microstructure

5.2.1.1 Grain Size

Figure 5.1 showed the significant reduction in grain size with increased cooling rate. It can be seen that the initial grain size is around 300 μm in the DC ingot sample and

was reduced to 230 µm and 90 µm in the specimens cast in the steel mould (preheated at 400 °C) and copper mould (at room temperature), respectively. This confirms that grain refinement during solidification can be accomplished by rapid cooling. It is known that nucleation is the first step in the transformation of a liquid into solid upon cooling. The number of nucleation sites present during freezing will determine the final grain size. Since liquid metals contain a wide variety of potential nucleants which become active at various degrees of undercooling, the rate of heat extracted from the liquid phase is one of the key factors affecting the formation and quantity of nuclei [11]. For a long cylindrical DC ingot, heat is lost primarily in a radial direction with a slow cooling rate. A few grains freeze toward the center along the heat flow direction. Therefore large grains are formed. Increasing the heat extraction as in the case copper permanent mould castings of small samples, a great amount of liquid metal is undercooled below its equilibrium freezing temperature. Such rapid solidification of the liquid promotes significant nucleation resulting in a fine grain size.

5.2.1.2 Intermetallic Phases

Figure 5.1 also showed intermetallic phases in three AZ31 specimens with different cooling conditions. It was noted that there is a significant effect of cooling rate on their size and shape. These intermetallic phases form along the grain boundaries or between dendrites arms, and are uniformly distributed. The higher the cooling rate, the finer the intermetallic phases with a more spherical morphology. This is due to the fact that rapid solidification refines the grain size or dendrite space, thus these phases will form only isolated particles at the grain boundaries or among dendrites. In addition, the rapid solidification restricts the diffusion of solute elements hindering the growth of these particles.

5.2.2 Effect of Ca, Sr, and Ce on Microstructure

5.2.2.1 Effect of Ca and Sr on Grain Size

The effect of alloying additions on grain size can be explained with the mechanisms of the growth restriction factor (GRF) and constitutional undercooling. GRF can be expressed as:

$$\sum_{i} m_i C_{0,i}(k_i - 1) \qquad \text{(Equation 5.1)}$$

Where m_i is the slope of the liquidus line, k_i is the distribution coefficient and $C_{0,i}$ is the initial solute concentration levels ^[2]. The greater the GRF value, the slower the grain growth. This mechanism is well suited for alloying additions present in dilute amounts. As can be seen in Table 5.6 ^[2], the GRF value of Ca is 3.4 times that of Sr, indicating a more powerful growth restriction. Therefore Ca has a stronger grain refining ability than Sr. In addition, the constitutional undercooling generated by solute rejection during solidification may increase the number of nuclei, since nucleants in liquid metal may be activated in this undercooling zone ^[1].

Table 5.6 Growth restriction factor (GRF) values for Ca and Sr in Mg binary alloys

Element	m	k	m(k-1)	System
Ca	-12.67	0.06	11.94	eutectic
Sr	-3.53	0.06	3.51	eutectic

5.2.2.2 Effect of Ca, Sr, and Ce on Formation of Second Phases

Results from EPMA show the refining effect of microalloying additions on second phases by the formation of microalloying phases in AZ31 base alloy. Most of these phases formed by the microalloys have been seen in the literature, but phase of Al₈CeMn₄ has not been found for Mg-Al-Zn base alloys, to the authors knowledge.

Effect of Ca and Sr on the formation of second phases in AZ31 alloy

Additions of alkaline earth metals (Ca and Sr) have been added into Mg-Al based alloys to increase creep resistance in casting alloys due to the formation of highly stable intermetallic compounds ^[3-5]. The contents of Ca or Sr in such Mg- $(4\sim7)$ %Al alloys were usually high ($\geq 1\%$ wt.), and phases Al₂Ca and Al₄Sr were observed. It was also reported

that if 0.2%Sr was added in Mg-5Al-1.8Ca-0.5Mn alloy, the Al₂Sr phase was observed, but the Al₄Sr phase cannot be seen ^[6]. In the present study, when 0.2%Ca or 0.2%Sr was added into AZ31 (Mg-3Al-1Zn) alloy, Al₂Ca or Al₂Sr was found. This suggests that the type of intermetallic compound of Al-Sr depends on the concentration of Sr in alloys, but the one of Al₂Ca is not sensitive to the contect of Ca. In addition, when similar small contents of both Ca and Sr were added into AZ31, the transition phase of Al₂(Sr, Ca) phase was observed as shown in Figure 5.9, as well as Al₂Sr and Al₂Ca.

Effect of Ce on the formation of second phases in AZ31 alloy

Compared to the higher solubility limit of Al and Zn in Mg (12.7%Al and 6.2%Zn in binary alloys of Mg-Al and Mg-Zn), a very limited solubility of Ce in Mg matrix (0.5% in Mg-Ce binary system) indicates that Ce can easily form precipitates. Microstructure and EPMA analysis revealed that Al₁₁Ce₃ exists in the alloy of AZ31with small amount of Ce in present examination. This is consistent with other investigations ^[7, 8]. Moreover, a ternary intermetallic phase of Al₈CeMn₄ was also found in microalloyed alloys with Ce. This has been found in a ternary phase diagram of Al-Ce-Mn at elevated temperatures ^[9], but it has never been seen in AZ based alloys, although many of these studies did not consider annealing at high temperatures followed by quenching.

Regarding the refining effect of Ce on second phases in as-cast structure, the formation of Ce phases ($Al_{11}Ce_3$ and Al_8CeMn_4) the irregular particles in Figure 5.7 are relatively small, and reduce the amount of $Mg_{17}Al_{12}$, which will tend to reduce the size of these precipitates. The smaller $Mg_{17}Al_{12}$ may also be related to the higher formation temperature of $Mg_{17}Al_{12}$ (Figure 5.13), which is due to adding Ce. Since, at a given cooling rate, this would give a higher undercooling (i.e. driving force) leading to a higher nucleation rates and finer $Mg_{17}Al_{12}$.

5.2.3 Effect of c/a Ratio (lattice parameter) on Deformation

Limited slip system activity in HCP Mg is a major deformation issue. At room temperature, only basal slip is activated because of the very high critical reserved shear stresses (CRSS) needed to activate the prismatic or pyramidal slip. The shear (Peierls) stress necessary to move dislocations is given by:

$$\sigma = P e^{(-2\pi d/b (1-v))}$$
 (Equation 5.2)

Where P is a factor that depends on the shear modulus (G) and Poisson's ratio (v), b is the Burger's vector of the dislocation and d is the interplanar spacing [10]. With increasing d, the CRSS will decrease. In the literature, some elements (Li, Ce, Au, Pd) have been found to decrease c/a in pure Mg [11,12]. Alloy additions of lithium (Li) have been found to increase the ductility of Mg by reducing the c/a ratio of magnesium crystals [12]. The results show that the value of c/a was reduced from 1.6235 for pure Mg to 1.6095 for the alloy of Mg-4.6 wt.% (14.5 at.%) Li. This reduction permits extensive prismatic slip and an increase in true fracture strain from 7.5% to 12.2% at 20 °C. It was also noted that more than 12 wt% lithium leads to a body-centered cubic structure [13,14].

Based on the investigation of microalloying with Ce on lattice parameters in this work, there is a consistent trend in slight reduction of c/a, regardless of the equipment or software for some AZ31 alloys with Ce, confirming the literature findings. In this respect, an addition of Ce might be beneficial to the improvement of the deformability for AZ31 alloy.

5.2 Summary

- Ca and Sr have a stable alloying efficiency; pure Ce has a higher alloying efficiency than that of mischmetal under the casting conditions used in this work;
- Generally, microalloying efficiency is not sensitive to raw materials;
- Higher cooling rates refine the as-cast microstructure both in grain size and second phases in AZ31;

- Microalloying additions of Ca and Sr have a strong effect on the grain refinement of the as-castAZ31 alloy; Ca has a much stronger effect than Sr;
- Microalloying levels of Ca, Sr, and Ce reduce the amount of Mg₁₇Al₁₂ phase and form the following phases: Al₂Ca, Al₁₁Ce₃, Al₂Sr, Al₈CeMn₄, and Al₂(Ca,Sr), which were well predicted by using FactSageTM thermal calculation and confirmed by EMPA;
- Ca, Sr, and Ce refine second phases in AZ31 alloy through the formation of new dispersive phases, with Ce shows a much stronger refining effect than that of Ca and Sr;
- Combined microalloying and higher cooling rate, even refined microstructure both in grain size and second phases can be achieved;
- Second phases other than Mg-Al formed in present study are thermally stable at 450
 °C for 10 hours, and may affects the subsequent hot working behavior;
- Microalloying with Ce addition led to a slight reduction in the c/a ratio.

References:

- 1. M.C. Flemings, "Solidification Processing", McGraw-Hill, (1974), p 290-301
- 2. Y.C. Lee, A.K. Dahle, and D.H. ST. John, "Grain Refinement of Magnesium", TMS, Magnesium Technology, (2000), p 211-218
- 3. M.O. Pekguleryuz and E. Baril, "Creep Resistant Magnesium Diecasting Alloys Based on Alkaline Earth Elements", Materials Transactions, 42, (2001), p 1258-1267
- 4. E. Baril, Pl Labelle, and M.O. Pekguleryuz, "Elevated Temperature Mg-Al-Sr: Creep Resistance, Mechanical Properties, and Microstructure," JOM, 55 (11), (2003), p 34-39
- 5. J. Bai, Y. Sun, F. Xue, S. Xue, J. Qiang, and T. Zhu, "Effect of Al Contents on Microstructrues, Tensile and Creep Properties of Mg-Al-Sr-Ca Alloy", Journal of Alloys and Compounds, 437, (2007), p 247-253

- 6. Y. Chino, J.S. Lee, Y. Nakaura, K. Ohori, and M. Mabuchi, "Mechanical Properties of Mg-Al--Ca Alloy Recycled by Solid--State Recycling", Materials Transactions, 46, (2005), p 2592-2595
- 7. W. Li, H. Zhou, W. Zhou, W.P. Li, and M.X. Wang, "Effect of Cooling Rate on Ignition Point of AZ91D-0.98 wt.% Ce Magnesium Alloy", Materials Letters, 61, (2007), p 2772-2774
- 8. W. Du, Y. Sun, X. Min, F. Xue, M. Zhu, and D. Wu, "Microstructure and Mechanical Properties of Mg-Al Based Alloy with Calcium and Rare Earth Additions", Materials Science and Engineering A, 356, (2003), p 1-7
- 9. P. Villars, A. Prince, and H. Okamoto, "Handbook of Ternary Phase Diagrams", Materials Park, OH: ASM International, (1995), p 2987
- 10. F.R.N. Nabarro, "Theoretical and Experimental Estimates of the Peierls Stress", Philosophical Magazine A, 75 (Nol 3), (1997), p 703-711
- 11. G.V. Raynor, "The Physical Metallurgy of Magnesium and Its Alloys", Pergamon Press, London, New York, Paris, Los Angerles, (1959), p 83
- 12. F.E. Hauser, P.R. Landon, and J.E. Dorn, "Deformation and Fracture of Alpha Solid Solutions of Lithium in Magnesium.", Transactions of the ASM, 50, (1958), p 856-883
- 13. F.W. Bach, M. Schaper, and C. Jaschik, "Influence of Lithium on hcp Magnesium Alloys", Materials Science Forum, 419-422, (2003), p 1037-1042
- 14. H. Haferkamp, M. Niemeyer, R. Boehm, U. Holzkamp, C. Jaschik, and V. Kaese, "Development, Processing and Applications Range of Magnesium Lithium Alloys", Materials Science Forum, 350-351, (2000), p 31-42

Chapter 6

Compression Testing

6.1 Results

6.1.1 One Hit Compression Testing

The hot compression behavior of the base AZ31 were investigated systemically under different conditions, and then the effects of microalloying on its deformation behaviors were compared under selected test conditions.

6.1.1.1 Flow Behavior of AZ31

Compressive true stress-true strain (σ-ε) curves for base alloy AZ31 cast in the steel mould under various temperatures and strain rates are displayed in Figures 6.1 and 6.2. As expected, the flow stress generally increased with decreasing temperature and increasing strain rate. At a high strain rate of 0.1 s⁻¹, the flow stress jumped up rapidly from 350 °C to 300 °C (Figure 6.1a); while at a fixed temperature of 300 °C, this increase in flow stress were also enhanced when the strain rate was increased from 0.01 s⁻¹ to 0.1 s⁻¹. The results suggest that compression behaviors of AZ31 alloy are sensitive to the testing conditions, which probably results from changes in deformation mechanisms.

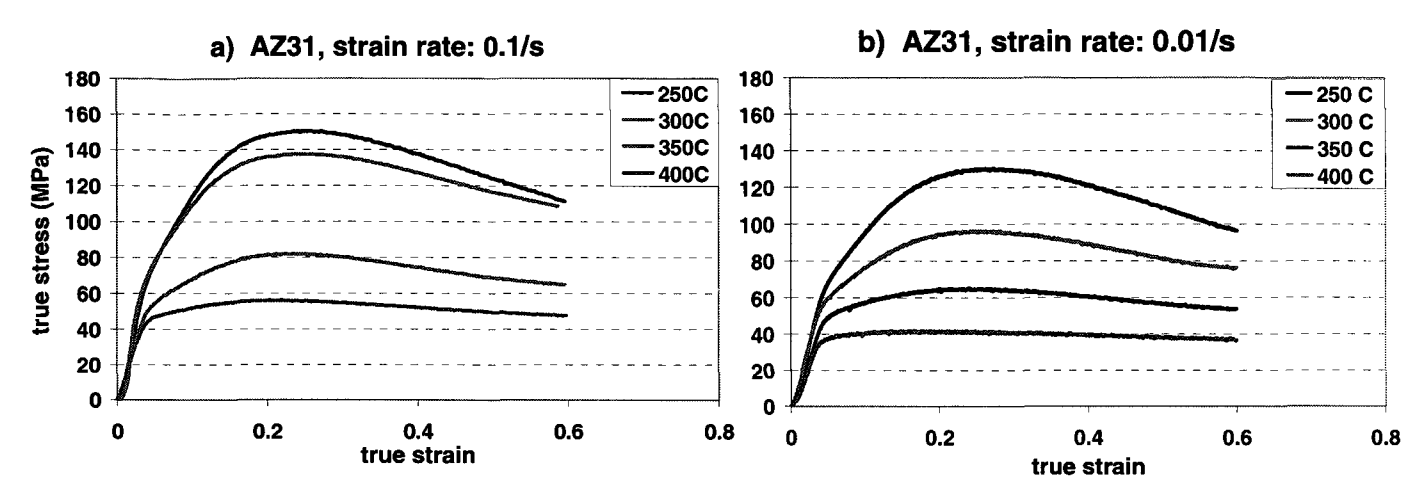


Figure 6.1 Compression flow curves for AZ31 base alloy tested at temperatures of 250 °C ~ 400 °C: a) strain rate of 0.1/s, and b) strain rate of 0.01/s

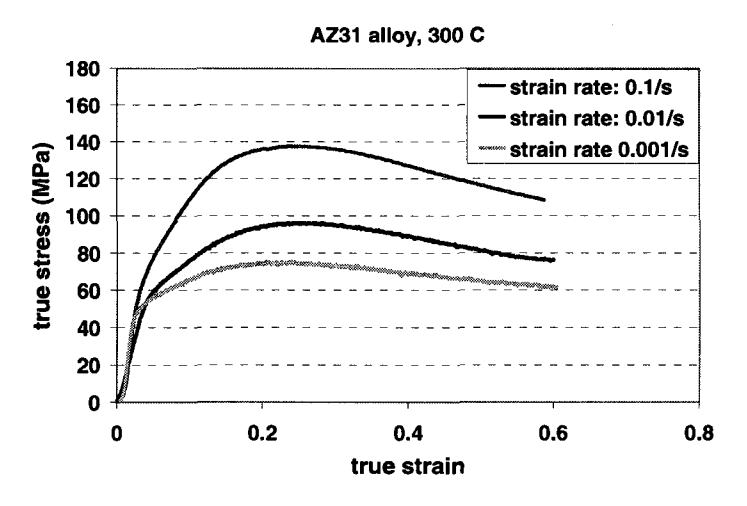


Figure 6.2 Compression flow curves for AZ31 base alloy tested at temperatures of 300 °C, strain rates of 0.1/s, 0.01/s, and 0.001/s

6.1.1.2 Dynamic Recrystallization (DRX) in AZ31

To have a better understanding of the evolution of DRX with strain for AZ31, testing was performed at 350 °C, a strain rate of 0.01 s⁻¹, with strains from 0.2 up to 1.0 for samples cast in Cu-mould with water cooling. As shown in Figure 6.3, the average

grain size of starting materials is 110 μ m within the range of 46 ~ 208 μ m by using the statistic analysis of EBSD. Second phase particles are distributed both in the grains and along grain boundaries of the primary α -Mg phase; these particles (>1 μ m) are widely spaced. Stress-strain (σ - ϵ) curves for the compression tests are presented in Figure 6.4, which verify the repeatability of the flow tests. Note that there is a steady state flow following a pronounced work softening in flow curves, which gives an indication that DRX has occurred [1-3].

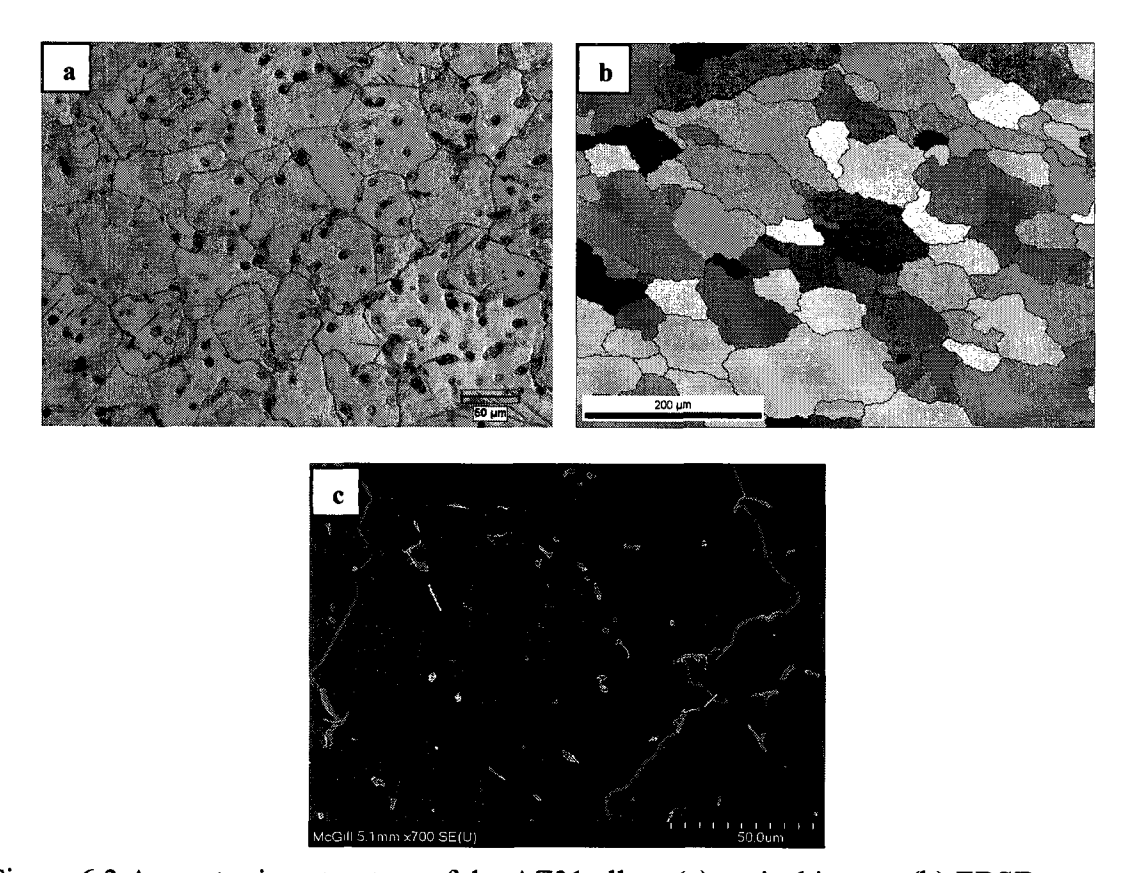


Figure 6.3 As-cast microstructure of the AZ31 alloy: (a) optical image, (b) EBSD map of as-cast grains, (c) SEM image of second phase

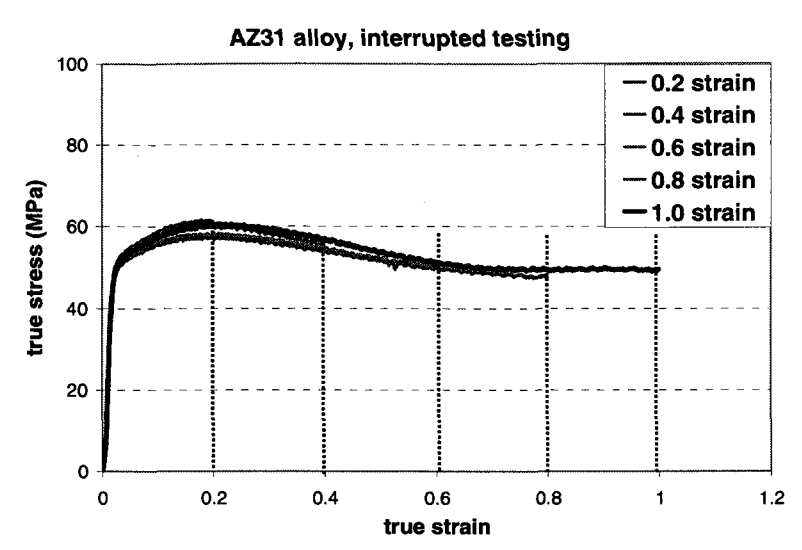


Figure 6.4 Compression flow curves for AZ31 base alloy tested at 350 °C, strain rate of 0.01/s, and strains of 0.2 up to 1.0

Dynamic recrystallization by necklacing

EBSD orientation micrographs in Figure 6.5 show the microstructural evolution of specimens deformed to strains from 0.2 to 1.0, in which different colors indicate different grain orientations. The volume fraction of DRX was estimated as the percentage of grains smaller than 10 μ m. The assumption of 10 μ m as the maximum of DRX grain size is based on the examination of DRX grains in these compressed samples, and also refers to results of other researchers ^[4]. The average DRX grain size, measured by EBSD, was 4.64 μ m. The general tendency of increasing strain, increasing the fraction of DRX, is seen.

At ϵ =0.2, some high angle grain boundaries (dark line: > 10° misorientation) turn into serrated boundaries, which could be a precursor to bulging and discontinuous DRX; subgrains with low angle misorientations (white line: > 2°) forms in the vicinity of high angle grain boundaries (zone I in Figure 6.5a). Meanwhile, there are small grains (<10 μ m) with high angle grain boundaries (zone II in Figure 6.5a). Possibly, these have been created by bulging or some subgrains have converted from low angle grain boundaries to

by rotating, and become DRX-grains (i.e. continuous DRX). At this stage the DRX fraction is measured as 4.5 %; twins are also present.

At a strain of 0.4, where softening takes place, more layers of fine grain necklaces are formed and subgrains are also seen in front of the necklaces inside the coarse as-cast grains (DRX fraction = 20.3 %). Note that the majority of the coarse grains now have their basal planes perpendicular to the compression axis (illustrated as red color), whereas some DRX-grains are random (shown as non-red color). On further deformation to the steady state region at a strain of 0.6, small equiaxed grains have consumed more of the initial grains boundaries (DRX fraction = 32.5 %), and some form within as-cast grains. Meanwhile, the grains in the necklace are much more random. At a strain of 1.0, more DRX grains form (DRX fraction = 38.9%), but the microstructure is not fully recrystallized even though steady state flow has been reached. At this stage, the fraction of necklaced grains with basal planes perpendicular to the compression direction appears to have increased significantly.

This microstructure evolution study reveals that grain boundaries are preferential sites for initiation of DRX, and necklacing, either by continuous and discontinuous DRX, is the dominant mechanism under these conditions and for as-cast grain size of approximate $110 \, \mu m$.

Recrystallization in the vicinity of second phase particles

Recrystallized grains formed near second phases in deformed specimens, as shown in Figure 6.6. This suggests that particle stimulated nucleation (PSN) occurred in this alloy, which is related to increased dislocation activity adjacent to the particles. To investigate the dislocation distribution in a deformed structure, an EBSD map of Kernel Average Misorientation (KAM) was utilized. KAM is defined as each point orientation compared to the neighboring points, i.e. for a given point, it is the average misorientation of that point with all of its neighbors. Figure 6.7 shows the EBSD map of KAM for the specimen deformed to a low strain of 0.2. The colors from dark to bright (blue, green,

yellow, orange, and red) display the values of KAM from 1 deg to 5 deg. It is noted that 'widely' spaced particles larger than $1\mu m$ (un-indexed black 'grains' in the orientation maps) lead to a deformation zones with a higher dislocation density (yellow and green color) near these particles.

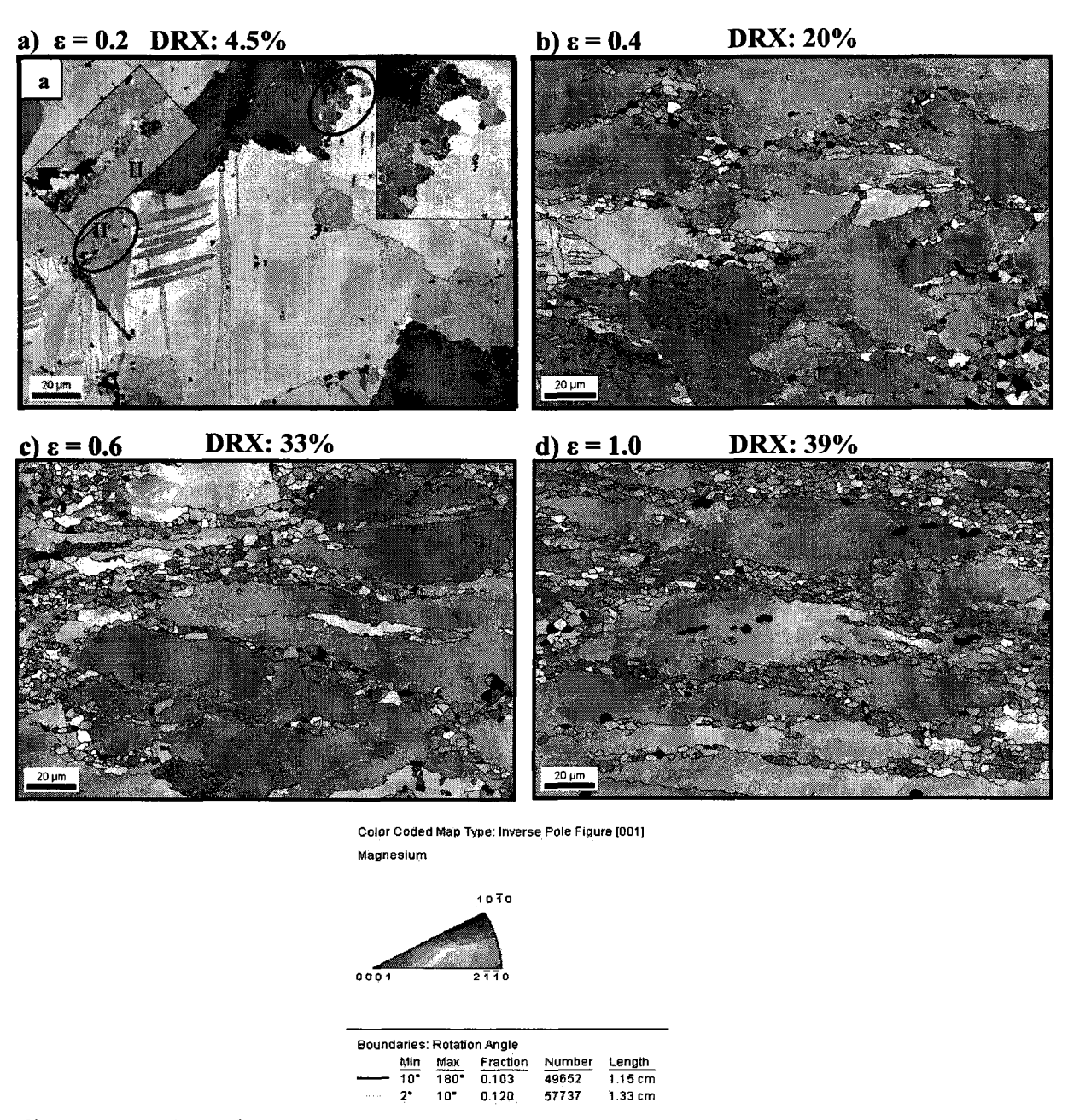


Fig. 6.5 Fraction of DRX using EBSD maps for samples compressed at 350 °C, strain rate of $0.01s^{-1}$: a) $\epsilon = 0.2$; b) $\epsilon = 0.4$; c) $\epsilon = 0.6$; and d) $\epsilon = 1.0$. Inverse pole figure map represents the grain orientations, and grains in red have (0001) poles perpendicular to the compression direction

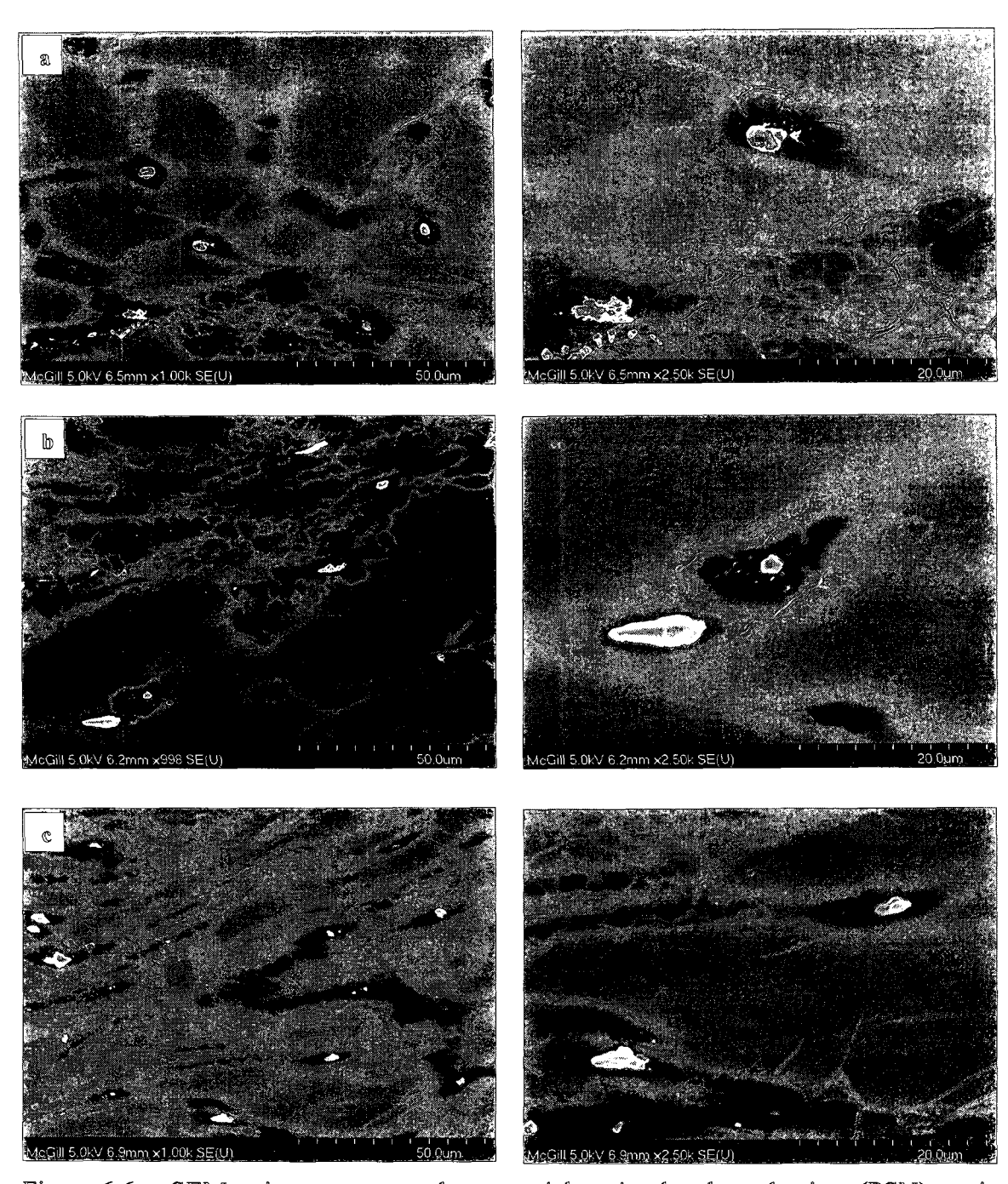
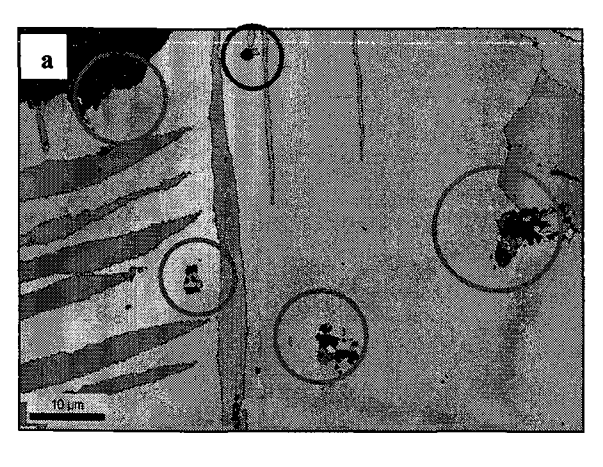
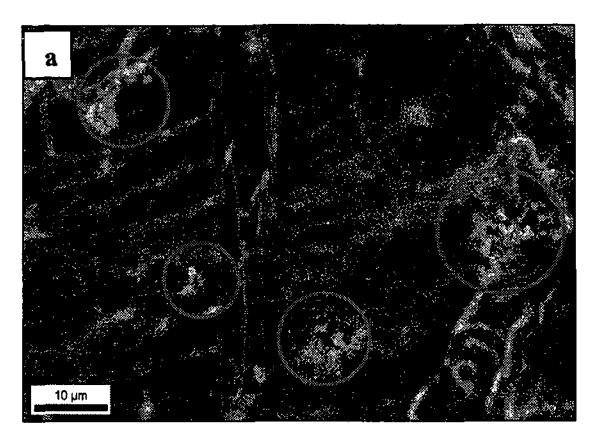
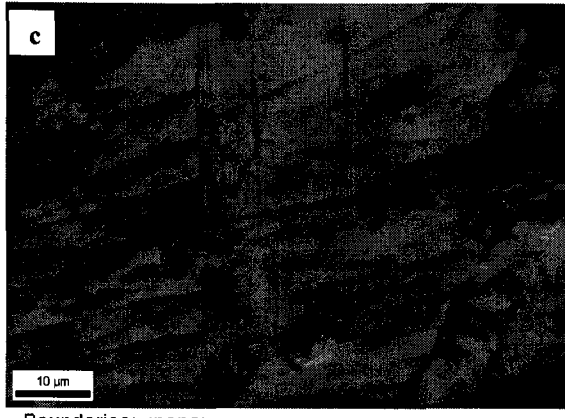


Figure 6.6 SEM microstructures show particle stimulated nucleation (PSN) grains associated with particles in the samples deformed at 350°C, a strain rate of 0.01s⁻¹, and to strains: a) 0.2, b) 0.6, and c) 0.8







Boundaries: <none>

Figure 6.7 EBSD maps for samples compressed at 350 °C, strain rate of $0.01s^{-1}$, and ε =0.2:, a) orientation map: new DRX-grains near these particles (black zone without index), b) the map of kernel average misorientation shows that the higher density (yellow and green colors) near particles, c)second phase particles

Twinning induced DRX

Only {10-12} extension twins were observed in compressed specimens as shown in Table 6.1 and Figure 6.8. The nature of these extension twin boundaries was identified using EBSD ^[5]. With increase of strain the fraction of twins reduces, and no twin were observed at a strain of 1.0. Some twins are associated with DRX as shown in arrows in Figure 6.8a and b, which indicates that twinning formed during hot compression testing may play a role to 'break-up' the coarse as-cast grains by inducing DRX.

Table 6.1 Representation of twin systems in EBSD maps

Type of twin	Twinning plane	Misorientation angle /axis	Legend
Extension Twinning	{10-12}	86°<1-210>	************
Contraction Twinning	{10-11}	56°<1-210>	
	{10-13}	64°<1-210>	
Double Twinning	{10-11}-{10-12}	38°<1-210>	
Double Twinning	{10-13}-{10-12}	22°<1-210>	100000000000000000000000000000000000000

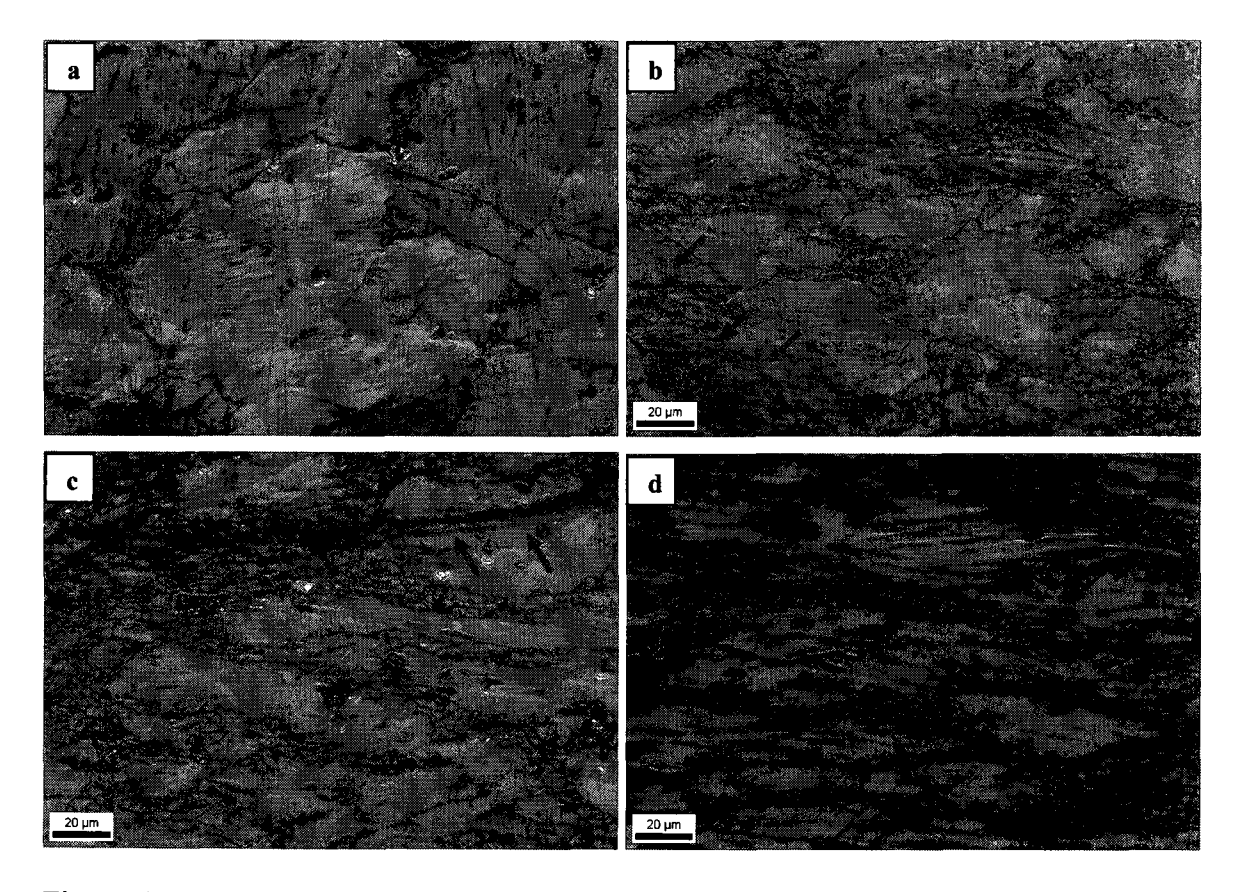


Figure 6.8 EBSD maps of twin identification for samples compressed at strain rate $0.01s^{-1}$, and strains: a) $\varepsilon = 0.2$, b) $\varepsilon = 0.4$, c) $\varepsilon = 0.6$, and d) $\varepsilon = 1.0$

6.1.1.3 Alloying Effect on Hot Compressive Behaviors of AZ31

Effect of alloying on flow curves

Figure 6.9 compares the compression flow curves tested under selected temperatures and strain rates for AZ31 based alloys cast in Cu-mould. Several observations can be noted. Firstly, broad peaks in flow stress curves were clearly seen for all alloys, and indicate the occurrence of dynamic recrystallization (DRX) [1-3]. Secondly, the peak flow stress was reduced for the alloys with additions comparing to the based AZ31 alloy, regardless of which additions were added, and whether individual additions (Ca, Sr, and Ce) or combined (Ca+Ce, Sr+Ce, or Ca+Sr+Ce). This 'flattening' associated with additions suggests that dynamic recrystallization (DRX) occurs more rapidly, thus reducing the strain hardening required to reach the peak. Thirdly, the true strain corresponding to the peak stress is in the range of 0.22~0.24, regardless of the alloy.

Effect of alloying on microstructure

To observe the effect of microalloying on DRX during hot compression testing, microstructure evolution along with strains of 0.2, 0.4, 0.6, up to 1.0, at a temperature of 350 °C and a strain rate of 0.01 s⁻¹ for base alloy AZ31 and the alloy of AZ31 with 0.19%Ca, was compared. Figure 6.10 shows the microstructure of the specimens deformed at the strain of 0.2 just around the strain at the peak stress (Figure 6.9 b). It can be seen that twinning is observed for AZ31 base alloy, and few recrystallized grains are seen in pre-existing grain boundaries and near second phases. However, for the alloy with Ca, more new recrystallized grains can be seen in the pre-existing grain boundaries and near second phases, and twinning is seldom observed.

By increasing the strain from 0.2, 0.4, 0.6, up to 1.0 (Figure 6.11), the process of dynamic recrystallization (DRX) for the two alloys (AZ31 and AZ31+0.19%Ca) is revealed. Necklacing is the main mechanism for both alloys. At 1.0 strain (Figure 6.12), there is a distinct difference between the AZ31 base alloy and alloys with additions. For AZ31 alloy some coarse dendrites are still present, and recrystallized zones seem to be aligned in certain direction which seems to be forming into shear bands. For other alloys almost all of the dendrites are deformed, and a more homogenous microstructure can be seen.

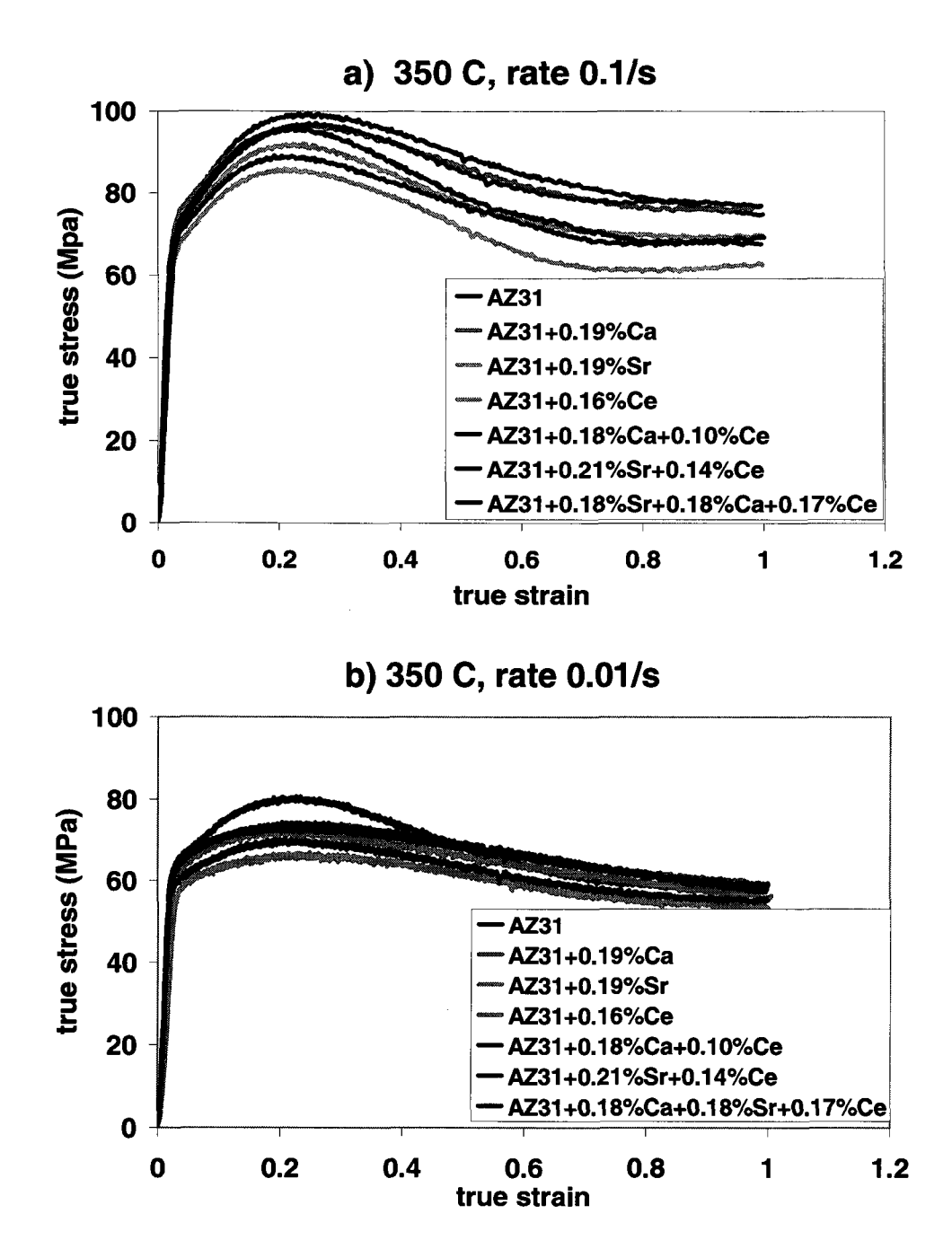


Figure 6.9 Alloying effect on compression flow curves tested at 350°C: a) strain rate of 0.1s⁻¹, b) strain rate of 0.01s⁻¹

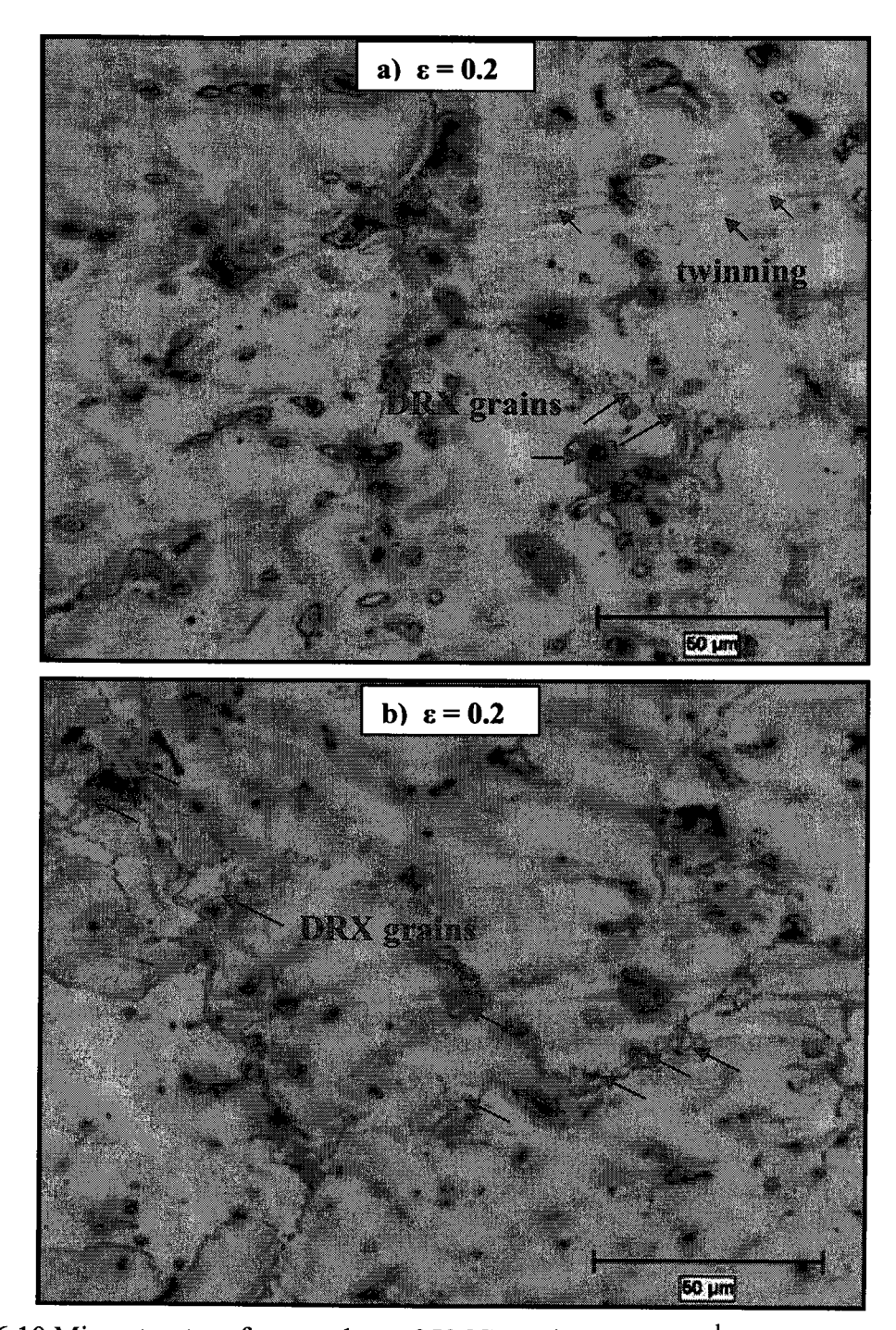


Figure 6.10 Microstructure for samples at 350 $^{\circ}$ C, strain rate: 0.01s⁻¹, and strain: 0.2, a) AZ31, b) AZ31+0.19%Ca

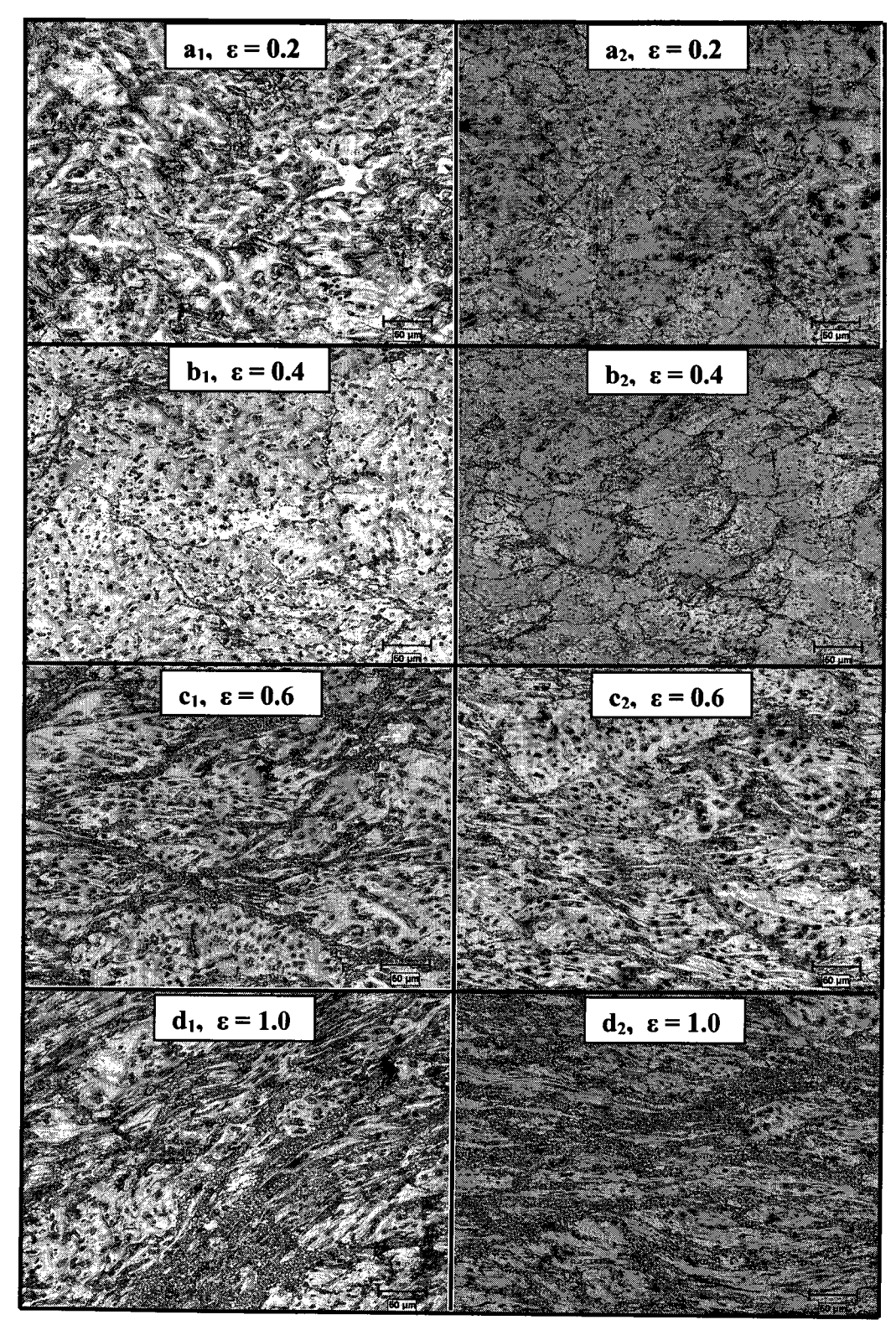


Figure 6.11 Microstructure evolution during hot compression at 350 °C, strain rate of $0.01s^{-1}$, and strains from 0.2 to 1.0: a_1), b_1), c^1) and d_1) corresponding to the alloy of AZ31; a_2), b_2), c_2) and d_2) corresponding to the alloy of AZ31with 0.19%Ca

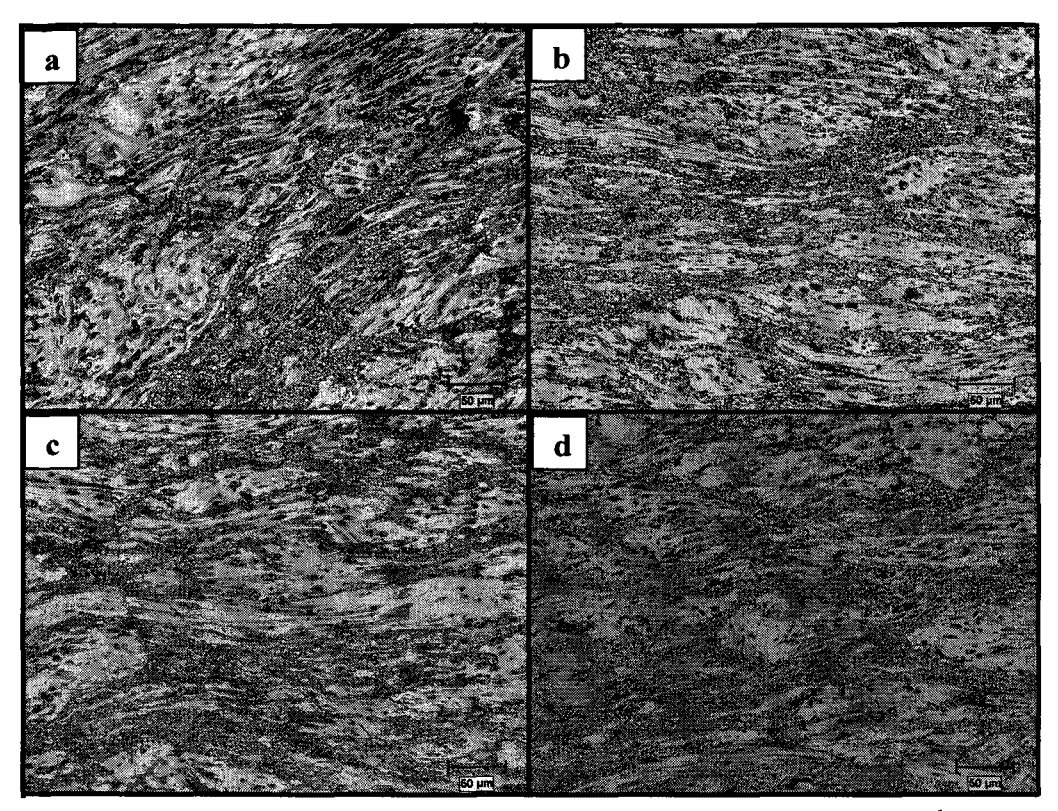


Figure 6.12 Microstructure for C-series samples at 350 °C, strain rate: 0.01s⁻¹, and strain: 1.0, a)AZ31, b) AZ31+0.19%Ca, c) AZ31+0.19%Sr, and d)AZ31+0.16%Ce

6.1.2 Two Hit Compression Testing

6.1.2.1 Flow Behavior and Interpass Softening

Figure 6.13 compares the double-hit σ-ε curves for two alloys of AZ31 and AZ31 with 0.22%Ca, 0.22%Sr and 0.21%Ce, tested at 400 °C and a strain rate of 0.1 s⁻¹. In the testing, an interpass holding time of 3 minutes was selected after the first hit to a strain of 0.22 (equivalent to a reduction of 20%). Table 6.2 displays the fraction of softening (X%) due to interpass heating for two hit compression testing. As can be seen, the static softening for AZ31 base alloy is significant (more than 60%), and is 36% higher than that of microalloyed AZ31.

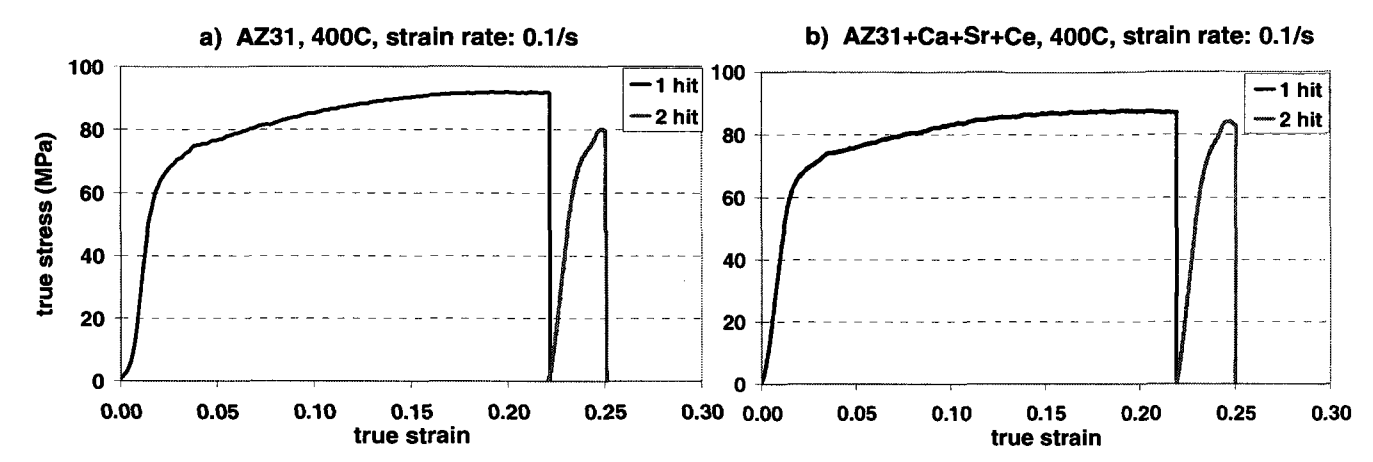


Figure 6.13 Two hits compression flow curves for alloys of AZ31 and AZ31 with Ca+Sr+Ce tested at 400 °C, strain rate of $0.1s^{-1}$, interpass heating at 400 °C for 3 minutes, the true strain of first hit: ε_1 = 0.22, the true strain of second hit: ε_2 =0.03.

Table 6.2 The fraction of softening due to interpass heating for two hit compression testing

$X = \frac{\sigma_m - \sigma_{y2}}{\sigma_m - \sigma_{y1}} $ (%)	AZ31	AZ31+ 0.22%Ca+ 0.22%Sr+ 0.21%Ce	
σ _{m (MPa)}	91.42	86.99	
σ _{v1(MPa)}	62.45	66.18	
σ _{y2 (MPa)}	72.75	78.40	
X (%)	64.4%	41.3%	

6.1.2.2 Microstructure Evolution

Microstructure evolution during the two-hit testing is shown in Figure 6.14. Before the first hit (specimens were preheated at 400 °C for 10 min), a larger grain size and a lower second phase volume fraction were observed for AZ31 base alloy compared with microalloyed AZ31 (Figure 6.13a). After the first hit, DRX at pre-existing grain boundaries and twinning occur for both alloys, but more of these deformation characteristics can be seen in the alloy with additions. Comparing the specimens held for 3 min after the first hit, it is found that DRX continues in different way for two alloys. The DRX-grains grow quickly for the base alloy AZ31, while the microalloyed DRX-grains have grown only slightly. The observations match the flow behaviour as shown in

Figure 6.14, i.e. the flow stress is higher for AZ31 base alloy after the first hit due to less DRX, and more softening happens after 3 min holding due to clear growth of DRX-grains.

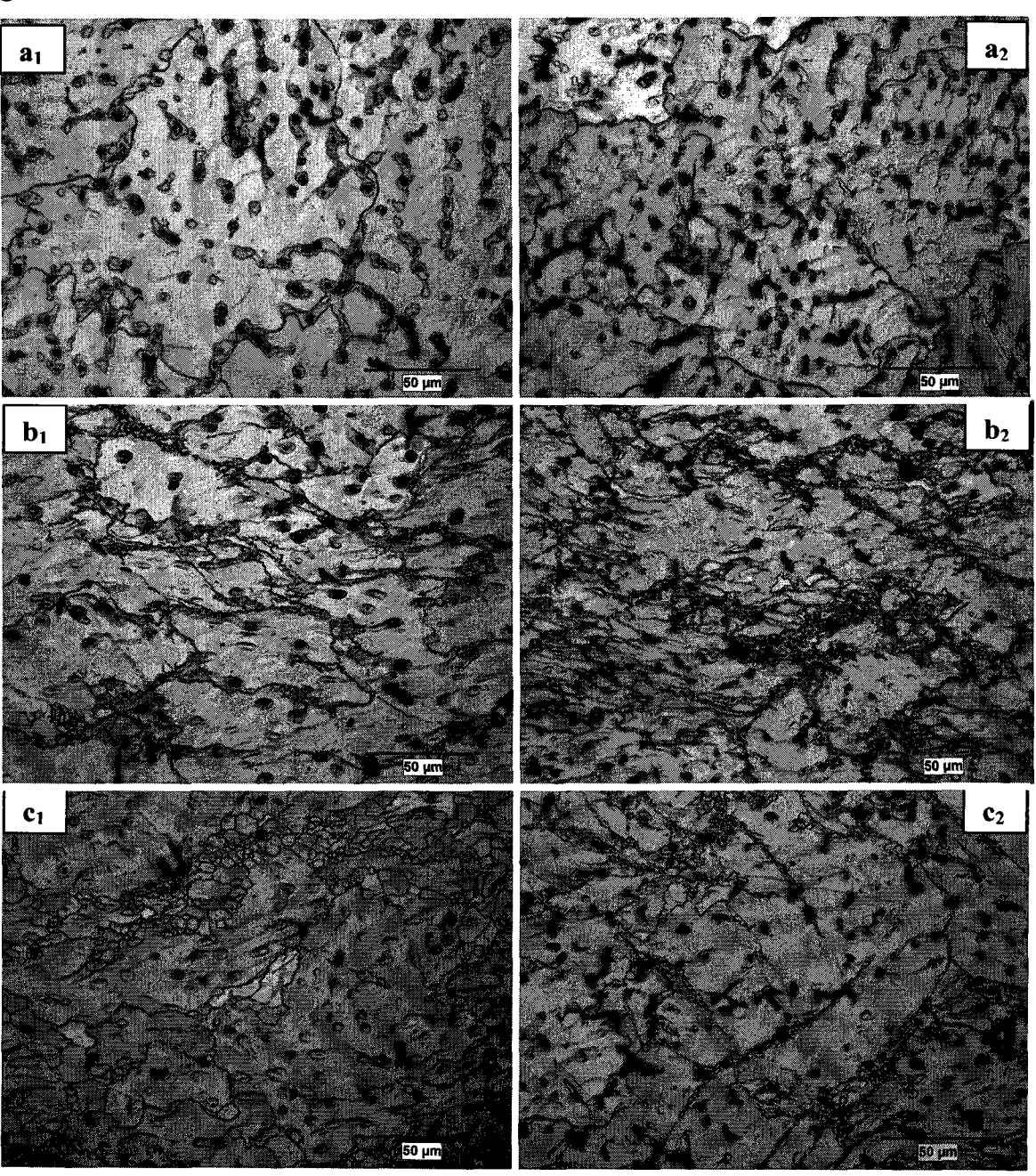


Figure 6.14 Microstructure evolution of two hit compression specimens for two alloys (a: preheating for 10 mins at start of the first hit, b: after the first hit to ε =0.22, and c: after the first hit for 3 mins just before the second hit): a_1), b_1), and c_1) corresponding to the alloy of AZ31; a_2), b_2), and c_2) corresponding to the alloy of AZ31with 0.19%Ca + 0.2%Sr + 0.2%Ce

6.2 Discussion

6.2.1 Influence of Deformation Conditions on the Flow Behavior

Deformation mechanisms of Mg include slip and twinning ^[6, 10-13] as well as DRX ^[14]. Therefore the change in the flow behaviors can give an insight into which deformation mechanisms or operating.

At high Zener-Hollomon parameter (high strain rate and low temperature), basal slip and twinning are preferentially activated due to the relatively low critical reserved shear stresses (CRSSs). Because of the lack of independent slip systems, twinning dominates. In addition, the operation of DRX is more difficult. Hence, a high flow stress due to a high strain hardening rate, is attained. In the case of low Z (low strain rate and high temperature), the prismatic and pyramidal slips can be activated because of the decrease in the values of CRSSs, and easier occurrence of DRX, so that lower flow stresses are obtained. An analysis of work hardening rate – strain at various conditions is shown in Figure 6.15. Note that the work hardening behaviour delineates two different families of curves: (i) 250 °C and 300 °C and (ii) 350 °C and 400 °C, with curves (i) having higher work hardening rates. This supports the previous statements concerning flow mechanisms. The general flow behaviors of AZ31 alloy in present work are consistent with other investigations of as-cast AZ31 alloy under a wide range of deformation conditions ^[6-9]: temperatures from ambient to 450 °C and strain rates from $10^{-3} \, \text{s}^{-1}$ up to $1 \, \text{s}^{-1}$.

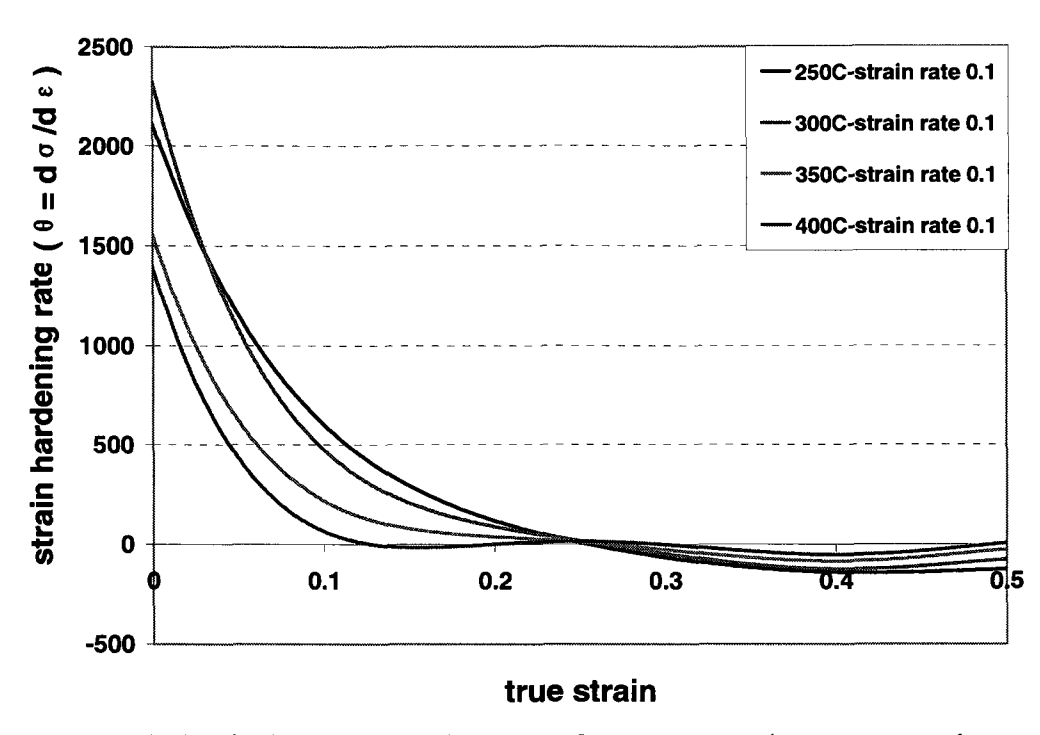


Figure 6.15 Strain hardening rate – strain curves for AZ31 samples compressed at a strain rate of 0.1 s⁻¹, temperatures of 250 °C, 300 °C, 350 °C, and 400 °C

Figures 6.16 and 6.17 compares the microstructure of deformed specimens tested under different conditions corresponding to flow curves in Figures 6.1a and 6.2, in which the changes of deformation mechanisms are clearly revealed. At a high Z (Figures 6.16 a and b), the microstructures reveal twinning dominated deformation, but very fine recrystallized grains are readily observed at the twins. At a low Z (Figures 6.16 c and d, and Figures 6.17 c), necklacing DRX dominates. The flow stress increases rapidly (Figure 6.1 a and Figure 6.2) when the temperature decreases from 350 °C to 300 °C (at a strain rate of 0.1 s⁻¹) mirroring the change in the deformation mode from necklacing DRX to twinning. It is worth noting that there is an intermediate deformation mode combining the necklacing DRX and twinning as illustrated in Figure 6.17 b. This may give an insight into hot rolling schedule design since, under this particular hot deformation condition, DRX forms transgranularly at twins, as well as at grain boundaries. Such a combination should lead to a more uniform grain size than if DRX only took place at grain boundaries.

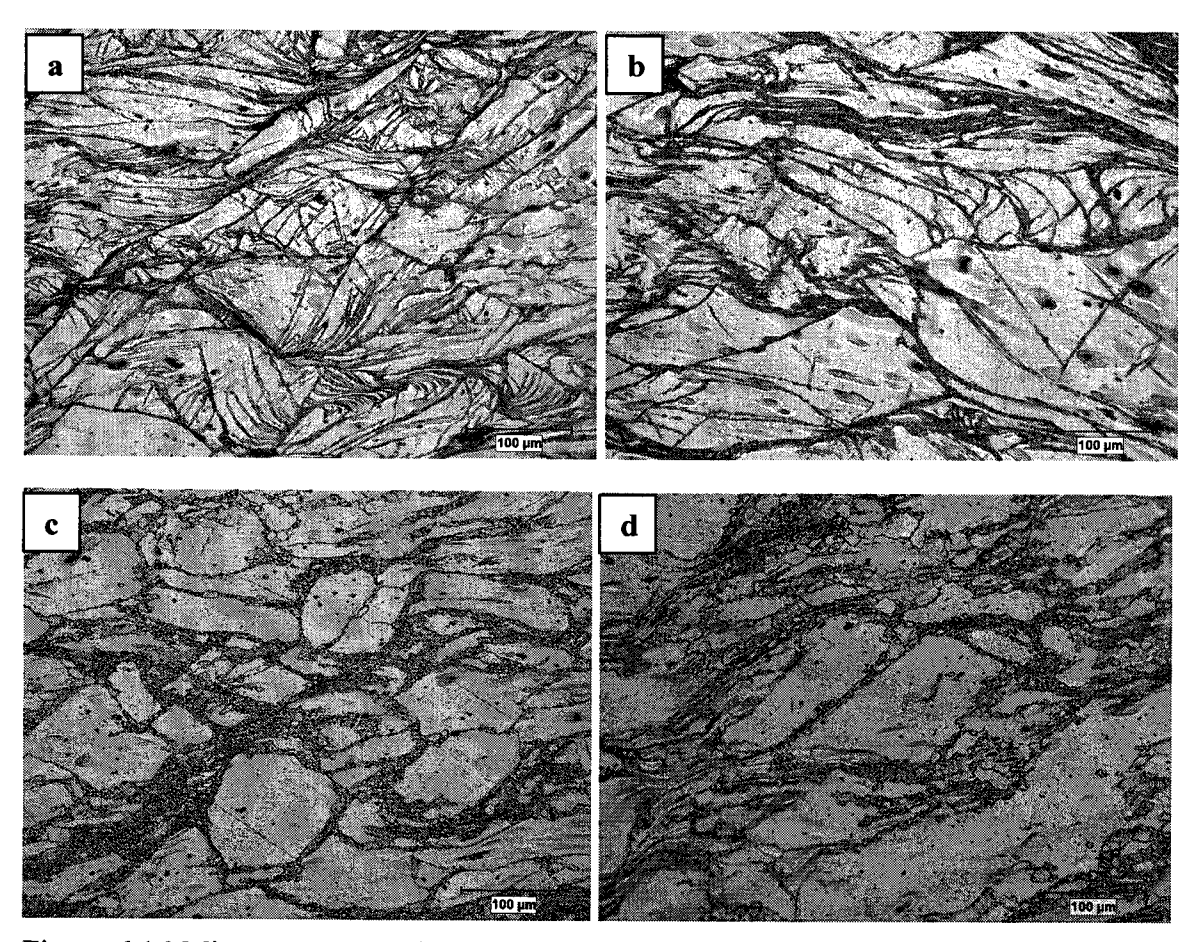


Figure 6.16 Microstructures of compression samples deformed to a true strain of 0.6 and $\not\in$ 0.1 s⁻¹at different temperatures: a) 250 °C; b) 300 °C; c) 350 °C; and d) 400 °C

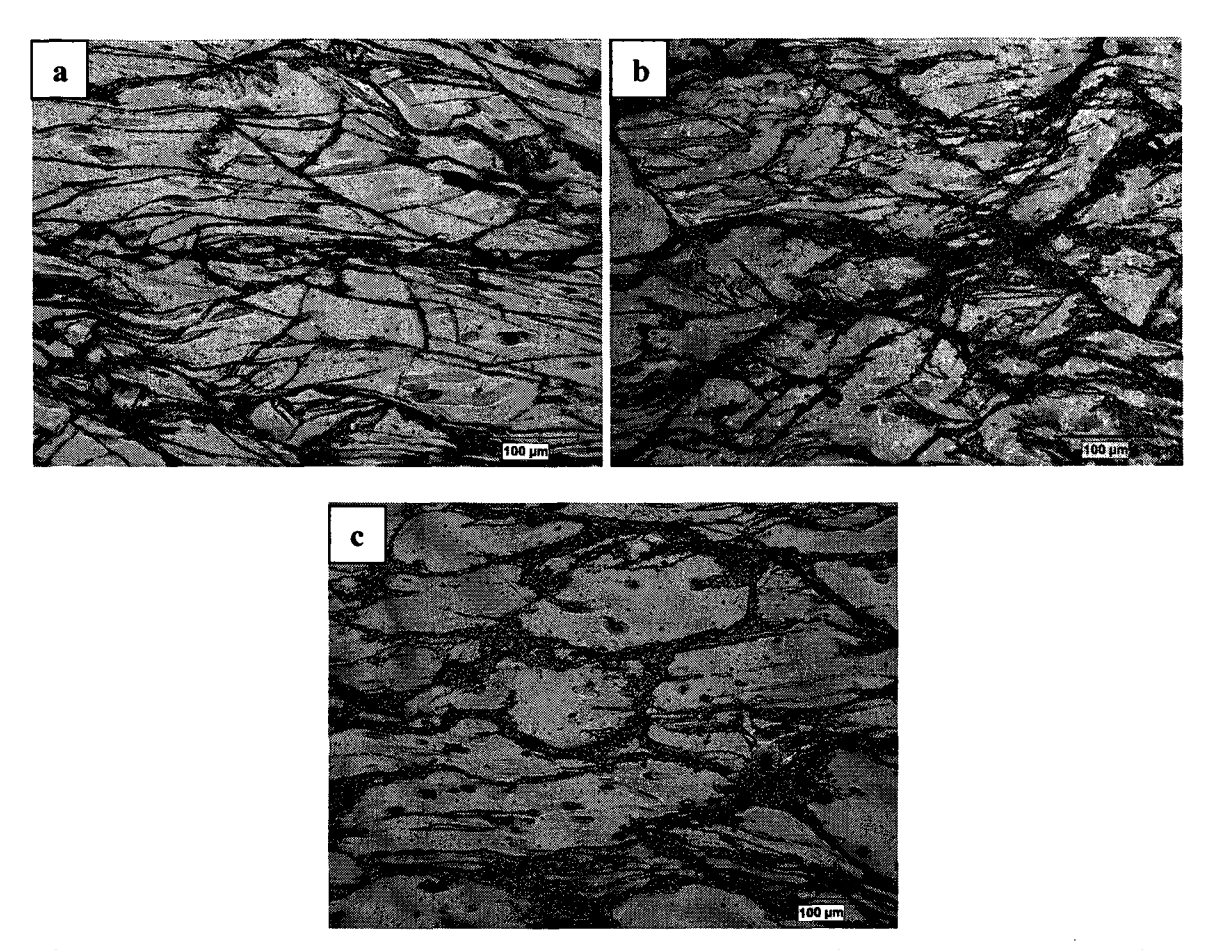


Figure 6.17 Microstructures of compression samples deformed at 300 °C to a true strain of 0.6: a) $\not\in$ 0.1 s⁻¹, b) $\not\in$ 0.01 s⁻¹, and c) $\not\in$ 0.001 s⁻¹

6.2.2 Dynamic Recrystallization (DRX) Mechanisms

As presented in the literature ^[15-18], DRX mechanisms of Mg-alloys depend on the deformation conditions. Discontinuous DRX, continuous DRX, and twinning induced DRX may operate based on their studies. In this work, the possible DRX mechanisms are discussed.

6.2.2.1 Discontinuous DRX and Continuous DRX

According to the observation of nucleation of DRX grains, discontinuous DRX and continuous DRX appear to be occurring together. In the case of discontinuous DRX, grain boundary bulging or strain induced grain boundary migration (SIBM) can be observed. The driving force for SIBM is the difference in dislocation density, hence stored energy, on opposite sides of a grain boundary. New grains form by bulging of a part of the pre-existing grain boundary, and eventually a new grain forms once a critical strain has been exceeded. As was shown in zone I of Figure 6.5a, new grains initially have similar orientations (similar color) to the old grains from which they have grown as.

Continuous DRX results from the formation of subgrains with low angle misorentations and rotation of these grains from low to high angle misorientations. The occurrence that subgrains initiate near grain boundaries may be due to microstructural inhomogeneities at these regions. Supporting evidence for this was seen in the EBSD KAM map for the specimens compressed at strains of 0.2 and 1.0 (Figure 6.18). It is noted that at a low strain of 0.2, deformed zones with low angle misorientations are generated near pre-existing grain boundaries. With increasing a strain to 1.0, deformation zones have more widely developed from necklace region (as-cast grain boundaries).

The combined result of continuous DRX or discontinuous DRX leads to less than 50% volume fraction of recrystallization at steady state. It seems that, once a this volume fraction of DRX is reached, DRX concentrates in the necklaced region, possibly because deformation is easier in the necklaced region because of enhanced grain boundary sliding and dynamic recrystallization.

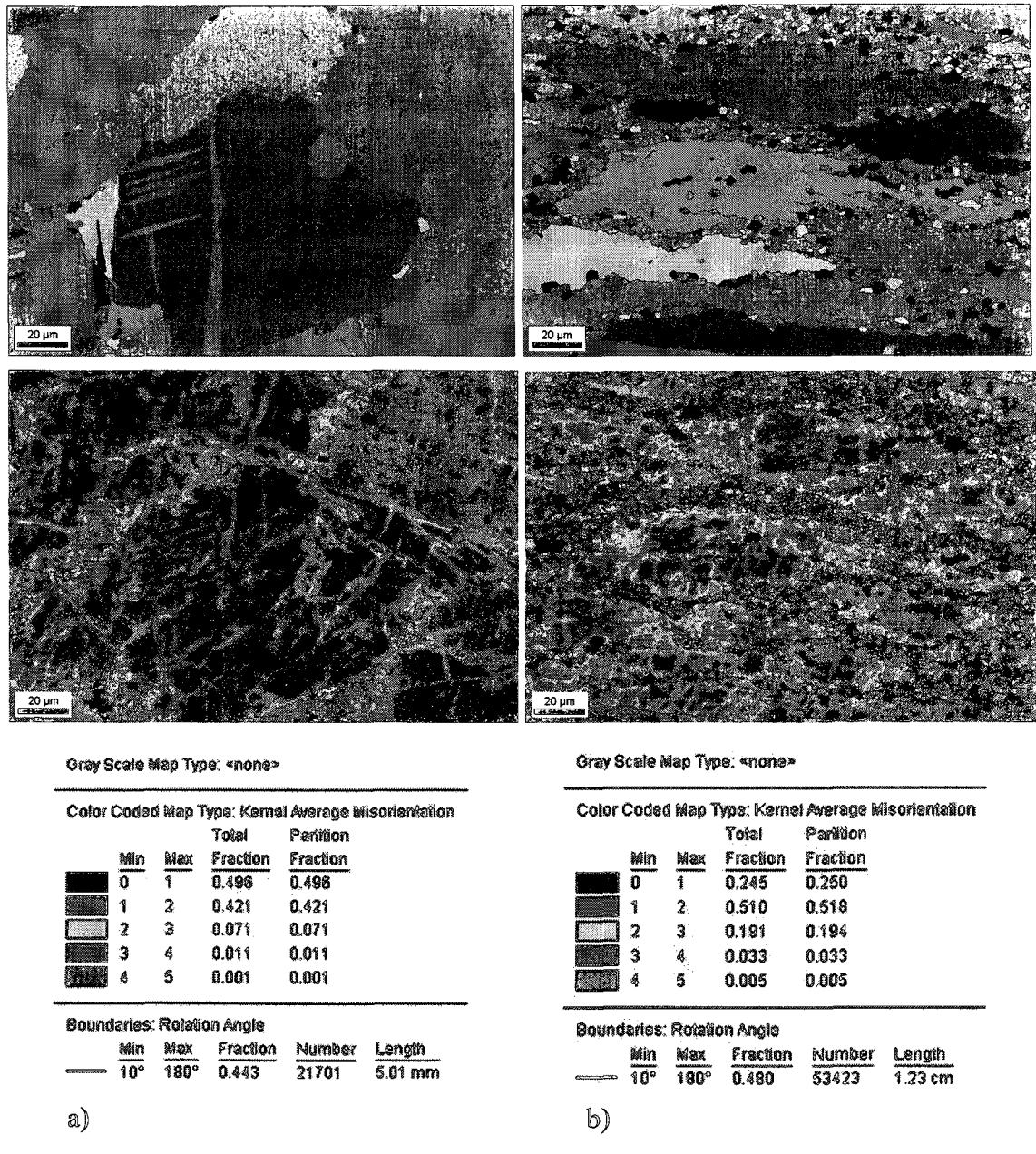


Figure 6.18 EBSD maps of grains and kernel average mismientation (1 \sim 5 deg) for sample compressed at 350 °C, strain rate 0.01 s⁻¹: a) strain 0.2 and b) strain 1.0

6.2.2.2 Particle Stimulated Nucleation (PSN)

PSN has been demonstrated in many studies of cubic alloys: aluminum, iron, copper and nickel [19-21]. A study in deformation behavior of Al-SiC particulate

composites concluded that two criteria for the occurrence of PSN ^[22]: 1) A particle deformation zone (PDZ) must form, and 2) The matrix must have enough stored energy for a nucleus to grow away from the particle. With high temperature deformation PDZ formation may be difficult due to dislocation climb over particles, while with a cold deformation, the nuclei may be difficult to grow away from particles.

Generally, PSN occurs when the maximum misorientation of the deformation zone is sufficient to form a high angle boundary with the matrix ^[1]. PSN is rarely reported in DRX of AZ31 alloy ^[15, 23, 24]. It might be due to that surveyed materials are usually homogenized and the majority of second phases have been dissolved. In present case, the as-cast structure with particles greater than 1 µm and widely spaced (Figure 6.3) was deformed. As analyzed by using EBSD KAM mapping (Figure 6.7 b), these second phase particles were shown to have an effect on the accumulation of dislocations and the formation of deformation zone in the vicinity of particles. PSN was able to occur when a critical value of misorientation in the deformation zone is reached as was observed in Figure 6.6. Since the interaction of dislocations and second phase particles is temperature dependent, the deformation temperature or the strain rate will be critical to the occurrence of PSN.

It is also noted that particles situated in regions where large strains and strain gradients arise, such as grain boundaries and deformation bands, may provide more favored nucleation sites than other particles (black no-index points in Figure 6.5). Further investigations are needed to increase understanding of the role of particles in recrystallization of magnesium alloys.

6.2.2.3 Twinning Induced DRX (TDRX)

Twinning in Mg usually takes places if other deformation mechanisms are not available. Thus, at low temperatures, basal slip dominates initially, but this rapidly leads to a basal texture which makes basal slip very difficult, and twins form intensively. It was found that twinning occurs from room temperature to as high as 450 °C since the

CRSS value to active twinning is independent on the deformation temperature [17]. Generally, less twinning occurs at higher temperatures and at lower stain rates due to the activation of non basal slip systems.

Studies in coarse as-cast AZ31 have shown that twin boundaries can act as sites for the nucleation of DRX-grains during hot compression and torsion testing ^[17, 25-27]. In this work, twins associated with DRX grains were also observed, as was shown, for example in AZ31 compressed at 350 °C and a strain rate of 0.01s⁻¹(Figure 6.8 b and c), in which these DRX-grains present the same misorientation angle /axis as extension twinning (red color) as defined in Table 6.1. Figure 6.19 displays TDRX in the alloy of AZ31with additions (Ca, Sr, and Ce) compressed at 400 °C and a strain rate of 0.1s⁻¹. The results suggest that the operation of TDRX during hot rolling at a high strain rate would lead to transgranular twins, which would lead to transgranular dynamic recrystallization, and, with DRX generated at grain boundaries, would contribute to a more uniform DRX grain structure.

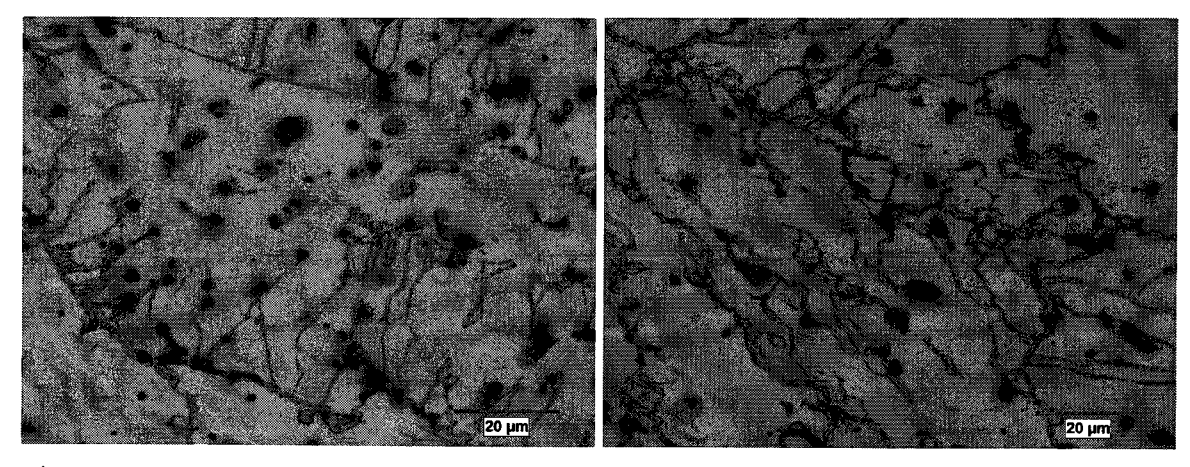


Figure 6.19 Twinning induced dynamic recrystallization in the alloy of AZ31 with 0.22%Ca + 0.22%Sr + 0.21%Ce, compressed at 400 °C, strain rate 0.1 s⁻¹, and a strain 0.22

6.2.3 Effect of Alloying on DRX

To have a better understanding of the microalloying effect on DRX of AZ31 alloy

during hot compression, the critical strain (ε_c) to initiate DRX was investigated by using a mathematical analysis of the σ - ε data [28-31]. Firstly, the σ - ε data were regressed into a 9th order polynomial smoothed stress-strain curve. From equation 6.1, the inflection point in the $\ln(d\sigma/d\varepsilon)$ - ε is the same point as the inflection point in the θ - σ curve (where θ is the work hardening rate, $d\sigma/d\varepsilon$), corresponding to the onset of dynamic recrystallization. By using Maple 10 software, the inflection point in the $\ln(d\sigma/d\varepsilon)$ - ε can be calculated.

$$\left(\frac{\partial \theta}{\partial \sigma}\right)_{\mathcal{E}} = \left(\frac{\partial \ln \theta}{\partial \varepsilon}\right)_{\mathcal{E}}$$
 (Equation 6.1)

Table 6.3 lists the critical strains of initiation of DRX for the different alloys tested at a true strain rate of $0.1 \, \mathrm{s}^{-1}$ and a temperature of 350 °C. As can be seen, the values of the critical strain for all alloys with additions are in the range of 0.09~0.11, and 11% ~ 26% less than the base alloy AZ31. The present results of ε_c agree reasonably with the data of other studies, i.e. $\varepsilon_c = 0.4 \sim 0.5 \, \varepsilon_{peak}$ for AZ31 ^[9] and approximate 0.5 ε_{peak} for AZ61 alloy ^[28]

Table 6.3 Critical strains to initiate DRX for compression specimens tested at strain rate of 0.1 s⁻¹, and temperature of 350 °C

Alloys	Critical strain: ε _c	Difference in ε _c comparing with AZ31 (%)	Peak strain: ε _p	$\epsilon_{c/} \epsilon_{p}$
AZ31	0.121	0	0.243	0.50
AZ31+0.19%Ca	0.101	16.5%	0.238	0.42
AZ31+0.19%Sr	0.108	10.7%	0.222	0.49
AZ31+0.16%Ce	0.093	23.1%	0.232	0.40
AZ31+0.18%Ca+0.10%Ce	0.089	26.4%	0.235	0.38
AZ31+0.21%Sr+0.14%Ce	0.104	14.0%	0.217	0.48
AZ31+0.18%Ca+0.18%Sr+0.17%Ce	0.095	21.5%	0.222	0.43

The slight decrease in the value of ε_c for alloys with additions suggests that microalloying may accelerate DRX. The smaller grain size for alloys microalloyed with Ca or/and Sr increases the volume fraction of grain boundaries, and, therefore, the nucleation sites for DRX. As well, more thermally stable second phases may promote

more occurrence of PSN. Note that the alloy with Ce exhibits similar features with the alloys with Ca or Sr, even though Ce has no effect on grain refinement. This may be due to its effect on the refinement of intermetallic particles, and more PSN The acceleration of DRX suggests that microalloyed AZ31 may be slightly easier to hot roll.

6.2.4 Alloying Effect on Interpass Softening

To investigate interpass (static) softening occurring during hot rolling, two-hit compression testing is routinely used for steels $^{[32]}$, but has not been reported for Mg-alloys. In this work, the interpass softening faction was quantitatively examined from σ - ϵ flow curves during two-hit compression testing. (Figure 6.13), and microstructure evolution (Figure 6.14) reveals that the significant softening occurring in AZ31 is revealed as grain growth, which is probably a metadynamic recrystallization process. Less softening occurs in the alloy with additions (0.22%Ca, 0.22%Sr, and 0.21%Ce), correlating with less grain growth.

In an alloy containing a dispersion of particles, it is found that whether recrystallizing grains will grow during recrystallization, mainly depends on two opposing factors ^[1]: 1) the driving force for growth (P_D) provided by the dislocation density (ρ), 2) the Zener pinning pressure (P_z) arising from particles (F_v/r : ratio of volume fraction and radius). When F_v/r is greater than a critical value, the net driving pressure will be negative, so that recrystallization growth can be suppressed. The value of F_v/r in the alloy with additions (0.22%Ca, 0.22%Sr, and 0.21%Ce) may be relative high to resist the growth due to obvious increase in the volume fraction of thermally stable second particles.

The results from this two-hit compression suggest that microalloying has an effect on decreasing the interpass softening by impeding the growth of recrystallized grains which could be beneficial to the control of grain size in as-rolled microstructure.

6.3 Summary

- Compression testing of AZ31 based alloys reveals that deformation mechanisms depend on testing conditions: at a high Zener-Hollomon condition (high strain rate and low temperature), twinning dominates and less DRX occurs, and high flow stresses were detected; In the case of a low Z condition (low strain rate and high temperature), twinning is suppressed and the consequential dislocation activity leads to intensive DRX necklacing, so that low flow stresses were measured. The microstructure evolution during compression testing provides confirmation of these deformation mechanism changes;
- The results of compression testing also indicate that an optimized as-compressed structure of a combination of DRX by necklacking and twinning could be achieved under a certain deformation condition. The industrial relevance is that a practical hot rolling process may be designed according to the concept that recrystallization (static and/or dynamic) occurs along with twinning, the latter to create intragranular recrystallization sites. This will promote a more uniform and finer as-hot rolled microstructure;
- EBSD analysis reveals that the following mechanisms of DRX occur during hot compression of AZ31 based alloys under the condition of 350 °C, and strain rate of 0.01s⁻¹: discontinuous DRX, continuous DRX, twinning induced DRX, and particle stimulated nucleation (PSN). The dominate mechanisms is DRX-necklacing by discontinuous DRX and continuous DRX;
- DRX by particle stimulated nucleation (PSN) is a supplementary mechanism when thermally stable second particles (widely spaced and greater than 1 μm) are present prior to hot deformation, as was shown under the condition of 350 °C and a strain rate of 0.01 s⁻¹ for as-cast AZ31 based alloys;
- Microalloying AZ31 with Ca, Sr, and Ce decreases the peak flow stress and slightly
 decreases the critical strain to initiate DRX; this indicates that DRX is accelerated.
 The more homogenous DRX in microalloyed materials is mainly due to the increase

in nucleation sites by refining initial as-cast grain size and increasing the numbers of second phases;

- by static recrystallization for AZ31 base alloy, due mainly to the growth of recrystallized grains. This suggests that the static recrystallization is metadynamic in the sense that recrystallization is progressing by growth of nucleated grains as opposed to the creation of new grains. In terms of hot rolling schedule design, a mechanism by which classic static recrystallization (i.e. the creation of new grains) is desirable. This may be possible by designing a hot rolling schedule to generate twins and DRX in the roll gap, and then having an interpass condition where new grains are nucleated at the twins;
- Microalloying has an effect on decrease of interpass softening by retarding the grain
 growth of the recrystallized grains due to the increase in volume fraction of second
 particles. This alloying approach could be combined with the above principles for
 hot rolling schedule design to get a fine and uniform as hot rolled grain size.

References:

- 1. F.J. Humphreys and M. Hatherly, "Recrystallization and Related Annealing Phenomena", second edition, Oxford, (2004), p 428, p 294, p 251, p 25-35
- 2. T. Sakai and J.J. Jonas, "Dynamic Recrystallization: Mechanical and Microstructural Considerations", Acta metal., 32, (1984), p 189
- 3. F.J. Humphreys, "Network model for recovery and recrystallization", Scr. Metal. Mater., 27 [11], (1992), p 1557
- 4. X. Yang, H. Miura and T. Sakai, "Dynamic Evolution of New Grains in Magnesium Alloy during Hot Deformation", Mater. Trans. JIM, 44 (1), (2003), p 197-203
- 5. M.D. Nave and M.R. Barnett, "Microstructures and Textures of Pure Magnesium Deformed in Plane-Strain Compression", Scripta Materialia, 51 (9), (2004), p 881-885
- M.R. Barnett, "Hot Working Magnesium AZ31", thermomechanical Processing, Mechanics, Microstructure & Control, ed. E.J. Palmiere, M. Mahfouf and C. Pinna, Sheffield University, Sheffield, (2003), p 56-62

- 7. A.G. Beer, "The Evolution of Hot Working Stress and Microstructure in Mg-3Al-1Zn", Ph.D. Thesis, Deakin Univerity, Australia, January (2004), p 72-73
- 8. G. Vespa,, "Hot Deformation Behavior of Magnesium AZ31", M.Eng. Thesis, McGill University, Canada, December (2006), p 38-39
- 9. G.G. Huang, L.Wang, G.S. Huang, and F.S. Pan, "Dynamic Recrystallization and Microstructure Evolution in AZ31 Magnesium Alloy during Thermomechanical Processing", Materials Secience Forum, 488-489, (2005), p 215-218
- 10. T. Obara, H. Yoshinga, and S. Morozum, "{12-22} <-1-123> Slip System in Magnesium", Acta Metallurgica, 21, (1973), p 845-853.
- 11. P. Ward Flynn, J. Mote, and J.E. Dorn, "On the Thermally Activated Mechanism of Prismatic Slip in Magnesium Single Crystals", TMS-AIME, 221, (1961), p 1149-1154
- 12. R.E. Reed-Hill and W.D. Robertson, "Pyramidal Slip in Magnesium", Acta Metallurgica, TMS-AIME, 212, (1958), p 256-259
- 13. S.R. Agnew, M.H. Yoo, and C.N. Tome, "Application of Texture Simulation to Understanding Mechanical Behavior of Mg and Solid Solution Alloys Containing Li or Y", Acta Materialia, 49, (2001), p 4277-4289
- 14. M.R. Barnett, "Influence of Deformation conditions and Texture on the High Temperature Flow Stress of Magnesium AZ31", Journal of Light Metals, 1, (2001), p 167-177.
- 15. A.G. Beer and M.R. Barnett, "Microstructural Development during Hot Working of Mg-3Al-1Zn", Metallurgical and Materials Transactions A, 38, August (2007), p 1856-1866
- 16. O. Sitdikov and R. Kaibyshev, "Dynamic Recrystallisation in Pure Magnesium", Materials Transactions, 42 No.9, (2001), p 1928-1937
- 17. M.M. Myshlyaev, H. J. McQueen, A. Mwembela and E. Konopleva, "Twinning, Dynamic Recovery and Recrystallisation in Hot Worked Mg-Al-Zn Alloy", Materials Science and Engineering A, 337 (1-2), (2002), p 121-133
- 18. X.Yang, H. Miura and T. Sakai, "Dynamic Nucleation of New Grains in Magnesium Alloy during Hot Deformation", Materials Science Forum, 419-422, (2003), p 515-520
- 19. N. Hansen, "Recristallisation Accélérée et retardée dans produits renforcés pas des dispesions", Mem. Sci. Rev. Met, 72, (1975), p 189-203
- 20. F.J. Humphreys, "The Nucleation of Recrystallization at Second Phase Particles in Deformed Aluminum", Acta metal., 25, (1977), p 1323-1344
- 21. D.T. Gawne and R.A. Higgins, "Associations between Spherical Particles of Two Dissimilar Phases", J. Mats. Sci. 6, (1971), p 403-412
- 22. F.J. Humphreys, "The Thermomechanical Processing of Al-SiC Particulate Composites", Mat. Sci. and Eng., A135, (1991), p 267-273
- 23. L. Jiang, G. Huang, S. Godet, J.J. Jonas and A.A. Luo, "Particle-Stimulated Nucleation of Dynamic Recrystallization in AZ31 Alloy at Elevated Temperature", Materials Science Forum, 488-489, (2005), p 261-264
- 24. L. Shang, S. Yue, E. Essadiqi, A. Javaid, J. Carter, and R.Verma "Effect of Initial Microstructure under Different Solidification Conditions on Hot Working Behavior of AZ31 Alloy", Material Science Forum, 561-565, (2007), p 325-328

- 25. A. Grosvenor, and C.H.J. Davies: "Microstructural Evolution During the Hot Deformation of Magnesium AZ31", Materials Science Forum, 488-489, (2003), p 426-432
- 26. R.O. Kaibyshev and O.S. Sitdikov, "Dynamic Recrystallisation and Mechanisms of Plastic Deformation", The Third International Conference on Recrystallisation and Related Phenomena, (1996), p 203-209
- 27. A.G. Beer and M.R. Barnett, "The Influence of Twinning on the Hot Working Flow Stress and Microstrucural Evolution of Magnesium Alloy", Materials Science Forum, 488-489, (2005), p 611-614
- 28. L. Liu, H. Zhou, Q. Wang, Y. Zhu and W. Ding: "Dynamic Recrystallization Behavior of AZ61 Magnesium Alloy", Advances in Technology of Materials and Materials Processing Journal, 6 [2], (2004), p 155-165
- 29. E.I. Poliak and J.J. Jonas, "A One-Parmenter Approach to Determining the Critical Conditions for the Initiation of Dynamic Recrystallization", Acta Materialia, 44 (Issue 1), (1996), p 127-136
- 30. G.R. Stewart, "Static and Dynamic Aging and Softening in 304 Stainless Steel", Ph.D these, January (2004), p 78-83
- 31. F. Zarandi, "The Effect of High Temperature Deformation on the Hot Ductility of Nb-Microalloyed Steel", Ph.D. Thesis, McGill University, Canada, July 2004, p 153-163
- 32. A. Najafizadeh, J.J. Jonas, G.R. Stewart, and E.I. Poliak, "The Strain Dependence of Postdynamic Recrystallization in 304 H Strainless Steel", Metaalurgical and Materials Transactions, June (2006), 37A, p 1889-1906

Chapter 7

Rolling

7.1 Results

7.1.1 Reheating Experiment

Reheating was performed at 450 °C for 15 min and 1 hour to determine an appropriate soaking time to dissolve the second phases and minimize the microsegregation in dendritic structure. Figure 7.1 displays the microstructure evolution during reheating by optical microscope and SEM observation. It is confirmed that second phases in as-cast microstructure are mainly circular or irregular Mg (Al, Zn) eutectics and short-rod (Al, Mn) compounds (Figure 7.1a and b). These coarse (1~5 µm) Mg (Al, Zn) particles in the as-cast sample partially dissolve into the Mg-matrix when the specimen is reheated to 450 °C and held for 15 minutes, but dendritic features still remain (Figure 7.1c and d). When held for one hour at 450 °C, the second particles dissolve much more (Figure 7.1e and f) and the dendritic structure is almost eliminated. The remaining particles were identified as Al-Mn phases by EDS.

Note that in the previous Chapter 5 the second phases containing microalloying elements were stable even after 10 hours at 450 °C. Therefore, based on this observation

plus the above experiment, reheating at 450 °C for one hour was selected as the soaking condition for the subsequent hot rolling experiments.

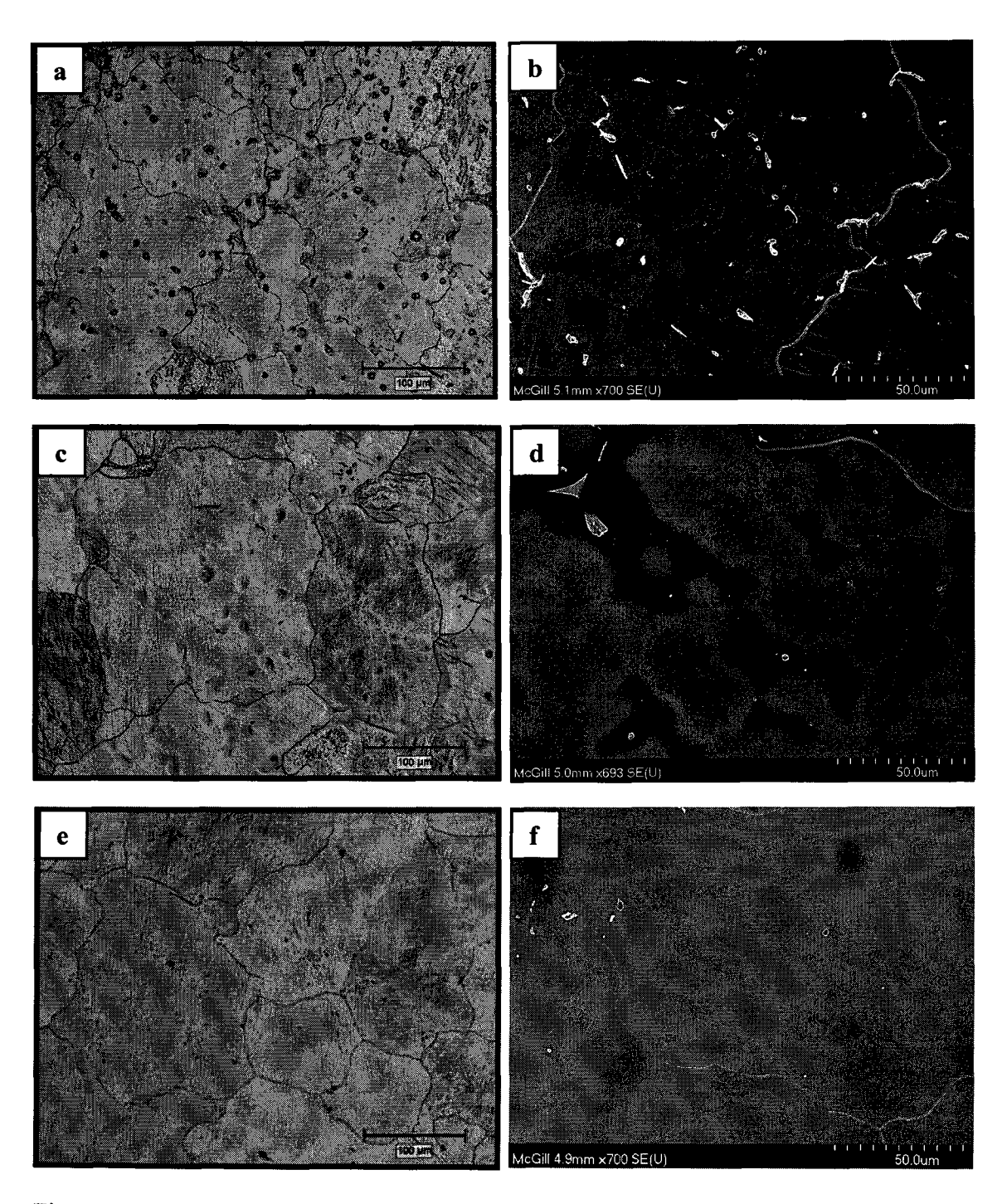
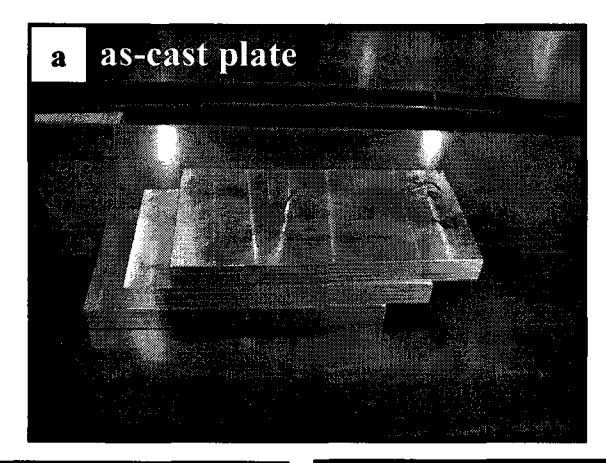


Figure 7.1 Reheating time effect on the grain structure and second phases: a and b) ascast; c and d) reheating at 450 °C for 15 min; e and f): reheating at 450 °C for 1 hour

7.1.2 Condition of the As-rolled Sheets

As hot rolled sheets approximate 1.6 mm thick were produced under two conditions, 300 °C with 30% reduction per pass and 400 °C with 20% reduction per pass, and are shown in Figure 7.2. It is noted that, although it was possible to roll at 300 °C, this condition was considerably more problematic than rolling at the higher temperature, leading to more rippling at the surface, increased edge cracking and general shape control issues.



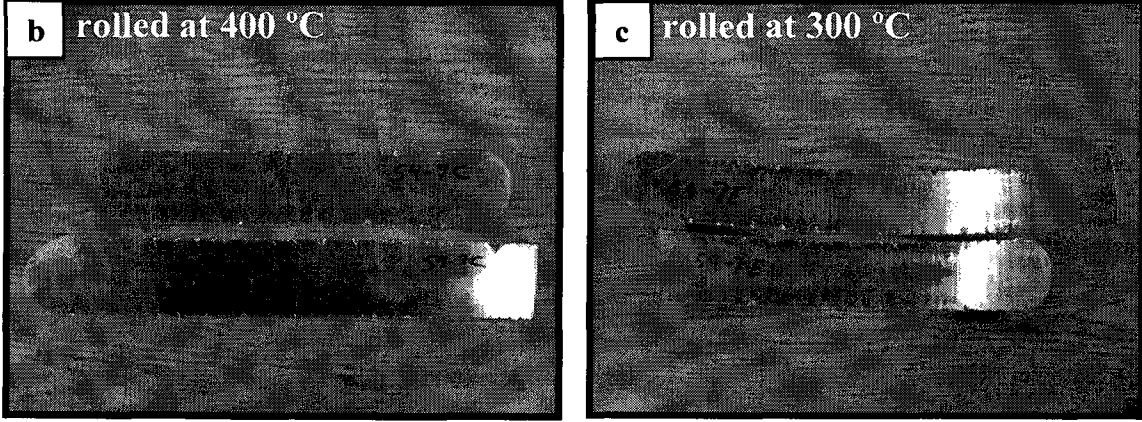


Figure 7.2 Materials before and after rolling: a) ingot cast in Cu-mould with water cooling, b) sheets rolled at 400 °C with 30% reduction per pass, and c) sheets rolled at 300 °C with 20% reduction per pass

7.1.3 As-Hot Rolled Microstructure

Figures 7.3-7.8 displays optical micrographs of a full section in the longitudinal edge view of sheets materials for the six kinds of alloys under two different rolling conditions.

The effect of rolling temperature is observed clearly. In general, sheets rolled at a lower temperature of 300 °C and 20% reduction per pass show more deformation bands (dark zones at a low magnification) which consist of small recrystallized grains and twins observed at a higher magnification as shown in Figure 7.9. For sheets rolled at 400 °C and 30% reduction per pass, there are some clusters of relatively coarse grains (Figure 7.3b and Figure 7.5b). Also, the average recrystallized grain structure rolled at 300 °C is smaller than that rolled at 400 °C. Since as-rolled microstructure consists of certain amount of unbroken coarse grains and deformation bands, it is difficult to get a more accurate measurement of the grain size for the rolled sheets. Thus, more qualitative observations are presented here.

The alloying effect on the as-rolled microstructure can be observed by comparing Figures 7.3-7.8. The main effect is that the clusters of coarse grains are rarely seen in the microalloyed sheets containing Ca either on its own, or in combination with the other microalloying elements. In other words, AZ31 with Ce only does not seem to decrease the incidence of coarse grain clusters compared to the base AZ31. The overall observation is that, apart from the Ce only addition, microalloying will contribute to a refined and more uniform sheet grain size.

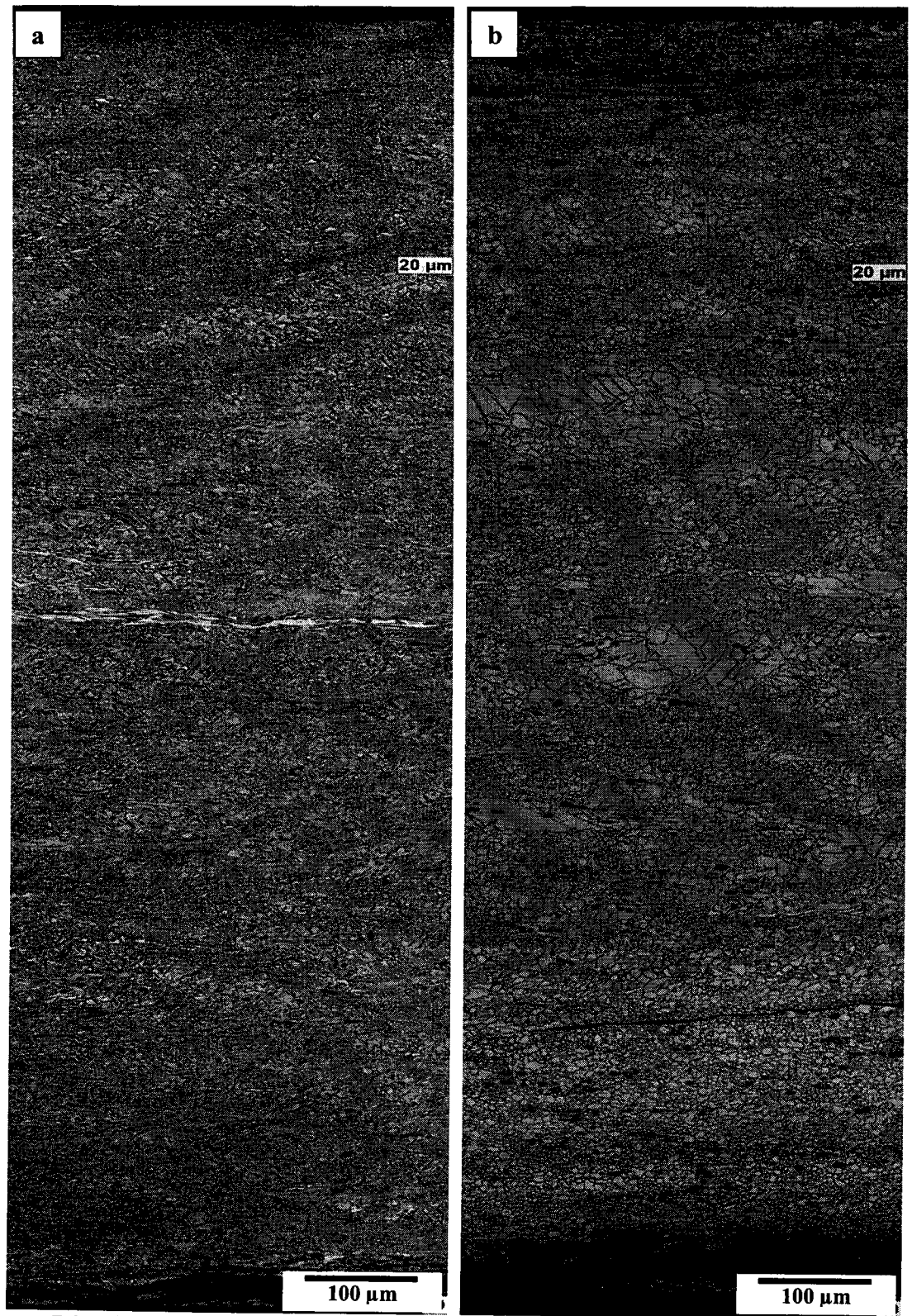


Figure 7.3 Microstructure of as-rolled sheets for AZ31 alloy: a) rolled at 300 °C, 20% reduction per pass, b) rolled at 400 °C, 30% reduction per pass

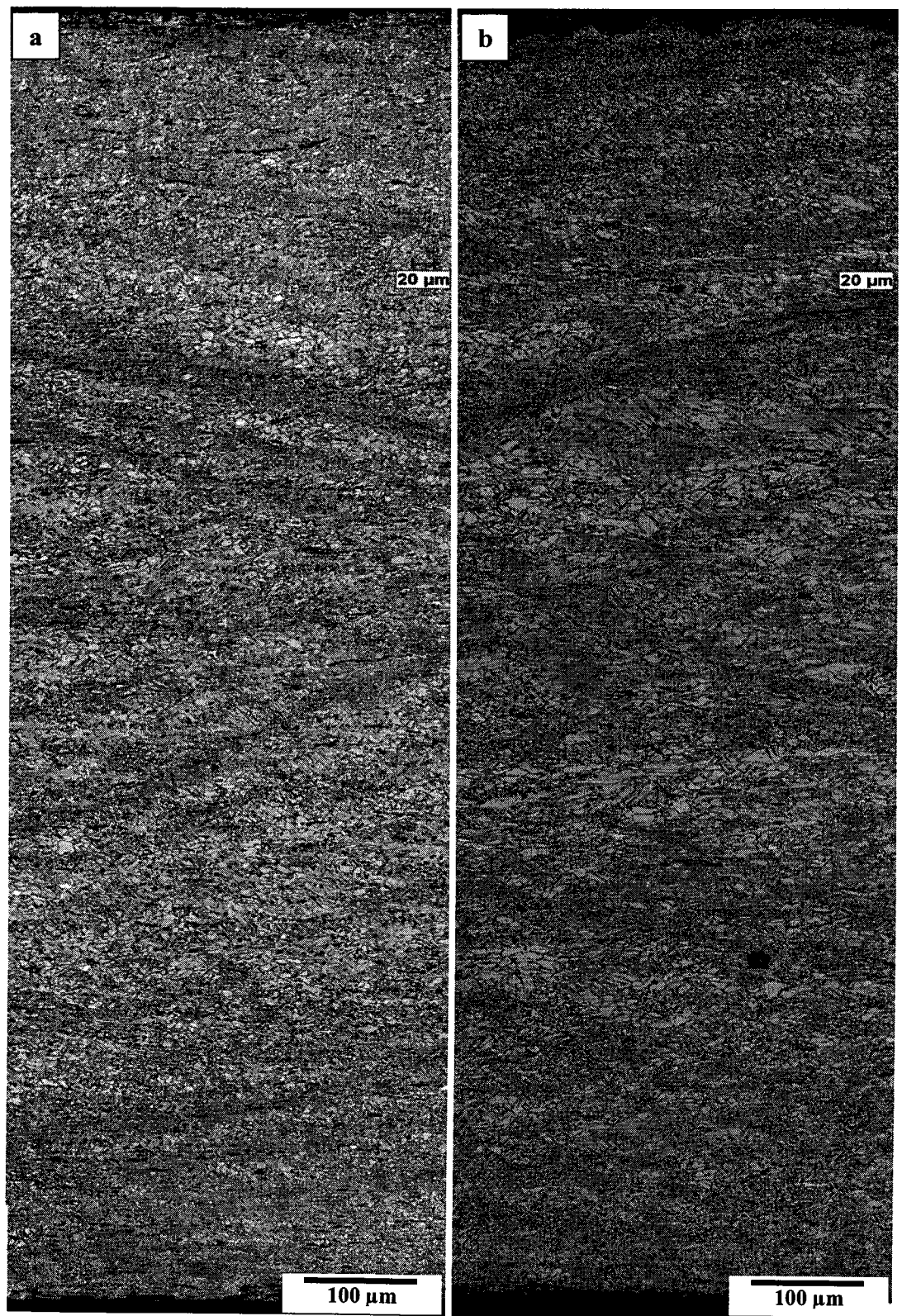


Figure 7.4 Microstructure of as-rolled sheets for AZ31 with Ca alloy: a) rolled at 300 °C, 20% reduction per pass, b) rolled at 400 °C, 30% reduction per pass

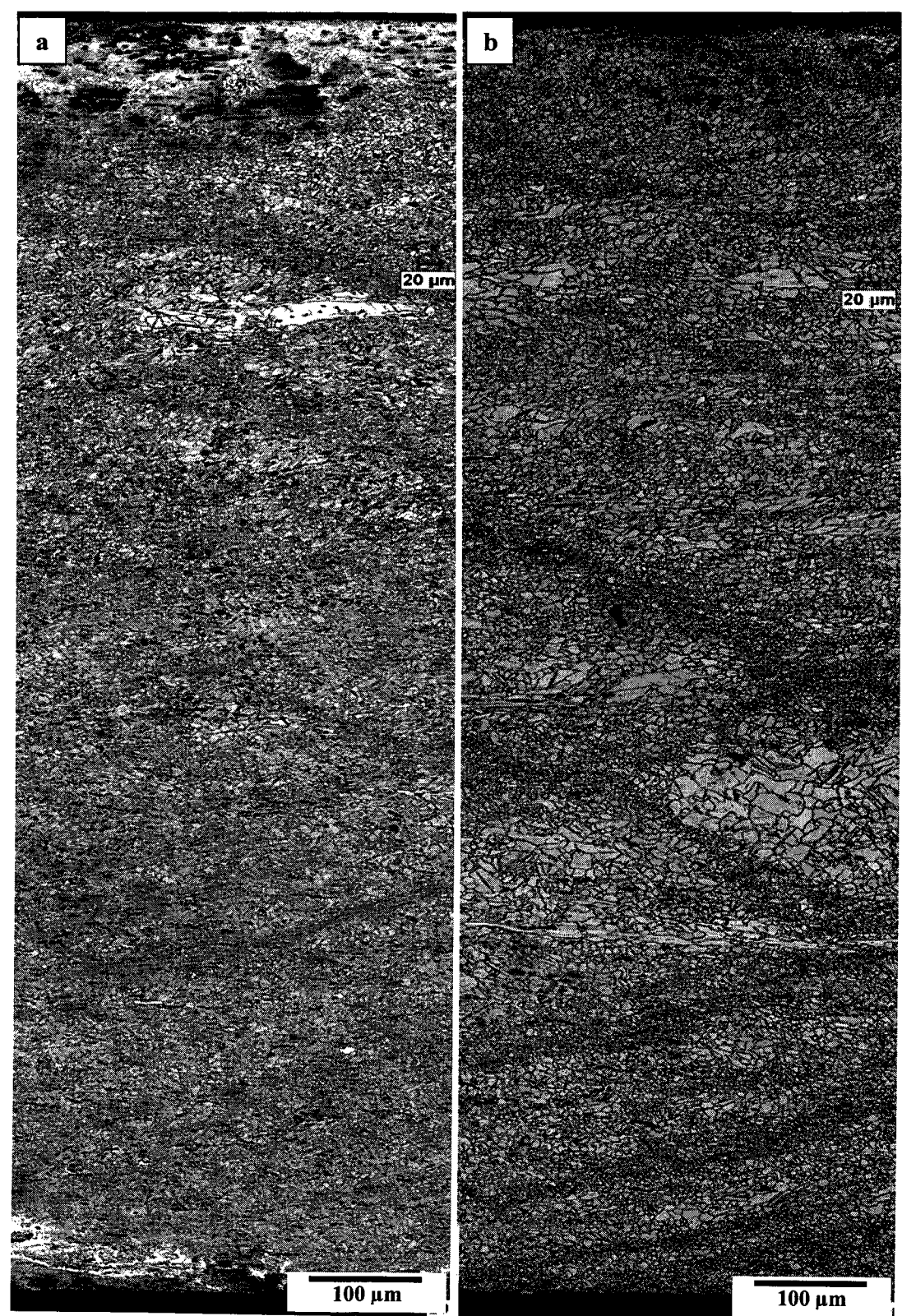


Figure 7.5 Microstructure of as-rolled sheets for AZ31 with Ce alloy: a) rolled at 300 °C, 20% reduction per pass, b) rolled at 400 °C, 30% reduction per pass

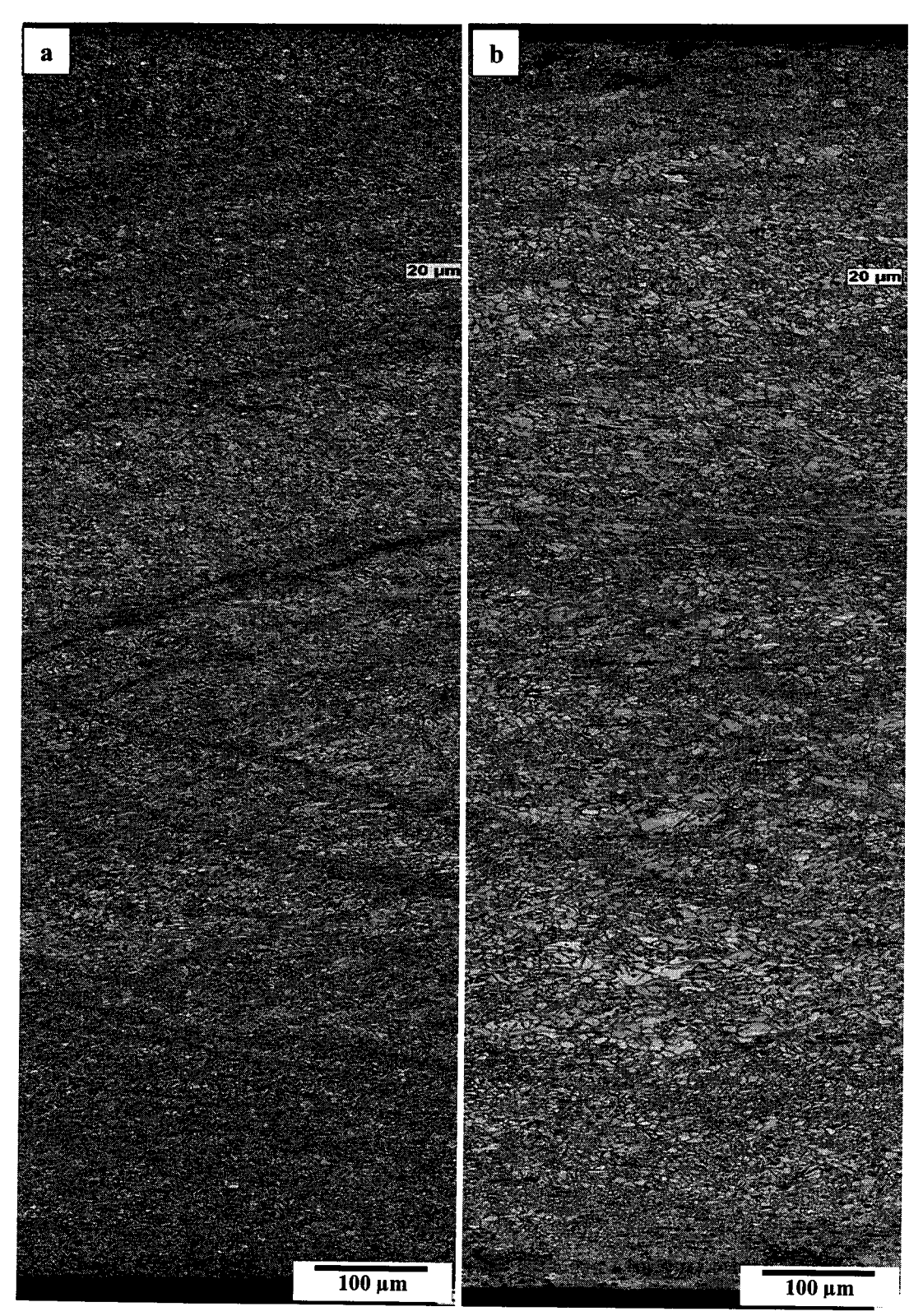


Figure 7.6 Microstructure of as-rolled sheets for AZ31 with Ca and Ce alloy: a) rolled at 300 °C, 20% reduction per pass, b) rolled at 400 °C, 30% reduction per pass

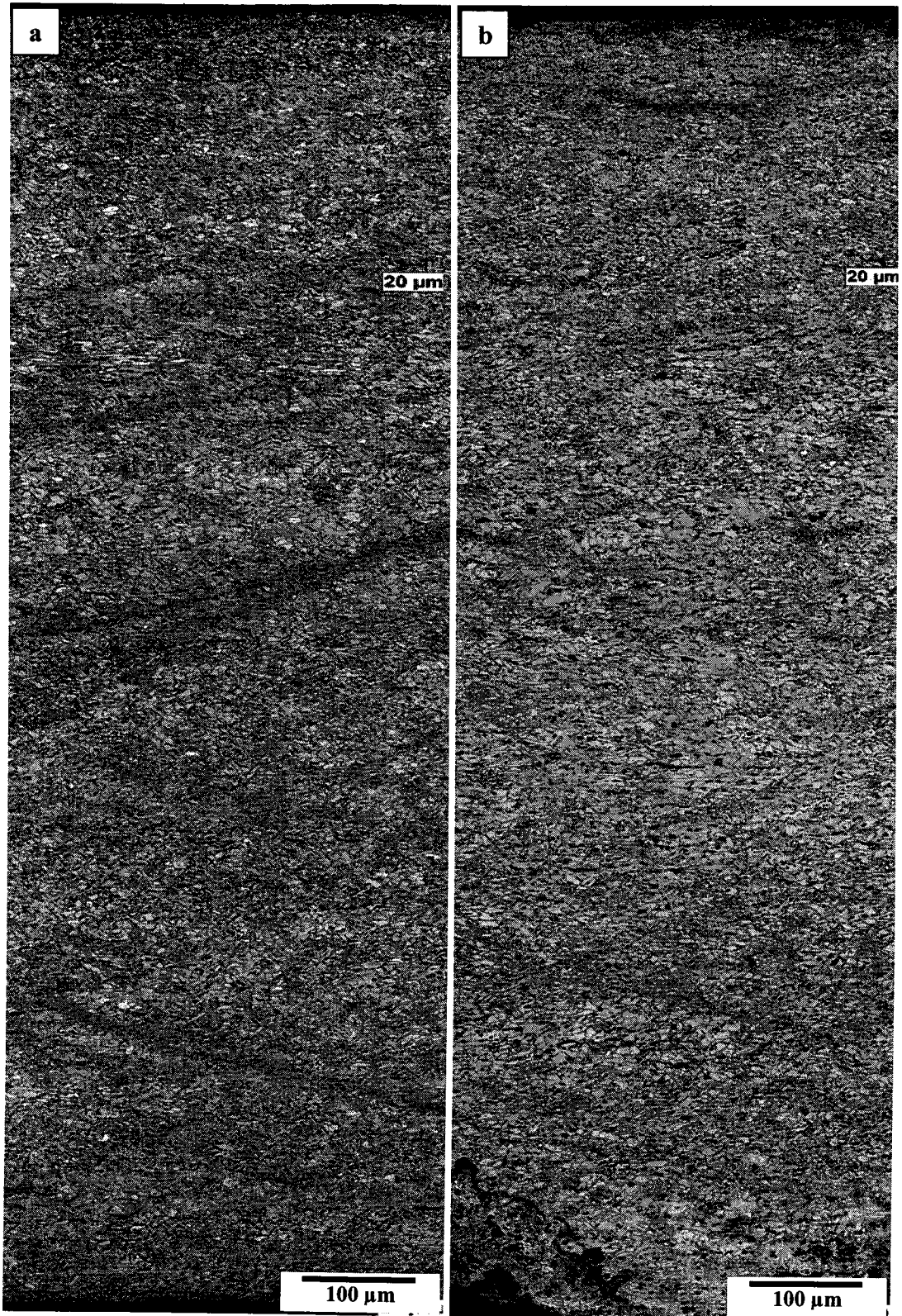


Figure 7.7 Microstructure of as-rolled sheets for AZ31 with Ca and Sr and Ce alloy: a) rolled at 300 °C, 20% reduction per pass, b) rolled at 400 °C, 30% reduction per pass

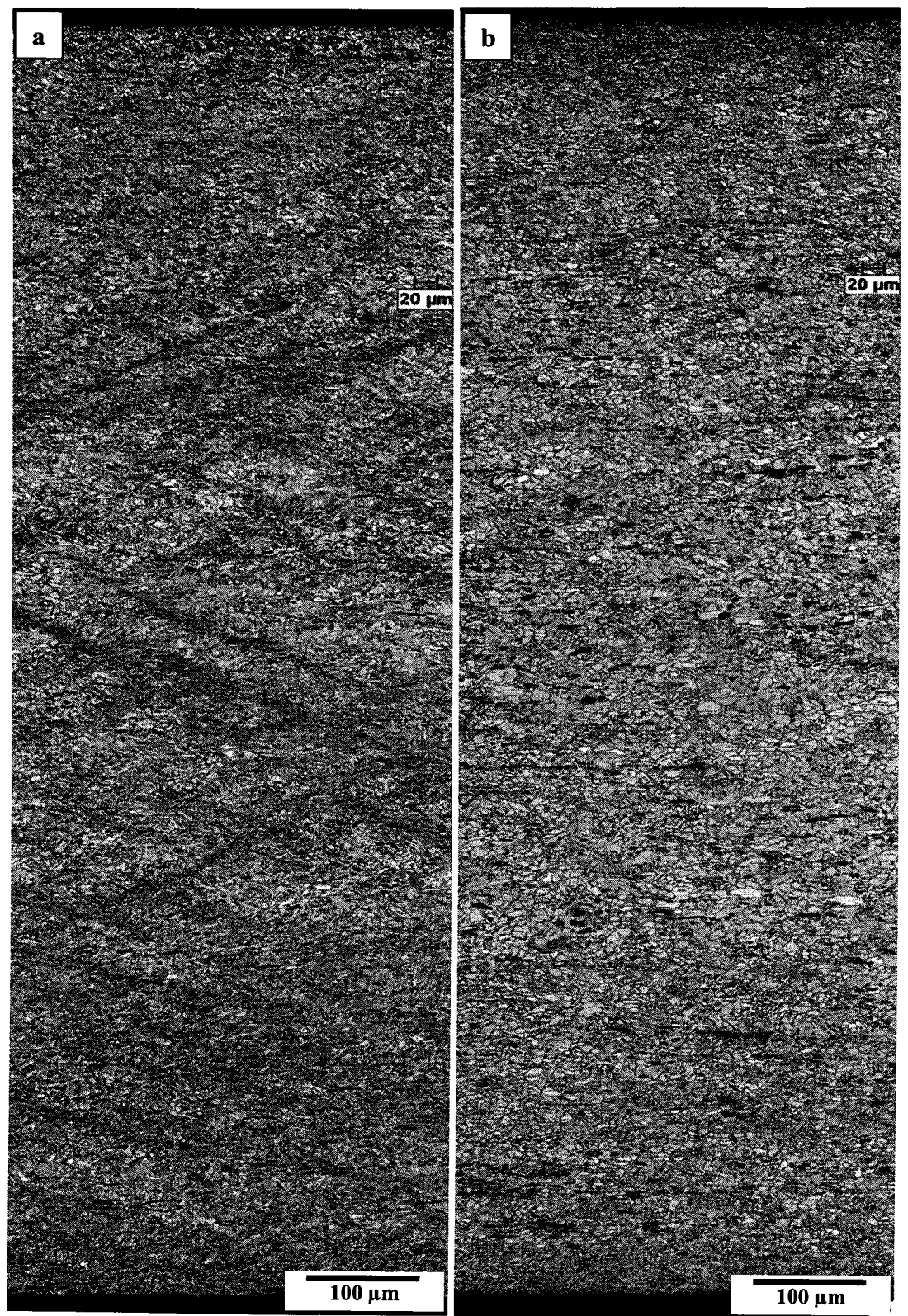


Figure 7.8 Microstructure of as-rolled sheets for AZ31 with Ca and Sr alloy: a) rolled at 300 °C, 20% reduction per pass, b) rolled at 400 °C, 30% reduction per pass

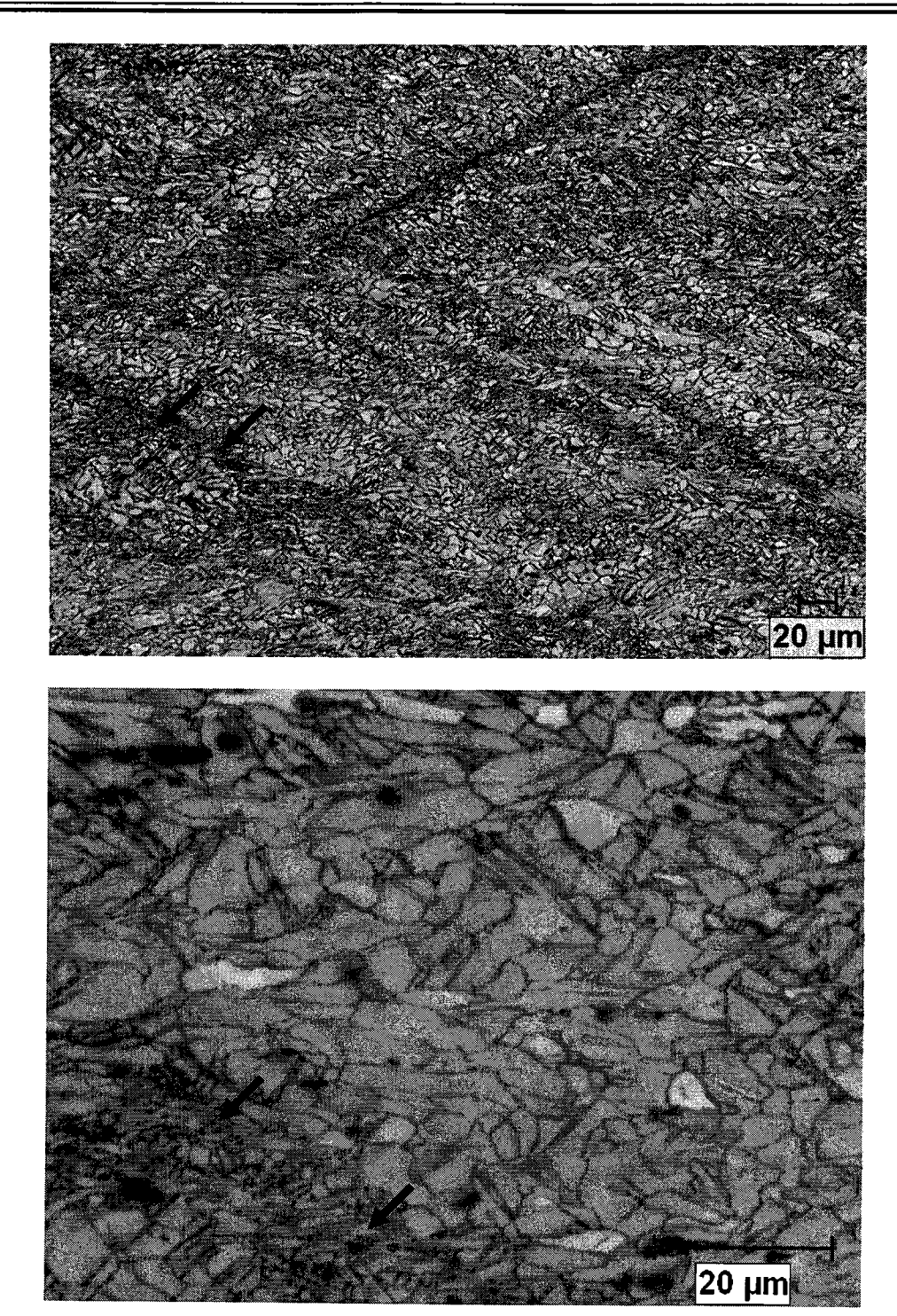


Figure 7.9 Deformation bands for AZ31 with Ca and Sr rolled at 300 $^{\circ}\!\text{C}$ and 20% reduction per pass

7.1.4 As-Annealed Microstructure

A series of annealing treatments for all alloys after the two rolling conditions was performed in a resistance furnace at temperatures of 300 °C, 400 °C, and 450 °C for 10 minutes. This simulated the thermal history at the start of the elevated temperature forming procedure. Thus, these microstructures are the ones that would be subsequently formed at elevated temperatures. Figures 7.10-7.12 present the typical microstructures for as-annealed sheets for AZ31 with additions (Ca, Sr and Ce). Even at 300 °C, recrystallization is noticeable with a much finer average grain size generated. Compared to 300 °C, it is observed that annealing at 400 °C gives a much more uniform grain structure and no deformation bands or coarse grain clusters remain, but the average grain size appears to be a little larger. For sheets rolled at 400 °C and annealed at 450 °C, there appears to be an increasing incidence of coarse grain clusters than for any of the other conditions.

Comparing the 400 °C annealed microalloyed AZ31 with the base AZ31 (Figure 7.13), a more uniform and relatively small grain structure can be seen in the alloy with alloying additions. Again, the as-annealed microstructure demonstrates the same tendency as was shown in as-rolled and as-cast microstructure, i.e. microalloying with Ca and Sr refines and promotes a more uniform grain structure.

7.1.5 Texture Measurement for As-Rolled Sheets

The crystallographic texture for sheets rolled at 300 °C with 20% reduction per pass was measured at the middle thickness areas. Figures 7.14 and 7.15 display the orientation distribution functions (ODF) and (0002) pole figures corresponding to six alloys. At first glance, alloy additions do not affect strongly the basal texture of Mg. Further quantifying the texture intensity by determining the volume fraction of the texture intensity > 3 (Table 7.1), it is found that alloy additions decrease this value of basal texture to a certain degree. The weaker basal texture suggests that microalloyed alloys would have an improved formability, at least at room temperature.

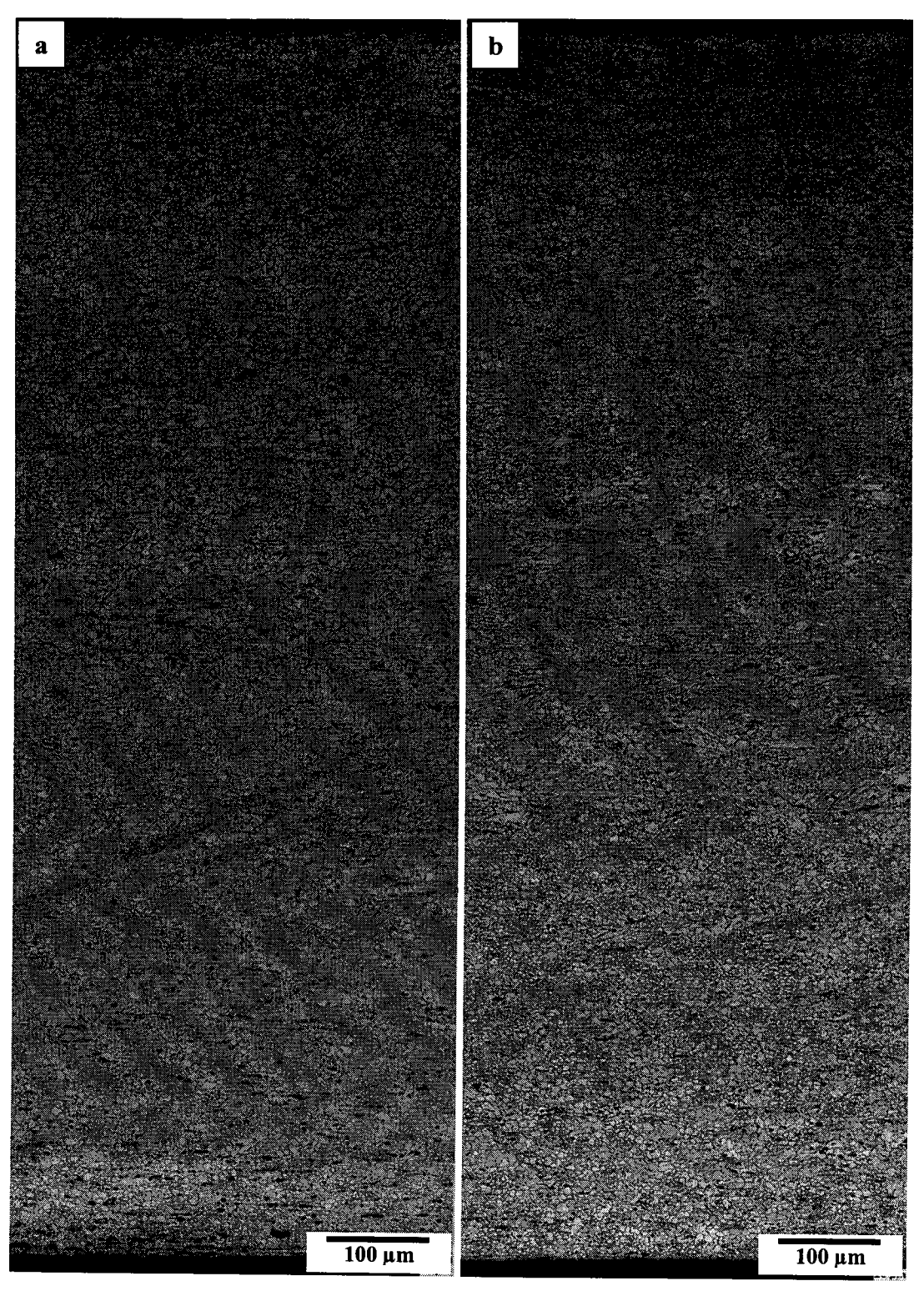


Figure 7.10 Microstructure of as-annealed sheets at 300 °C for 10 minutes for AZ31 with Ca and Sr and Ce alloy: a) rolled at 300 °C, 20% reduction per pass, b) rolled at 400 °C, 30% reduction per pass

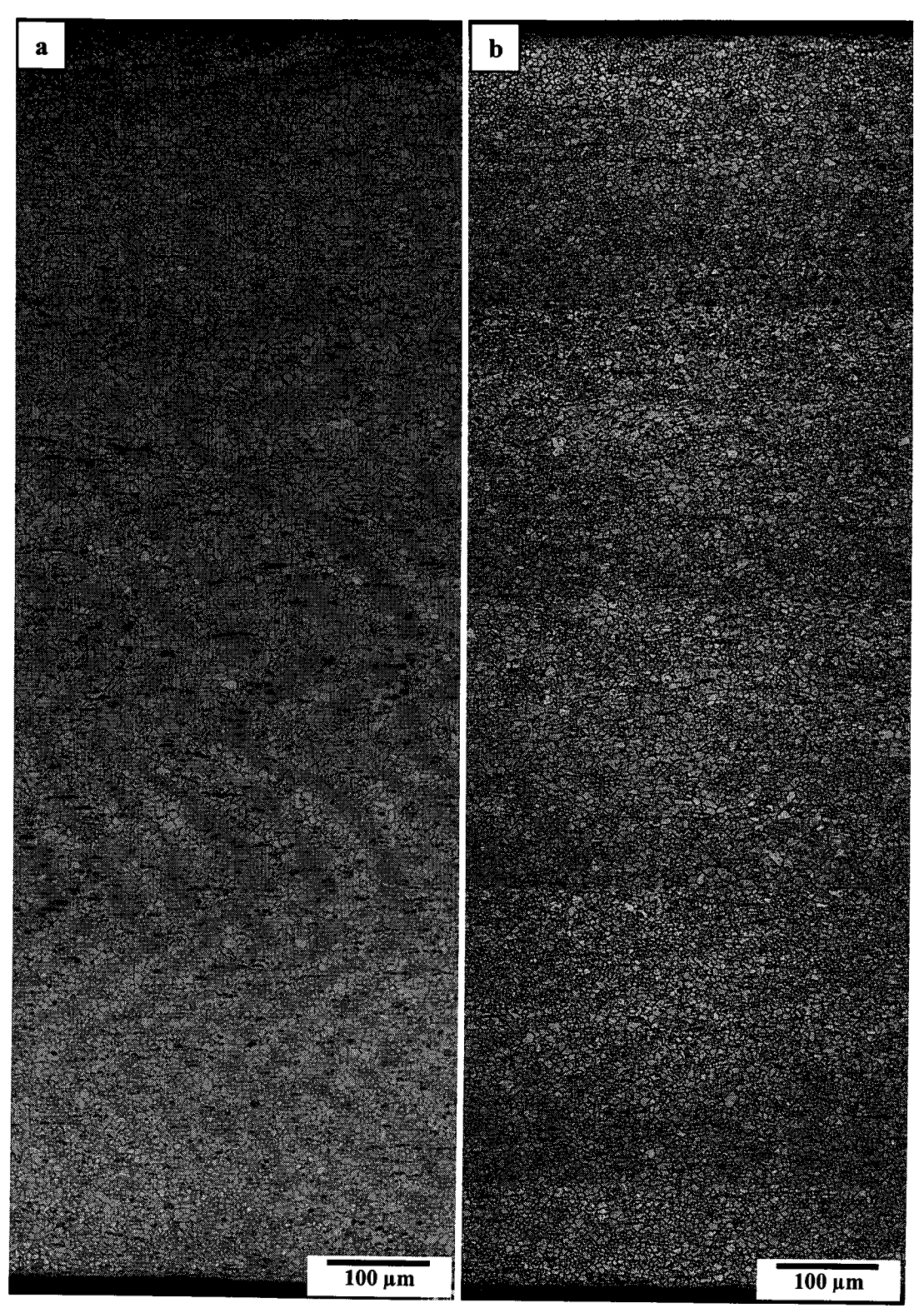


Figure 7.11 Microstructure of as-annealed sheets at 400 °C for 10 minutes for AZ31 with Ca and Sr and Ce alloy: a) rolled at 300 °C, 20% reduction per pass, b) rolled at 400 °C, 30% reduction per pass

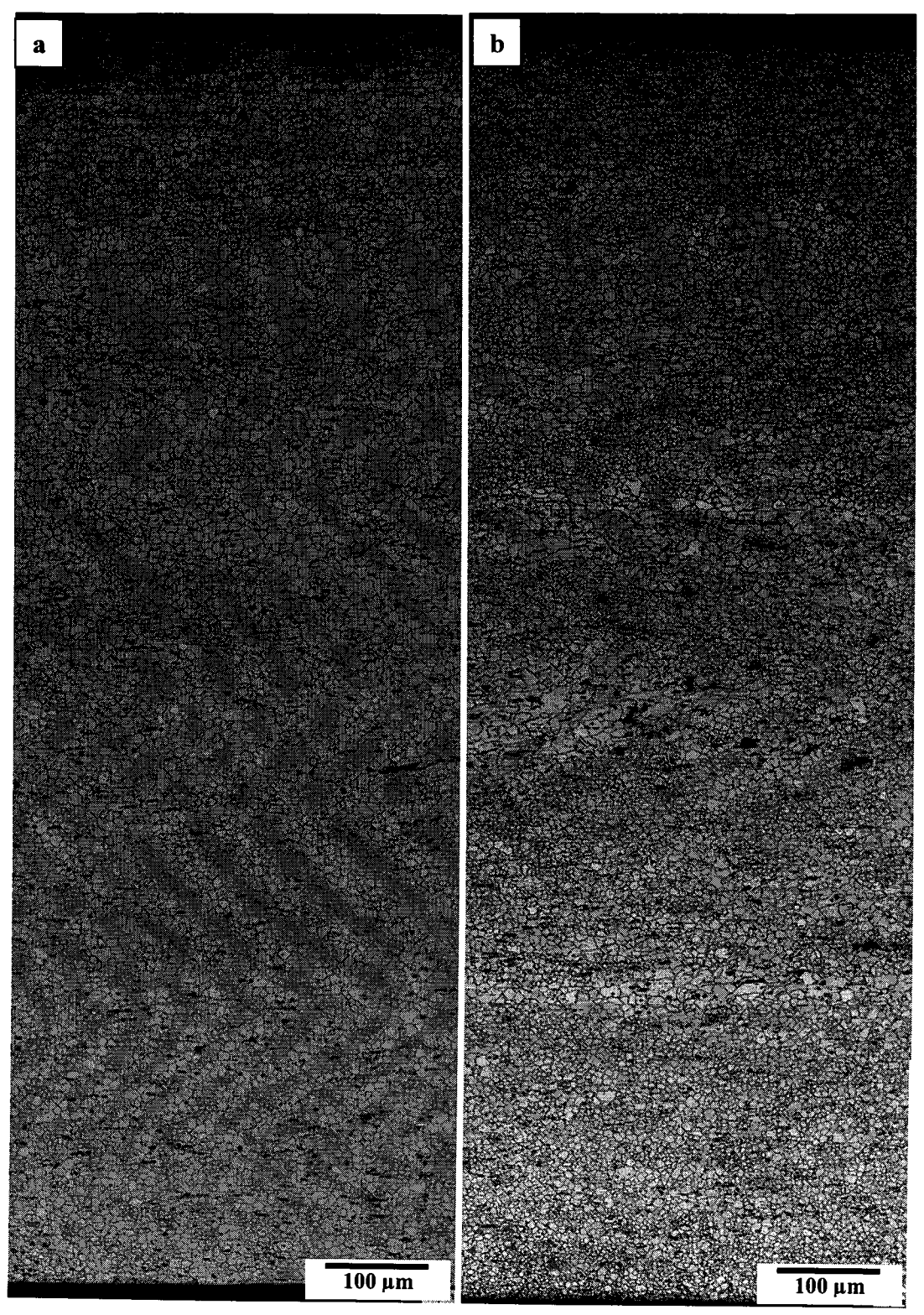


Figure 7.12 Microstructure of as-annealed sheets at 450 °C for 10 minutes for AZ31 with Ca and Sr and Ce alloy: a) rolled at 300 °C, 20% reduction per pass, b) rolled at 400 °C, 30% reduction per pass

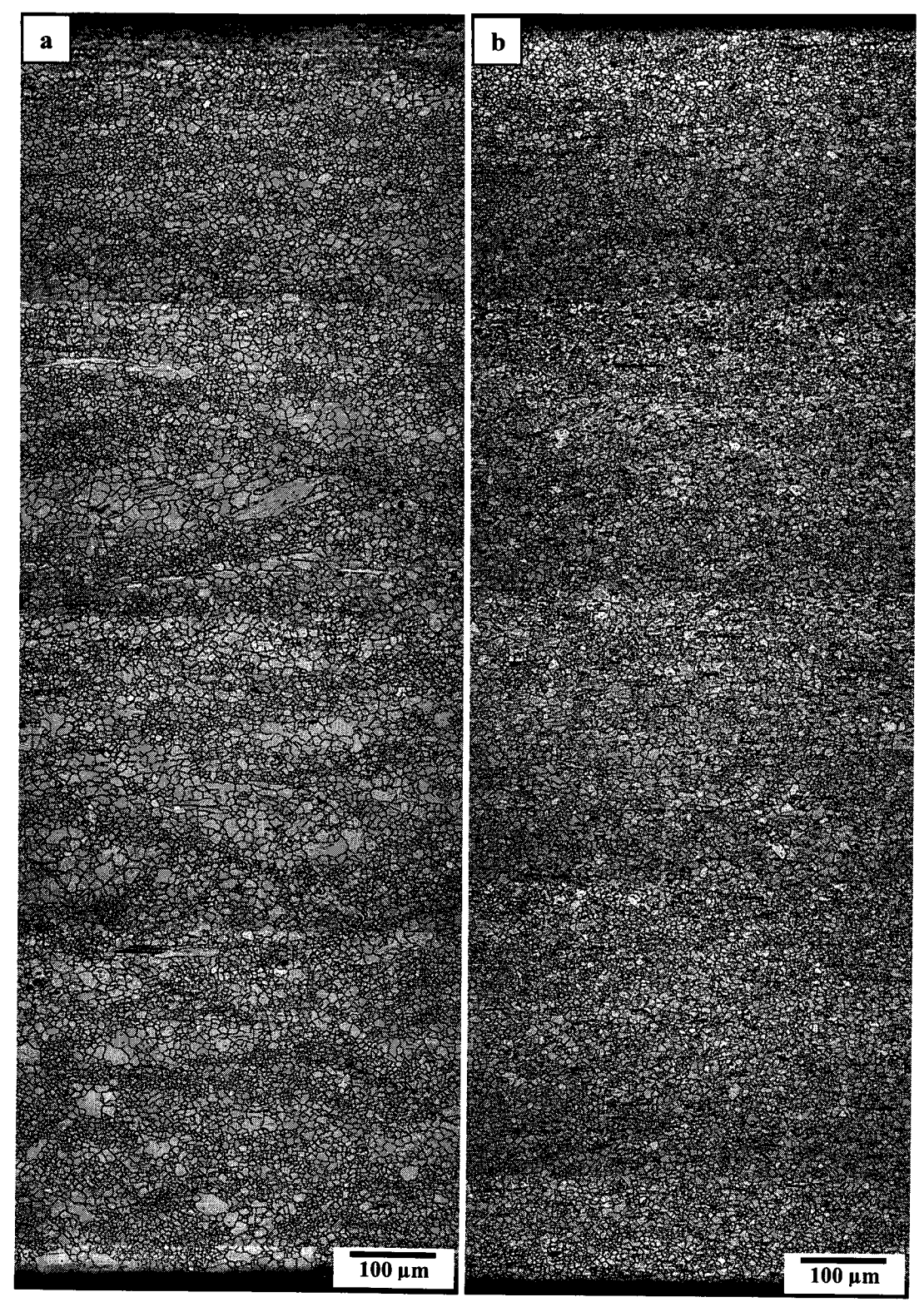


Figure 7.13 Microstructure of as-annealed at 400 °C for 10 minutes for sheets rolled at 400 °C, 30% reduction per pass: a) AZ31, b) AZ31 with Ca and Sr and Ce

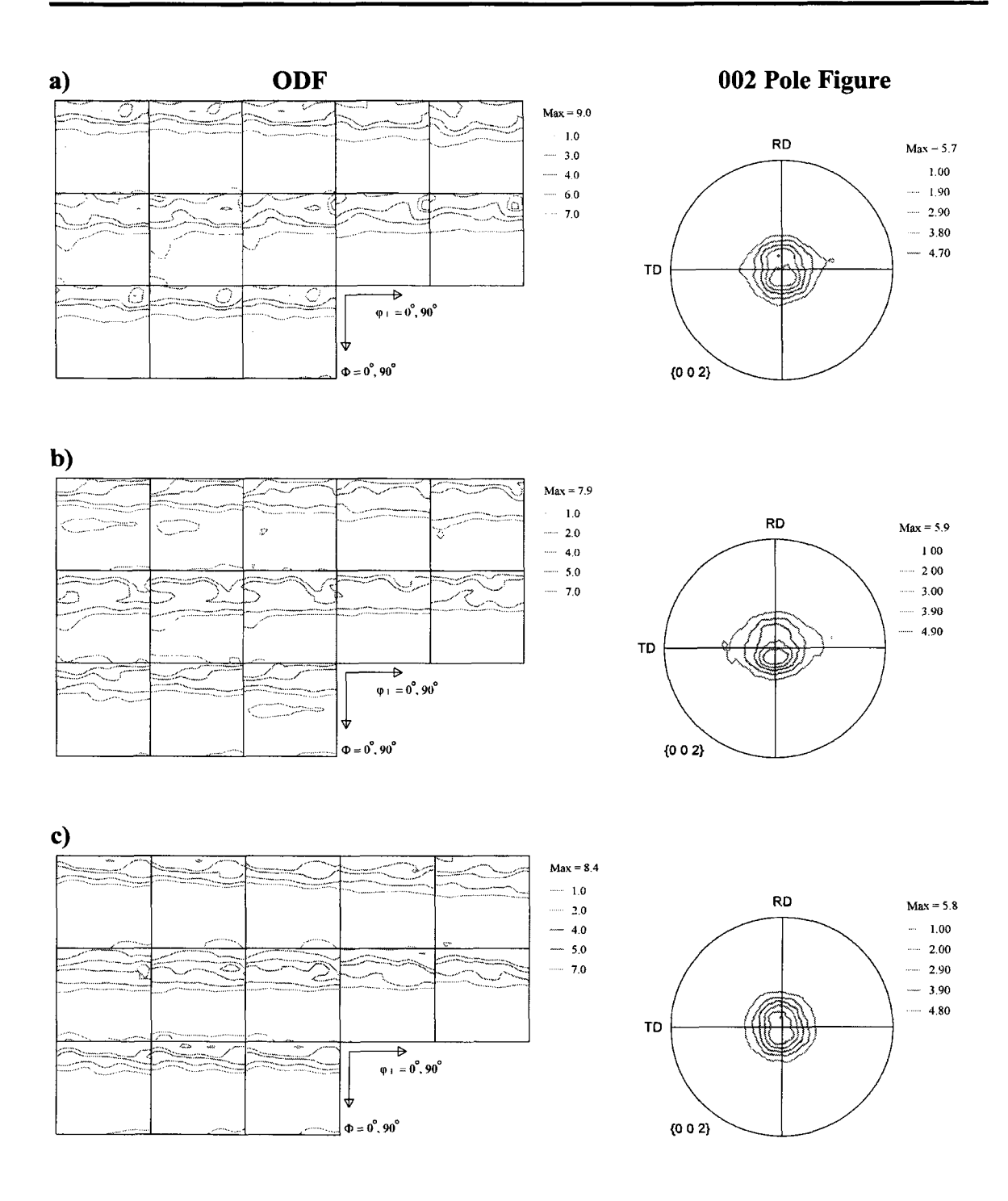


Figure 7.14 Texture measured for sheets rolled at 300 °C with 20% Red. per pass: a) AZ31, b) AZ31 with Ca, c) AZ31 with Ce

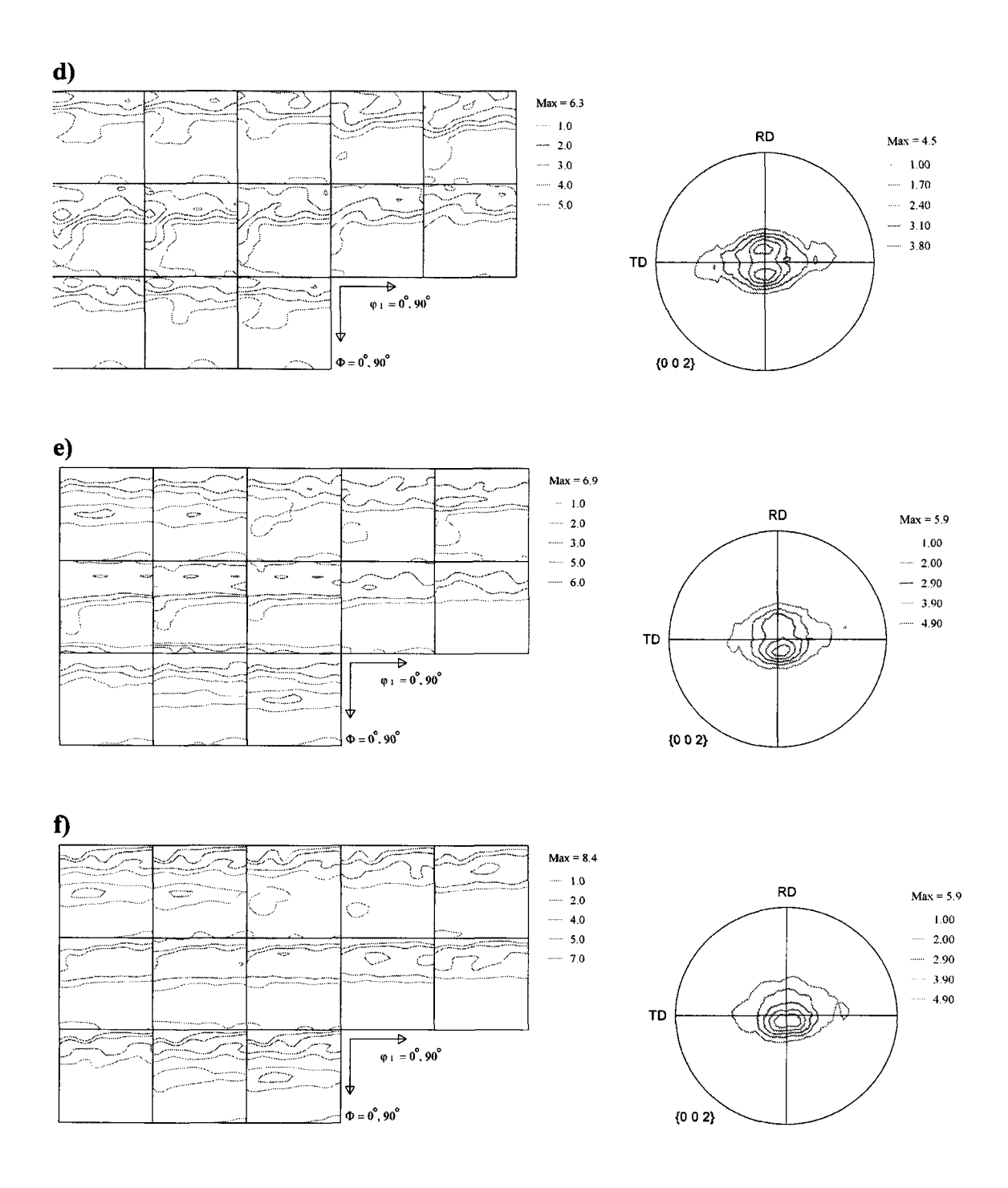


Figure 7.15 Texture measured for sheets rolled at 300 °C with 20% Red. per pass: d) AZ31 with Ca and Ce, e) AZ31 with Ca and Sr, f) AZ31 with Ca and Sr and Ce

Table 7.1 Texture measurement for sheets rolled at 300 °C with 20% Red. per pass

Alloys	AZ31	AZ31 +Ca	AZ31 +Ce	AZ31 +Ca+Ce	AZ31 +Ca+Sr	AZ31 +Ca+Sr+Ce
Volume fraction of texture intensity (%) (>3)	47%	37%	38%	34%	27%	27%
Texture intensity (Max.)	9.0	7.9	8.4	6.3	6.9	8.4

7.2 Discussion

7.2.1 Hot Deformation Mechanisms under Rolling Conditions

Based on the results of compression testing (chapter 6), it was shown that hot deformation mechanisms depend on the testing conditions. Compared with the strain rate used in the compression testing $(0.001 \sim 0.1 \text{ s}^{-1})$, the strain rate in hot rolling is relatively very high, in the approximate range of $5 \sim 20 \text{ s}^{-1}$ (Table 4.5), which is calculated from the equation 7.1 ^[1].

$$\dot{\varepsilon} = (2\pi R(n/60)/\sqrt{(Rh_0)})(\sqrt{r})(1+r/4)$$
 (Equation 7.1)

where:

R: roll radius (m);

n: roll speed (rpm);

h₀: gauge before rolling (m)

h_f: gauge after rolling (m)

r: reduction, r= $(h_0 - h_f)/h_f$

In rolling, the much higher strain rate compared to the compression tests should be conducive to twin formation. However, in the compression tests conducted at 300 °C, and strain rate 0.1s⁻¹, twinning dominated deformation did not lead to extensive recrystallization (Figure 6.17a), whereas in hot rolling, there is extensive recrystallization even at 300 °C. As revealed in Figure 7.16, an intensive operation of twinning and

twinning induced recrystallization plays a role in breaking down the as-cast structure during rolling process. It then appears that increasing strain rates increase the level of recrystallization, but this should be with respect to static recrystallization rather than dynamic, since, theoretically, increasing strain rate increases the critical strain for DRX.

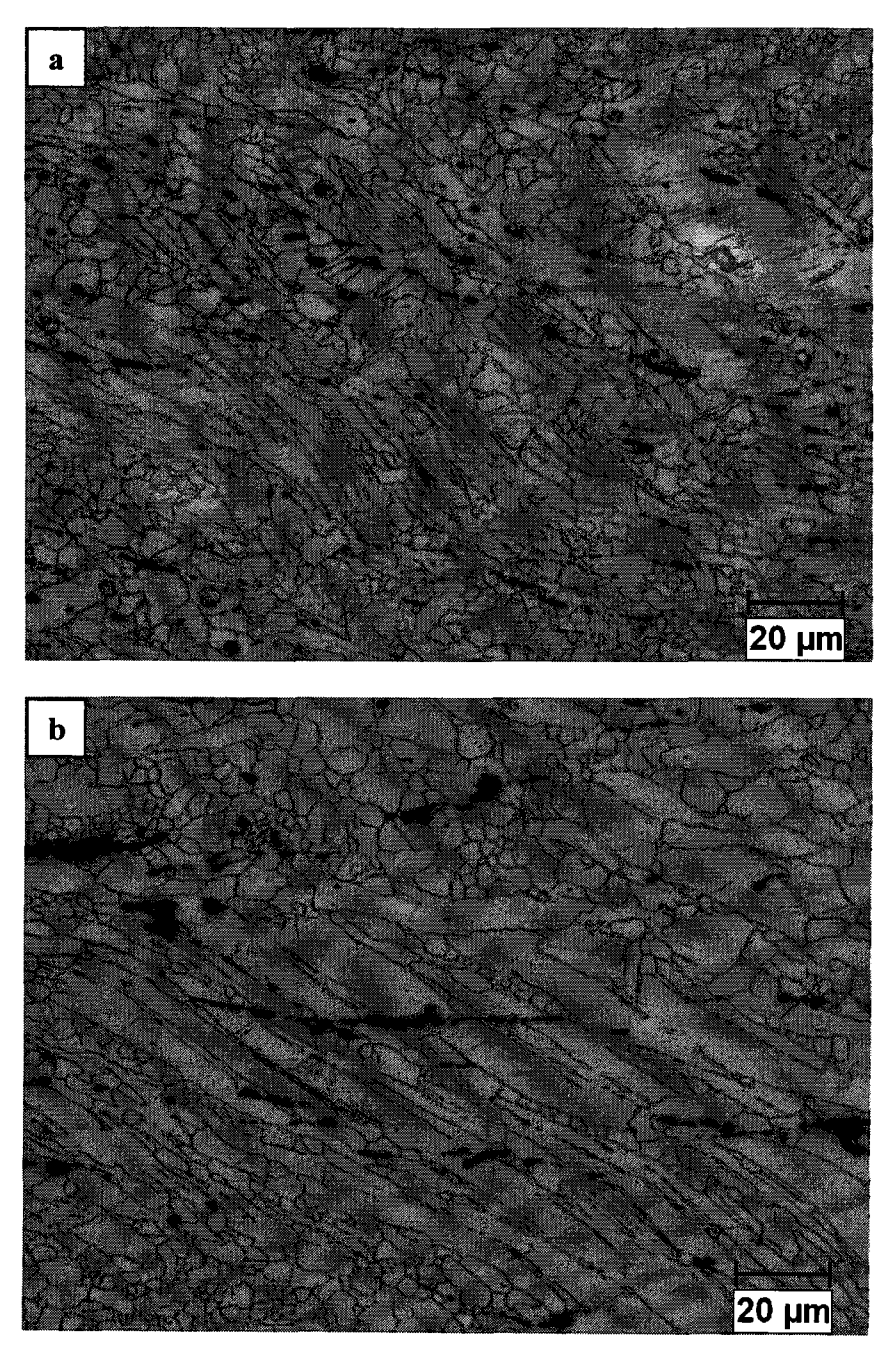


Figure 7.16 Effect of twinning and twinning induced DRX on breaking as-cast structure in AZ31 with Ce sheet rolled: a) at 300 °C and 20% Red. per pass, and b) at 400 °C and 30% Red. per pass.

Recrystallization at the grain boundaries is also a significant mechanism as shown in Figure 7.17. Therefore, at the lower rolling temperature of 300 °C, twinning is much more intensive so that angular grains induced from twinning are presented (Figure 7.18a), and deformation bands consisting of twinning and small DRX-grains (Figure 7.9) are frequently seen. At the higher temperature rolling (400 °C) relatively more equiaxed recrystallized grains are observed grain boundaries, and less recrystallized grains at twins (Figure 7.18b).

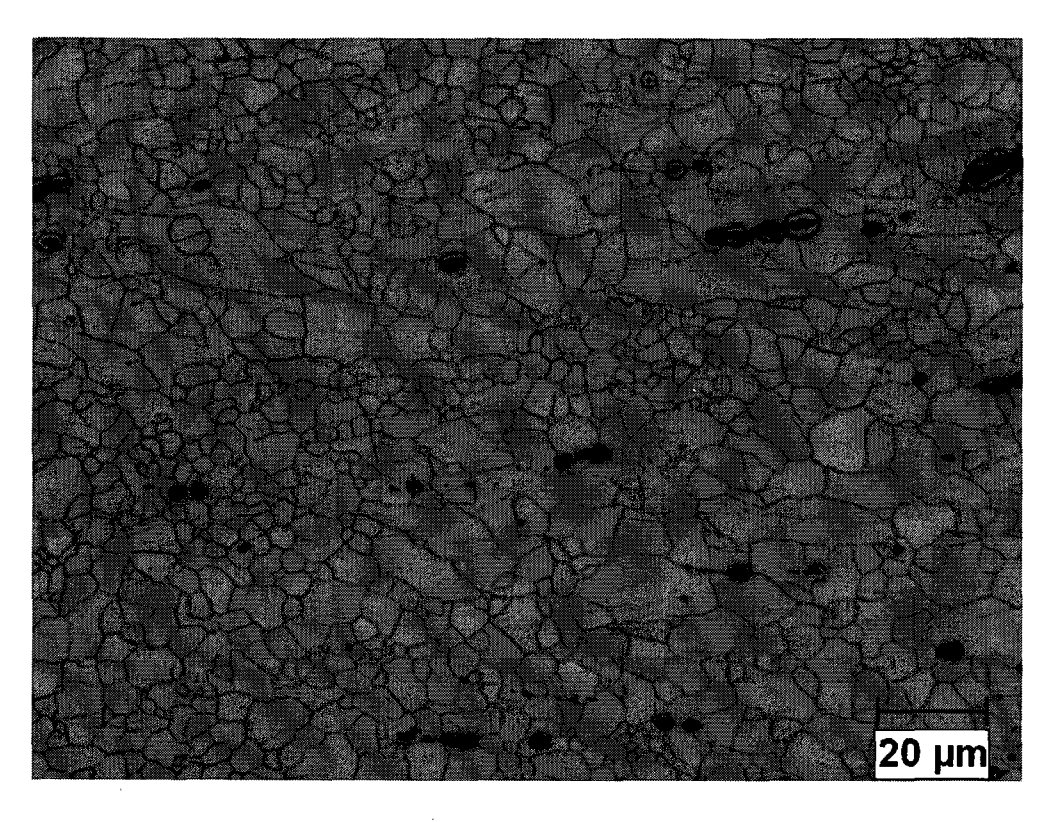


Figure 7.17 DRX grains necklacing at grain boundaries observed in AZ31 sheet rolled at 400 °C and 30% reduction per pass

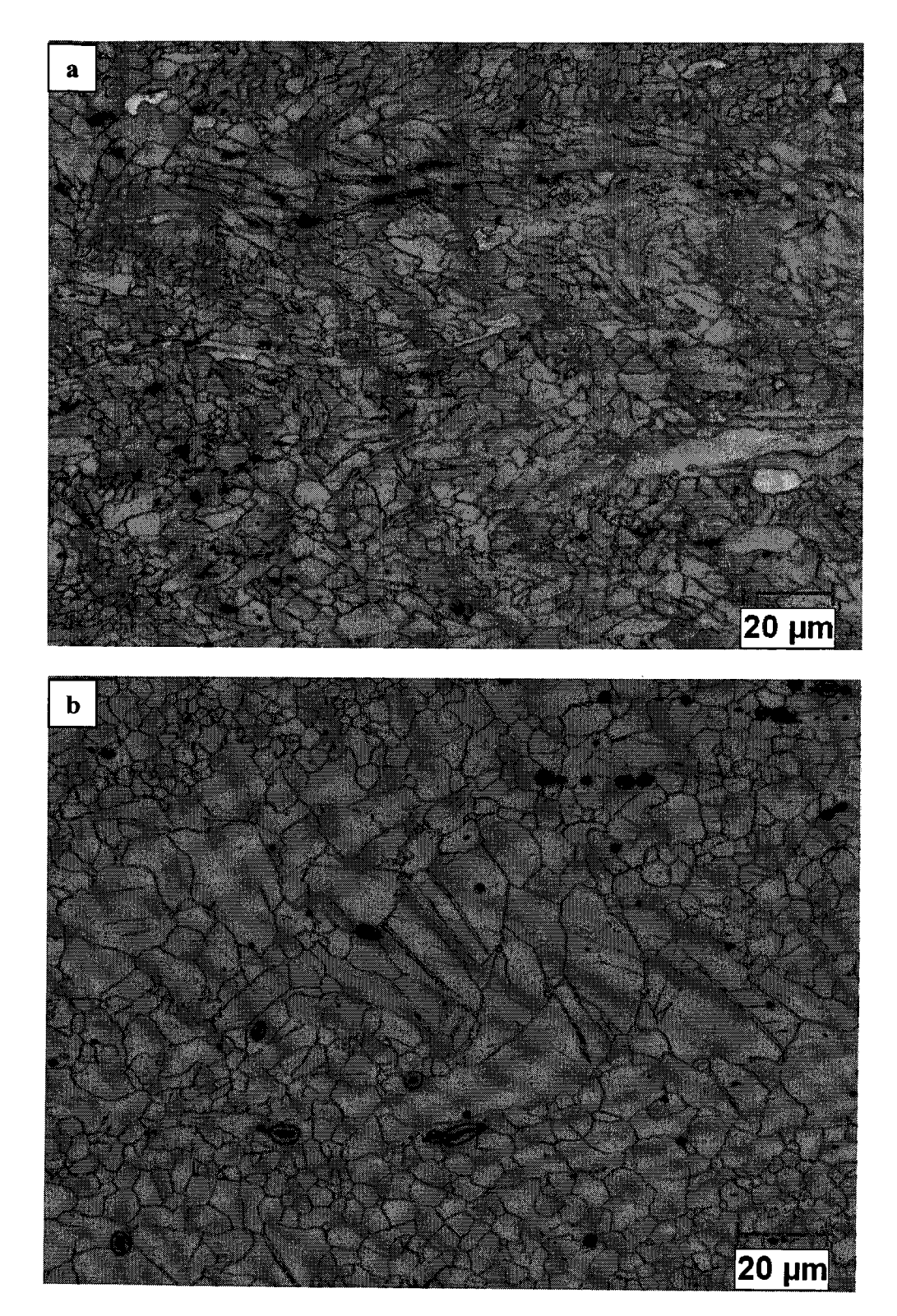


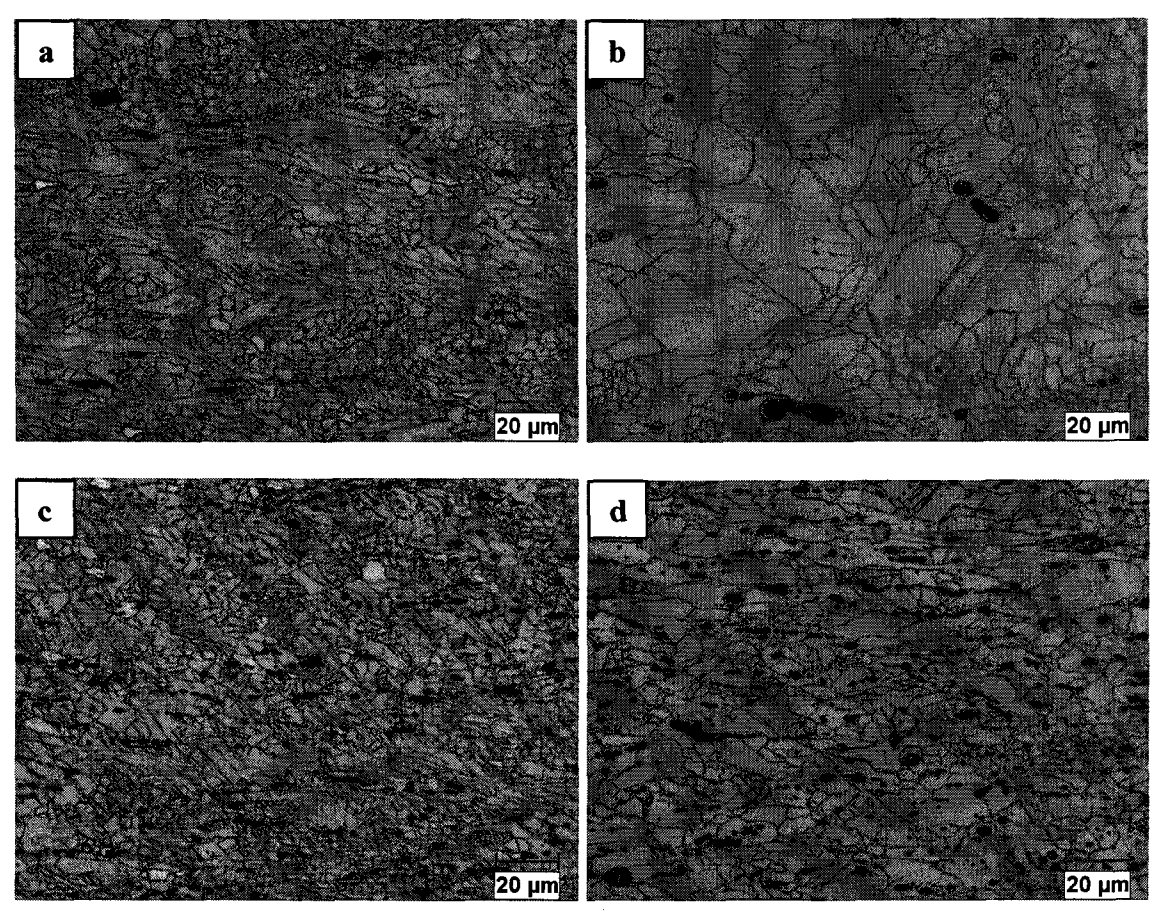
Figure 7.18 As-rolled microstructure in AZ31 sheet: a) rolled at 300 °C with 20% reduction per pass, b) rolled at 400 °C with 30% reduction per pass

Recently, Essadigi et al. [2] studied the microstructural evolution during hot rolling of AZ31 alloy under various conditions: temperatures of 350, 400 and 450 °C, two rolling speeds of 20 and 50 rpm, and two reductions of 15% and 30% per pass. The same mechanisms were found, i.e. the coarse as-cast grain structure is broken down by twin bands, where DRX occurs in these twins and at grain boundaries. In addition, their results of the high strain rate compression testing using a camplastometer for the same AZ31 alloy showed that, with increasing Z, the degree of shear localization increases, along with twinning within the shear bands. This suggests that an optimized rolling condition with both recrystallization of twins and grain boundaries is required to achieve a refined and uniform hot-rolled structure. In this work, at 300 °C there is still a high incidence of shear bands, whereas at 400 °C there are coarse grain clusters in alloys of AZ31 and AZ31 with Ce. Therefore 350 °C may be an optimized temperature for AZ31 alloy for 50 rpm. Clearly, quantification regarding the effect of deformation conditions on twinning and recrystallization is required to design an optimum rolling schedule. All of the previous published work has concentrated on DRX. However, static recrystallization is important for the hot rolling conditions used the work in this thesis, as shown in the twohit compression testing, and also needs to be incorporated in rolling schedule design.

7.2.2 Alloying Effect on Microstructure during Rolling and Annealing

The as-rolled microstructure revealed that additions of Ca and Sr can refine the asrolled grain structure and improve its uniformity, which is more significant at higher
rolling temperatures as seen in Figure 7.19. Same effect is exhibited in as-annealed sheets
as displayed in Figure 7.13. The effect of microalloying could be due to refined as-cast
grain size and the formation of thermally stable second phases by adding these elements.
On the one hand, a smaller initial grain size increases the volume fraction of grain
boundaries, promotes recrystallization during hot rolling, and improves the
microstructural uniformity. On the other hand, more numerous second phase retard the
growth of recrystallized grains during rolling and annealing by the pinning effect of these

particles ^[3], as suggested by the double hit compression test. Therefore, grains in microalloyed AZ31 alloys with Ca or / and Sr present a relatively smaller and uniform structure than AZ31 base alloy. Since Ce does not have an effect on grain refinement, the alloy with Ce still keeps the similar grain structure as base alloy.



7.19 as-rolled microstructure: a) AZ31 rolled at 300 °C with 20% reduction per pass, b) AZ31 rolled at 400 °C with 30% reduction per pass, c) AZ31 with Ca, Sr and Ce rolled at 300 °C with 20% reduction per pass, d) AZ31 with Ca, Sr and Ce rolled at 400 °C with 30% reduction per pass

7.2.3 Alloying Effect on the Texture of AZ31 Based Sheets

In the literature, several experiments on heavily rolled polycrystals containing large particles have shown that the PSN generates either a weak or an approximately random texture [4-8]. It was also found that that the texture of T6 aged WE54 (Mg-5.2%Y-

1.74%Nd-0.95%RE-0.59%Zr) extruded bar is random with no basal plane alignment in the longitudinal direction, under conditions where PSN is the dominant nucleation mechanism responsible for its recrystallization ^[9]. A study ^[10] in texture of some cold rolled Mg alloys showed that Mg-0.2%Ce alloy is considerably more rollable than pure Mg and AZ31 alloy, and a weaker texture persisted until high strains were achieved, although the precise reasons for this are unclear. Recently, the static recrystallized textures for RE-containing Mg alloys of WEK531, WEK111, and WK51, were investigated ^[11]. A remarkable randomization of the texture was observed for all surveyed alloys. Since alloys of WEK111 and WK51 were basically a solid solution at the deformation and annealing temperatures, PSN may not be responsible for the randomization. It seems to be shear band nucleation and an absence of oriented grain growth related to solute drag. Regardless of PSN or other operative mechanisms, all of this indicates that alloying additions leads to the changes in texture of Mg-alloy.

In the present work, the results of texture measurement for AZ31 based sheets by X-ray diffraction reveal that the volume fraction of texture intensity (>3) decreases with adding alloying additions. A more significant effect can be seen in the multiple-alloyed sheets, such as AZ31 with Ca and Sr, and AZ31 with Ca and Sr and Ce. This may be related to the increasing volume fraction of second phase particles increasing PSN. Although twinning induced recrystallization and recrystallization at the grain boundaries are the two main mechanisms during hot rolling, some PSN may occur during rolling, as was revealed in compression testing, which could lead to a change in the deformation texture. Hence, even if the overall basal texture cannot be changed, this weaker texture may improve the formability of AZ31 alloy in some degree, at least at room temperature.

7.3 Summary

• Twinning and twinning induced recrystallization plays a role in breaking up the ascast structure during rolling;

- Twinning induced recrystallization and recrystallization at the grain boundaries are the two main mechanisms responsible for recrystallization under the surveyed conditions;
- Rolling at 300 °C, twinning and twining induced recrystallization is the dominant mechanism. More deformation bands were observed and these bands consist of small recrystallized grains and twins; while at 400 °C rolling, twinning relatively less occurs than rolled at 300°C and recrystallized grains can be seen at twins and grain boundaries, but coarse grained clusters were observed in alloys of AZ31 and AZ31 with Ce. Clearly, quantification regarding the effect of deformation conditions on twinning and recrystallization is required to design an optimum rolling schedule;
- In rolling, the much higher strain rate compared to the compression tests should be conducive to twin formation, and the extensive recrystallization observed at 300 °C is due to static recrystallization. Therefore, static recrystallization also needs to be incorporated in rolling schedule design;
- The alloying additions of Ca and Sr promote a more refined and uniform microstructure in as-rolled and as-annealed sheets. This may be due to the refined as-cast structure and the more numerous second phase particles. Note that the Ce only addition shows no obvious effect on the refinement of the as-cast, as-rolled and as-annealed structures;
- Samples annealed at temperatures of 300 °C, 400 °C, and 450 °C for 10 minutes show that a favourable and uniform microstructure can be obtained at 400 °C;
- Crystallographic texture measurements reveal that microalloying does not change
 the basal texture of Mg, but reduces its intensity, which may contribute to the
 improvement of formability.

References:

- 1. J. M. Alexander and H. Ford, "Simplified Hot-Rolled Calculations", J. Inst. Met., 92, (1964), p 397-404
- E. Essadiqi, M.T. Shehata, A. Javaid, C. Galvani, K. Spencer, S. Yue, and R. Verna, "Microstructure Evolution in AZ31 Mg Alloy during Thermomechanical Processing", Proceedings of the Third International Conference on Light Metals Technology, September 24-26, 2007, Saint-Sauveur, Quebec, Canada, p 177-182
- 3. F.J. Humphreys and M. Hatherly, "Recrystallization and Related Annealing Phenomena", second edition, Oxford, (2004), p 285-309, p 300-301, p 436-441
- 4. G. Wassermann, H. W. Bergmann, and G. Fromeyer, "Textures of Materials", Proc. ICOTOM 5 (2), (eds. G. Gotttstein and G. Wassermann, H.W. Bergnann, and G. Fromeyer, (1978), Springer-Verlag, Berlin, (1978), p 37
- 5. P. Herbst and J. Huber, "Texture of Metallic Materials", eds, Gottstern and Lücke, Springer-Verlag, Berlin, (1978), p 452
- 6. H.M. Chan and F.J. Humphreys, "Effect of particle stimulated nucleation on orientation of recrystallized grains", Metal Science, 18, (1984), p 527–529
- 7. F.J. Humphreys and I. Brough, "Recrystallization and Texture of Al-Si alloys Containing Bimodal Particle Distributions", Proc. Rex'96, the Third International Conference Recrystallization and Related Phenomena, ed. T.R. McNelley, Monterey, California, (1997), p 315-322
- 8. O. Engler, "On the Influence of Dispersoids on the Particle Stimulated Nucleation of Recrystallization", Proc. Rex' 96, Recrystallization and Related Phenomena, ed. T. R. McNelley, Monterey, Califonia, (1997), p 503-510
- 9. E.A. Ball, and P.B. Prangnell, "Tensile Compressive Yield Asymmetries in High Strength Wrought Magnesium Alloys", Scripta Metallurgica et Materialia, 31 (No.2), (1994), p 111-116
- 10. M.R. Barnett, M.D. Nave, and C.J. Bettles, "Deformation microstructures and textures of some cold rolled Mg alloys", Materials Science and Engineering A, 386, (2004), p 205-211
- 11. J.W. Senn and S.R. Agnew, "Texture Randomization of Magnesium Alloys Containing Rare Earth Elements", ", in Proceedings of Magnesium Technology 2008, ed. M.O. Pekguleruz et al., TMS, New Orleans, (2008), p 153-158

Chapter 8

Tensile Testing

8.1 Results

8.1.1 Ambient Temperature Tensile Testing

Room temperature properties of AZ31 based sheet materials were tested after samples had been annealed at 400 °C for 10 minutes. $4 \sim 6$ samples were tested for each alloy under two rolling conditions. The average values are summarized in Tables 8.1 and 8.2. Since no obvious yield points can be seen, the yield strength is defined as the offset stress at 0.002 strain.

In general, the EL% of microalloyed AZ31 alloys is equal or greater than base alloy AZ31, except the alloy with Ca only, which is slightly lower. It is also noted the yield strength is higher for the microalloyed grades, particularly for the specimens rolled at the lower temperature, but there is no significant effect of microalloying on the UTS.

Table 8.1 Mechanical properties at room temperature for AZ31-base sheets rolled at 300°C and 20% reduction per pass, annealed at 400 °C for 10 minutes

Target composition	Plate No.	YS (offset 0.2%)(MPa)	UTS (MPa)	Elongation (%)
AZ31	40-5a	188.95 ± 6.0	276.81 ± 1.3	17.10 ± 2.0
AZ31+0.2%Ca	56-12c	209.60 ± 4.2	275.00 ± 1.7	15.27 ± 1.7
AZ31+0.2%Ce	61-8b	186.47 ± 5.9	271.15 ± 7.8	19.43 ± 3.0
AZ31+0.2%Ca+0.2%Ce	60-25b	207.70 ± 3.5	273.00 ± 1.8	17.03 ± 0.9
AZ31+0.2%Ca+0.2%Sr+0.2%Ce	65-8d	192.36 ± 8.1	261.39 ± 9.2	21.49 ± 1.3
AZ31+0.2%Ca+0.2%Sr	54-8b	216.34 ± 4.5	276.82 ± 3.3	21.13 ± 2.3

Table 8.2 Mechanical properties at room temperature for AZ31-base sheets rolled at 400°C and 30% reduction per pass, annealed at 400 °C for 10 minutes

Target composition	Plate No.	YS (offset 0.2%)(MPa)	UTS (MPa)	Elongation (%)	
AZ31	40-9c	176.92 ± 4.1	276.39 ± 1.0	20.70 ± 2.4	
AZ31+0.2%Ca	56-3a	176.50 ± 2.5	270.94 ± 3.2	18.84 ± 1.1	
AZ31+0.2%Ce	61-2a	178.27 ± 3.5	271.86 ± 3.9	20.30 ± 2.2	
AZ31+0.2%Ca+0.2%Ce	60-1b	190.77 ± 3.2	272.24 ± 3.2	24.74 ± 1.5	
AZ31+0.2%Ca+0.2%Sr+0.2%Ce	65-11a	191.97 ± 3.0	268.53 ± 2.6	19.37 ± 2.1	
AZ31+0.2%Ca+0.2%Sr	54-7c	189.78 ± 5.6	269.32 ± 2.0	20.71 ± 1.5	

8.1.2 Elevated Temperature Tensile Testing

8.1.2.1 Flow Behaviour under Various Conditions

Shape of flow curves

Figures 8.1-8.3 plot the tensile flow curves at three temperatures (300 °C, 400 °C, and 450°C) and four strain rates (0.1s⁻¹, 0.01s⁻¹, 0.001s⁻¹, and 0.0003s⁻¹) for the six alloys rolled at 400 °C with 30% reduction per pass. It is noted that there are three basic shapes of flow curves. Generally, type I curves can be seen at a high Zener-Hollomon parameter (high strain rate and low temperature) with a very short pre UTS region and relatively longer post UTS region (e.g. all curves obtained at strain rates of 0.1s⁻¹ and 0.01s⁻¹). On the contrary, type III curves occur at a low Z conditions (low strain rate and high temperature) with a much longer pre UTS region and a very short post UTS region (e.g. curves in Figure 8.3d). In type II curves, pre and post UTS regions occupy similar strains (e.g. curves in Figure 8.2c, Figure 8.2d and Figure 8.3c); these were observed at an intermediate Z condition. In other words, with decreasing Z value, the shape of flow curves for these alloys changes from type I, type II, to type III and is accompanied by increasing ductility. This suggests a change in deformation mechanisms under different testing conditions. Another observation is that alloying additions slightly increase the flow stress under most test conditions; only at the lowest Z condition (450 °C and 0.0003s⁻¹) is a slight flow stress decrease observed in the pre UTS region (Figure 8.3d).

Elongation vs. testing conditions

Figure 8.4 shows the relationship between EL and testing conditions. It is clearly observed that at the lowest Z condition (450 °C and $0.0003s^{-1}$) the materials have the highest EL (347% ~ 552%), which is in the range of superplastic deformation.

Effect of microalloying on hot tensile flow behaviour

Microalloying additions also show effects on both flow curve shape and the EL except for the alloy microalloyed with Ce only. As shown in Figures 8.1-8.3, for type I curves, microalloying additions generally increase the region of post UTS region, while for type III curves, they increase the pre UTS region. Regardless of the testing conditions,

ductility was improved. At a low Z (450 °C and strain rate of 0.0003 s⁻¹), The EL was improved by 17% with Ca only, 26% with Ca and Ce, 51% with Ca and Sr, and 59% with Ca, Sr and Ce, i.e. multiple alloying has a stronger effect.

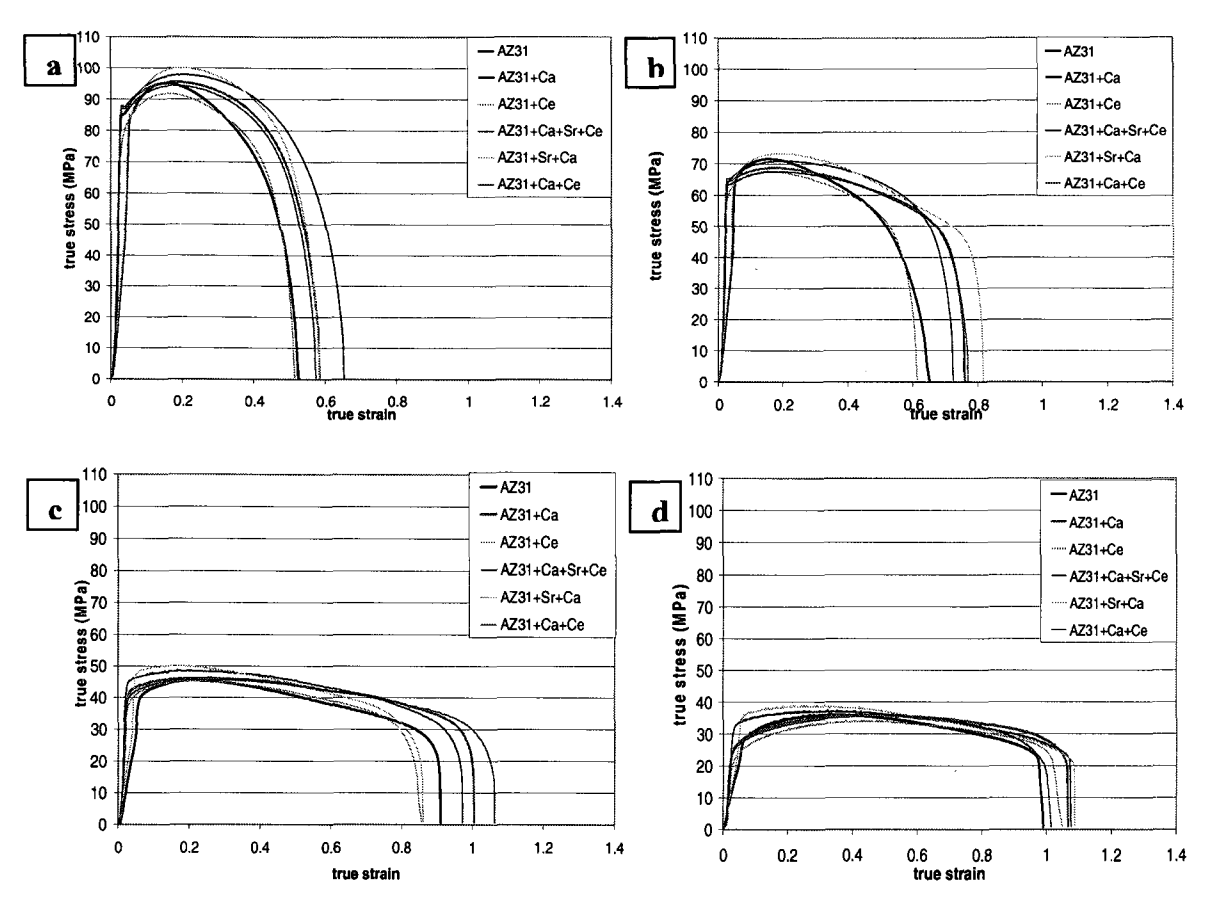


Figure 8.1 Tensile flow curves tested at 300 °C, and strain rates: a) &=0.1s⁻¹; b) &=0.01s⁻¹; c) &=0.001s⁻¹; and d) &=0.0003s⁻¹

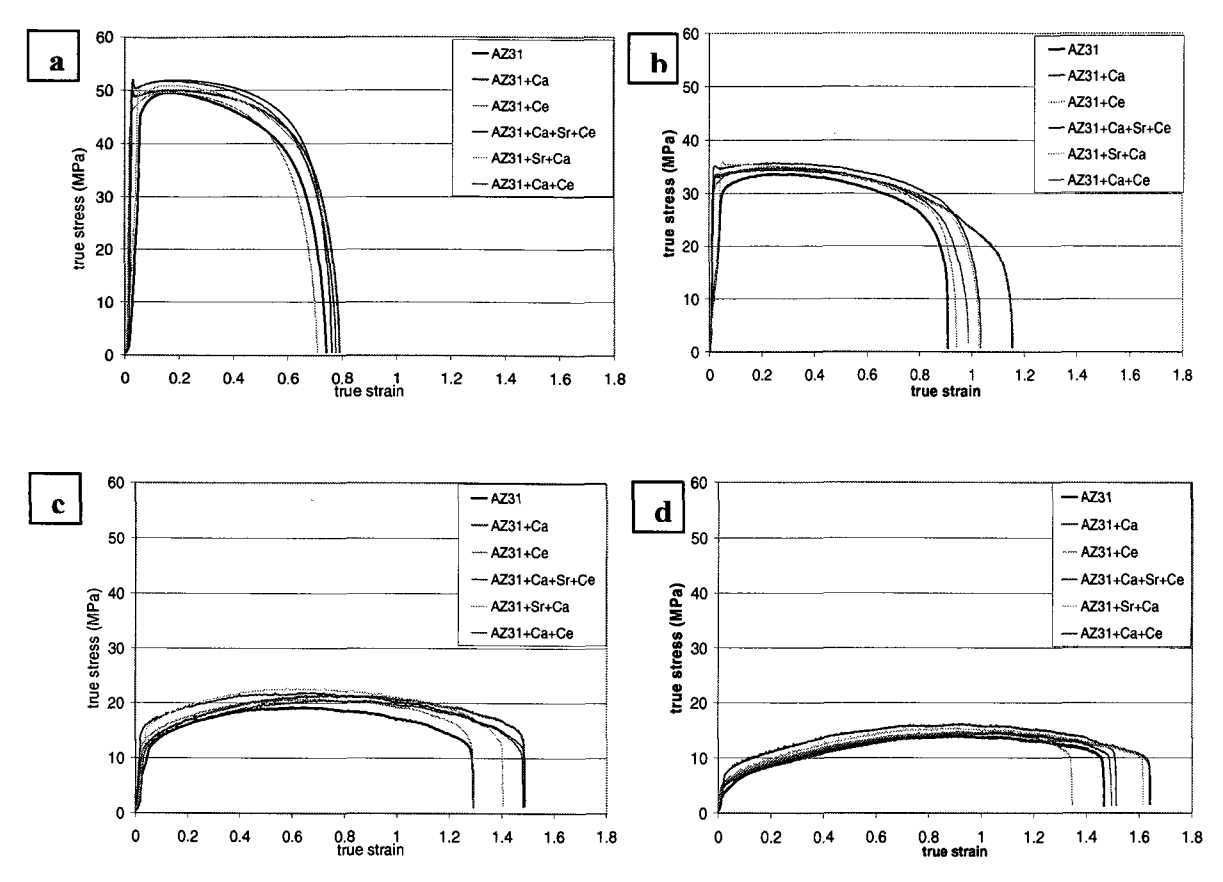


Figure 8.2 Tensile flow curves tested at 400 °C and strain rates: a) $\dot{\epsilon}$ =0.1s⁻¹; b) $\dot{\epsilon}$ =0.01s⁻¹; c) $\dot{\epsilon}$ =0.001s⁻¹; and d) $\dot{\epsilon}$ =0.0003s⁻¹

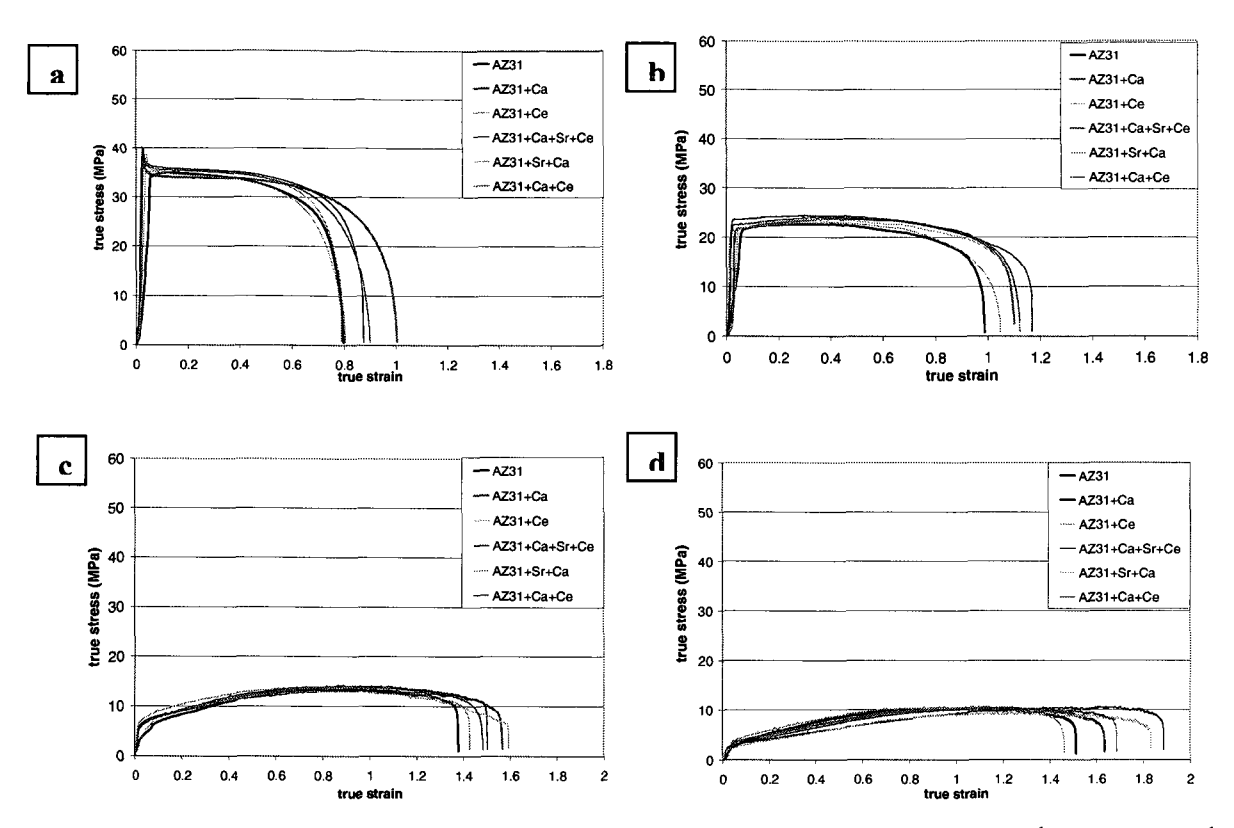


Figure 8.3 Tensile flow curves tested at 450 °C, and strain rates: a) &=0.1s⁻¹; b) &=0.01s⁻¹; c) &=0.001s⁻¹; and d) &=0.0003s⁻¹

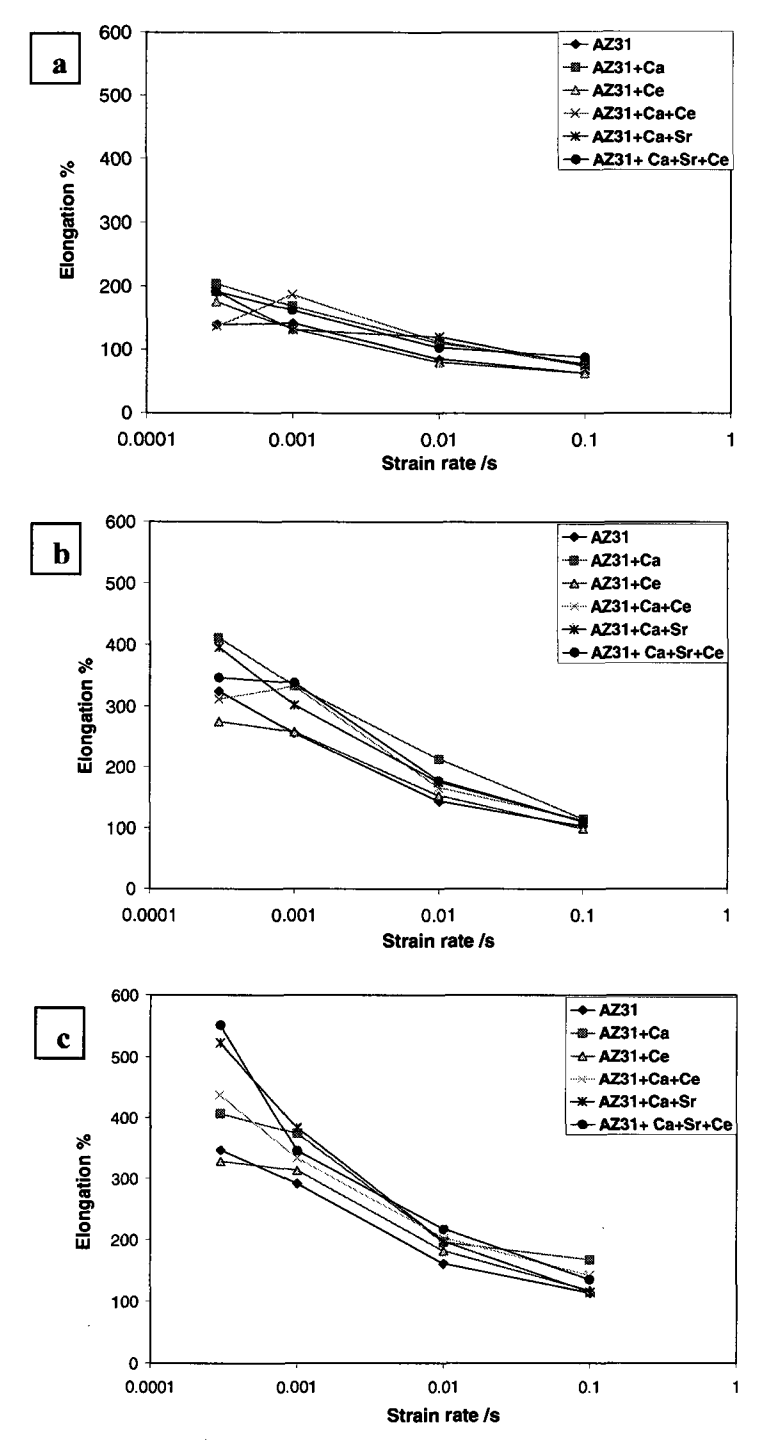


Figure 8.4 Elongation vs. strain rate for sheets tested at strains rates of 0.1, 0.01, 0.001 and $0.0003~{\rm s}^{-1}$, temperatures: a) 300 °C, b) 400 °C, and c) 450°C

8.1.2.2 Fracture Behaviour

Figures 8.5 compares the fracture tips for alloys of AZ31 and microalloyed AZ31 with Ca and Sr and Ce at same temperature of 450 °C and strain rates of 0.1s⁻¹. A brittle failure with flat edge and abnormal grain growth at tip area was observed. Although microalloying does not change the brittle fracture appearance, it plays some role in improving the ductility since it reduces the size of the grains in the crack tip region of abnormal grain growth.

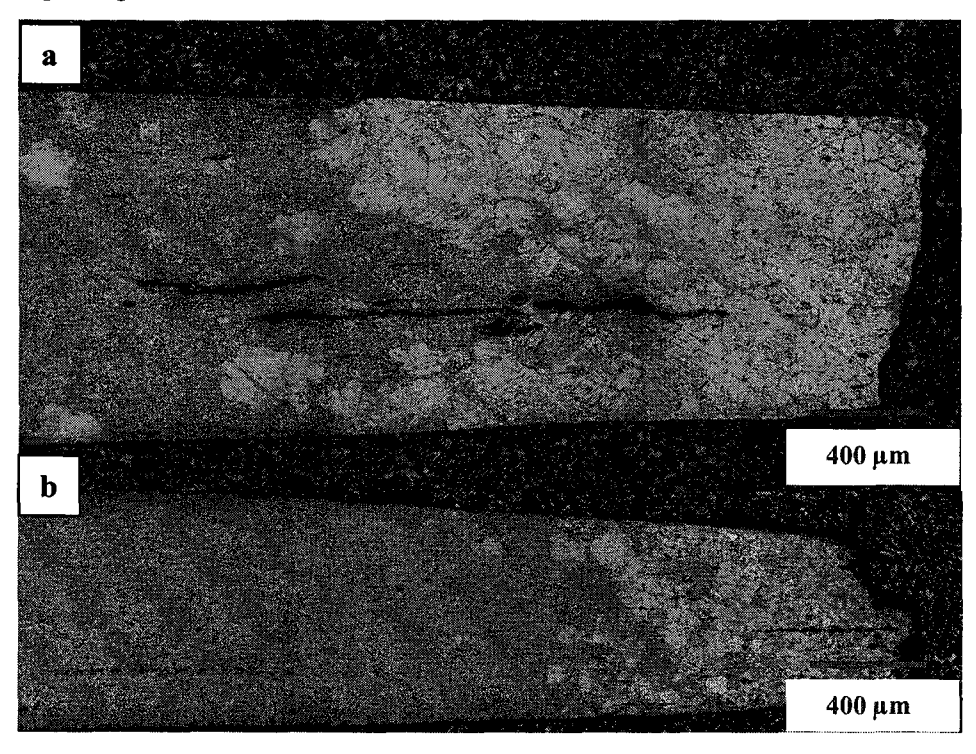


Figure 8.5 Microstructure of tensile fracture tips tested at 450 °C and strain rate of 0.1s⁻¹: a) AZ31, b) AZ31 with Ca and Sr and Ce

A much more ductile fracture with well developed cavitations was observed in Figure 8.6 for samples tested at 450 °C and a low strain rate of 0.0003 s⁻¹. Fibrous fracture tips were clearly shown indicating to different deformation and fracture mechanisms. Moreover, it is found that alloys with alloying additions of Ca, Ca and Ce, Ca and Sr and Ce, and Ca and Sr show more dispersed and discontinuous cavitations, while alloys without additions and with individual Ce show continuous and larger cavitations.

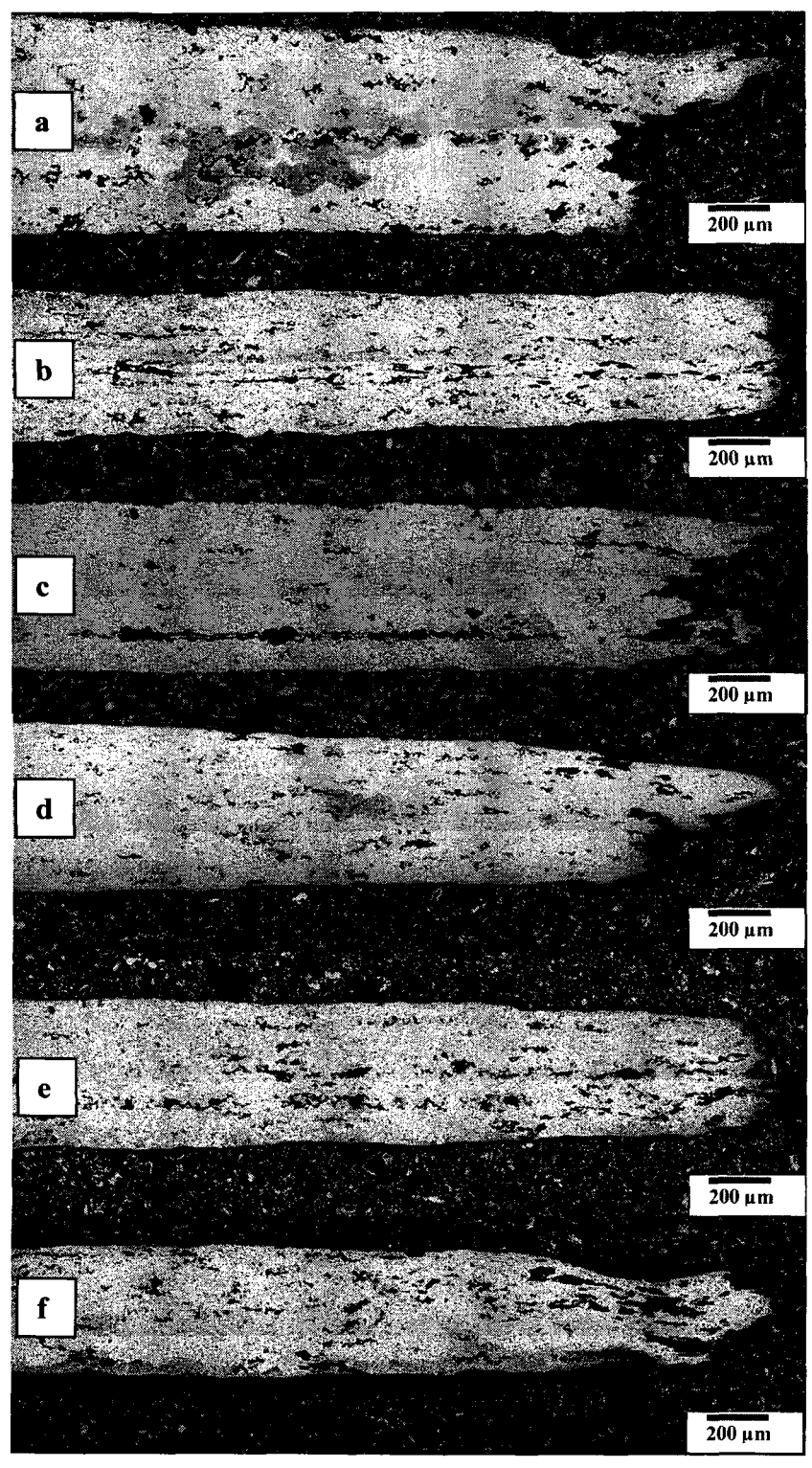


Figure 8.6 Cavitations in tensile fracture tips tested 450 °C, and strain rate of 0.0003s⁻¹: a) AZ31, b) AZ31 with Ca, c) AZ31 with Ce, d) AZ31 with Ca and Ce, e) AZ31 with Ca and Sr and Ce, and f) AZ31 with Ca and Sr

Figure 8.7 also shows coarser grain sizes in AZ31 and AZ31 with Ce, compared to alloys with Ca and Ce, and with Ca and Sr and Ce. The typical dimple feature of ductile fractures was further observed in Figure 8.8. It is revealed again that dimples are finer and more uniformly distributed in microalloyed alloys compared to AZ31 base alloy and the alloy with Ce only. Therefore, alloying additions show some effects on retarding the growth of cavitations.

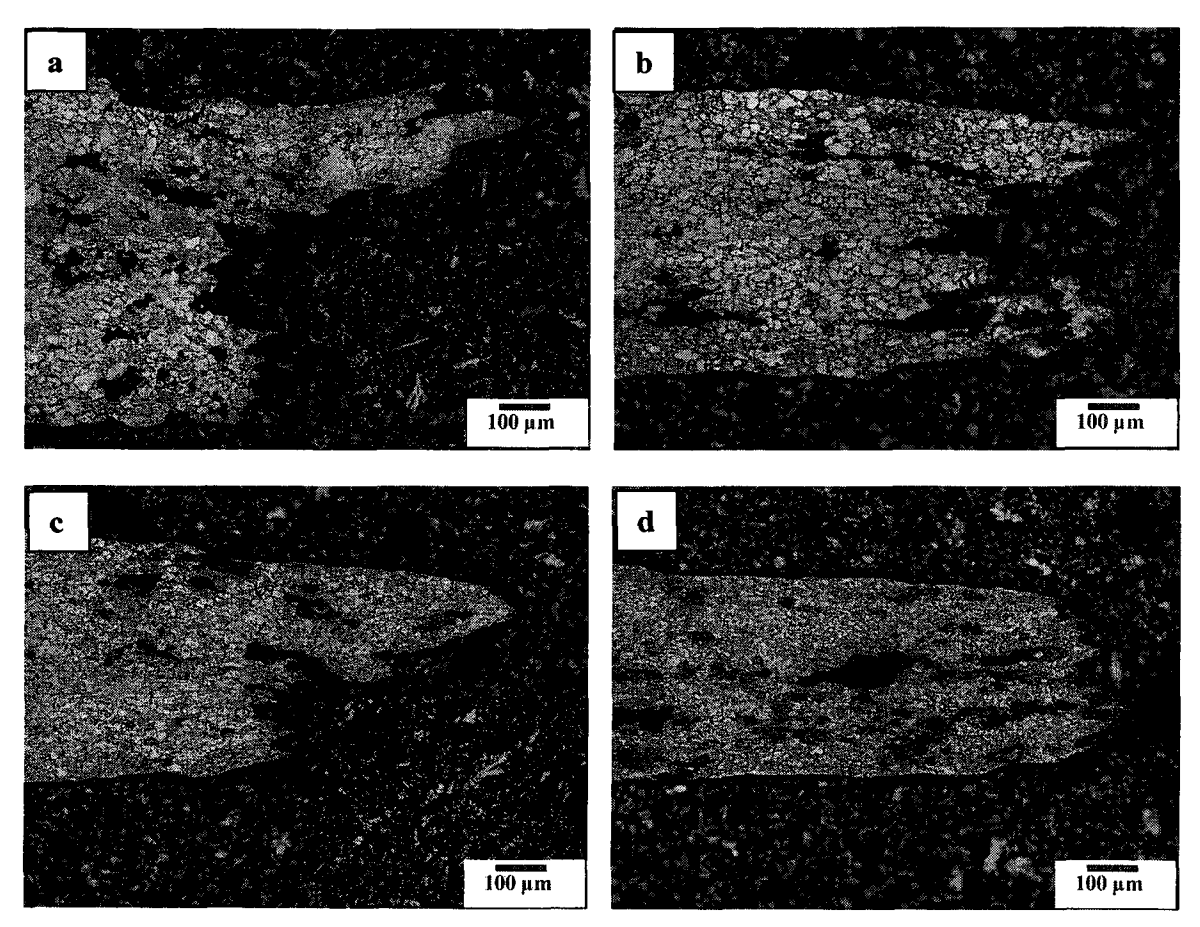


Figure 8.7 Typical optical images for tensile fracture tips tested 450 °C, and strain rate of 0.0003 s^{-1} : a) AZ31, b) AZ31 with Ce, c) AZ31 with Ca and Ce, and d) AZ31 with Ca and Sr and Ce

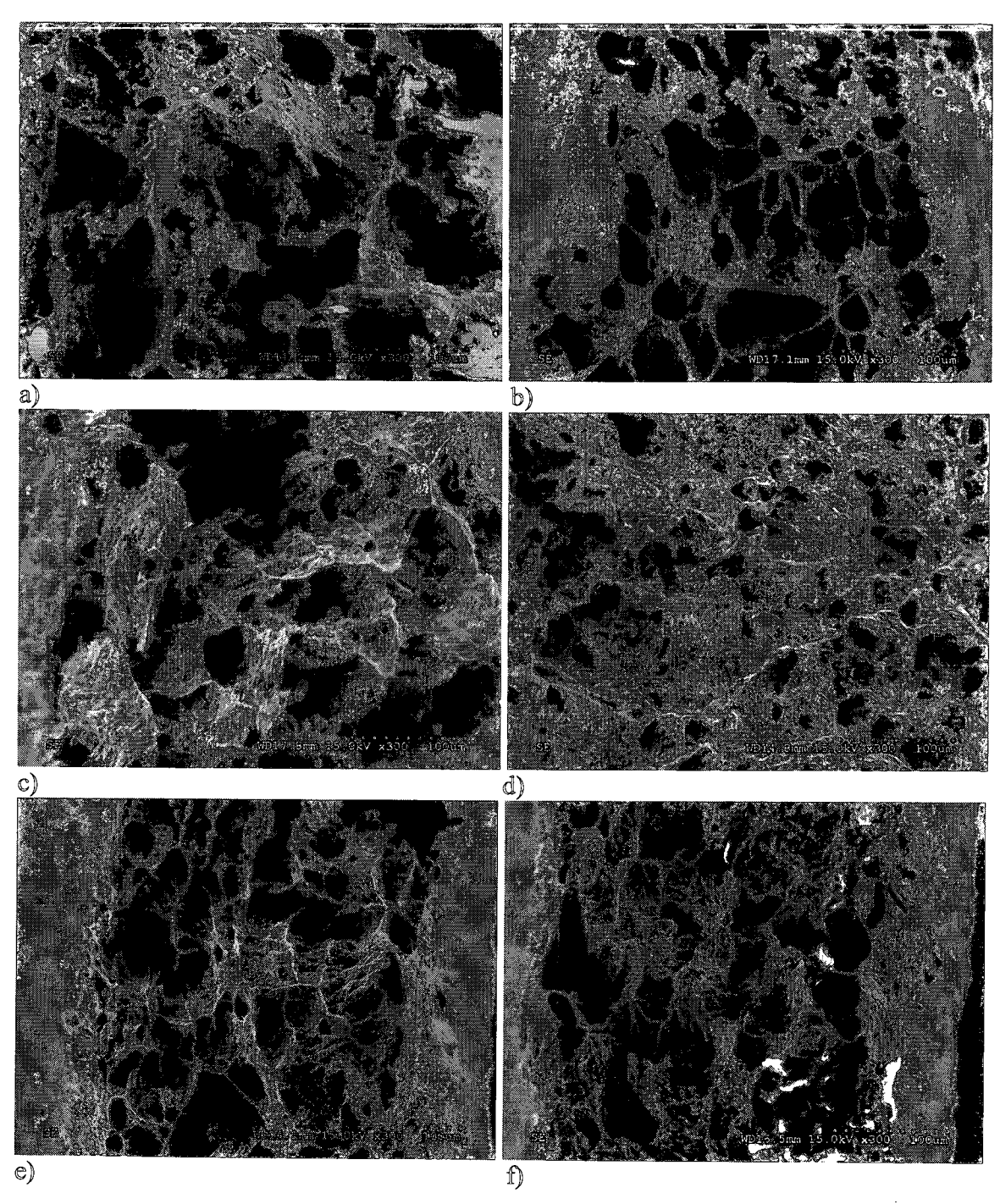


Figure 8.8 SEM images for tensile fracture tips tested 450 °C, and strain rate of $0.0003s^{-1}$: a) AZ31, b) AZ31 with Ca, c) AZ31 with Ce, d) AZ31 with Ca and Ce, e) AZ31 with Ca and Sr and Ce, and f) AZ31 with Ca and Sr

8.1.2.3 Interrupted Testing under a Superplastic Deformation Condition

Repeatability of flow behaviour

A series of interrupting tests were performed at 450 °C, a strain rate of 0.0003s⁻¹, and strains of 0.1, 0.6, 1.0, 1.4, up to failure. Figure 8.9 shows the specimens tested at different strains. Figure 8.10 plots the flow curves corresponding to those specimens, in which a good repeatability of hot working behaviour is displayed.

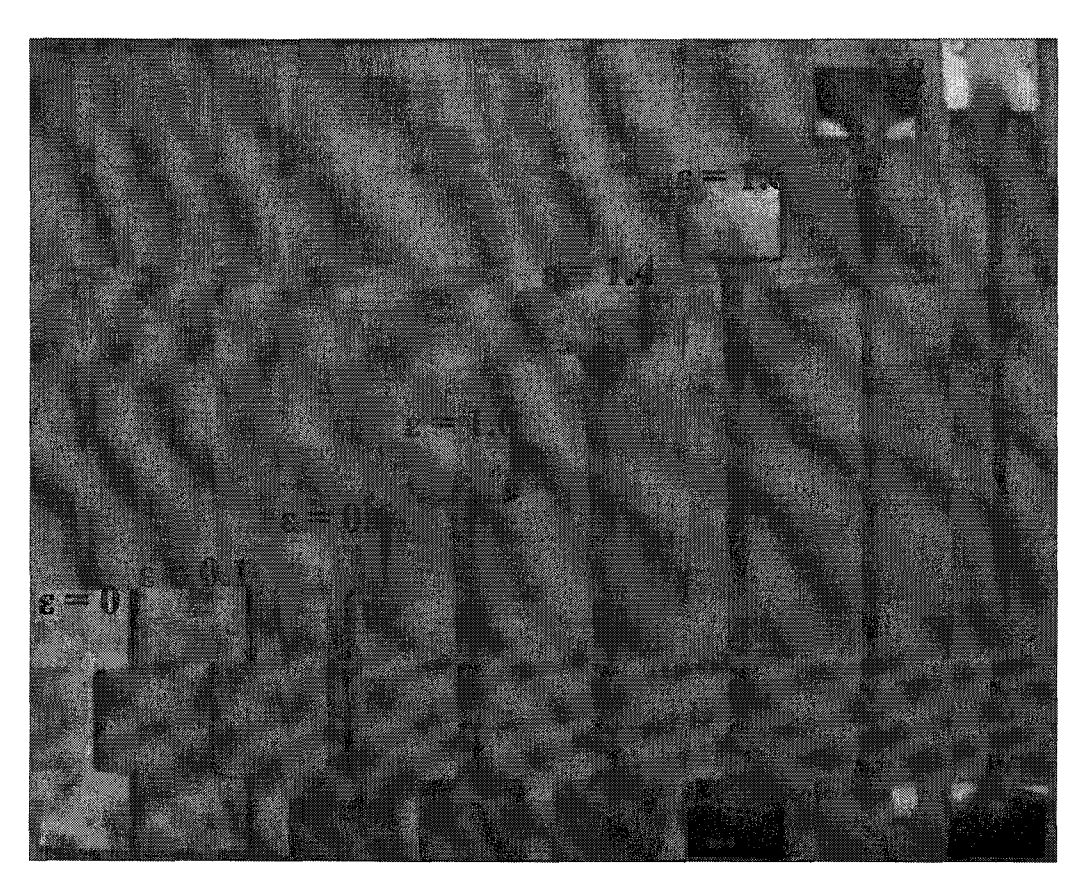


Figure 8.9 Samples of interrupting tensile tests at 450 °C, strain rate of 0.0003 s⁻¹ for the microalloyed AZ31 with Ca and Sr and Ce

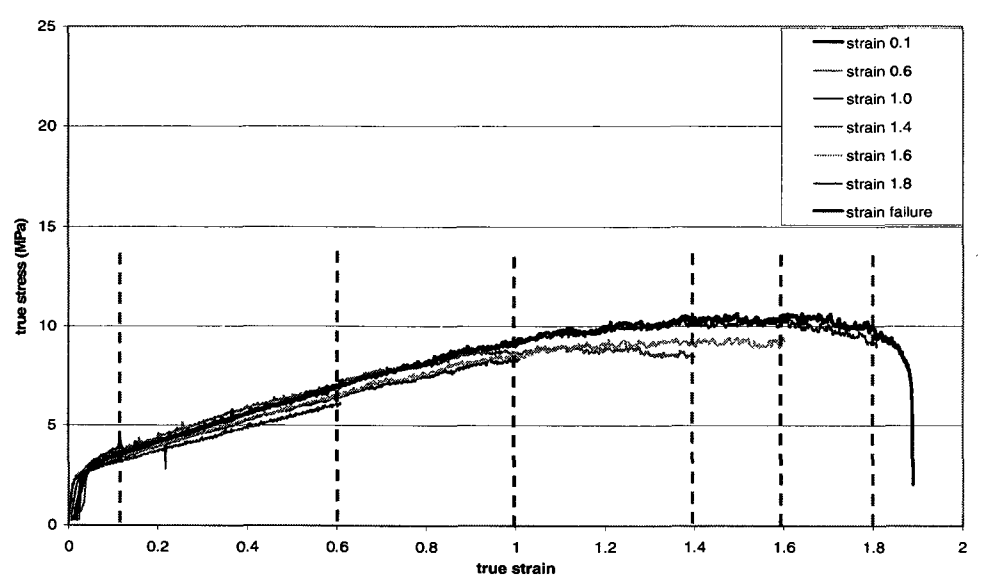


Figure 8.10 Typical tensile flow curves of interrupting tensile tests for the microalloyed AZ31 with Ca and Sr and Ce, tested at 450 °C and strain rate of 0.0003 s⁻¹

Effect of microalloying on necking development

Figure 8.11 shows a clear necking in the sample pulled to a strain of 1.4 for AZ31 base alloy, while all microalloyed alloys demonstrate no necking and a uniform

deformation.

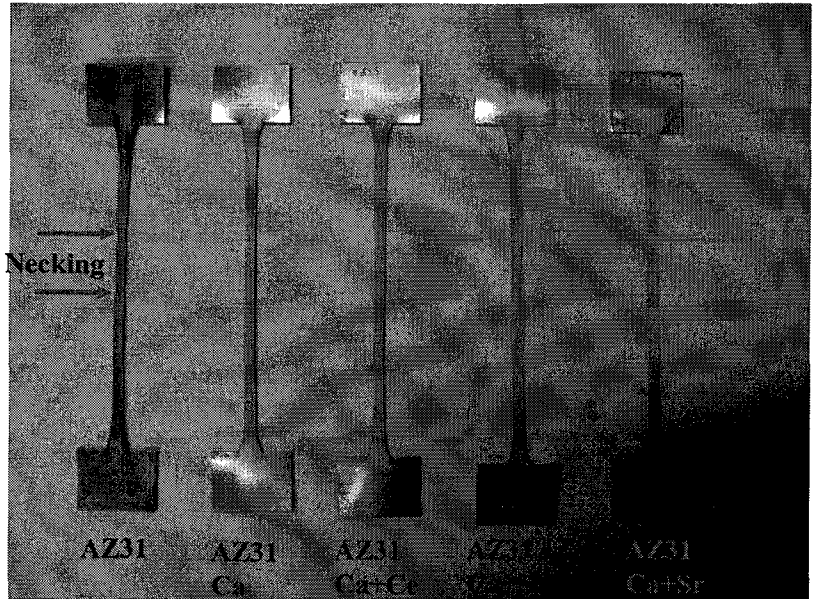


Figure 8.11 Samples of interrupting tensile tested at 450 °C, strain rate of 0.0003 s⁻¹, and strain of 1.4

Cavitation evolution

A comparison of cavitation evolution during hot tensile for AZ31 base alloy to AZ31 with Ca, Sr and Ce is shown in Figure 8.12 and Figure 8.13. No cavities can be seen at a low strain of 0.1. Cavitation was found in the specimen strained at 0.6 for both alloys, and then further developed with increasing deformation. Again, the alloy with Ca, Sr and Ce shows a slow development, which is consistent with the results of reduction area (%) observed in Figure 8.11, i.e. microalloying slows down the development of cavitations during tensile testing.

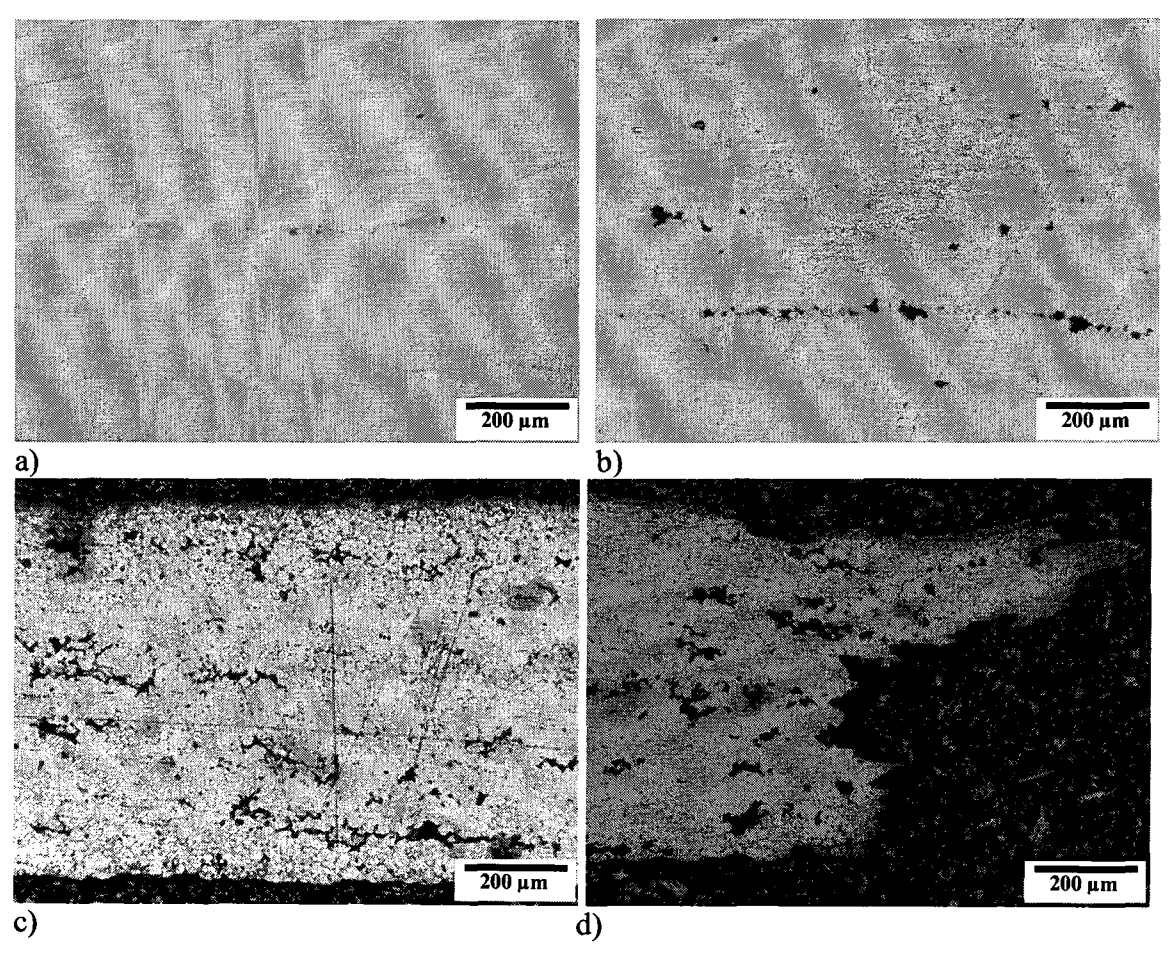


Figure 8.12 Cavitation evolution during interrupting tensile tests at 450 °C, strain rate of 0.0003 s⁻¹ for AZ31 alloy: a) ε =0.6, b) ε =1.0, c) ε =1.4, and d) at failure

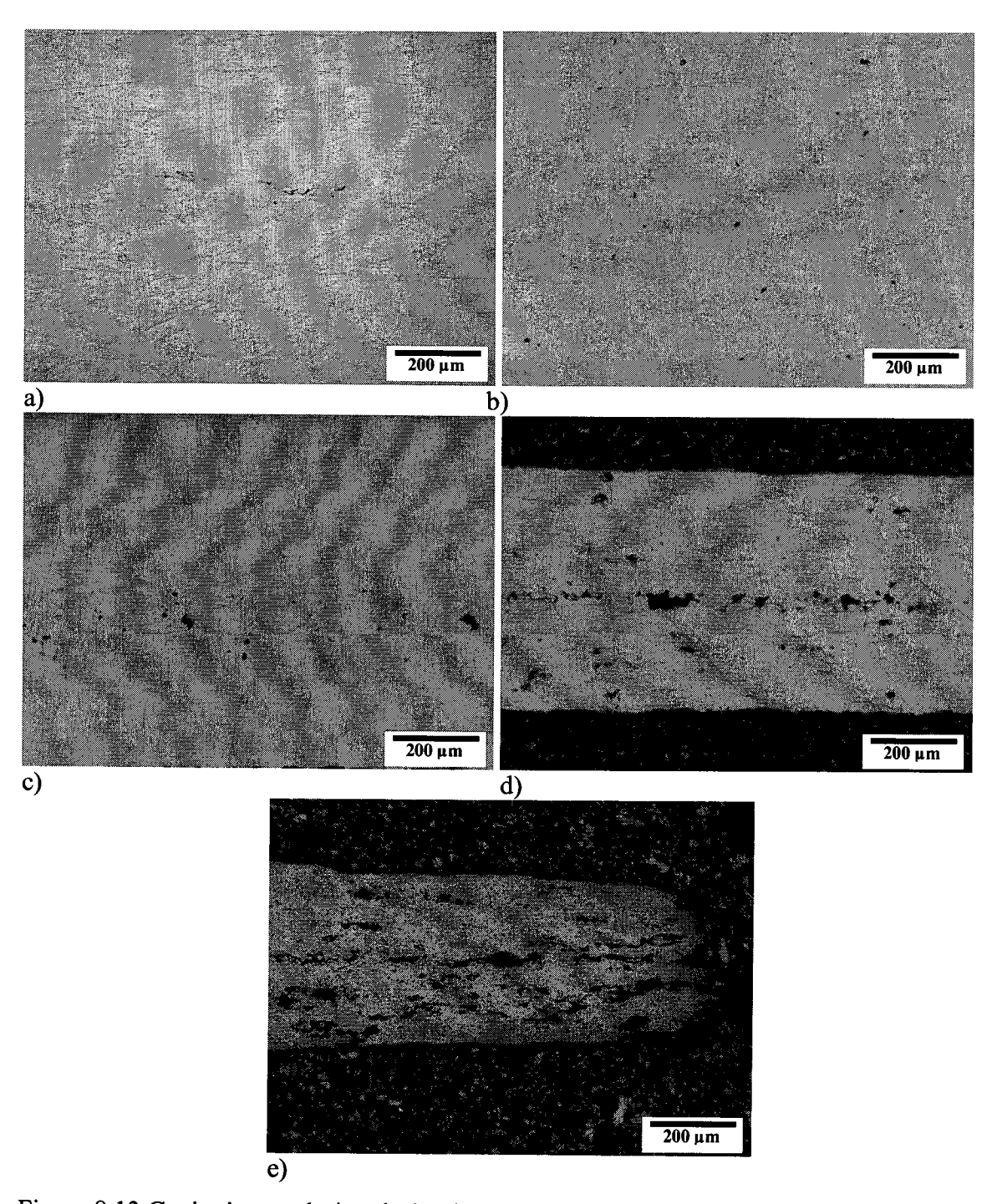


Figure 8.13 Cavitation evolution during interrupting tensile tests at 450 °C, strain rate of 0.0003 s⁻¹ for AZ31 with Ca & Sr &Ce: a) ε =0.6, b) ε =1.0, c) ε =1.4, d) ε =1.8, and e) at failure

8.2 Discussion

8.2.1 Effect of Alloying on Room Temperature Properties

As early as 1962 it was found that the room temperature ductility of Mg-alloys can be significantly enhanced by decreasing the grain size [1]. Fine-grained Mg-alloys attained by equal cannel angular extrusion (ECAE) and equal channel angular pressing (ECAP) have exhibited a good combination of high strength and high ductility at room temperature [2, 3]. Therefore, a refined and more uniform as-rolled and as-annealed grain structure will be beneficial to the improvement of ductility. Regarding the effect of second phases on ductility, two aspects were observed [4]: in the case of crack initiation, second phases can act to disperse the dislocations which lead to cracking, but also can initiate cracks which propagate into the matrix. Some experimental evidence suggested that there is a critical range of particle size and spacing at which the former beneficial effect predominates.

In the present study, for most of the microalloyed AZ31 alloys, the ductility is unchanged or greater than the base alloy AZ31 due to the combination effect of grain size and second phases. Figures 8.14 and 8.15 compare the tensile curves and corresponding as-rolled and as-annealed microstructures for two sheets rolled at 300 °C. It is noted that multiple-microalloyed alloy with additions (Ca, Sr and Ce) display more refined and uniform structures in both as-rolled and as-annealed conditions than those of AZ31 without alloying. This may explain the increased EL (%) from 17.1% to 21.5%. For the sheets rolled at 400 °C, similar results can be seen. The value of EL (%) has increased from 20.7% to 24.7% for the alloy with alloying additions (Ca and Ce).

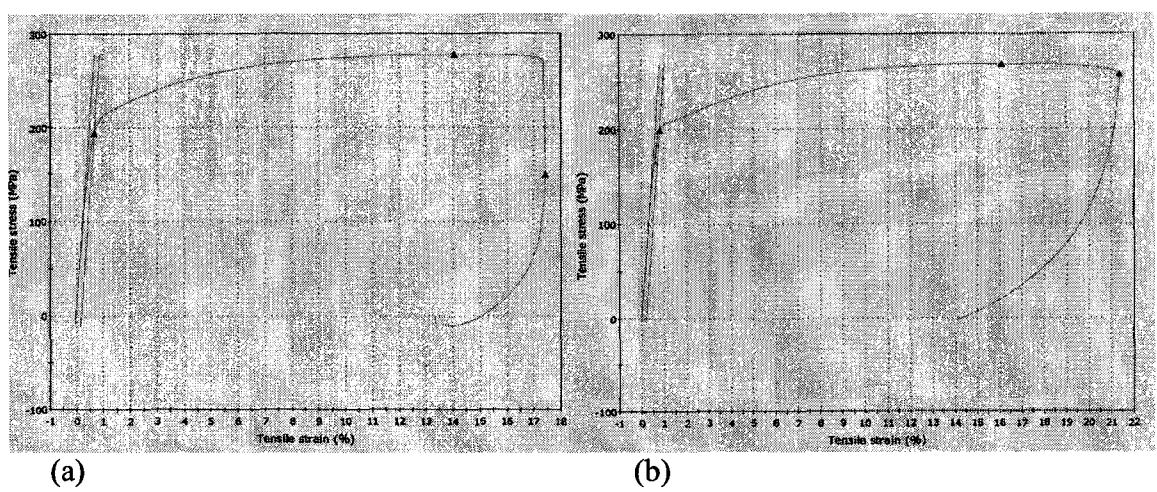


Figure 8.14 Representative strain-stress curves test at room temperature for sheet materials rolled at 300 °C, 20% reduction per pass: a) AZ31, b) AZ31 with additions (Ca, Sr, and Ce)

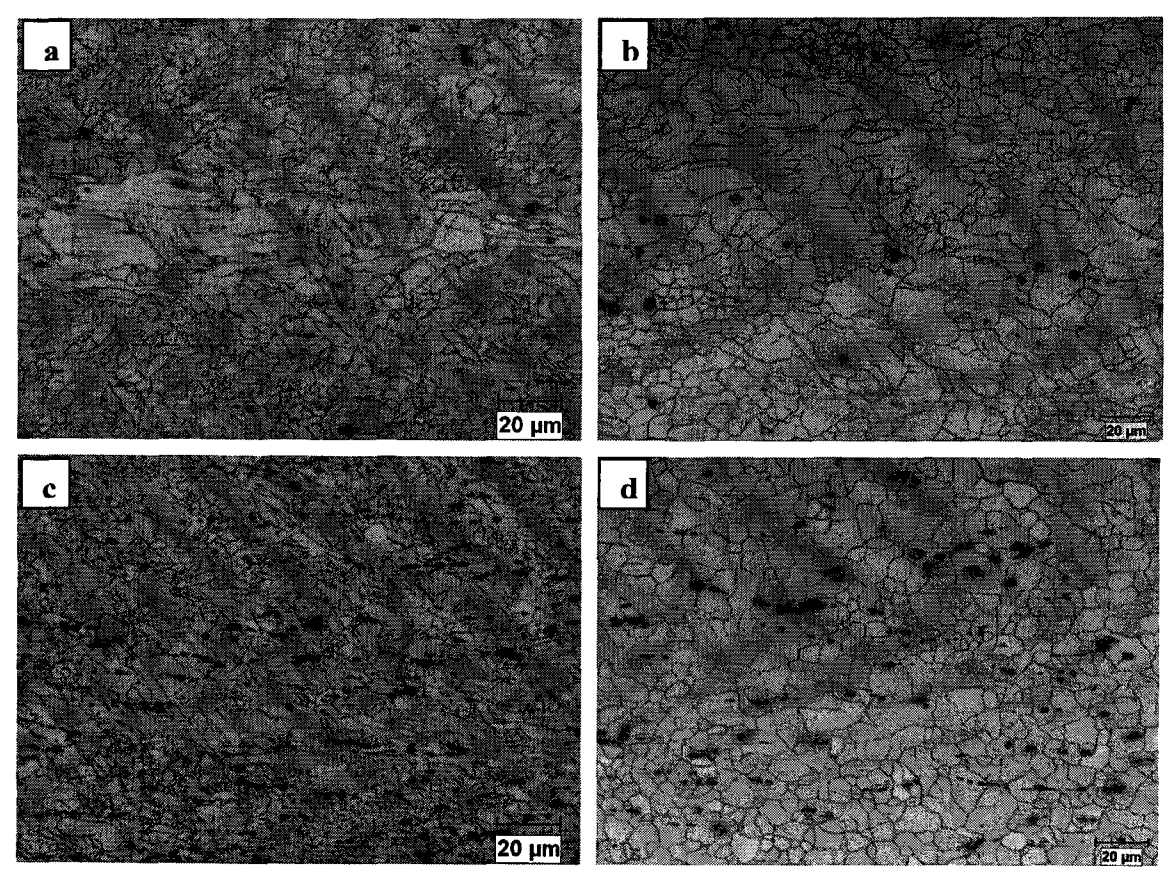


Figure 8.15 Microstructure of sheets rolled at 300 °C, 20% reduction per pass: a) AZ31 as-rolled, b) AZ31 annealed at 400 °C for 10 minutes, c) AZ31 with additions (Ca, Sr and Ce) as-rolled, d) AZ31 with additions (Ca, Sr and Ce) annealed at 400 °C for 10 minutes

Regarding the 'anomalous' reduced ductility of AZ31 with Ca, this may be due to the formation of Al-Ca phases even though the structure is refined, whether as-cast, as-rolled, or as-annealed grain structure. A somewhat similar result has been reported in the investigation of effect of 0.4% ~ 1.9%Ca addition on the room tensile properties for as-cast AZ91 alloy ^[5]. The results showed that with the Ca addition, the tensile strength and elongation of AZ91 were reduced. Fractographs revealed that Ca addition increased cleavage and the extent of the radial or parallel tearing ridge. However, in this work, multiple alloying with Ca and other additions (Sr, Ce), improved room temperature ductility can be seen. Other studies also show this in AZ31 sheet with 0.3%Ca and 0.3%Ce ^[6], and as-cast AZ91 with 0.3%Ca and 0.3~3.0%Ce ^[7]. This may be due to the modifying effect of Ce or Sr on the second phases, e.g. Ce can refine second phases by formation new phases, and Sr may form new phase with Ca in AZ31 alloy as shown in Chapter 5.

As for the reason for the increase in yield strength for most microalloyed alloys, this is probably due to more volume fraction of second phases. These second particles could strengthen the matrix and prevent the slippage of the grain boundaries and dislocations, and lead to the improvement of yield strength. The result is consistent with previous investigation [7].

8.2.2 High-temperature Deformation Mechanisms

According to the general mechanisms of high-temperature deformation for fine grain materials summarized by Nieh et al. $^{[8]}$, the deformation modes are defined by the stress exponent n, which is equal to 1/m, where m is the strain rate sensitivity component. When $n \le 2$, grain-boundary sliding occurs for fine grained superplastic materials. When $n=4\sim5$, and sometimes as high as 6, climb-controlled dislocation creep becomes the main mechanism, and deformation is controlled by the climb of dislocations over physical obstacles. The case of n>8 is characterized for alloys strengthened by the dispersion of

fine and hard particles. In order to identify the deformation modes in this hot tensile testing, m was calculated with following equation:

$$m = \left(\frac{\Delta \log \sigma}{\Delta \log \varepsilon}\right)_{\varepsilon, T}$$
 (Equation 8.1) [9]

Where σ is a nominal yield stress, and a stress corresponding to a true strain of 0.1 was selected in present work. $\dot{\epsilon}$ is the strain rate.

Table 8.3 lists the m and n values under testing conditions for two alloys of AZ31 and AZ31 with additions (Ca, Sr and Ce). As can be seen, only at lower Z conditions (≥ 400 °C and at strain rate of $0.0003s^{-1}$) does superplastic deformation occur. All other conditions basically fit in the dislocation creep mode, which matches the observations in flow behaviour (Figures 8.1-8.4) and fracture (Figures 8.5-8.7). This confirms that testing conditions can change the deformation mechanism in Mg-alloys.

Table 8.3 Strain rate sensitivity component (m) and stress exponent (n) under various testing conditions

		at 4	at 450 °C		at 400 ° C		at 300 °C			
Alloys	Strain rate (s ⁻¹)	Stress (MPa)	m	n	Stress (MPa)	m	n	Stress (MPa)	m	n
	0.1	35.5			48.7			92.6		
AZ31	0.01	22.1	0.21	5	32.2	0.18	6	70.3	0.12	8
	0.001	6.9			13.8			43.0		
	0.0003	3.8	0.50	2	6.9	0.58	2	31.0	0.27	4
	0.1	36.0			51.6			94.4		
AZ31+0.21%Ca	0.01	23.8	0.18	6	35.2	0.17_	6	69.4	0.13	_7.5
+0.20%Sr+0.20	0.001	8.0	<u>.</u>		17.5			47.7		
%Ce	0.0003	3.5	0.69	1.5	9.5	0.51	2	35.3	0.25	4

It is also noted that microalloying does not alter the deformation mode under a specific testing condition, but it does have some effect. This can be observed in Table 8.3 under the testing condition of 450°C and strain rate of 0.0003s⁻¹. The n value was decreased to 1.5 through additions (Ca, Sr and Ce), which indicates an improvement in superplasticity. Again, the fractographs in Figures 8.5-8.7 reveal the effect of

microalloying on the improvement of plasticity by comparing base alloy AZ31 and microalloyed AZ31 alloys, i.e. at high Z (450 °C, ϵ =0.1s⁻¹), alloying additions reduce the abnormal grain growth region; while at low Z (450 °C, ϵ =0.0003s⁻¹), alloying additions retard the growth of cavitations.

8.2.3 Effect of Microalloying on Superplasticity

8.2.3.1 Second Phases and Grain Structure

To have a better understanding of the effect of alloying during hot tensile tests, second phases in the grip region of samples tested to fracture at 450 °C and 0.0003s⁻¹ were examined and the area fraction (%) was measured. Table 8.4 and Figure 8.16 show the results. It was found that thermally stable second phases formed during solidification have been further refined by hot rolling and aligned in the rolling direction. Amounts of second phases show an increase with more alloying additions. These small second particles were maintained throughout the hot tensile tests even though at 450 °C some tests lasted more than two hours (e.g. 2.16 hour for the alloy with Ca, Sr and Ce).

Table 8.4 Statistic results of area fraction (%) of second phases in tensile samples

Alloys	Materials status	Area fraction (%)	Standard deviation	
AZ31	a) sheets rolled at 400 °C	0.46	0.07	
AZ31+ 0.20%Ca	with 30% Red. per pass;	0.77	0.19	
AZ31+ 0.20%Ce	b) tensile sample at grip	2.55	0.20	
AZ31+0.21%Ca+0.20%Ce	region;	2.89	0.29	
AZ31+ 0.21%Ca+0.21%Sr	c) tensile test until failure: at 450 °C, and strain rate	3.24	0.35	
AZ31+0.21%Ca+0.20%Sr+0.20%Ce	of 0.0003s ⁻¹	4.52	0.48	

Figures 8.17-8.19 present the grain structure in the grip region for six alloys. Note that AZ31 base alloy and the alloy with only Ce illustrate slightly coarser and nonuniform grains (Figure 8.17a and Figure 8.18a), while for all other alloys, smaller and more uniform grain sizes were observed. Based on the observation of second phases and grains in the grip region, it may be inferred that these thermally stable particles have effects on

resisting the grain growth during hot deformation and therefore promoting the grain boundary sliding and improving superplasticity of AZ31. The relatively coarse grains (Figure 19a) in the alloy with individual Ce may be detrimental to EL.

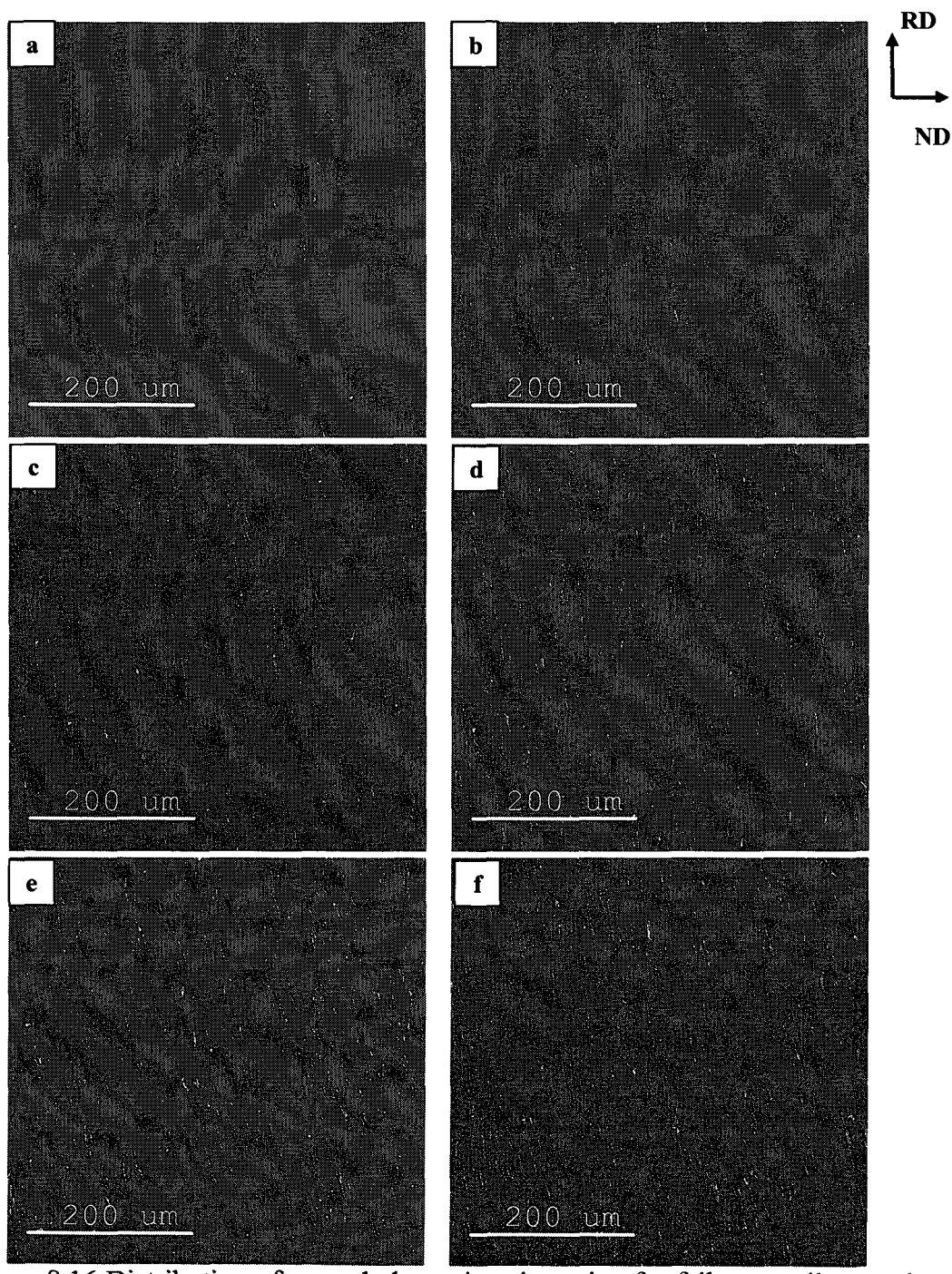


Figure 8.16 Distribution of second phases in grip region for failure tensile samples tested at 450 °C and strain rate of 0.0003s⁻¹: a) AZ31, b) AZ31 with Ca, c) AZ31 with Ce, d) AZ31 with Ca and Ce, e) AZ31 with Ca and Sr, and f) AZ31 with Ca and Sr and Ce

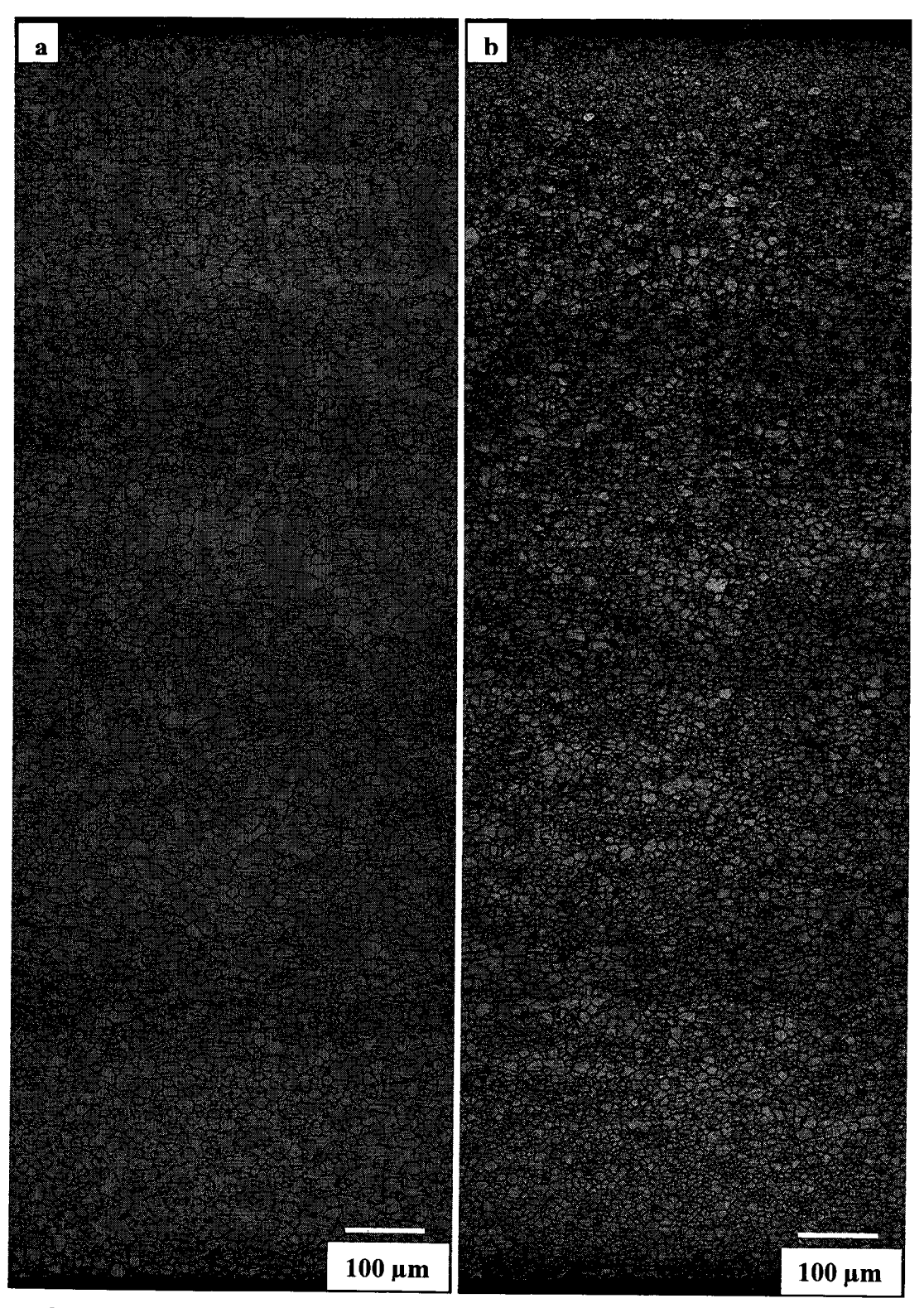


Figure 8.17 Microstructures in grip region of tensile samples at failure (no strain) tested at 450 °C, and strain rates 0.0003s⁻¹: a) AZ31, and b) AZ31 with Ca

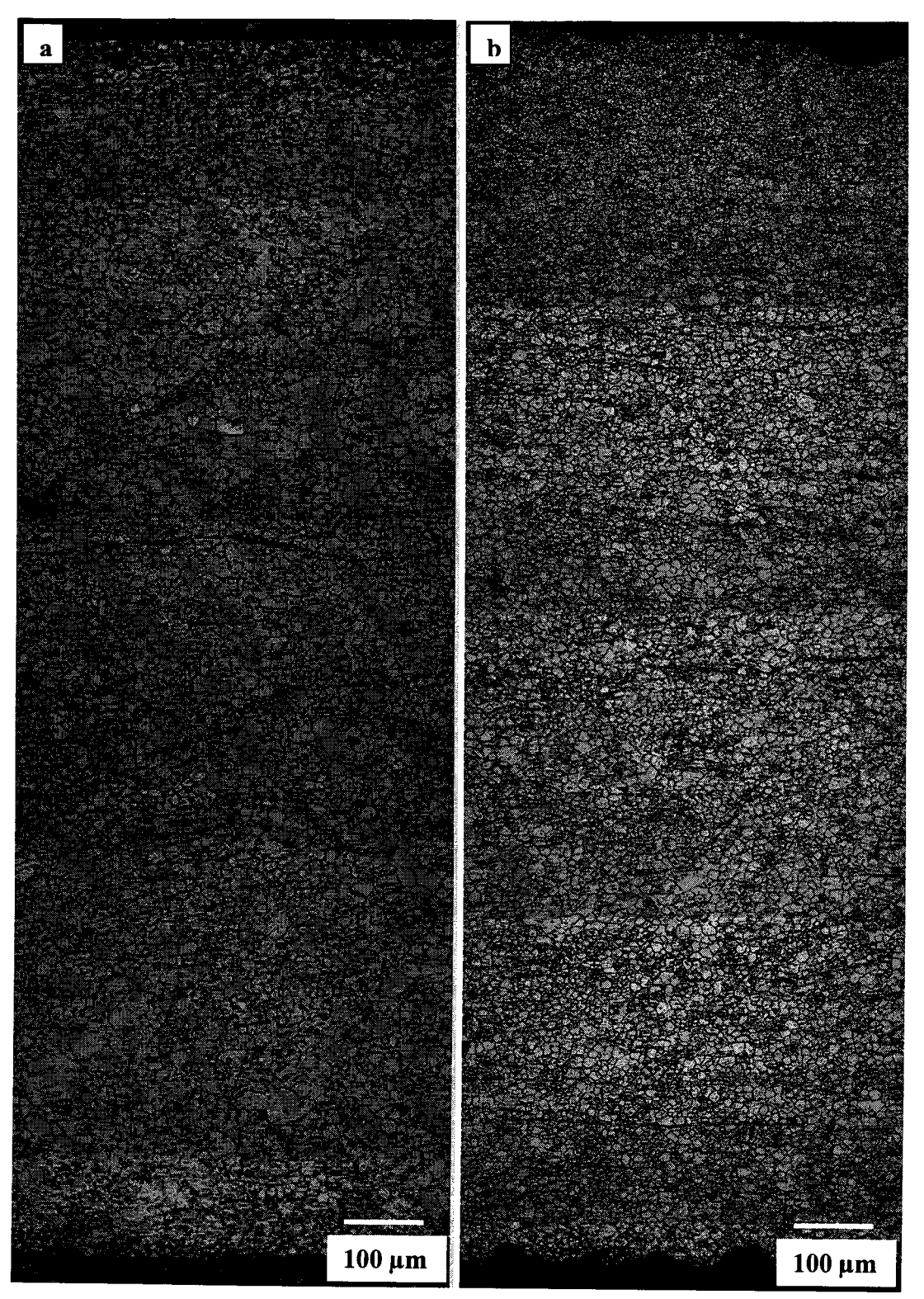


Figure 8.18 Microstructures in grip region of tensile samples at failure (no strain) tested at 450 °C, and strain rates 0.0003s⁻¹: a) AZ31with Ce, and b) AZ31 with Ca and Ce

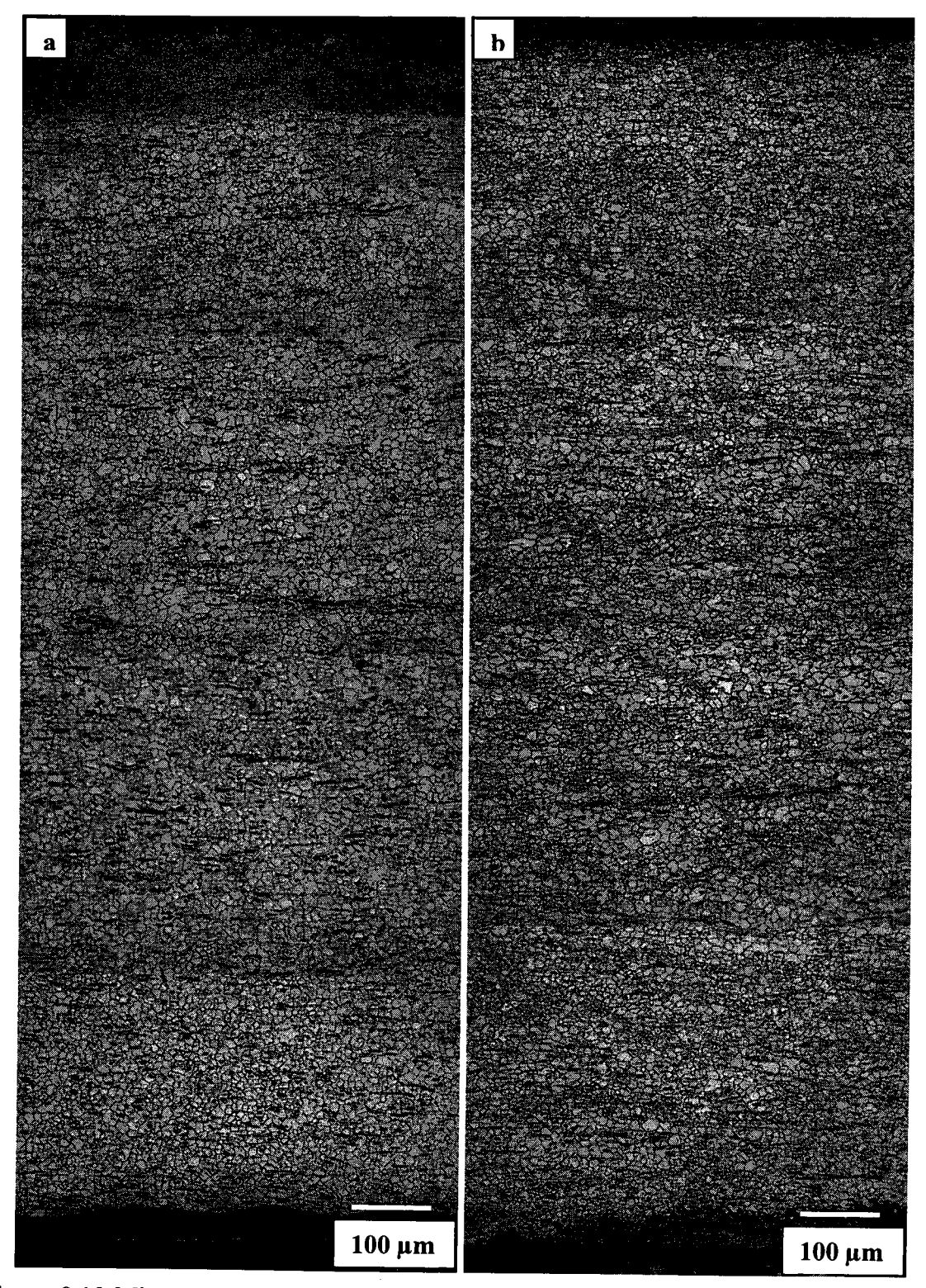


Figure 8.19 Microstructures in grip region of tensile samples at failure (no strain) tested at 450 °C, and strain rates 0.0003s⁻¹: a) AZ31 with Ca and Sr, and b) AZ31 with Ca and Sr and Ce

8.2.3.2 Microstructure Evolution and Occurrence of DRX

The microstructure evolution during hot tensile testing (at 450 °C and a strain rate of 0.0003 s⁻¹) for AZ31 base alloy and AZ31 with additions (Ca, Sr and Ce) is compared in Figure 8.20 and Figure 8.21. Several observations can be made. Firstly, the grain size in AZ31 alloy is easier to grow during testing, while the alloy with additions tends to maintain its refined grain structure until failure. Secondly, a smaller grain size and/or higher volume fraction of second phases in microalloyed alloys retards the development and growth of cavitations. Thirdly, grains in the failure area show a uniform grain structure for both alloys, although the initial grain size is mixed in the AZ31. Actually, at a strain of 0.6, a uniform grain structure can be achieved in AZ31 (Figure 8.20c). This may be due to the occurrence of dynamic recrystallization during the hot tensile test. Figure 8.22 gives evidence that DRX has occurred in the early deformation stage, at a strain of 0.1. A smaller grain size still cannot be achieved in AZ31 alloy due to lack of fine second particles although a uniform grain structure can be developed by DRX. Since new DRX grains nucleate at existing grain boundaries (although no necklacing is apparent), more DRX will occur in microalloyed materials due to its high volume grain boundary fraction (finer grain structure). Thus, formability is improved by microlloying through maintaining finer grain size, which promotes grain boundary sliding and DRX.

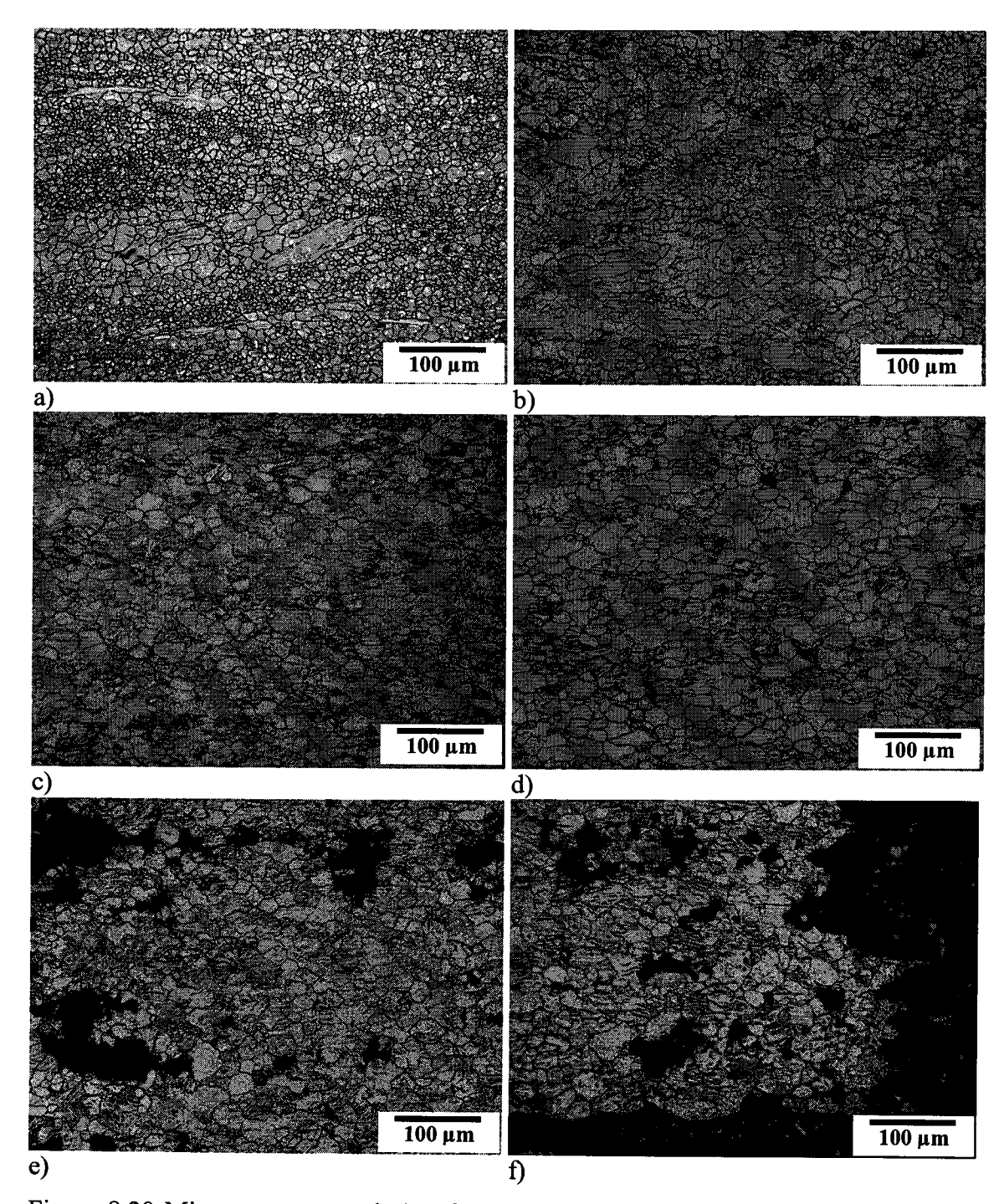


Figure 8.20 Microstructure evolution for AZ31 alloy during interrupting tensile tests at 450 °C, strain rate of 0.0003 s⁻¹: a) ϵ =0, b) ϵ =0.1, c) ϵ =0.6, d) ϵ =1.0, e) ϵ =1.4, and f) at failure

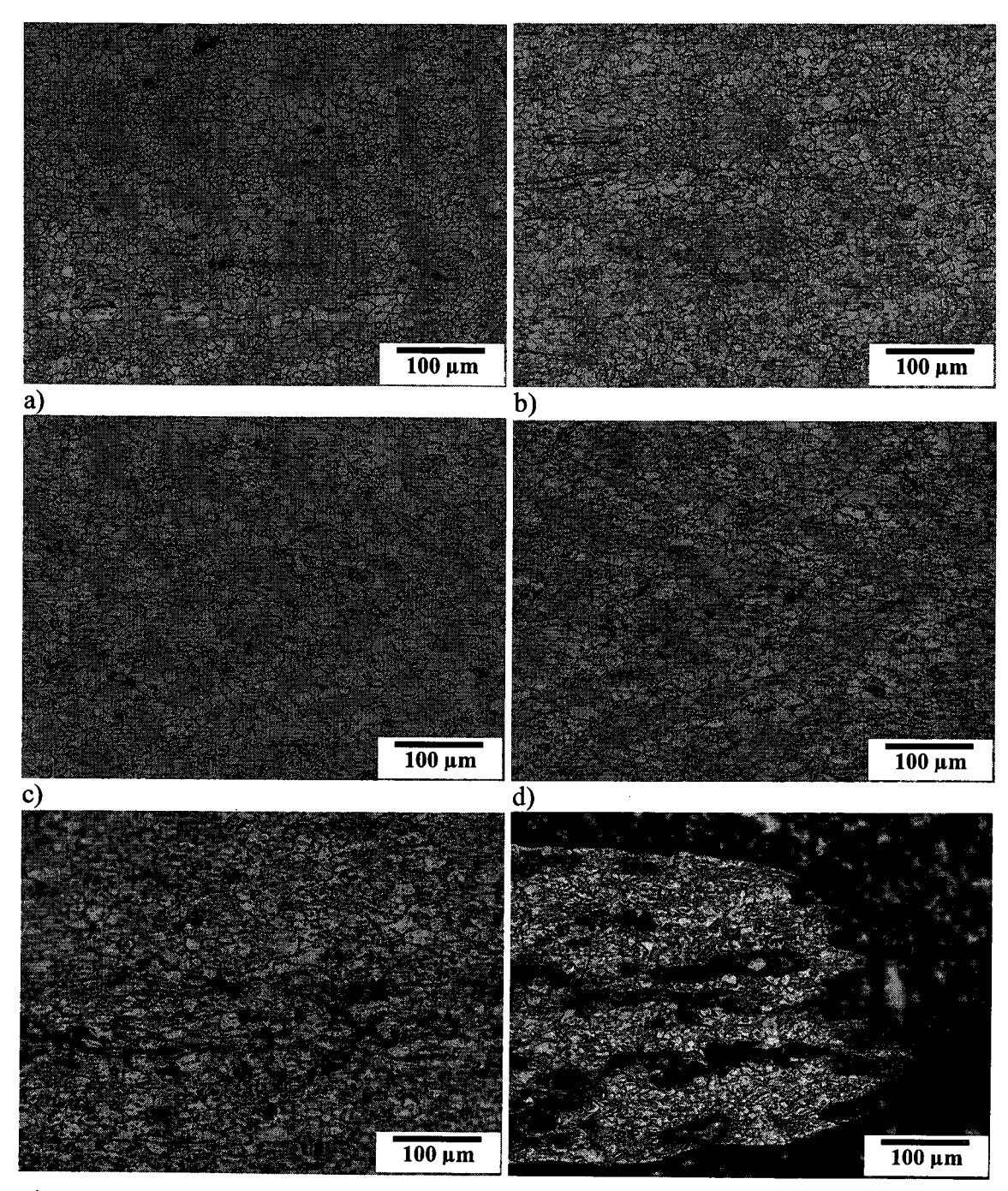


Figure 8.21 Microstructure evolution for the alloys of AZ31 with Ca & Sr & Ce during interrupting tensile tests at 450 °C, strain rate of 0.0003 s⁻¹: a) ε =0, b) ε =0.1, c) ε =0.6, d) ε =1.0, e) ε =1.4, and f) at failure

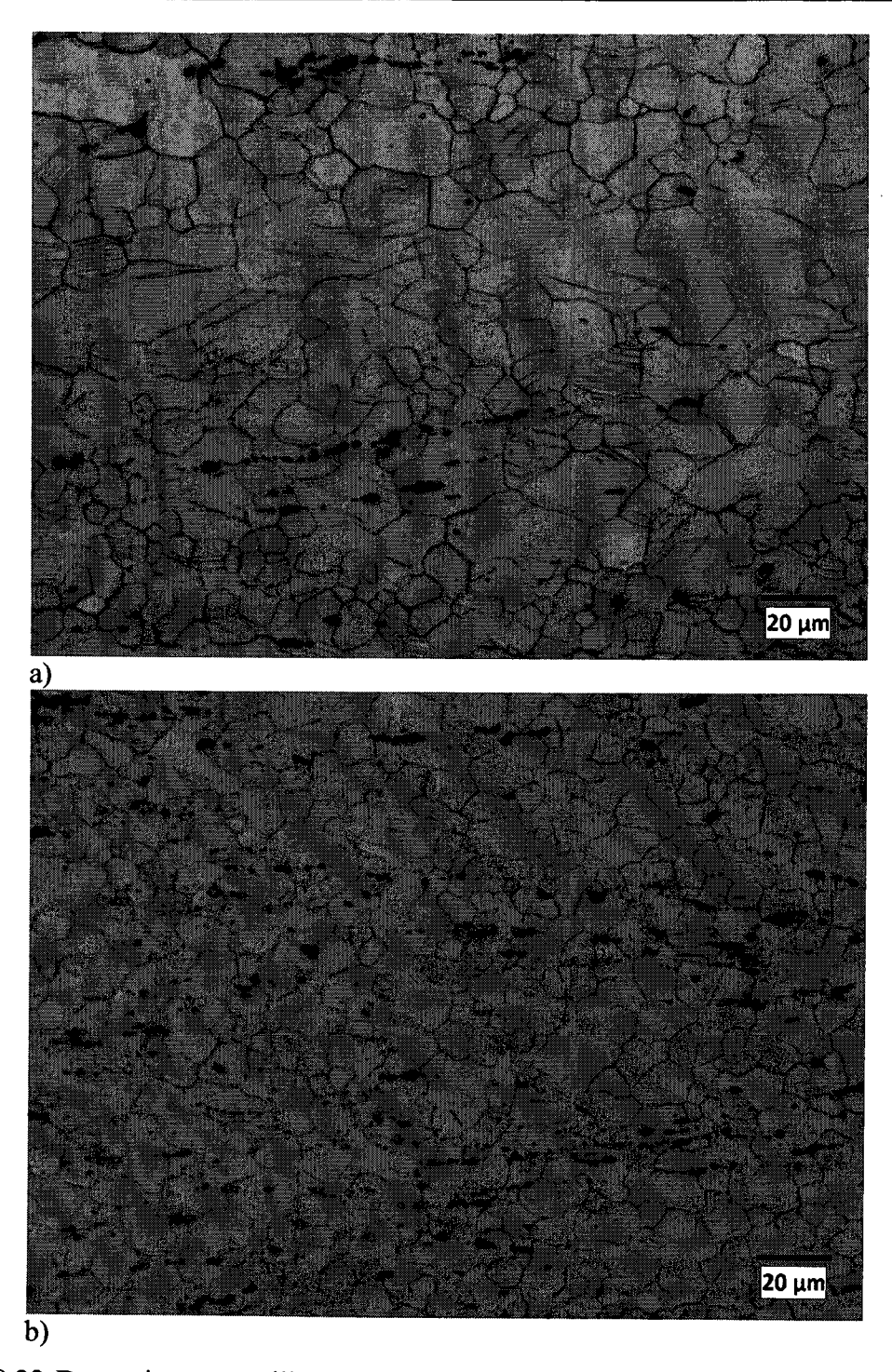


Figure 8.22 Dynamic recrystallization in tensile samples tested at 450 °C, strain rate of 0.0003 s⁻¹: a) ϵ =0.1 for AZ31 alloy, b) ϵ =0.1 for the alloy of AZ31 with additions (Ca, Sr and Ce)

The results in the present work show good agreement with those of an investigation in deformation mechanisms responsible for the high ductility in AZ31 sheets with EBSD performed by Del Velle et al. [10]. In their work, two temperatures of 300 °C and 375 °C, and four strain rates of 0.01s⁻¹, 0.002 s⁻¹, 0.0003 s⁻¹, and 0.00005 s⁻¹ were selected. In the lower strain rate regime, greater than 300% EL and n values from 1.7 to 2.5, were obtained, which are characteristic of grain boundary sliding (GBS). Moreover, the microstructure evolution revealed that the grain size starting from 17 μm increased to 29 μm after a strain of 150% (true strain of approximate 0.9), and maintained this level until failure at 320% (true strain of 1.44). EBSD analysis shows that after 150%EL, the fraction of low-angle boundaries increased significantly, which indicates that an intensive operation of continuous DRX may occur.

In addition, Del Velle et al.'s EBSD work also reveal that basal texture is generated during deformation, which suggests the occurrence of crystallographic slip (CS) as well as the operation of GBS under superplastic testing conditions. If GBS is the sole mechanism, a random texture would be attained due to the random rotation of grains along grain boundaries. Therefore, it is possible that there is concurrent operation of CS, in particular as grain growth occurs. Further investigation is needed regarding the roles of CS and GBS.

8.3 Summary

- Room temperature tensile tests show that new alloys have an equal or a better EL (%) and slightly higher yield strength than AZ31 base alloy, except for the alloy with Ca only. This indicates that the refined second particles by adding Ce in multiple alloyed materials with Ca and Sr are beneficial to the improvement of their room temperature EL(%) although the yield strength increase may be slight;
- Hot tension flow behavior changes with the testing conditions, resulting from different hot deformation mechanisms. At a high Z (i.e. at high strain rates and low temperatures, when stress exponent is 4<n<8.) flow curves show a very short pre

UTS region and relatively long post UTS region, and climb-controlled dislocation creep becomes the main mechanism. At a low Z (at $T \ge 400$ °C and strain rate of 0.0003 s⁻¹, when stress exponent n=2,) flow curves show a much longer pre UTS region and a very short post UTS region, and superplastic deformation by grain boundary sliding occurs;

- Tensile testing under various conditions displays various ductilities for several potential manufacturing operations: at T≥400 °C and € < 0.001 s⁻¹, EL% is approximate 300% for most of AZ31 based alloys; at T≥400 °C and € < 0.01 s⁻¹, EL% of 200% may be achieved; at T≥400 °C and € < 0.1 s⁻¹, EL% of 100% is usually ensured;
- At elevated temperature, alloys with multiple microalloying additions (Ca, Sr, and Ce) or only Ca show an improvement in ductility at almost all testing conditions although microalloying does not change the deformation modes under the specific testing conditions. Under the superplastic deformation condition, the maximum EL for the alloy with three microalloying additions is as high as 552%, and is improved by 59% compared to the base alloy AZ31 (EL: 347%);
- The microstructure in the grip region of tensile samples and fracture behavior observations reveal that microalloyed alloys (except with individual Ce) maintain their finer grain size during hot tension deformation, and therefore contribute to the promotion of grain boundary sliding and the improvement of ductility;
- Interrupting testing at superplastic conditions (450 °C and strain rate of 0.0003s⁻¹) displays good repeatability of the flow behavior. The microstructure evolution shows that microalloying resists grain growth, promotes dynamic recrystallization in the matrix, and retards the development of cavitations and necking during hot deformation.

References:

- 1. J.A. Chapman and D.V. Wilson, "The room-temperature ductility of fine grained magnesium", J. Inst. Met., 91 (1962), pp. 39-40
- 2. K. Kubota, M. Mabuchi, and K. Higashi, "Review Processing and Mechanical Properties of Fine-grained Magnesium Alloys", J. Mater. Sci., 34, (1999), p 2255-2262
- 3. J. Koike, T. Kobayashi, T.Mukai, H. Watanabe, M. Suzuki, K. Maruyama, and K. Higashi, "The Activity of Non basal Slip Systems and Dynamic Recovery at Room Temperature in Fine-grained AZ31B Magnesium Alloys", Acta Materialia., 51, (2003), p 2055-2065
- 4. G. T. Hahn and A. R. Rosenfield, "Effects of Second-phase Particles on Ductility", Jan. (1966), Accession Number: AD0480038, NTIS Collection
- 5. Q. Wang, W. Chen, X. Zeng, Y. Lu, W. Ding, Y. Zhu, and X. Xu, "Effects of Ca Addition on the Microstructure and Mechanical Properties of AZ91 Magnesium Alloy", J. Mater. Sci., 36, (2001), p 3035-3034
- 6. Y. Liu, W.P. Chen, W.W. Zhang, W. Zhang, and Y.Y. Li, "Study on the Bending-Bulging formability' of AZ31 Mg alloy sheet by microalloying of RE and Ca", Rare Metal Materials and Engineering, 35 (6), (2006), p 925-928
- 7. W. Du,, Y. Sun, X. Min, F. Xue, M. Zhu, and D. Wu, "Microstructure and Mechnical Properties of Mg-Al Based Alloy with Calcium and Rare Earth Additions", Materials Science and Engineering A, 356, (2003), p 1-7
- 8. T.G. Nieh, J. Wadsworth and O.D. Sherby, "Superplasticity in Metals and Ceramics", Cambridge University Press, (1997), p 32-57
- 9. G.E. Dieter, H.A. Kuhn, and S.L. Semiatin, "Handbook of Workability and Process Design", ASM International, The Materials Information Society, (2003), p 62
- 10. J.A. Del Valle, M.T. Pérez-Prado, and O.A.Ruano, "Deformation Mechanisms Responsible for the High Ductility in a Mg AZ31 Alloy Analyzed by Electron Backscattered Diffraction", Metallurgical and Materials Transactions A, 36, June (2005), p 1427-143

Chapter 9

Conclusions

In the present research, the effects of microalloying additions (Ca, Sr, and Ce) on microstructure and hot working behavior of AZ31 magnesium alloy were systematically investigated by a series of experiments, including casting microalloyed alloys under different cooling rates, compression testing and rolling the as-cast alloys under various schedules. The as-rolled sheets were tensile tested at ambient and elevated temperatures under a variety of strain rates. The following conclusions can be drawn:

Effect of Microalloying Ca, Sr and Ce on Microstructure and Hot Working Behaviors of AZ31 Alloy:

As-Cast Microstructure

• Adding microalloying levels of Ca, Sr, and Ce in AZ31 alloy leads to the formation of the following phases during solidification: Al₂Ca, Al₂Sr, Al₂ (Ca, Sr), Al₁₁Ce₃, and Al₈CeMn₄, at the same time reducing the amount of Mg₁₇Al₁₂. These second phases are thermally stable at temperatures that hot rolling process is usually performed (250 °C ~ 450°C);

- Small amounts of Ca and Sr can be used as grain refiner in AZ31 alloy. By comparison, Ca has a much stronger effect than Sr;
- Ca, Sr, and Ce refine second phases in AZ31 alloy through the formation of new dispersive phases as mentioned above, and Ce shows a much stronger refining effect than that of Ca and Sr;
- Under a high cooling (solidification) condition, the effect of microalloying on refining microstructure (both grain size and second phases) of AZ31 is more obvious than that under a slow cooling (solidification) condition.

Microstructure and Hot Compression Flow Behaviors

- For microalloyed AZ31 alloys, the DRX mechanism of necklacing at grain boundaries by discontinuous DRX and continuous DRX is promoted due to increasing nucleation sites by refining initial grain size. Meanwhile, DRX by particle stimulated nucleation (PSN) might also be promoted due to increasing the numbers of second phases (> 1 μm and widely spaced) by microlloying. Thus, a more homogenous DRX microstructure was observed in microalloyed materials;
- Microalloying AZ31 with Ca, Sr, and Ce decreased the peak flow stress and slightly decreased the critical strain to initiate DRX under some testing conditions. This indicates that an accelerated DRX occurs;
- Microalloying has an effect on decreasing interpass softening by retarding the growth of the recrystallized grains due to pinning generated by the increased volume fraction of second particles, which can be used for controlling the as hot worked grain size.

As-rolled and As-annealed Microstructure as well as Texture of Rolled Sheets

- Ca and Sr promote a more refined and uniform microstructure in as-rolled and asannealed sheets. This may be due to the refined as-cast grain structure and the more numerous second phase particles. However, the sheet with Ce only addition shows no such effect; here there was no grain refinement but there was an increase in the numbers of second phase particles. This suggests that grain refinement is more important that the numbers of particles, in this case;
- Microalloying does not change the basal texture of Mg-sheets, but reduces its
 intensity, which may be due to the operation of recrystallization by PSN. The
 weaker basal texture would contribute to the improvement of formability.

Tensile Behavior and Microstructure

- At room temperature, microalloyed alloys have an equal or a better EL (%) than AZ31 base alloy although the yield strength increase may be slight, except for the alloy with Ca only. This indicates that multiple alloying (e.g. Ca+Ce, Ca+Sr, or Ca+Sr+Ce) are beneficial to the improvement of their room temperature EL (%);
- At elevated temperature, alloys with multiple microalloying additions (Ca, Sr, and Ce) or only Ca show an improvement in ductility at almost all testing conditions although microalloying does not change the deformation mechanisms (climb-controlled dislocation creep deformation when stress exponent 4<n<8; or superplastic deformation by grain boundary sliding when stress exponent n=2). Under the superplastic deformation condition, the maximum EL for the alloy with three microalloying additions is as high as 552%, and is improved by 59% compared to the base alloy AZ31 (EL: 347%);
- The microstructure evolution under superplastic conditions (450 °C and strain rate of 0.0003s⁻¹) reveals that dispersive second phases in microalloyed AZ31 sheet materials with multiple additions (Ca, Sr, and Ce) or only Ca, play important roles in maintaining their finer grain size during hot tension deformation, promoting

dynamic recrystallization in the matrix, and retarding the development of cavitations and necking during hot deformation, and therefore contribute to the promotion of grain boundary sliding and the improvement of formability;

Ce on Lattice Parameter of c/a Ratio in AZ31 Based Alloys

 Microalloying with Ce addition in AZ31 based alloys led to a slight reduction in the c/a ratio, which may contribute to the improvement of their formability;

Suggested Microalloyed AZ31 Alloys

• Multiple microalloyed AZ31 alloys with Ca+Sr+Ce, Ca+Sr; and Ca+Ce, (nominal additions of 0.2%, respectively), are suggested for producing Mg-sheets in this study. These alloys show optimized microstructure, improved hot deformation behaviors (especially under superplastic deformation conditions), and equivalent or better general mechanical properties comparing with AZ31 base alloy.

Design of Microalloyed Wrought Mg-Alloys

From the above study based on AZ31, to improve formability and maintain a reasonable strength, the following general principles are key points.

- Refining the as-cast grain structure, which would lead to refined as hot deformed and as annealed grain structure in subsequent processing;
- Forming small and dispersive second phases during solidification, which can be thermally stable in the temperature range of hot deformation process and uniformly distributed in matrix after hot working;

 Multiple microalloying is strongly suggested due to its combined and complementary advantages for balanced mechanical properties and formability under various application conditions;

Process Design of Mg Wrought Alloys

To produce a refined, homogenous structure:

- A refined and uniform as-cast microstructure is indispensable, since it promotes a fine and uniform as-hot rolled microstrucure; these can be obtained by casting at high cooling (solidification) rate and suitably alloying;
- Hot rolling conditions should be chosen to generate DRX by necklacing at grain boundaries and transgranular DRX at twins. This should lead to a fine and uniform as hot rolled grain structure;
- A certain amount of fine, homogenously dispersed second phases in uniform fine grained matrix seems to be desirable for good formability of sheet materials, especially under superplastic deformation conditions.

Chapter 10

Contributions to Original Knowledge

- 1. A full investigation on the effect of micoralloying (Ca, Sr, and Ce) on microstructure and hot deformation mechanisms of AZ31 was performed for the first time;
- 2. The formation of new phases in AZ31 base alloy by microalloying with Ca, Sr, and Ce, was well predicted by using FactSageTM thermal calculation and confirmed by EPMA for the first time;
- 3. Microalloying levels of Ca and Sr promote fine grain microstructure in as-cast, as-hot rolled, and as annealed materials, and resist the grain growth during further hot deformation. The effect of the initial microstructure on subsequent hot working microstructure was delineated for the first time;
- 4. It was for the first time identified that the effect of Ca and Sr on as-cast grain size is significant under high cooling (solidification) conditions as well as low solidification rates;
- 5. The mechanism of refining second phase in AZ31 by microalloying is due to forming dispersive new phases and reducing the amount of Mg-Al phase, which was revealed for first time;

- 6. With EBSD analysis, DRX mechanisms during hot compression in AZ31 based alloys were defined clearly, in which the operation of PSN mechanism was identified for the first time;
- 7. It is for the first time proposed that to obtain a fine and uniform as-hot rolled microstructure for Mg-alloys, a combination of DRX by necklacing at grain boundaries and DRX at transgranular twins is desirable for the design of process parameters;
- 8. Two hit compression testing was pioneered for Mg-alloys, which demonstrates the effect of microalloying on retarding the DRX-grain growth and the significance in control the grain size during multiple hot rolling process;
- 9. A thorough microstructure examination under superplastic tensile testing conditions was performed (microstructure evolution at different strains and fracture analysis) to define the effect of microalloying during hot deformation for microalloyed AZ31 sheets. It was revealed for the first time that the significantly improved formability is due to the existence of fine and dispersive second particles, which maintain the fine grain structure, therefore promoting gain boundary sliding and retarding the development of cavitations and necking;
- 10. It was for the first time consistently shown that multiple microalloying is a promising way to obtain an optimized microstructure and significantly improved hot formability due to their combined and complementary advantages;
- 11. The following principles for the design of Mg-alloys for producing sheets by multiple microalloying have been defined: i) obtain a refined grain structure; ii) form dispersive and thermally stable second phases; iii) obtain a fine and uniform as-rolled grain structure by DRX of necklacing, at twins and PSN; and iv) maintain some amount of dispersive and fine second phases to resist grain growth during further hot deformation.